INFRARED SPECTRAL MAPS OF STAR-FORMING REGIONS AND COOL-CORE GALAXY CLUSTERS

Geneviève Escande de Messières
Boyds, MD

B.A., Swarthmore College, 2004

M.S., University of Virginia, 2006

A Dissertation Presented to the Graduate
Faculty of the University of Virginia
in Candidacy for the Degree of
Doctor of Philosophy

Department of Astronomy

University of Virginia
August, 2011

Robert W. O'Connell

Rémy Indebetouw

Aaron S. Evans

Megan Donahue

Peter Arnold

Abstract

In this dissertation, I use infrared spectral maps of star-forming regions to explore the circumstances of star formation in the centers of cool-core galaxy clusters. Using *Spitzer*'s IRS and MIPS instruments, we present a rich spectral map of the nearest super star cluster, 30 Doradus, which acts as as a laboratory for extreme modes of star formation. Photoionization from local hot stars dominates in the region. We present IRS spectra based on sparse spectral maps of BCGs in nine cool-core galaxy clusters. Eight of the nine targets show optical and ultraviolet evidence of star formation. We compare MIR indicators of obscured star formation to evidence of exposed star formation. We find that the BCGs have weaker thermal dust continuum emission than expected for normal star-forming galaxies, relative to several metrics. In six of the targets, we find that star formation is progressing in an unusually exposed environment, consistent with a model of extended filaments with fine substructure containing star-forming knots. Two other galaxies in the sample evidently have vigorous star formation in a normal disk or nuclear starburst. The efficiency of star formation is high, assuming that the cooling gas is the source of fuel. We find temperatures and masses of the warm H_2 and contrast with other luminous sources of H_2 associated with shocks. We find that star formation powers the PAH and dust emission, but another source of heat (perhaps associated with the surrounding hot ICM) is responsible for the molecular gas emission in the galaxies in at least some targets. We consider shocks and energetic particle heating for the H_2. There are inconsistencies between our data and the type of shocks that power other MOHEGs, and our data are consistent with the particle heating model, but we do not rule out shock heating.

Acknowledgements

The composite image of Hydra A on the cover page shows 10 million degree X-ray-emitting gas in blue and jets of radio emission in pink. Optical observations in yellow show galaxies in the cool core cluster.

Image credit: Chandra Photo Album. X-ray: NASA/CXC/U.Waterloo/Kirkpatrick et al. (2009). Radio: NSF/NRAO/VLA. Optical: Canada-France-Hawaii-Telescope/DSS.

Professional

I gratefully thank the many scientists who have taken the time to advise me on my work and to discuss their research and mine. Any errors in this work are mine alone.

Foremost on the list is my excellent advisor, R.W. O'Connell, closely followed by my thesis committee (R. Indebetouw, A. Evans, M. Donahue, and P. Arnold) and my co-authors, particularly R. Indebetouw, M. Donahue, B.R. McNamara, G.M. Voit, M.W. Wise, A. Hoffer, and the SAGE team.

Thanks as well to the anonymous referees who have made a number of useful suggestions, and to R. Antonucci (for discussions including the emission profile of large vs small dust grains at a given radiation field). P. Appleton (especially for help with 24 μm diagnostics), L. Armus (for discussing the relationship of star formation and dust formation, and the role of emission lines as coolants to enable star formation), D. Calzetti and A. Crocker (for supplying tabulated plot data and discussion of star formation rates including the complications of star formation rates based on PAH emission), M. Cluver (for discussions on fitting the 7.7 μm PAH and for giving additional context on her work on Stephan's Quintet), A. Hicks (for valuable discussions and for significant assistance in determining UV-based evidence of star formation), D.C. Kim (for providing extensive discussion of the GOALS survey), P. Ogle (for taking extensive time to discuss the cool-core galaxy cluster spectra and their implications, their relationship to radio galaxies, and especially for his consultation on the warm H_2), J.D. Smith (who contributed significant software assistance), and M. Sun (for discussions on star formation in cool core galaxy clusters).

Those who have loaned data, contributed helpful discussions and suggestions, or assisted with software in the course of this project include in part J. Carlberg, J. Dickel, M. Dopita, E. Blanton, D. Farrah, G. Ferland and his students, B. Groves, N. Gugliucci, J. Hibbard, K. Johnson, J. Lazendic, J. Leisenring, C. O'Dea, J. Raymond, K. Sheth, G. Sivakoff, S. Points, L.M. Walker, D. Weedman, D. Wik, and G. Zasowski.

This project would not have been possible without extensive use of NASA's Astrophysics Data System Bibliographic Services, and the SIMBAD database. This project makes use of data products from the Two Micron All Sky Survey, which is a joint project of the University of Massachusetts and the Infrared Processing and Analysis Center/California Institute of Technology, funded by NASA and NSF. This project also makes use of products from NASA's distributed Space Science Data Services (SDSS) including the Multimission Archive at STSci (MAST), and of products from the NASA/CXC/SAO collaboration.

This work is based on observations made with the *Spitzer* Space Telescope, which is operated by the Jet Propulsion Laboratory, California Institute of Technology under a contract with NASA. I was supported by three Spitzer/NASA/JPL grants including #1288328.

Personal

I could never have gotten through graduate school alone. The ways in which I have been supported by those around me are too many to list here. My heartfelt thanks go to ...

... Bob, for being a teacher, a guide, and an understanding and patient advisor who could always identify what confused me and clarify it. Geelee, for being probably the sweetest person I know. Like you said, he's a lucky guy.

... the wonderful faculty and staff at the University of Virginia Department of Astronomy, and especially to the professors who taught me and to Jackie, Barbara, Janice, Howard, Jim and Charles who keep the place running.

... David, my "the rest is history" astronomy professor and advisor at Swarthmore College.

... Jeff - yeah, sorry about Pluto.

... Sela, for motivating me. I thought I was working hard until I moved in with you.

... my awesome, supportive and hopelessly nerdy classmates and friends at the department. ... Joleen, for being so interesting that we can't share an office. ... Jake, for pointing out the obvious, with style. Both of you, for luring me to UVa. ... Greg, for the cinnamon. ... Chengyu, for sharing quiet times. ... Janice, for rescuing my poor plants. ... Molly, for opening your home to me, and showing me how mojitos and guacamole are done. ... Lisa May, for swapping in to Musical Roommates. Maybe now we can finish *Gilmore Girls*. ... Nicole, who has taught me a lot about having a skeptical eyebrow. ... Kris, for telling me how to finish up. ... Ori, for never telling me about the jinx. ... Gail, for taking in a stray, and for the daily dose of awesome. ... Jarron, for a lovely drawing of Austen's leprechaun. Both of you, for explaining how R + L = J, because otherwise I would surely have gone insane by now. ... Paul. Who am I going to mooch camera equipment from now? ... Marios, roomie! ... Dan, for letting me take *one* normal picture. ... Kristen. Now it's down in writing - your brownie debt is paid. ... Kelsey and all the volunteers and kids for "Dark Skies, Bright Kids!" You provided a desperately needed sanity break, and tried my sanity at the same time. ... Howard, without whom I wouldn't last five minutes. Sorry I blew up your oven.

... Steph, for showing me that the real path to victory in Taboo leads through Queen Victoria and the East India Company and eventually to Mars.

... Kerrie and John, for the truckful of landscaping, the worms, and the walks. You're the best guides to the Monticello gardens. And especially for your inspiring words; I keep your cards forever.

... Joseph, who sustained me with delicious pizza and chewy debates.

... Michelle and John, who take me into the frozen wilderness, and show up on my doorstep with moving boxes or asparagus soup just when I need them the most. I'm so glad I don't own a car!

... Megan, for being my first grown-up roommate, for the delicious recipes (of course we have to add sugar), for letting me fall into you getting off the ski lift, and - this is huge - for getting me to start using a calendar.

... Jess, sister of my heart. Having thousands of pages of writing behind us made me feel that I could manage three hundred.

... My wonderful and growing family, who edited, rooted for me, beat me in Boggle, and lovingly shooed me away to get back to work. And to my baby nephews and niece, who provided me with the strongest motivation of all to finish up: to have more opportunities to play with them.

To my father, a gentleman and a scholar.

Table of contents

List of Figures

List of Tables

Chapter 1

General Introduction

Though stars make up less than one percent of the mass-energy budget of the Universe, star formation has a fundamental impact on the evolution and morphology of astronomical systems at all size scales, from the details of how a molecular core fractures into nascent solar systems, to the enrichment of the interstellar medium, up to the mechanics that help to regulate enormous cool core galaxy clusters.

The study of star formation is an active and changing field. While star formation leaves its signature across the electromagnetic spectrum, two major windows into its processes are in the optical / ultraviolet and infrared electromagnetic bands. The optical and ultraviolet evidence of star formation includes the distinctive continuum light profile of young, hot stars and narrow line emission from hydrogen gas ionized by the light of the newborn stars. Optical wavelengths are easily accessed from the ground, and space-based missions have expanded the ultraviolet study of star formation. The optical and ultraviolet wavelengths, however, are extremely vulnerable to attenuation from intervening material. Considering that star formation occurs within dark molecular cores, some absorption is inevitable. In active, embedded starbursts, the optical and ultraviolet light of the young stars can be almost completely absorbed by the clouds of gas and dust.

The infrared regime offers several major advantages in the study of star formation. The grains of dust or aromatic molecules that enshroud the star-forming regions effectively absorb the optical to FUV light of hot young stars. Large dust grains in thermal radiative equilibrium absorb most of the high-energy light, re-radiating the energy as a thermal infrared continuum at long wavelengths ($\sim 20 - 1000\ \ \mu$m). Smaller dust grains and molecules are stochastically heated when they absorb individual high-energy photons. Temporarily reaching temperatures between 100 and 1000 K, they emit continuum and broad line emission at short to intermediate MIR wavelengths ($\sim 5 - 20$ μm). The missing light from the optical and ultraviolet bands can be recovered by studying star-forming regions in the infrared. Hot young stars also ionize atomic gas and excite molecular hydrogen, giving rise to a range of interesting and useful transitions in the mid-infrared.

The infrared band, a double-edged tool, has a second major advantage in that gas and dust are also poor absorbers of infrared light. The distinctive profile of infrared absorption can allow an observer to distinguish whether a source of light lies in front of or behind a cloud of dust, or even to distinguish whether the source is completely unrelated to star formation. However, when high-energy light is reprocessed into infrared emission by dust, it is generally able to escape unhindered, allowing an observer to stare into the dark heart of a molecular core and find the stars being born there.

The *Spitzer* Space Telescope, launched in 2003, threw open a window into the infrared world. The near-infrared bands can be observed from the ground, but the atmosphere absorbs most mid- and far-infrared light. The new satellite telescope greatly improved upon the sensitivity of earlier missions, permitting sophisticated analysis of the infrared properties of large surveys of objects ranging from bodies in our own solar system to nearby star-forming regions to galaxy clusters. In particular, the Infrared Spectrograph (IRS), available during *Spitzer*'s cold mission from 2003 to 2009, offered sensitive spectroscopy of the active 5 - 30 μm band. Its mapping mode allows the construction of spectral maps giving detailed spectroscopic information across a region, a powerful tool for spatially resolving the complex processes that contribute to infrared emission.

The wavelengths accessed by the IRS cover a wealth of spectroscopic indicators. These include:

- Thermal emission from warm dust grains, heated by (and yielding clues about) star formation or the light from an active galactic nucleus (AGN);
- Broad, complex bands of emission from aromatic molecules heated by star formation or diffuse galactic light;
- Narrow emission lines of atomic gas which offer information about the conditions under which the gas was ionized, such as the hardness of the radiation field shining upon the gas (which can indicate the age of recently formed nearby stars), or the density of the gas, or the violent presence of an AGN;
- A series of narrow emission lines from the rotational modes of molecular hydrogen, the most abundant molecule in the Universe, tracing the processes that heat the molecules. These might include star formation, shocks, or interaction with an AGN jet and the surrounding hot gas.

1.1 Parts of the Thesis

In Chapter 2, we construct a rich spectral map of the 30 Doradus star-forming region, the massive complex that dominates the Large Magellanic Cloud. Nearby and easily studied, 30 Doradus provides a laboratory to study the processes of star formation in detail, and acts as a bridge between the smaller star-forming regions distributed in the disk of our galaxy and large, extreme forms of star formation in the more distant universe. Star formation processes in 30 Doradus are potentially a template for the early universe, where small irregular galaxies were commonplace and the overall metallicity lower. We use the strong low to moderate ionization emission lines that dominate the spectra to analyze the physical conditions in the ionized gas, as well as studying other features like regions of high extinction.

In Chapter 3, we present *Spitzer* IRS spectra based on sparse spectral maps of a sample of nine brightest cluster galaxies (BCGs) residing in cool-core galaxy clusters. Galaxy clusters have deep gravitational potential wells, dominated in mass by dark matter and a diffuse halo of the X-ray-emitting intracluster medium (ICM) at millions of degrees K. The BCGs at their cores are large ellipticals which generally do not exhibit signs of active star formation. However, about half of nearby galaxy clusters have low central entropy, allowing the cooling time in the center of the galaxy to fall below the age of the cluster. The inner mass of the ICM begins to contract under the overlying pressure, and radiates away its heat. Unchecked, it would quickly condense onto the BCG in a cooling catastrophe, fueling large rates of star formation. Evidence demonstrates that there is a remarkably efficient feedback process, not fully understood but probably linked to cooling-fueled jets from the AGN, to maintain the gas at a high temperature and prevent major cooling. Radio jets carving out X-ray cavities are a common feature of cool core BCGs, as demonstrated by the cover page image of Hydra A (citation above). While most of the gas is maintained in a hot state, 10% is able to cool down and provides fuel for star formation, which is measured in optical and ultraviolet light in 70% of cool core BCGs, and in eight of our nine targets (see Chapter 4). Cool core BCGs are undergoing active study in X-ray, radio, optical/UV, and infrared fields. The spectacular filamentary networks of ionized gas and warm H_2 emission detected in the nearer, better-resolved systems are of particular interest. We seek to expand the understanding of star formation in BCGs by studying them in infrared light. We expect to find high rates of star formation based on infrared evidence, considering that the optical and ultraviolet evidence represents only the amount of light able to escape from star forming regions which may be deeply embedded.

We find most of the BCGs to have strong emission from low-ionization atomic and rotational molecular hydrogen lines. We measure emission from dust and PAH features and, and analyze the properties of the material emitting these separate spectral components, and the character of their heating sources. We model the spectra with a set of simulated time-averaged starburst spectra.

In Chapter 4, we expand upon the analysis of the IRS spectra of the cool core BCGs, focusing on the indicators of star formation activity. We review the conclusive optical and ultraviolet evidence that star formation is actively occurring in these targets. We analyze the MIR features, including the low-ionization atomic emission lines, the PAH emission, and continuum emission, to obtain information about the extinction, excitation levels, and temperature of the infrared-emitting material. We derive star formation rates from a variety of mid-infrared features (atomic line, PAH, and continuum emission) and compare with existing estimates in an attempt to refine the overall rate and character of star formation occurring in these targets. We use the relative strengths of the star formation rate indicators as a metric of the relative power of each component of the spectrum. We calculate the efficiency of star formation in these targets relative to the cooling rate, which nominally provides most of the fuel for star formation.

Finally, in Chapter 5, we analyze the extraordinarily luminous pure rotational emission lines of H_2. The most abundant molecule in the universe, composing the dense molecular clouds inside which normal star formation takes place, is nearly invisible. It can be directly studied in distant targets, however, when it is heated up to temperatures between 100 and 2000 K by the processes of star formation, in shocked regions, or potentially by some of the heating processes that act in a cool core galaxy cluster BCG. H_2 gas may exist in a filament morphology in these sources, dredged out of the core of the BCG by the jets from the AGN and magnetically supported in a complex thread structure. In such a morphology, the H_2 is vulnerable to an array of heating sources which may also include shocks, or cosmic rays from the hot radio lobes, plasma waves, or conduction from the surrounding hot ICM.

We perform excitation analysis to find temperatures and masses of warm H_2, and compare to other luminous sources of warm H_2 emission. We contrast with other MOHEGs, in which H_2 is generally heated by shocks, and consider whether shocks or saturated conduction from the ICM are more likely to heat the H_2 in the filaments. We test the efficiency of the H_2 heating relative to the power of star formation and relative to low-ionization emission, and discuss the source of heat for the H_2.

1.2 Explanation of Credit

The thesis comprises four major chapters, as well as a general introduction and conclusion. Each chapter is intended to stand alone as a refereed publication. In this letter, I explicate my contributions. While I have major contributions to each chapter, all of which played a significant role in my development as a scientist, the last two chapters are the ones in which the scientific analysis and writing should be considered primarily my work.

Chapter 2 appears as Indebetouw et al. (2009). As the second author, I prepared the IRS spectral map of 30 Doradus, wrote the data reduction sections including the appendices, prepared many of the figures, created the Humphreys extinction map, and performed and wrote much of the extinction analysis. In addition to advising me on that work, the first author reduced the MIPS cube, performed almost all of the analysis, particularly the analysis of the ionized conditions in 30 Doradus, and wrote the majority of the paper. The paper benefited significantly from the SAGE collaboration and the contributions of co-authors.

I have also participated in subsequent collaboration on this work, including serving as a fourth co-author and editor for Martínez-Galarza et al. (2011, accepted), which employs the reduced MIR spectral map of 30 Doradus as a test case for Bayesian models of starburst SEDs based upon the Groves et al. (2008) models.

Chapter 3 appears as Donahue et al. (2011). As the second author, I prepared the IRS spectra of cool core galaxy cluster BCGs and the extracted feature strengths and other measurements of the spectra. I prepared several figures and tables. I wrote the observations and data analysis section, which received major revision from the first author. I contributed revision, editing and close discussion throughout the paper. The first author performed most of the writing and analysis, as well as closely advising my work. The third author, R. O'Connell, served as the primary advisor to my work as well as working closely with us on the content. Co-author A. Hoffer prepared the IRAC and MIPS broadband photometry, which plays a key role throughout Chapters 3 and 4. Additional co-authors contributed discussion and review.

Chapters 4 and 5 will be submitted for publication shortly, appearing under my name. They are primarily my work, with major help from the second author (R.W. O'Connell) who served as the primary advisor as well as contributing some of the writing for Chapter 4. The thesis committee and co-authors offered significant and helpful feedback. In particular for Chapter 4, co-author B. McNamara provided evidence and discussion of optical and UV evidence for star formation, and co-author M. Donahue consulted throughout upon this work.

Chapter 2

Physical Conditions in the Ionized Gas of 30 Doradus

2.1 Abstract

We present a mid-infrared spectroscopic data cube of the central part of 30 Doradus, observed with *Spitzer*'s IRS and MIPS/SED mode. Aromatic dust emission features are well-detected but not particularly strong. Also present are emission lines of Si II, molecular and atomic hydrogen. The dominant spectral features are emission lines from moderately ionized species of argon, neon, and sulphur, which are used to determine the physical conditions in the ionized gas. The ionized gas excitation shows strong variations on parsec scales, some of which can plausibly be associated with individual hot stars. We fit the ionic line strengths with photoionization and shock models, and find that photoionization dominates in the region. The ionization parameter U traces the rim of the central bubble, as well as highlighting isolated sources of ionization, and at least one quiescent clump. The hardness of the ionizing radiation field T_{rad} reveals several "hot spots" that are either the result of individual very hot stars or trace the propagation of the diffuse ionizing field through the surrounding neutral cloud. Consistent with other measurements of giant H II regions, $\log(U)$ ranges between -3 and -0.75, and T_{rad} between 30000 and 85000K.

2.2 Introduction

The 30 Doradus region of the Large Magellanic Cloud (LMC) is an ideal laboratory in which to study the effect of massive star formation and its feedback on the circumcluster interstellar medium (ISM). Star formation processes in the Magellanic Clouds are potentially a template for the early universe, where small irregular galaxies were commonplace and the overall metallicity lower. In particular, the star formation rate measured relative to molecular mass may be high in the LMC compared to our Galaxy, but that measurement is complicated by interpretation of CO data in molecular clouds that are known to be more porous and deeply penetrated by ultraviolet radiation, and an uncertain CO-H_2 conversion factor (e.g. Poglitsch et al. 1995; Bernard et al. 2008).

30 Doradus itself, the brightest star formation region in the LMC, contains several 10^5 $M_\odot$ of molecular hydrogen traced by ^{12}CO(1-0) (Johansson et al. 1998), much of which is in two elongated clouds that form an arc or ridge in the center of the nebula (see Figure 2.1 for a multiwavelength view and Figure 2.2 for the distribution of CO). That molecular material is probably only the remnant of the cloud that formed the central cluster and thousands of OB stars. Observations of higher energy CO transitions suggest that this remnant ridge of molecular gas is quite warm and dense (Kim 2007), and near-infrared observations have revealed that it is actively forming new stars (Hyland et al. 1992; Rubio et al. 1998; Maercker & Burton 2005)

The dominant star-forming cluster of the 30 Doradus H II region is NGC 2070, whose dense center, R136, is usually considered the nearest super star cluster (SSC). R136 contains 39 O3 stars, a total stellar mass of $\simeq 5 \times 10^4$ $M_\odot$ within 2.5 pc, and stellar densities exceeding 5×10^4 $M_\odot pc^{-3}$ (Hunter 1999; Walborn 1991). Extragalactic SSCs are the hosts of one of the most extreme modes of star formation in the universe, may develop into globular clusters, and play a key role in galaxy formation (Johnson 2004). At a distance of 50$\pm$2.5 kpc (see discussion of the LMC distance and uncertainty in Schaefer 2008), 30 Doradus is close enough to study at the parsec-scale resolution that is required to understand the formation and feedback effects of individual stars, and a prime target for detailed study of the same mechanisms which operate in more distant and massive SSCs.

Observations at mid-infrared (MIR) wavelengths offer several advantages for studying star formation and its interaction with circumcluster dust and gas. MIR (here roughly defined as 5-50 μm) continuum emission is generally dominated by radiation from very small dust grains (VSGs); the broad shape of the continuum is sensitive to the VSG size and temperature distribution, and hence indirectly to the radiation intensity in photon-dominated regions, and to the destruction of smaller grains as would be expected above 2000K and in H II regions. Broad ($\sim$1 μm) dust emission features are also present between 3 and 19 μm. These previously named "unidentified infrared bands" result from distortion (bending, stretching) modes of aromatic molecules containing tens to hundreds of carbon atoms. (Most features have been attributed to polycyclic aromatic hydrocarbons, PAHs, but unique astrophysical identification is a work in progress). Analysis of relative strengths of PAH features reveals their size and ionization state which is expected to change in intense radiation fields. Extinction by dust in the infrared is low compared to other wavelength regimes. Observations in the MIR can pierce cold molecular clouds and reveal the star-forming regions that they shroud. There are two major bands of absorption by silicate dust at 9.7 and 18 μm, whose shape and strength provide further diagnostics of the dust in the region. Mid-infrared (MIR) spectroscopy of the entire 30 Doradus region with *ISO-SWS* (Sturm et al. 2000) revealed a continuum-dominated spectrum with very weak silicate absorption and also only modestly strong aromatic emission features. The 4 spectra taken in 30 Doradus with ISOPHOT (Vermeij et al. 2002) similarly show low ratios of PAH strength to IR continuum.

The most recent and sensitive MIR continuum observations of the Magellanic Clouds were obtained as part of the *Spitzer* (Werner et al. 2004) Legacy program "Surveying the Agents of a Galaxy's Evolution" (SAGE), using IRAC (3–8 μm; Fazio et al. 2004) and MIPS (24-160 μm; Rieke et al. 2004). The goals of SAGE are to conduct a detailed study of the dust processes in the ISM, to complete a census of newly formed stars in order to find the star formation rate in the LMC, and to study evolved stars with high mass loss rates in order to determine the rate of mass injection into the ISM (Meixner et al. 2006). Figure 2.1 places the MIR emission from 30 Doradus in its multiwavelength context. 8 μm emission traces the same arc-shaped ridge seen in the optical, delineating the edge of a bubble probably blown by R136 and filled with hot X-ray emitting plasma. The remaining molecular material in the region is also located in that ridge.

This paper presents a new spatially filled spectral cube of 30 Doradus with the low-resolution modules of *Spitzer*/IRS (Houck et al. 2004) and with the SED mode of *Spitzer*/MIPS (Rieke et al. 2004; Lu et al. 2008). The sensitivity of this dataset greatly exceeds the previous ISOCAM-CVF data (Madden et al. 2006), which only provided maps of the few strongest ionic lines, but tentatively showed a gradient of decreasing excitation in the [Ne III]/[Ne II] ratio as a function of distance from R136, and signs of PAH destruction in the central regions of the nebula.

The data are described in sections §2.3. In particular, §2.3.1 and §2.8 discuss reduction and artifacts, §2.3.3 the line and feature fitting procedure, and §2.9 quality assurance tests including a comparison with high-resolution IRS data from Lebouteiller et al. (2008). In §2.4.1 we describe the general results – the spatial distribution of emission lines and their ratios. §2.5 describes the derived distribution of matter – electron density and dust, and §2.6 the distribution of radiation evident in the excitation of the gas. We compare the data with photoionization and shock models, and summarize and discuss implications in §2.7.

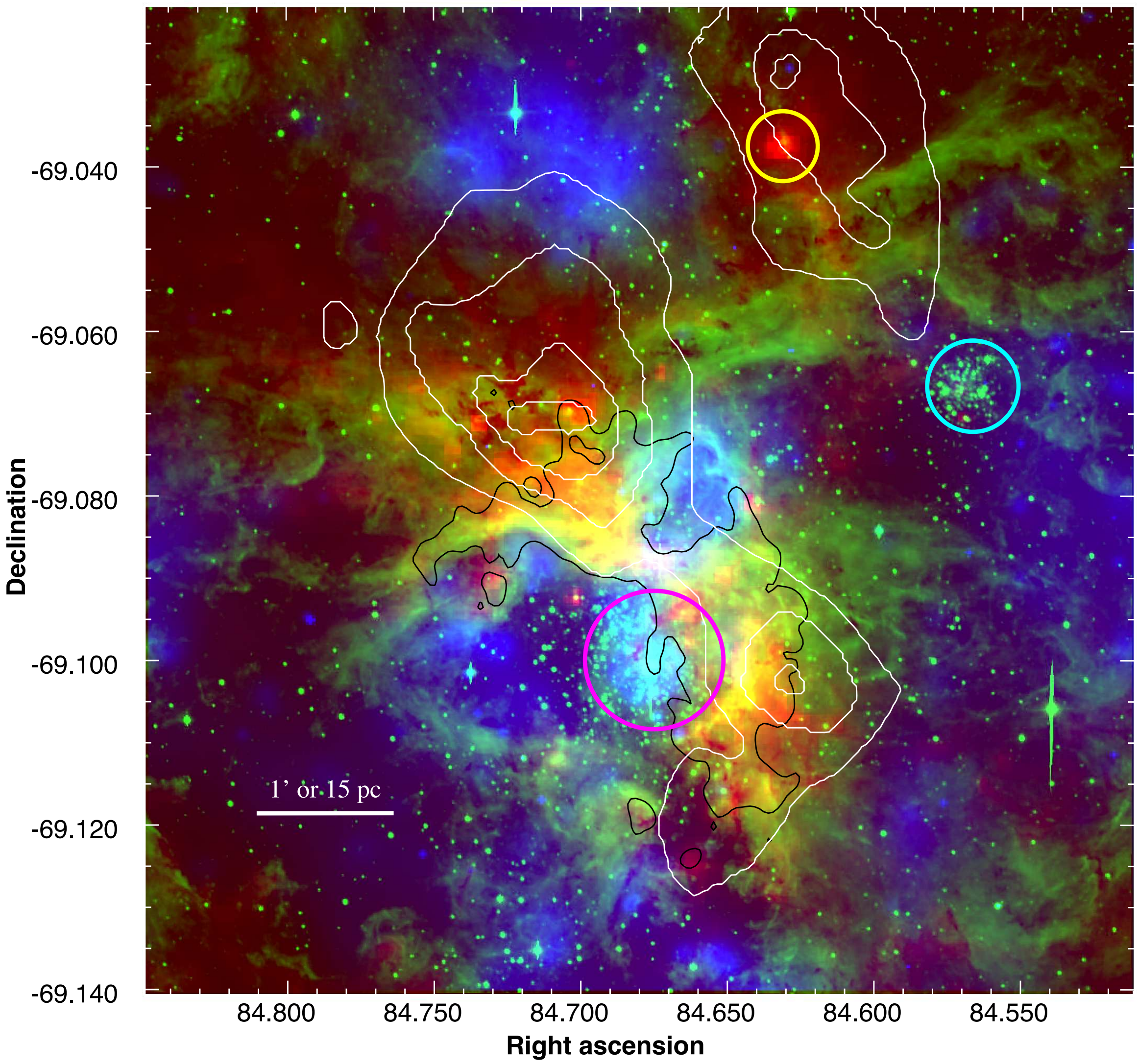

Fig. 2.1.— The 30 Doradus nebula. Red: IRAC 8 μm image (SAGE). Green: EO B-band image. Blue: broad-band soft X-ray image, $0.5-2$ keV (private correspondence and Townsley et al. 2006). All images are on a linear scale. White contours: ^{12}CO(1-0) emission (Johansson et al. 1998). Black contour: a single level of 3cm radio emission, to guide the eye (see Figure 2.2). Magenta mark: the star cluster R136, core of NGC 2070, at $5^h38^m42^s$ -69°06′00″. Cyan mark: the star cluster Hodge 301, at $5^h38^m16^s$ -69°04′00″. Yellow mark: an IR point source in the molecular cloud [JGB98] Dor-06 (Johansson et al. 1998), at $5^h38^m31.63^s$ -69°02′14.6″. This source is also marked in white in Figure 2.4 and discussed in §2.3.2.

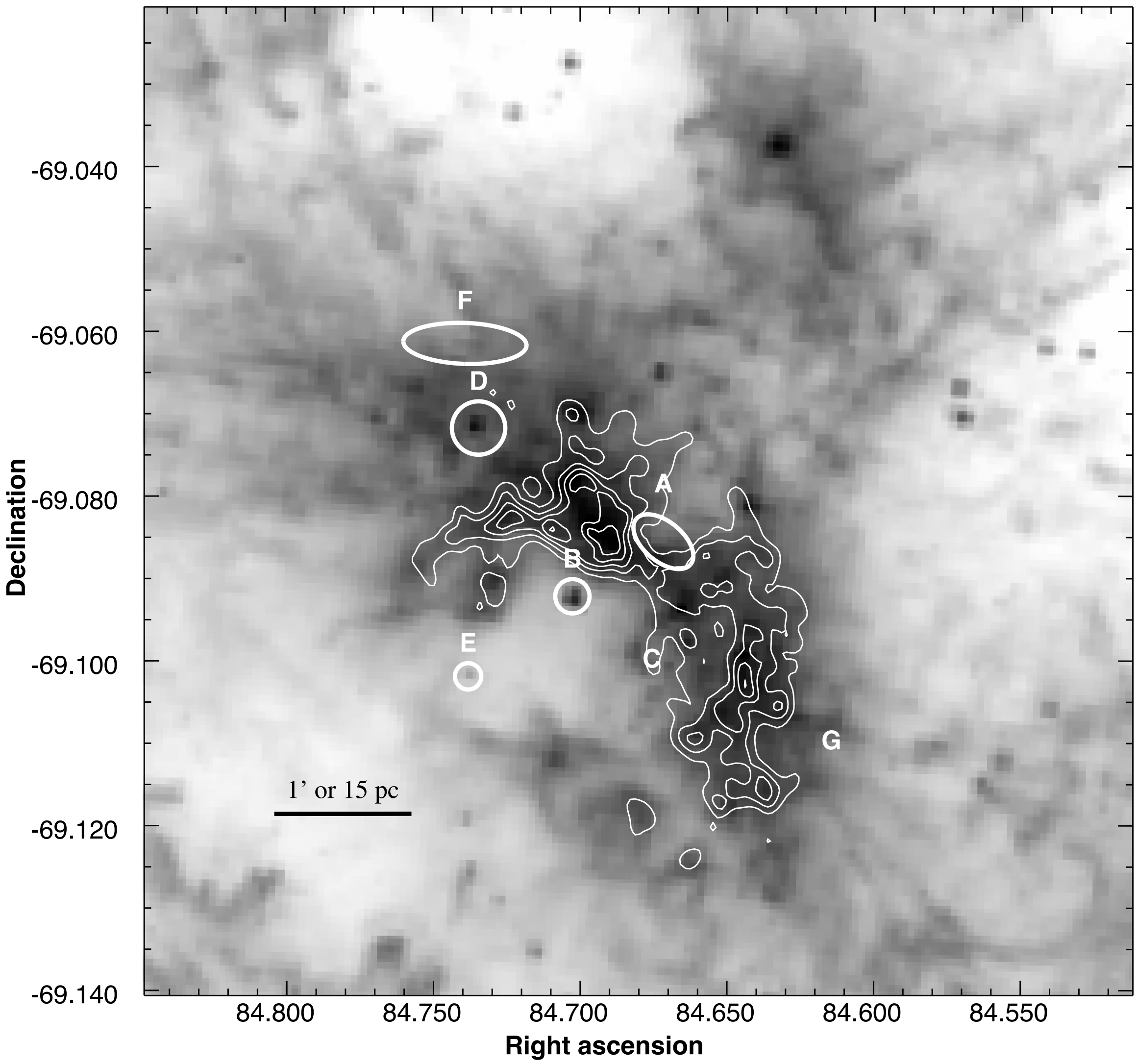

Fig. 2.2.— IRAC 8 μm image (log scale). White contours: high-resolution 3cm continuum from Lazendic et al. (2003). Contour levels: 6, 9, 12, 15, 18, and 21 $\times 10^{-3}$ Jy/bm. Sources of interest marked here are listed in Table 2.2, described in §2.4.3, and their spectra shown in Figure 2.17.

2.3 Observations

The *Spitzer* Infrared Spectrograph has $\gtrsim$100 times greater spectroscopic sensitivity than the previous premier infrared observatory, *ISO-SWS*, and $\gtrsim$10 times higher spatial resolution than the SWS aperture size. We used the four low resolution modules of the IRS. The spectral resolution ranges from 60 to 120 (Spitzer Science Center 2006)[1], with reliable wavelength coverage as noted in section 2.8.3. The four modules are the short wavelength / low resolution second order (SL2), short wavelength / low resolution first order (SL1), long wavelength / low resolution second order (LL2), and long wavelength / low resolution first order (LL1). Our data is divided into eighteen Astronomical Observing Requests (AORs), each containing many BCD (basic calibrated data) frames, which are pipeline-processed images of the IRS chip.

We observed 30 Doradus over five days in September of 2006, using *Spitzer's* spectral mapping mode in order to obtain detailed spatial information. The total amount of time on target was 74 hours. We used 3440 slit pointings, covering 40.5 square arcminutes in the short-wavelength modules and 69.1 square arcminutes in the long-wavelength modules (see Figure 2.3). Each slit overlaps half of the preceding one, and each row of slits overlaps half of the preceding row, so every point on the map was observed at four separate slit pointings. There were three repetitions per pointing for the SL observations, at 14 seconds each (for a total time of 168 s for each point on the SL maps), and four repetitions per pointing for the LL observations, at 6 seconds each (for a total time of 96 s for each point on the LL maps). The result is four large and dense spectral cubes, one for each module.

We also made separate observations of a nearby region of comparatively blank sky, bracketing our target observations in time, to comprise background observations

[1]Available at: http://ssc.spitzer.caltech.edu/documents/SOM/

and to better characterize rogue pixel response. The total time on background was 44 minutes.

2.3.1 Reduction of IRS data cube

We used the basic calibrated data (BCD) from the Spitzer Science Center pipeline version S14.4.0. The main tool for the assembly and reduction of our data cube was CUBISM (Smith et al. 2007a), which is designed for spatially dense IRS maps. The functions of CUBISM include tools to reduce the data (subtracting background, applying a slit loss correction function, trimming the slit in the spatial direction, masking pixels that are flagged by the pipeline, and applying algorithms to identify rogue pixels) and to extract spectra and maps from the data cube.

§2.8 describes in detail our procedure for calibrating and adjusting the flux levels such that the different spectrograph modules could be combined into smooth spectra. In brief, we used contemporaneous off-source background observations to subtract the thermal background. We used measurements of the slit-loss correction function provided by the *Spitzer* Science Center to undo that part of their point-source-based calibration (since our observations are more similar to a uniform diffuse source than a point source). Finally, we adjusted spectra from different modules to match each other.

§2.9 describes our comparisons of high and low-resolution spectra in 30 Doradus to test the fidelity of our fitting process. We find that the strengths of even somewhat blended lines are recovered well in the low-resolution spectra.

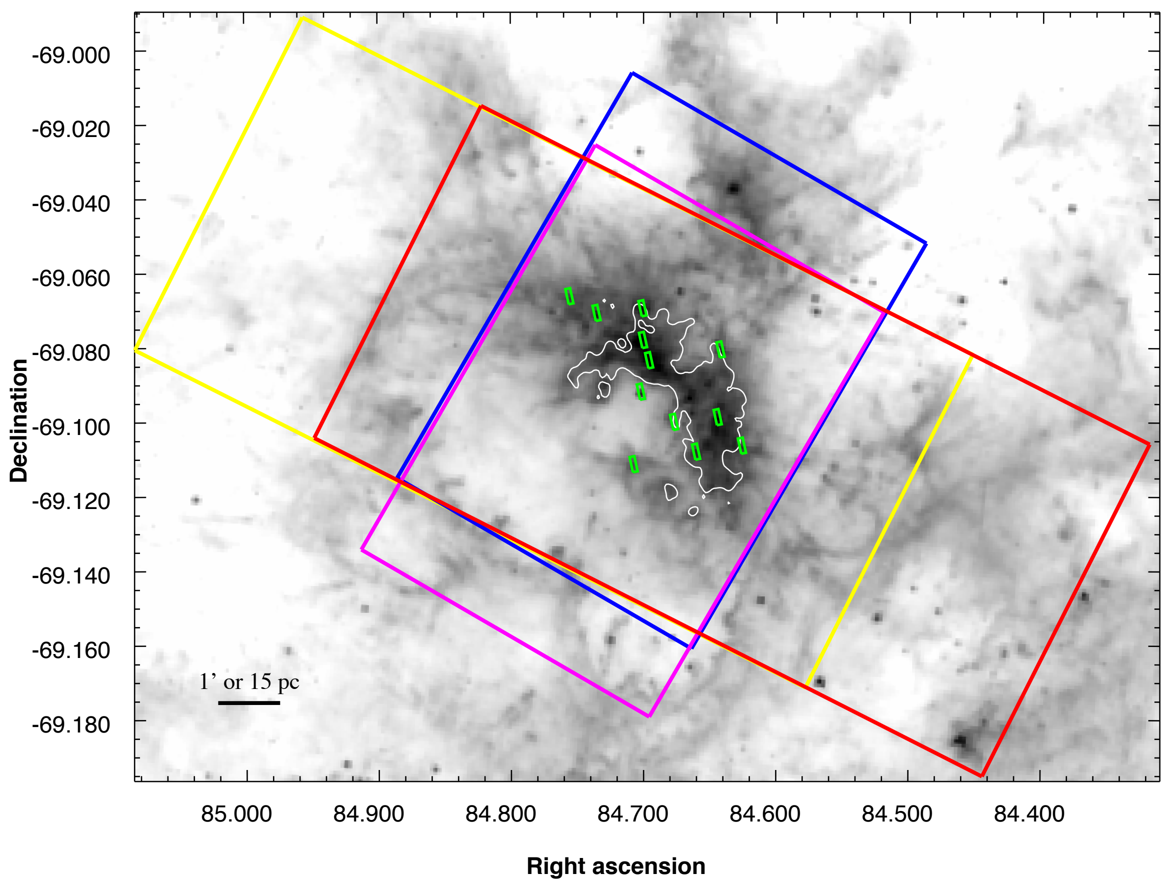

Fig. 2.3.— IRAC 8 μm image with the scope of coverage in each of the IRS modules shown. Red: LL1. Yellow: LL2. Blue: SL1. Magenta: SL2. Green: high resolution GTO apertures (see §2.9).

2.3.2 Artifacts in IRS data cube

There are two major artifacts which appear in a 2-D map of our data cube at any given wavelength. In all four modules, there are numerous faint stripes, one pixel wide, which cross the map in the direction that the slit scans. In the two SL modules, there is a broad intensity discontinuity and associated bright region in one area of the map. The affected region varies with wavelength. The faint stripes appear to be mainly caused by hot pixels on the IRS chip. As the slit was stepped across 30 Doradus, each hot pixel was "dragged" across the map, creating a bright stripe. They can be eliminated via two cleaning methods: wavsamp trimming and rogue pixel masking. The intensity discontinuity is caused by saturation in the peak-up image, and must be corrected by fitting a correction factor to the regions of the chip between the SL modules.

The Spitzer Science Center has defined a polygon, called the wavsamp, defining the active area to extract from the IRS chip for each module. In the case of 30 Doradus, the default wavsamp tends to be too generous in the spatial direction, including a few pixels where the spectral response is reduced. By trimming it, we were able to eliminate some of the faint stripe artifacts.

It is possible to determine which pixels on the IRS chip contribute to a given point in the data cube, using a CUBISM tool called backtracking. Backtracking from the artifacts in the maps demonstrated that most, if not all, of the remaining faint stripes are caused by individual rogue pixels, whether hot or cold. In addition to masking the pixels automatically flagged by the Spitzer Science Center pipeline, we employed CUBISM's automatic rogue pixel masking algorithms at both the global and record levels. At the global level, we masked any pixel which deviated by at least 2.5 sigma from the median pixel level in at least 35% of the records. At the record level, it was necessary to be much more conservative to avoid masking out real spectral features. We masked any pixel which deviated by at least 7.5 sigma in 70% of its occurrences in the cube. The procedure missed some pixels which were clearly hot or cold, so we also manually marked a set of global and record level rogue pixels. In the resulting cubes, the faint stripes were greatly reduced.

The other major artifact, the intensity discontinuity, is caused by saturated sources on the peak-up image (PUI), primarily by bright point sources in the northern part of the region which are marked in white in Figure 2.4. The northernmost of these is the source marked in yellow in Figure 2.1. By examining the records associated with the affected region on the map, we can see that where a source saturates several neighboring pixels in the peak-up image, there is a bleed-over effect that reduces the response of the rest of the IRS chip (BCD image) in those rows, and may increase the response in neighboring rows. The result is broad, uneven dark or bright stripes in a 2D map extracted from the cube. The location varies with wavelength because as the PUI is scanned across the bright source in space, the artifact changes position on the BCD frame, i.e. changes wavelength. Simply masking all affected pixels at the record level results in holes in the maps at many wavelengths. Instead, we chose to mend the response. We selected all rows that intersected a group of saturated pixels on the peak-up image, with a margin of two rows on either side. These are the affected rows. We found the continuum level in adjacent rows, excluding major emission lines, and linearly interpolated across the affected rows. In the case of affected rows that corresponded to continuum emission, we replaced the values with the interpolated values. In the case of affected rows that corresponded to atomic or PAH emission, we attempted to restore the base continuum level below the emission line by adding the interpolated value, and subtracting out the median value of the affected rows in the region between the SL1 and SL2 chips, which is the bias level of the affected rows. The artifact is reduced, though not eliminated. The result is a complete cube, but with localized regions that have larger uncertainty in the SL1 and SL2 modules (see the cyan and magenta regions marked in Figure 2.4). For the purposes of presentation, the areas where the artifact's effect is still distinct have been cropped out of each map.

At some wavelengths in the SL cubes, a large region of somewhat elevated emission is still visible after our corrections. This artifact appears to be another result of the saturation in the peak-up images. After a saturation event, the response of the chip is elevated for the remainder of the AOR. The resulting artifact, which can be seen in maps at a variety of wavelengths (for example, 5.2, 6.3 and 10.7 μm), is localized in space. This low-level artifact is also generally reduced in continuum-subtracted images, because the effect is broad on the BCD frame, and thus broad in wavelength as well.

2.3.3 Spectral Features and Line Fitting

Hot dust emission is responsible for the overall shape of the continuum in 30 Doradus and its strong rise toward the red. Using the fitting package PAHFIT (Smith et al. 2007b), we fit the continuum with an assortment of four thermal functions from 40 to 300K and a stellar blackbody of 5000K (the fit is insensitive to exact temperature as long as it peaks blueward of our shortest wavelength 5 μm). The integrated spectrum of the entire region is shown below in Figure 2.5, and astrophysically interesting spectra are described below in §2.4.3.

The broad PAH bands and unresolved atomic lines are blended in some parts of the spectrum. In order to decompose them, we fit the whole suite of emission lines

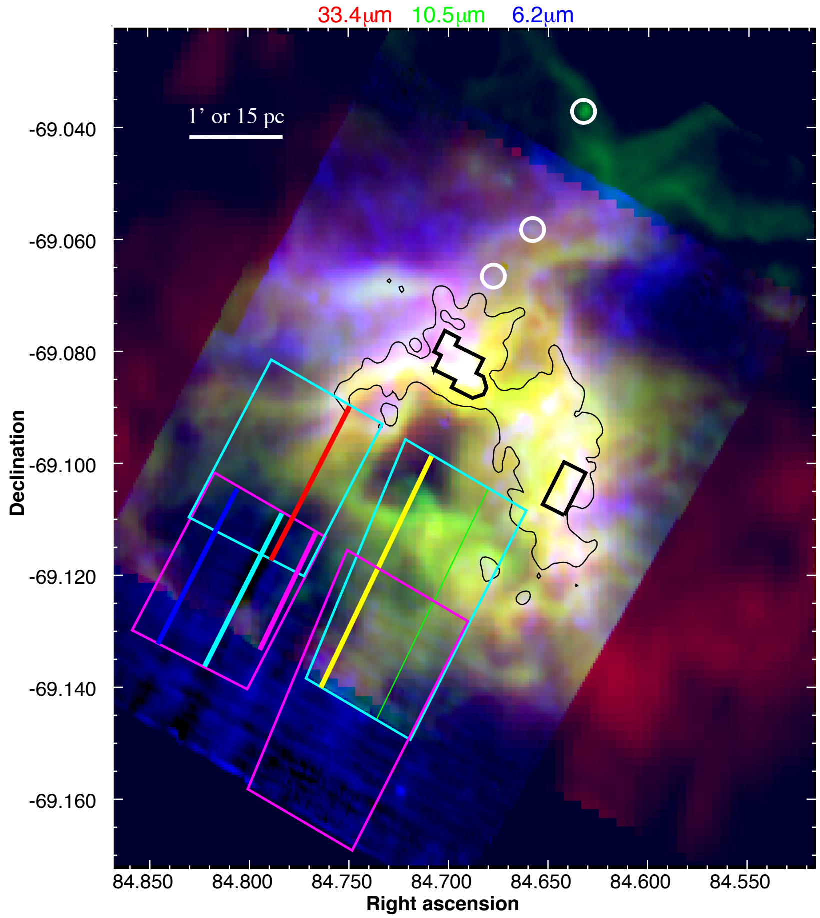

Fig. 2.4.— Three-color log-scale image generated from the IRS cube (see §2.3.1) with regions of interest overlaid. Black contour: a single radio contour to guide the eye (see Figure 2.2). The emission line maps are continuum-subtracted, and each is plotted at a scale that brings out detail. Red: [S III]λ33.4 μm, in the LL1 module. Green: [S IV]λ10.5 μm, in the SL1 module. Blue: PAH at 6.2 μm, in the SL2 module. The areas outlined in bold black are vulnerable to falling response (saturation) and strong fringing in the LL1 module (see §2.9). Continuum fits in these areas should be regarded with caution, as should the fitted line strengths of long-wave emission lines. The sources marked in white saturated the peak-up camera and caused dark stripes and other artifacts in the SL modules elsewhere in the map. The cyan regions represent the total affected area for the SL1 module, while the magenta regions represent the total affected area for the SL2 module. However, the main effect of the saturation is a stripe across the map that changes with wavelength. There are generally no severe effects in the rest of the map for a given wavelength. The approximate location of this stripe is marked by a series of bold lines, for several wavelengths corresponding to major emission lines in our spectra. Blue: [Ar II]λ7.0 μm. Cyan: PAH at 6.2 μm. Magenta: Humphreys-γ λ5.90 μm. Green: [Ar III]λ9.0 μm. Yellow: [S IV]λ10.5 μm. Red: [Ne II]λ12.8 μm. See §2.3.2 for more detailed discussion.

at once. Detailed analysis of the dust features will be addressed in a future work. The feature of greatest potential concern is blending of [Ne II]λ12.8 μm with the 12.7 μm PAH feature. The PAH contribution is much lower than the atomic line over much of 30 Doradus. In particular, Sturm et al. (2000) found that at the higher spectral resolution of *ISO-SWS*, the 12.7 μm PAH feature was undetectable relative to [Ne II]λ12.8 μm within the two *ISO-SWS* apertures (located on the ridge) – the lowest ratio of PAH to [Ne II] of any H II region they studied. We used comparisons with high-resolution spectra (see §2.9) and tests in parts of 30 Doradus that should be completely PAH-free, like the core of R136, to determine that the joint fitting of those two features is robust in 30 Doradus and uncertainties are properly accounted for.

2.3.4 MIPS SED cube

We also made contemporaneous observations[2] of 30 Doradus using the SED mode of the MIPS (Rieke et al. 2004; Lu et al. 2008). The raw data are responsivity-corrected, dark-subtracted, and illumination-corrected using the MIPS germanium pipeline (Gordon et al. 2007), with the difference that the illumination correction is derived from Galactic cirrus rather than zodiacal light. Wavelength correction is derived from observations of bright planetary nebula. Since 30 Doradus is so bright, we use the chopped "background" area simply as additional on-source observation, and assume that the thermal background is much less intense than the emission from the nebula itself. As with the IRS data, mapping the area with offsets equal to half of the slit width, perpendicular to the slit direction, yields a fully sampled spectral cube, with resolution $\lambda/\delta\lambda \simeq$25. Even with such poor resolution, we detect [N III]λ57.3

[2]AOR keys 18633728 and 18634240

μm with high significance over most of the map, and tentatively [O I]λ63.1 μm in the very center (§2.4.1). The shape of the dust continuum will be discussed in a future publication on the dust content of 30 Doradus, but we note that the SED peaks shortward of 75 μm, consistent with very high average dust temperatures (Figure 2.5).

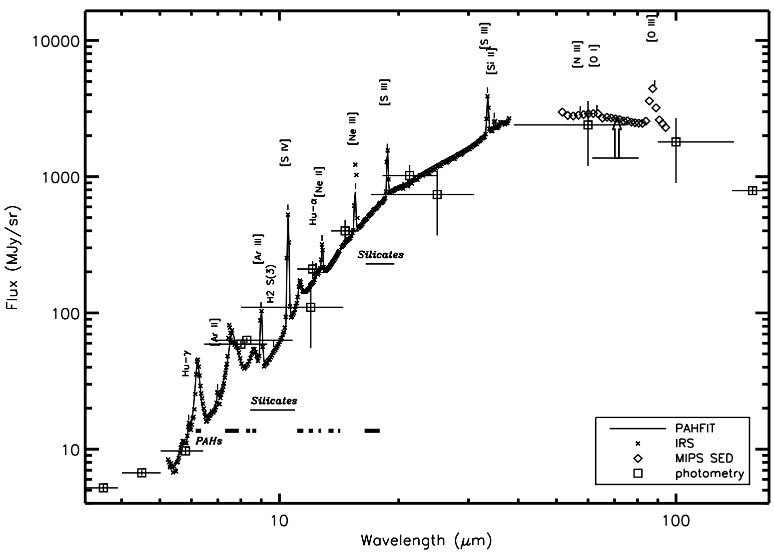

Fig. 2.5.— The spectrum of the entire 30 Doradus nebula (a square about 4' or 60 pc on a side centered on $05^h38^m44^s$ $-69°05'28''$). The observed spectra from IRS and MIPS/SED, and infrared photometric points, are plotted with symbols, while the fit we made to the IRS data is displayed with a solid line.

2.4 Results

Figure 2.5 shows the integrated spectrum of 30 Doradus, with dust and atomic features labeled. The overall continuum shape is typical of hot small dust grains in H II regions. The MIPS/SED data clearly show that the spectral energy distribution of the entire nebula peaks shortward of 70μm, indicating a quite warm average dust temperature. A full discussion of dust properties will be the subject of a subsequent publication. We note that the aromatic features are well-detected but not extremely strong - comparable to Galactic compact H II regions or compact blue galaxies, and weaker than the integrated spectra of entire spiral galaxies or the diffuse emission of the Milky Way (Galliano et al. 2008a; Peeters et al. 2002). The equivalent width of the 6.2 μm feature, averaged over this large aperture, is 0.61 μm. In particular, the weak 17μm feature may indicate a dearth of large neutral PAHs (Smith et al. 2007b) in this intensely ionized environment. The strongest spectral features are the ionic emission lines which are sensitive to physical conditions in the ionized gas. In the following sections we describe the spatial distribution of emission lines and their ratios, and show spectra of notable compact regions.

2.4.1 Spatial distribution of emission

Figures 2.6-2.14 show maps of ionic line emission in 30 Doradus. To first order, line emission follows the diffuse emission pattern seen at other wavelengths, of a broad arc or "ridge" surrounding an evacuated hole. The overall excitation of the region is immediately clear from the distribution of [Ar II] and [Ar III] – there is no detected [Ar II] in the evacuated hole. With an ionization potential of 15.7eV, the photoionization cross section and charge transfer with hydrogen ensures very little Ar^+ within an H II region (e.g. Sofia & Jenkins 1998). (Ionization potentials are listed in Table 2.1 for reference.) We note that the Ar^{++} recombination rate is highly uncertain, so absolute calibration of [Ar III]/[Ar II] has large systematic uncertainty (Morisset et al. 2004; Stasińska & Schaerer 1997). The similarity of overall morphology amongst the Ar, Ne, and S lines suggests that any variation of excitation across the nebula will be correlated with the structure seen in continuum from radio to infrared, although as we will explore thoroughly below, the shape of the hole varies somewhat, and there are some distinct locations of high excitation. The [Si II] distribution appears somewhat displaced away from R136 and the cavity, as would be expected since the line is strong in PDRs as well as ionized gas.

Lower ionization species have tentative detections in a few places, but never very strongly or widely distributed. Of particular interest is a peak near $5^h38^m44.9^s$ -69°05′13″ (source "0", §2.4.3), at which we also detect [N III]λ57.3 μm and [O I]λ63.1 μm in MIPS SED observations (see the northeastern region marked in Figure 2.11). The spectra in this part of the map are affected by fringing in the LL1 module (>20 μm), so a [Fe II]λ26.0 μm detection in the same region is considered tentative. The ratios of [Ne III]/[Ne II] and [S IV]/[S III] (and the MIR continuum) are high in this general area, but this region in the center of the ridge is complex, and the higher ionization species do not peak in exactly the same location as these lower ionization species. In fact, the peak of low-ionization species falls between two peaks of the [Ne III]/[Ne II] map.

Molecular hydrogen emission is detected in the central molecular ridge and marginally detected in several other locations. Only the S(3) 9.67μm line is reliably detected over much of the map. Tentative detections in our low-resolution spectra of the S(0) 28 μm line can be ruled out by examining the handful of high-resolution spectra in 30 Doradus. Detection of the S(2) 12.28 μm line independently of the neighboring

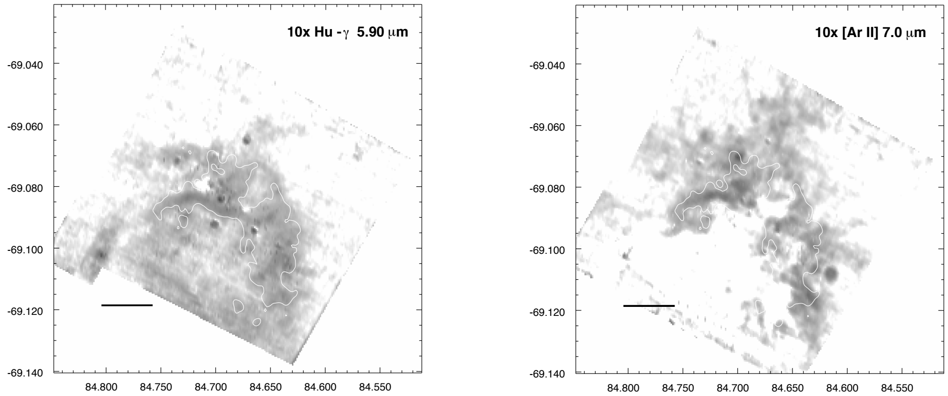

Fig. 2.6.— through Figure 2.11: Fitted atomic line maps. All plots are on the same log scale, ranging from 10^{-7} to 10^{-5} $Wm^{-2}sr^{-1}$. Note that four of the fainter maps have been multiplied by 10, and the brighter [O III] map has been divided by 100. The length of the black bar is 1" or 15 pc. White contours: a single level of 3cm radio emission, to guide the eye (see Figure 2.2).

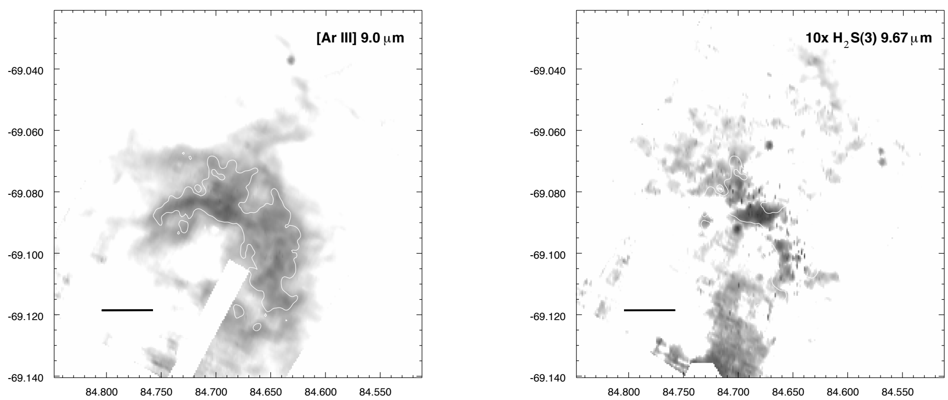

Fig. 2.7.— Fitted line maps (see caption, Figure 2.6).

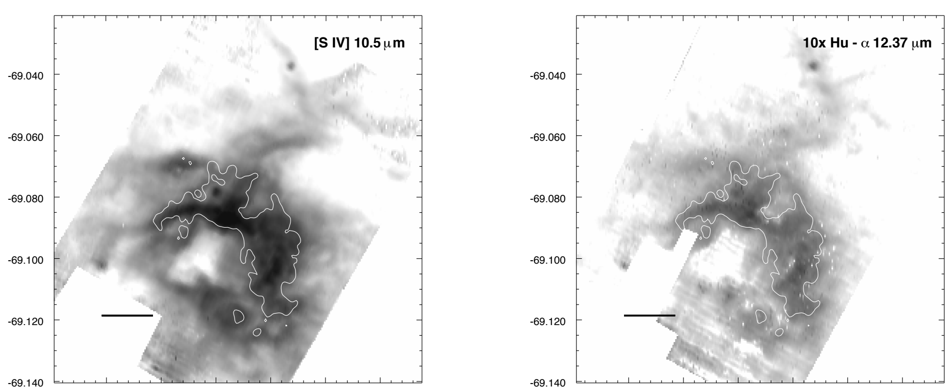

Fig. 2.8.— Fitted atomic line maps (see caption, Figure 2.6).

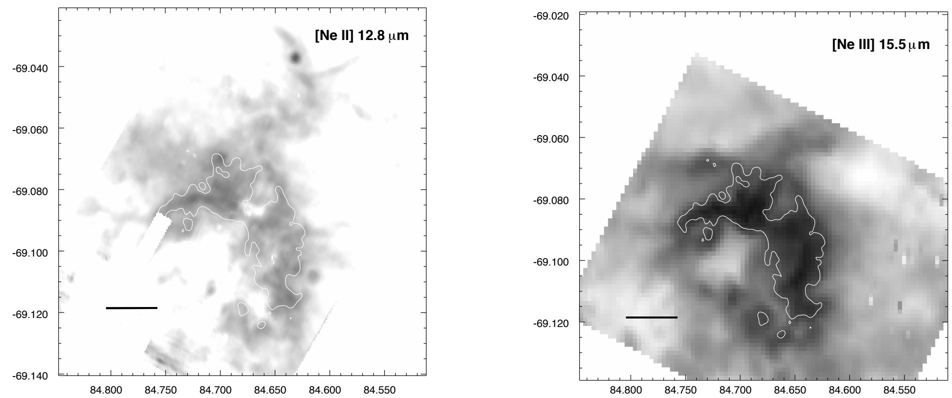

Fig. 2.9.— Fitted atomic line maps (see caption, Figure 2.6).

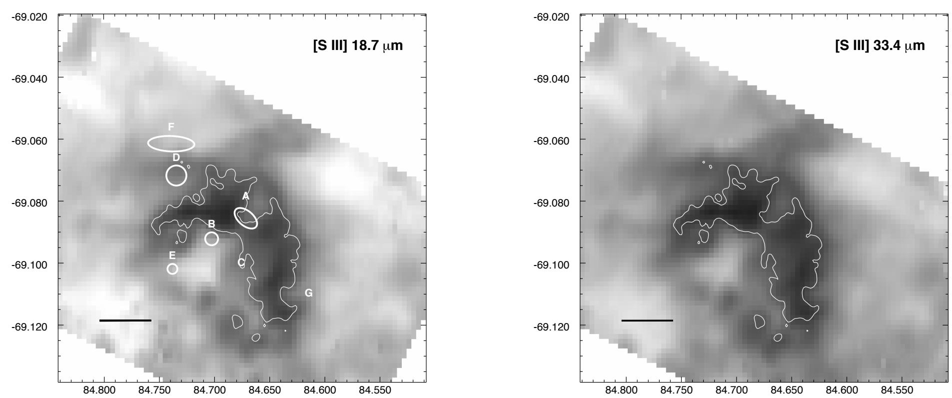

Fig. 2.10.— Fitted atomic line maps (see caption, Figure 2.6). The [S III]λ18.7 μm map is marked with regions of interest listed in Table 2.2.

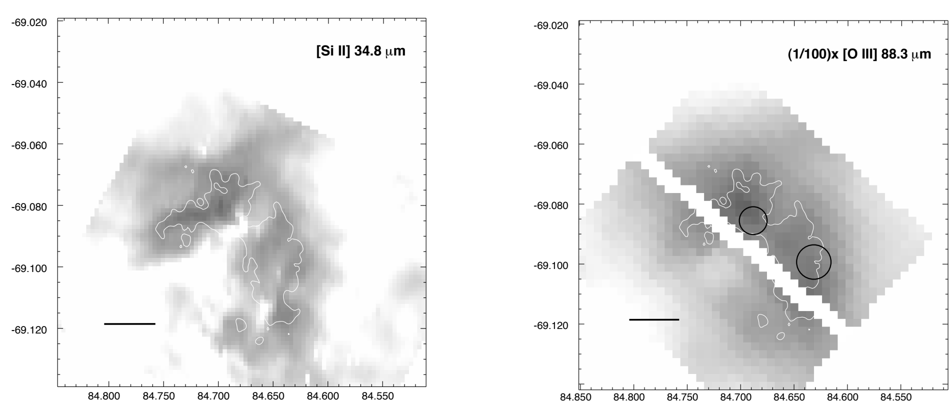

Fig. 2.11.— Fitted atomic line maps (see caption, Figure 2.6). The black circles on the [O III]λ88.3 μm map mark the detected peaks of [O I]λ63.1 μm and [N III]λ57.3 μm.

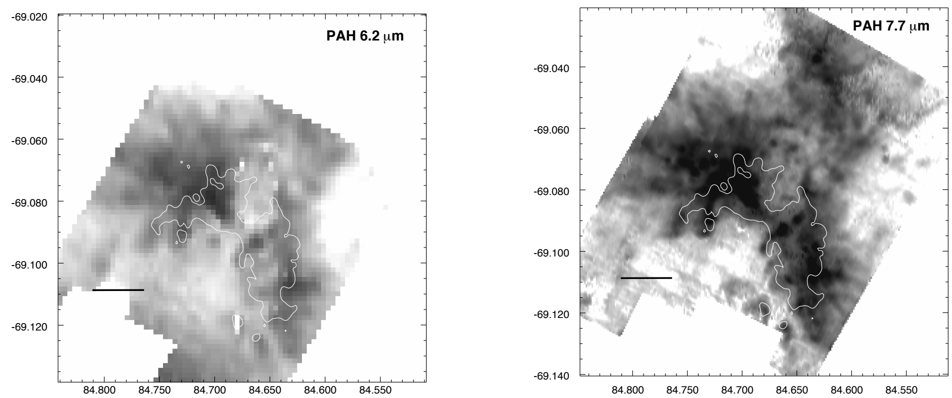

Fig. 2.12.— through Figure 2.14: Fitted PAH feature maps. For details, see caption, Figure 2.6.

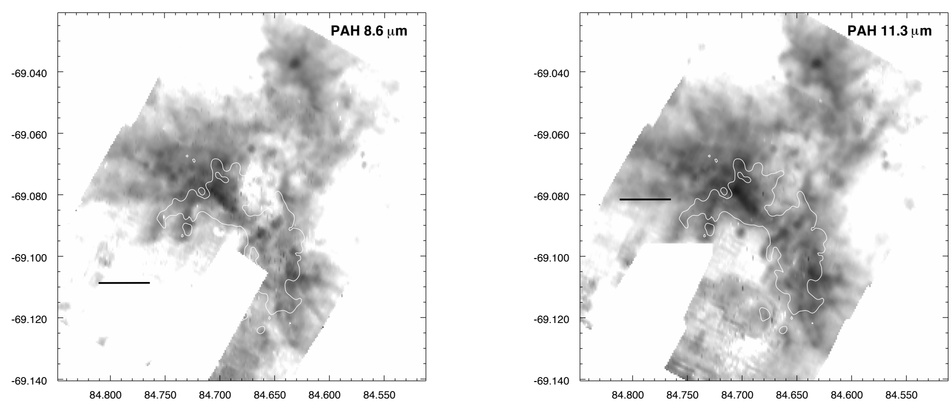

Fig. 2.13.— Fitted PAH feature maps (see caption, Figure 2.6).

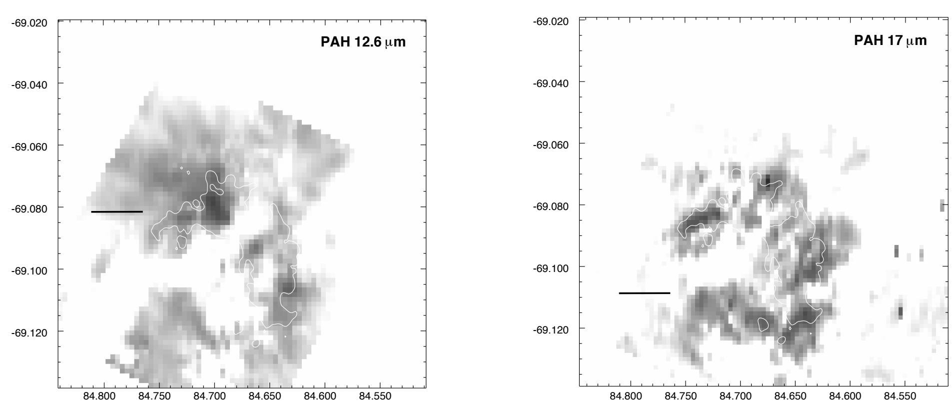

Fig. 2.14.— Fitted PAH feature maps (see caption, Figure 2.6).

Humphreys-α λ12.37 μm line is not very reliable with low-resolution spectra as described in more detail below, and from the high-resolution spectra we find that the molecular line is weaker than the atomic line everywhere, and less than 15% over most of the central part of the map.

Higher excitation species [O IV] and [Ne V], which have strong lines in the IRS bandpass, are not detected in our maps. As discussed in §2.6.2, this favors photoionization over shocks as the dominant physical process in the region.

Table 2.1. Ionization Potentials.

	I	II	III	IV
O	13.62	35.12	54.94	77.41
Ne	21.56	40.96	63.45	97.11
S	10.36	23.33	34.83	47.30
Ar	15.76	27.63	40.74	59.81

Note. — Units are eV.

2.4.2 Line Ratios

Figure 2.15 shows the three line ratio maps [Ar III]λ9.0 μm/[Ar II]λ7.0 μm, [Ne III]λ15.5 μm/[Ne II]λ12.8 μm, and [S IV]λ10.5 μm/[S III]λ33.4 μm. These species all have ionization potentials above 13.6eV, and thus are sensitive to the shape or hardness of the ionizing spectrum (we will call this T_{rad}, because it is often parameterized by the temperature of the best-fitting black-body over λ <912Å) and the intensity of ionizing radiation. The latter is usually quantified as the dimensionless ionization parameter

$$U = \frac{1}{n}\int_{13.6eV}^{\infty} \frac{F_\nu}{ch\nu} d\nu,$$

or ratio of ionizing photon density to atom density. Any single line ratio cannot distinguish between elevated U or T_{rad}, but because the spacing of the ionization potentials differs with atom, different ratios have different U and T_{rad} dependencies, and measuring two ratios can break the degeneracy. (This has been discussed by many authors, see especially the discussions in Morisset et al. 2004; Martín-Hernández et al. 2002; Dopita et al. 2006, ,and §2.6.1 and Fig 2.20 below.).

All ratios increase with U, but locations where the ratios are not well correlated can indicate changes in the hardness of the ionizing field. In 30 Doradus the ratios are very well correlated (correlation coefficient of 0.7 between the neon ratio and argon ratio map, 0.8 between the neon and sulphur ratios, and 0.7 between the argon and sulphur ratios). The Ne and S ratios are telling us similar things over much of the region. For example, there is high excitation in a "hot spot" between the two lobes of the ridge (source "A", §2.4.3), and in the region to the south of the bubble. There is a low excitation ridge to the north (source "F", §2.4.3). The location noted above for low argon emission (source "G", §2.4.3) is significantly low in all three line ratios.

Interestingly, the Ne and S line ratios show quite different behavior on the eastern

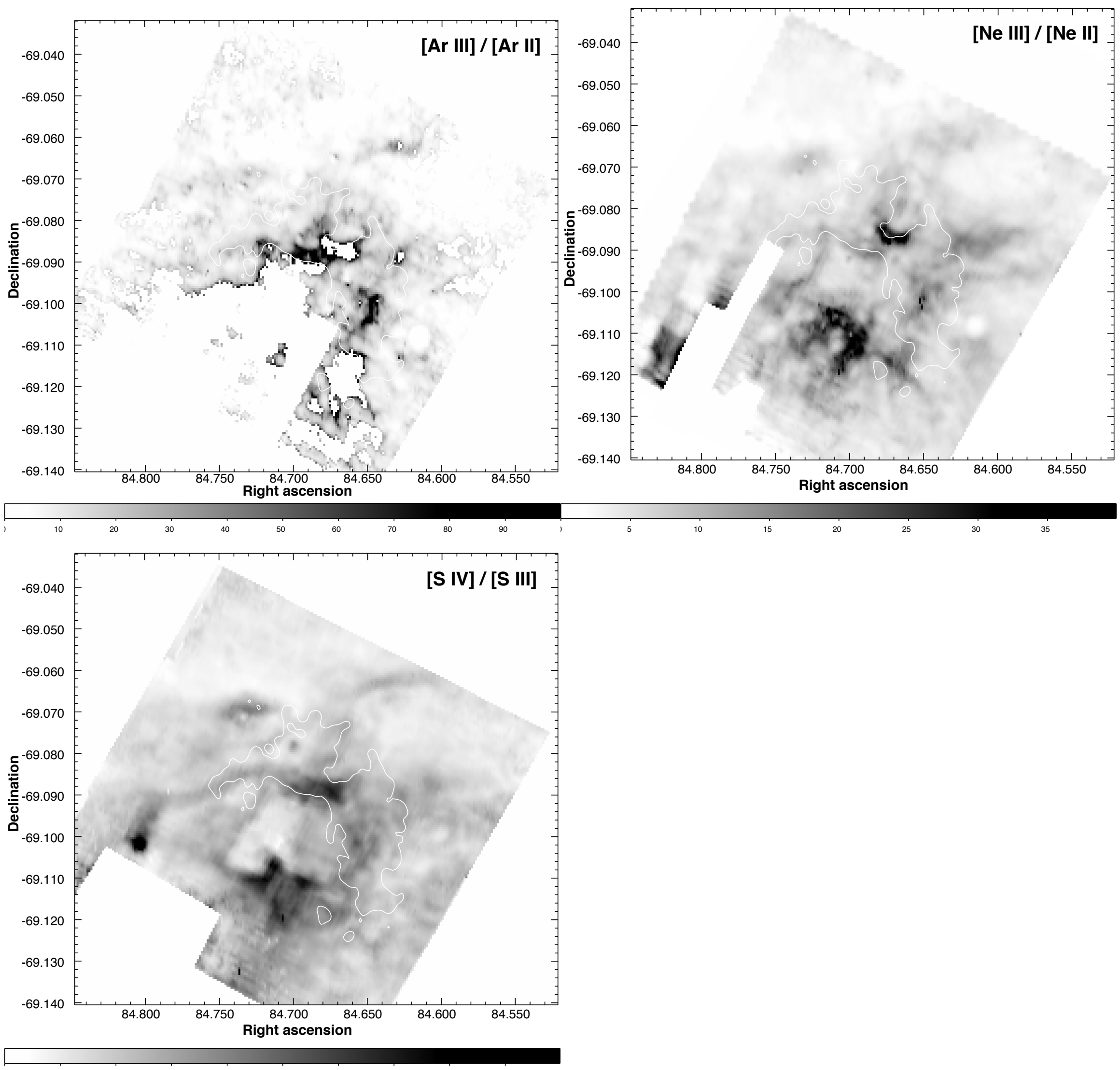

Fig. 2.15.— Line ratios on a linear scale. White contours: a single level of 3cm radio emission, to guide the eye (see Figure 2.2). The white region in the middle of the argon ratio plot indicates nondetection of [Ar II]λ7.0 μm and a very high value of the ratio. Small masked regions in the lower left of the plots are affected by artifacts (see Fig. 2.4).

edge of the bubble, where [Ne III]/[Ne II] is high but [S IV]/[S III] is low (the red region in Figure 2.6.1 below, centered on source "E", §2.4.3). The S ratio is more affected by extinction since [S IV]λ10.5 μm is in the silicate dust absorption feature, so that could be a region of very high extinction or a region of particularly hard ionizing radiation. In this case, the sulphur ratio does not vary dramatically throughout the bubble, and it is the neon ratio which is higher at the western end, which argues for harder ionizing radiation. An extinction effect would require simultaneous increase in the ionization parameter or strength of the ionizing field *and* increased extinction. The specific extinction difference (A([S IV]λ10.5 μm)-A([S III]λ18.7 μm))/A(2.1 μm) equals 0.42$\pm$0.03 (uncertainty reflects differences between published extinction curves; we used that in PAHFIT, Smith et al. 2007b), whereas the effect of extinction on the neon ratio is small (A([Ne III]λ15.5 μm)-A([Ne II]λ12.8 μm))/A(2.1 μm) = 0.0$\pm$0.07. Reproducing the observed line ratios without changing the *hardness* of the ionizing field would require A(2 μm)$\simeq$0.75, or $A_V \simeq$6. Such significant extinction seems unlikely given the overall relatively low extinction in the region, and is not detected in our extinction maps (§2.5.1).

One question that is possible to investigate with this dataset is whether the optically known hot stars in 30 Doradus can completely account for the ionization structure, or whether embedded star formation affects gas excitation measured in the infrared that otherwise might be concealed by at other wavelengths. On Figure 2.16 we plot show the location of Wolf-Rayet stars and early O stars (there are discrepancies between spectral types determined by different authors, and our intent is to show the most massive stars, not provide the most precise spectral typing possible). There is a cluster of WR stars between the two lobes of the ridge, coincident with very high excitation gas. There is not a dramatic increase of excitation centered on R136, although the excitation is generally high in the area. Figure 2.16 also shows the 3.5 μm-excess sources of Maercker & Burton (2005), representing a crude selection of possible protostellar candidates. Other kinds of sources, including some of the previously identified WR stars, can also display infrared excess. Nevertheless, this selection of sources does trace what is known from more precise studies with incomplete spatial coverage (e.g. Rubio et al. 1998; Brandner et al. 2001), that the young embedded sources in this region are concentrated along the IR-bright ridge. The protostellar candidates shown here do not show any particularly striking correlation with regions of high excitation – in fact the southern part of the region has high excitation and few protostellar candidates. We conclude that the ionization structure in 30 Doradus is primarily determined by the (optically) known hot stars.

2.4.3 Notable Regions

Figure 2.17 shows the spectra of small regions which stand out in the continuum (Fig 2.1), in the feature maps (Figures 2.6 through 2.14), or in the line ratio maps (Fig 2.15). They have been chosen to illustrate the range of excitation, extinction, and continuum shape in the 30 Doradus nebula. These regions of interest were marked on Figure 2.2, and are listed for reference in Table 2.2.

Table 2.2. Notable Sources

label	RA	Dec	description
“0”	5h38m45s	-69d05m13s	brightest point on ridge
“A”	5h38m42s	-69d05m05s	hot spots between molecular clouds
“B”	5h38m49s	-69d05m32s	Parker (1993) #1445 MI star
“C”	5h38m42s	-69d06m00s	R136
“D”	5h38m56s	-69d04m18s	example of high extinction
“E”	5h38m57s	-69d06m07s	isolated WN6 star R145
“F”	5h38m57s	-69d03m42s	low-excitation trough
“G”	5h38m28s	-69d06m30s	SW low-excitation region

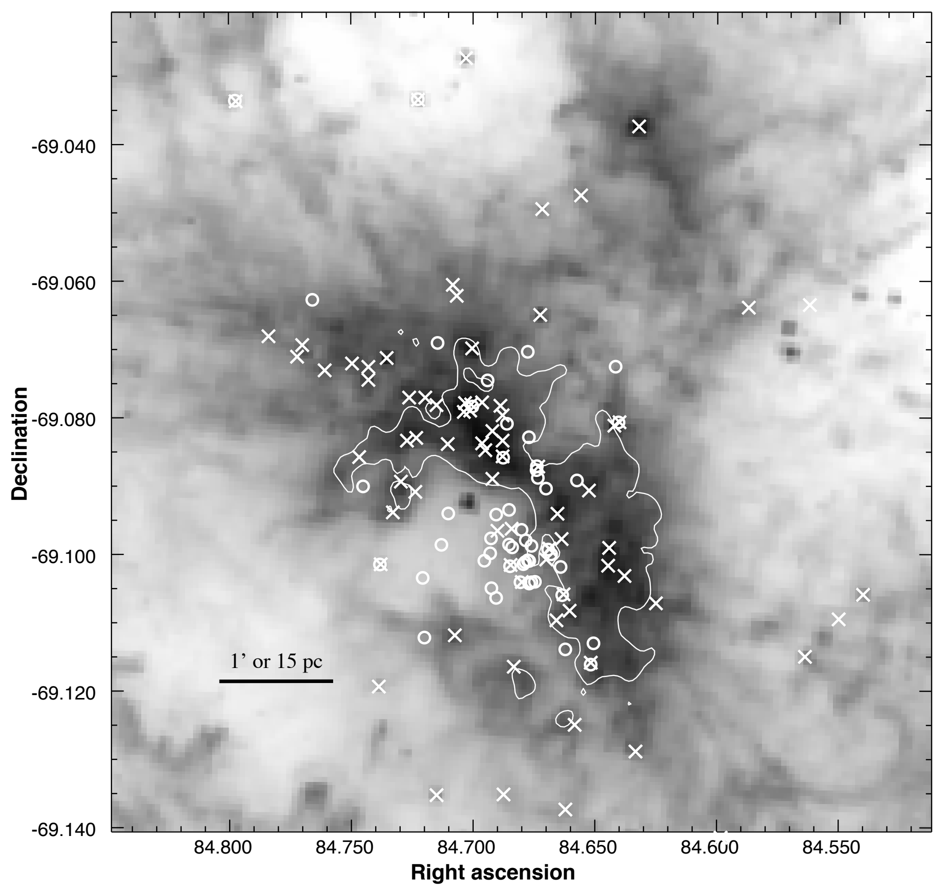

Fig. 2.16.— IRAC 8 μm image (log scale) with two types of relevant point sources: Circles show the most energetic stars in the region - Wolf-Rayet stars and early O stars, from Breysacher et al. (1999); Parker (1993), and X's show protostellar candidates determined from 3 μm excess emission by Maercker & Burton (2005). White contours: a single level of 3cm radio emission, to guide the eye (see Figure 2.2).

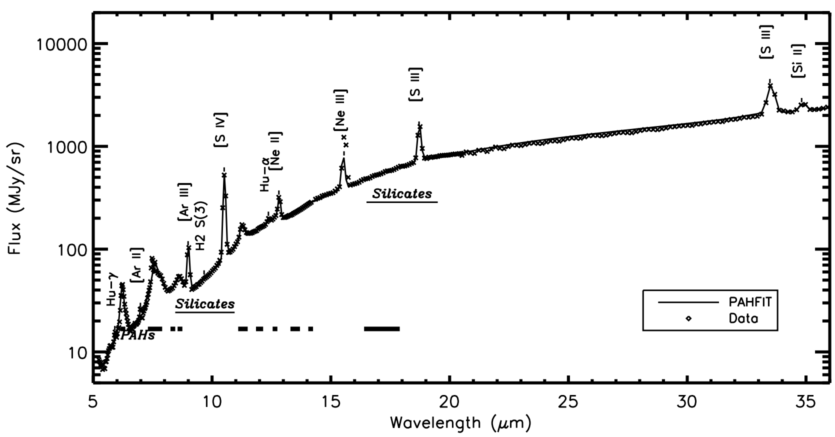

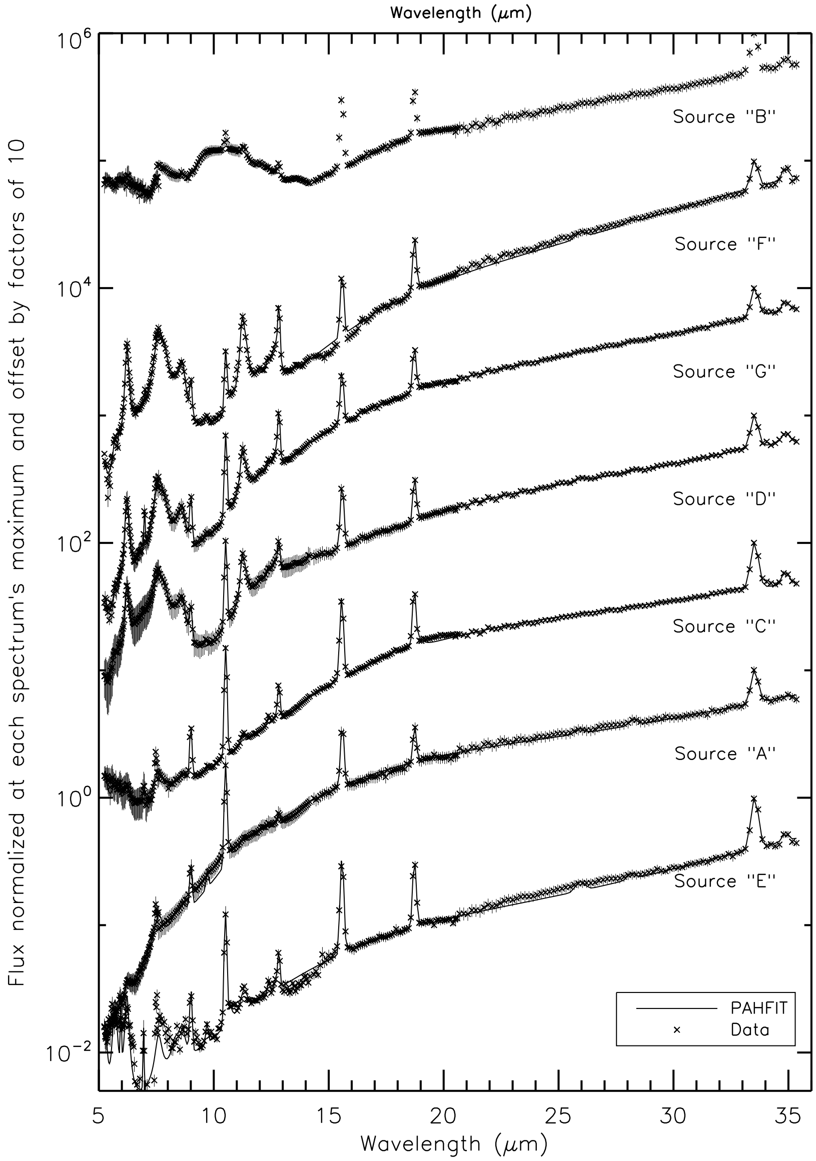

Fig. 2.17.— Spectra of the seven regions described in §2.4.3, with errorbars. For comparison, the spectrum of the entire region (Fig 2.5) is repeated at the top, with feature labels.

Source "0" is the brightest point on the ridge in most tracers, including infrared continuum, many lines, and centimeter continuum. We detect [N III]λ57.3 μm and [O I]λ63.1 μm in MIPS SED observations at this location, and tentatively [Fe II]λ26.0 μm, although this small region of the map is affected by residual fringing and saturation in the LL1 module, raising the uncertainty of the [Fe II]λ26.0 μm detection.

Source "A" is a diffuse region between the two lobes of the molecular ridge. We describe it as a "hot spot" because it has locally elevated excitation seen in the line ratios (Fig 2.15), and when analyzed with photoionization models, is best fit with a hotter or harder radiation field (Fig 2.6.1, §2.6.1). There are known hot stars in the vicinity, but it is not completely clear if they are responsible for the locally higher excitation in the H II region.

Source "B" is a prominent point source from optical to MIR wavelengths, and has been spectroscopically classified as an M supergiant Parker (1993, ; see also refs therein). Their quoted absolute V magnitude appears to place the star at twice the distance to the LMC, but other authors note that it is likely in the foreground. It seems unlikely in any case that it is located in the bubble or affecting the ionization structure. Because this source exhibits silicate emission at 9.8 and 18 μm rather than absorption, PAHFIT cannot be applied to it using the parameters used on the rest of the spectral cube. It is the only source in Figure 2.17 without the fitted spectrum overlaid on the data points and errorbars.

Source "C" is the R136 cluster core.

Source "D" is a prominent mid-infrared point source outside the main cluster and bubble. The surrounding ionized gas has quite high atomic line ratios and thus appears quite highly excited, but we were unable to find a hot star cataloged in the literature which might be responsible for this local excitation. This region also shows relatively high extinction compared to the rest of 30 Doradus. Extinction can raise the sulphur line ratio but has relatively small effect on the neon line ratio, so in our opinion the extinction is not responsible for the apparently high excitation.

Source "E" is a known WN6 star R145, fairly isolated from other catalogue hot stars at the eastern end of the bubble. The high fitted radiation temperatures in the neighborhood of this source (§2.6.1) are consistent with excitation by the harder expected radiation field from a Wolf-Rayet star.

Source "F" is an east-west extended region that appears to be a trough or low point in the excitation and line ratios. The electron density is not remarkable, neither does there appear to be any molecular gas traced by CO emission in the vicinity. It is possible that the feature is in the foreground of this three-dimensional nebula.

Source "G" is a region associated with two peaks in the CO emission [JGB98] 30 Dor-12 and 13 (Johansson et al. 1998), just to the west of the main ridge. There is a peak in both argon line maps at this location, and the region is a low point in all three excitation ratios [Ar III]/[Ar II], [Ne III]/[Ne II] and [S IV]/[S III]. There are in fact several discrete parsec-sized regions of low excitation in the vicinity There is little 3cm continuum at those locations, which lie almost exactly on the opposite side of a molecular cloud from R136. One spot coincides with a knot in the infrared diffuse continuum (#29) noted by Hyland et al. (1992). There is a 3.5 μm-excess protostellar candidate (Maercker & Burton 2005, and Fig. 2.16) nearby, but not coincident with the low-excitation spots. High resolution and sensitivity molecular observations may reveal dense, starless molecular clumps in this part of 30 Doradus, (self)-shielded from the intense radiation.

2.5 Distribution of Matter: Extinction and n_e

2.5.1 Extinction

Previous estimates of the extinction in 30 Doradus found A_V=1.1±0.1mag (Dickel et al. 1994, and refs therein), with two possible locations of higher extinction at $05^h38^m39^s$ -69°07′30″ and $05^h38^m32^s$ -69°06′22″. Rosa & Mathis (1987) found extinction corrections at Hβ of 0.5-1.0 (A_V=0.4-0.8) at ten locations in the outer parts of the region we are studying. We make three estimates of extinction in the region, two directly from our dataset. All methods suffer from systematic uncertainty and modest signal-to-noise, but we can be confident of higher extinction in the regions that all three methods agree.

First we use the ratio of centimeter continuum to Hα emission to derive a map of extinction in 30 Doradus, following the procedure used in Lazendic et al. (2003) and using their centimeter data that they kindly provided (magenta contours, in Fig. 2.18). We assume that all of the centimeter continuum emission in the 30 Doradus region is thermal. Single dish measurements estimated that the nonthermal component contributes less than 2% at 6cm (Shaver et al. 1983, and refs therein). Lazendic et al. (2003) identified two possible supernova remnants from comparison of cm synthesis images and optical recombination lines, but their own analysis and subsequent followup with optical and Xray imaging and optical spectroscopy suggests that these are merely extinguished H II regions (Chu et al. 2004). The relationship between thermal bremsstrahlung centimeter continuum and hydrogen recombination line emission depends weakly on the electron temperature, but Rosa & Mathis (1987) and Peck et al. (1997) both found that T_e variations are small in 30 Doradus ($\lesssim$ ±300K), so it is unlikely that the calculated extinction variations are actually misinterpreted T_e

variations.

We derived two more maps of extinction directly from the IRS spectral cube. Amorphous silicate dust is responsible for two broad bands of absorption at 9.7 and 18 μm. The PAHFIT package reports the fitted optical depth at 9.7 μm. The resulting map for 30 Doradus is shown in Figure 2.18, in green contours. The fit to the absorption feature is sensitive to noise in the spectrum. We cropped away southern parts of the map that were clearly artifacts, and any part of the map where the signal-to-noise was less than 2. Finally, we median-smoothed the resulting map with a window of 3 pixels. The result is a sparse map showing the regions of comparatively reliable elevated silicate absorption.

The ratio of Hydrogen recombination line strengths can also be used to calculate extinction, most commonly by assuming an intrinsic (unextincted) ratio from Case B recombination. Our dataset includes Humphreys-α (7-6) and Humphreys-γ (9-6). Due to modest signal-to-noise and to a systematic tendency of PAHFIT to slightly underestimate the continuum level near these wavelengths, the absolute value of extinction calculated from this ratio has a large systematic uncertainty. It is also difficult to resolve the weak Humphreys-α line from H_2 S(2) 12.28μm in low-resolution spectra. We quantified the amount of potential contamination to the Humphreys-α line strength in several ways: We fit our low-resolution spectra with and without the molecular hydrogen line (the central wavelengths of both lines are very tightly constrained by PAHFIT), and found that the Humphreys-α line strength was only decreased by 15% (that flux was attributed to H_2) when both lines were included. We also fit the high-resolution GTO spectra, in which the lines are easily separated and reliably measured, and found that over most of our area, H_2 was less than 20% of Humphreys-α. We examined fits to both the high and low-resolution spectra in the few high-resolution apertures where the H_2 and Humphreys-α strengths are comparable (H_2 never exceeds Humphreys-α in strength) and found that the low-resolution Humphreys-α strength used in our analysis was at most overestimated by 40% by the presence of the H_2 line on the wing of the Humphreys-α line. While some level of contamination of Humphreys-α by H_2 S(2) may be present in our maps, we do not expect that to change any of our conclusions including the regions of high extinction identified in Figure 2.18.

Further systematic uncertainty arises in the choice of extinction curve, since the lines lie on the wings of the silicate absorption features, which vary in amplitude and width in different studies. However, all extinction curves that we considered show greater relative extinction at Humphreys-α $\lambda 12.37$ μm than at Humphreys-γ $\lambda 5.90$ μm. We examined the extinction curves of Chiar & Tielens (2006) for the Galactic Center and the ISM, and the average LMC extinction curve[3] based on the carbonaceous-silicate grain model of Weingartner & Draine (2001). All of the extinction curves roughly agree in the vicinity of the Humphreys-α emission line. Near the Humphreys-γ line, the Chiar & Tielens curves agree well with the near-infrared extinction for the ISM found by Indebetouw et al. (2005). Thus, extinction correlates with the flux ratio of Humphreys-γ $\lambda 5.90$ μm to Humphreys-α $\lambda 12.37$ μm, and we can still find the relative level of extinction across 30 Doradus from the Humphreys-α/Humphreys-γ ratio, even though the absolute normalization is uncertain.

We calculated the signal-to-noise of the ratio based on the RMS variance of the individual maps of emission line strength, and removed all regions of the map where the signal-to-noise was less than 2. We cropped away the parts of the map where an additive correction was made to the SL spectra (see §2.8.3), because this subset of the map encloses some spectra which have an unphysical plunge at the red edge

[3]Available at: www.astro.princeton.edu/~draine/dust/dustmix.html

of the SL2 module. The fit to those spectra generally underestimates the continuum near the Humphreys-γ line, and thus overestimates the ratio of Humphreys-γ to Humphreys-α. We also cropped away the parts of the map where the reduced χ^2 of the fit was greater than 5. Finally, even after applying these filters, it was necessary to trim away some regions from the low-signal edge of the map where the noise levels were still untrustworthy. The ratio map shown in grayscale in Figure 2.18 is now mainly limited to those areas of 30 Doradus where we obtained both good detections of these two faint lines and a good fit.

Despite the level of noise in the maps of extinction, particularly the map derived from the Humphreys-α and Humphreys-γ lines, there are three areas where all three methods agree on especially high extinction. These areas have been marked on Figure 2.18. Generally, there is not much extinction by dust in 30 Doradus. As discussed above, extinction has a small effect on the Neon excitation ratio, but raises the [S IV]/[S III] (due to the shape of the extinction curve), which in turn will get interpreted as higher T_{rad} in our photoionization models. The regions of interestingly high T_{rad} do not turn out to correspond to regions of clearly high extinction, but the effect should be kept in mind in interpreting the data.

2.5.2 Electron Density

Figure 2.19 shows the electron density calculated from [S III]λ18.7 μm/[S III]λ33.4 μm. The [S III]λ18.7 μm map was convolved to the lower resolution of the [S III]λ33.4 μm map, and the line ratio converted to electron density using the conversion in Dudik et al. (2007) at T_e=10^4K (their Figure 9 and section 6: Those authors calculated the line ratio as a function of density and temperature for a five level atom using the collision strengths from Tayal & Gupta (1999) and radiative transition probabilities

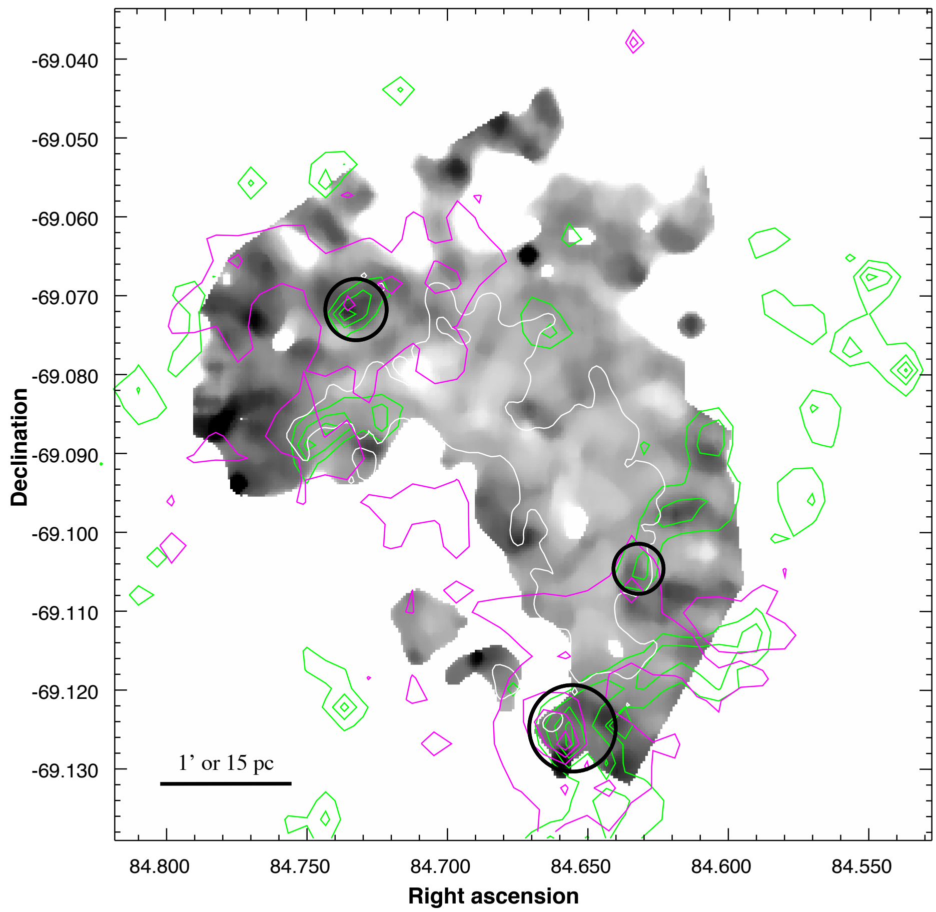

Fig. 2.18.— Map of extinction in 30 Doradus. Grayscale linear image: the IRS Humphreys-γ/Humphreys-α ratio, which is proportional to extinction. Dark areas of the map indicate high extinction. The Humphreys lines are weak, and this map has been severely cropped to remove areas of the worst signal-to-noise. Green contours: the optical depth of silicate absorption from the IRS spectral map, $\tau = 0.10, 0.27, 0.43, 0.60$. Areas of low signal-to-noise have been masked out of this map as well. Magenta contours: The ratio of the 3cm continuum (Lazendic et al. 2003) to Hα emission (MCELS, http://www.ctio.noao.edu/∼mcels/), also proportional to attenuation. The northernmost magenta source corresponds with the molecular cloud marked in yellow in Figure 2.1. White contours: a single level of 3cm radio emission, to guide the eye (see Figure 2.2). The areas where all three maps tend to agree on high extinction have been marked in black. The northeasternmost corresponds with source "D" in Figure 2.2 and §2.4.3.

from Mendoza & Zeippen (1982)). The calculated ratio is not a strong function of temperature. The ridge is prominent in the [S III] ratio or n_e map, and in fact the n_e map is quite similar to the 3cm continuum in morphology. The density is elevated to the south of the bubble and R136, in a region of relatively high excitation.

2.5.3 Abundances

Variations in elemental abundances can in principle change the diagnostic ratios that we are using to measure physical conditions in the 30 Doradus nebula. Previous studies have found very small internal abundance variations in 30 Doradus and other giant H II regions. Peck et al. (1997) found no significant variations on 15″ scales in the He abundance $Y^+ = He^+/H^+ = 0.13 \pm 0.02$ measured from radio recombination lines. Rosa & Mathis (1987) found little variation between several positions measured with optical spectroscopy. Of more direct relevance to this work, Lebouteiller et al. (2008) found less than 0.01 dex dispersion of Ne/H, S/H, and Ar/H, using the high resolution GTO Spitzer spectra mentioned above.

Small scale abundance variations in H II regions including 30 Doradus (Tsamis & Péquignot 2005) have been proposed to explain discrepancies between optical and infrared abundance determinations. We might hope to detect sub-parsec scale abundance variations in this dataset by using three infrared line ratios to solve simultaneously for U, T_{rad}, and Z. In practice, we find that the excitation variations can be adequately explained without abundance variations, which would be seen as residuals in our fitting of U and T_{rad}. The signal-to-noise especially in our argon line ratio is insufficient to detect abundance *variations* at the 0.1 dex level predicted by Tsamis & Péquignot (2005).

Overall, abundances in 30 Doradus are not particularly low: Rosa & Mathis (1987)

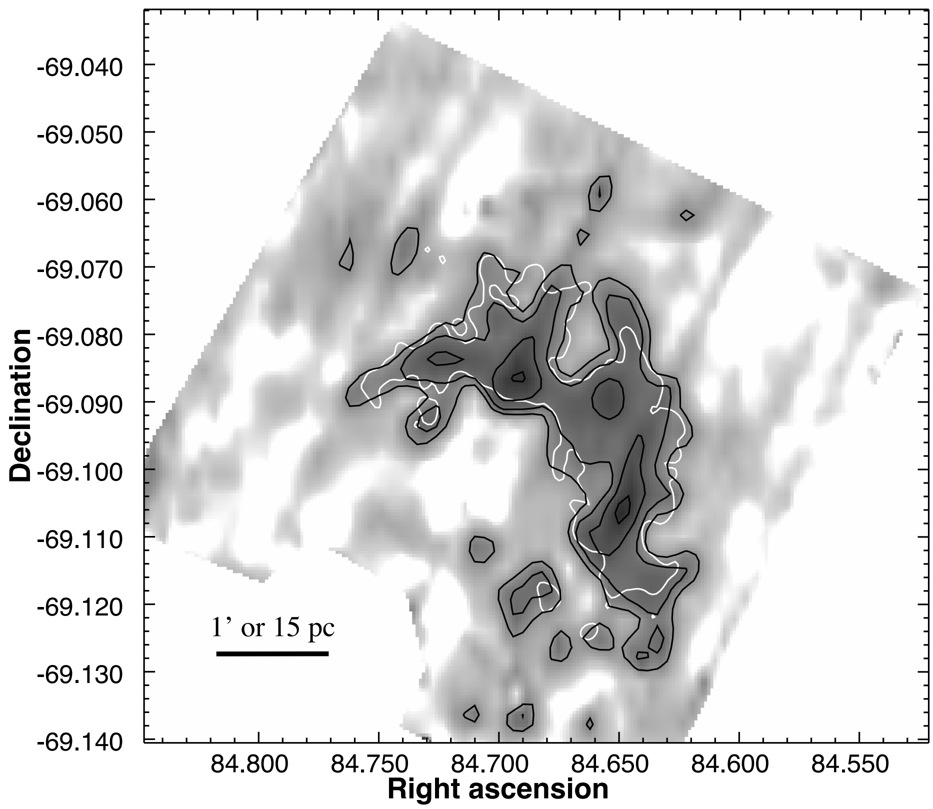

Fig. 2.19.— n_e calculated from [S III]λ18.7 μm/[S III]λ33.4 μm. Black contours: log n_e = 2.4, 2.5, 2.6, 2.7. White contour: a single level of 3cm radio emission (see Figure 2.2). The ridge is prominent, as well as a region of increased density to the south.

found Ne/O, S/O, and Ar/O ratios close to solar. Lebouteiller et al. (2008) found Ne/H and Ar/H of 12+log(X/H)=7.76±0.02 and 6.32±0.06, respectively, within 0.25 dex of the range of solar values (Lodders 2008, 2003; Asplund et al. 2005). They found S/H of 6.77±0.03, only about 0.3 dex sub-solar. We also find that on average, half-solar abundances result in modestly better agreement between the three infrared line ratios in our photoionization models than solar or 0.1-solar models. In practice, systematic effects such as the argon recombination rate have a larger effect on this agreement than the abundances (Morisset et al. 2004; Stasińska & Schaerer 1997).

2.6 Distribution of Radiation and Gas: Excitation

2.6.1 Photoionization models

As mentioned above, if photoionization is assumed to be the dominant physical process, the ionic line ratios depend on U, T_{rad}, and to a lesser degree metallicity. If one assumes constant abundances and hardness or T_{rad}, then the line ratio maps in Figure 2.15 are maps of the ionization parameter U, varying from log $U \simeq$-3 to log $U \simeq$-1.5.

A somewhat more sophisticated analysis is to solve for T_{rad} and U simultaneously. We prepared a grid of photoionization models using Cloudy (Ferland et al. 1998) as a 0-dimensional tool to solve for the ionization structure and line emissivities given a specified radiation field and ionization parameter (we used the output of the first zone in each simulation). We explored different input spectra, including ATLAS (Castelli & Kurucz 2004), Tlusty (Hubeny & Lanz 1995), CoStar OB and Wolf-Rayet atmospheres (Schaerer & de Koter 1997; Smith et al. 2002), and black-bodies. In the end we used a grid of Tlusty atmospheres calculated at half-solar metallicity, extrapolated to hotter effective temperatures using black-body atmospheres to set the functional dependence of line ratios on effective temperature, and normalizing the ratios to those of the hottest Tlusty models. (We found that adopting different stellar atmospheres primarily changes the line ratios by a constant multiplicative factor, and has very little effect on the functional dependence of the line ratios on effective temperature and ionization parameter.) We were not able to find freely available grids of more modern atmospheres (e.g. WMBASIC, CoStar) at subsolar metallicity, but we performed careful comparisons of our modeling at solar metallicity to understand the systematic effects. If nebular abundances are set at solar levels in the photoionization models, and stellar atmospheres calculated at solar abundance are used for self-consistency, the derived ionization parameter U decreases systematically by about 0.1 dex, and the derived radiation temperature increases systematically by 10%. At solar metallicity, WMBASIC atmospheres result in about a factor of two lower [Ne III]/[Ne II]ratio and a 50% lower [S IV]/[S III]ratio. That would increase the derived ionization parameter in 30 Doradus systematically by ~0.15 dex, and lower the derived radiation temperature by 5–10%. These effects have been explained in detail by other authors, especially Morisset et al. (2004). None of the changes in stellar atmospheres or metallicity that we explored would result in qualitative changes in our conclusions, merely small systematic shifts in derived parameters. We also varied the dust prescription in terms of abundance and grain size. Neither had a strong effect on the line ratios as a function of T_{rad} and U, provided that U was calculated locally, i.e. from integrating the diffuse ionizing field in the simulation above 1 Ry, rather than assuming some geometry-dependent expression such as $N_\star/c4\pi r^2 n_e$.

Figure 2.20 shows typical behavior - each measured ratio defines a curve in $U-T_{rad}$ space, but the lines have different slopes because the ionization potentials are spaced differently for the different atoms. This is equivalent to the nearly parallel arrows for U and T_{rad} in Morisset et al. (2004) (see also Martín-Hernández et al. 2002; Dopita et al. 2006). Two measured ratios can better constrain U and T_{rad}. We will focus on the Ne and S ratios since [Ar II] is not detected over large parts of the H II region.

Figure 2.6.1 shows the fitted U and T_{rad} across 30 Doradus. The ridge is a region of high ionization parameter, as previously noted from simple examination of the line ratios. The region around the relatively isolated source at $5^h38^m56.5^s$ -69°04′17″ to the north of the ridge is also highly excited, probably due to the local effects of that star (source "D", Figure 2.2, §2.4.3). We note two regions of high U in particular.

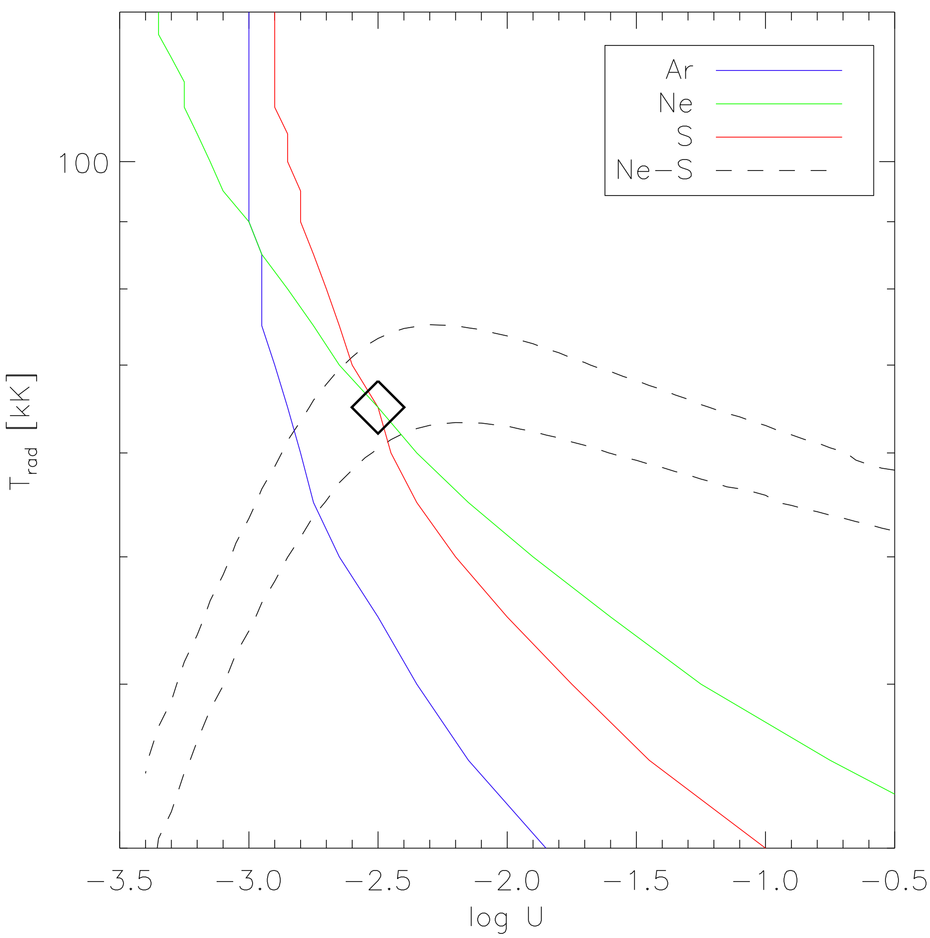

Fig. 2.20.— Fits to U and T_{rad} at a representative location $05^h38^m37^s$ -69°06′12″. Loci of consistency with the data are shown for fitting Ar, Ne, and S ratios alone (lines from upper left to lower right), the difference between the S and Ne ratios (log([S IV]/[S III])-log([Ne III]/[Ne II]), dashed lines, 1-sigma confidence interval shown), and the combination of all ratios (bold diamond). See text §2.6.1 for discussion.

The most prominent is between the two parts of the ridge (just south of source "A", §2.4.3), where young stars may be locally ionizing the gas and beginning to lower the density and disperse the ridge (see Figure 2.16 for the location of protostars and the most energetic optically identified stars). Alternately, the density is simply lower there and ionizing radiation can more easily leak out from the bubble region around R136. The northern side of this "hot spot" shows evidence for hardening of the radiation field, which could result of the radiation originates in the bubble or on its rim, and is propagating northward, and being absorbed by gas and dust (both of which will harden the field). The high degree of porosity and mixing between molecular and ionized material in 30 Doradus is well known (see e.g. Poglitsch et al. 1995). On the south side of the bubble is another region of high ionization parameter - this region also shows high electron density in the [S III] ratio, so the field must be locally strengthened, perhaps by the WR stars known in that region (Fig 2.16). Particularly interesting is the region on the eastern side of the bubble, which shows up in the fitted parameter maps as high T_{rad}, but not particularly high U. There is a single catalogued Wolf-Rayet star (R145, WN6 type, source "E", §2.4.3) in the center of that area, which may be energizing the eastern end of the bubble.

The radial variation of physical conditions in 30 Doradus, as a function of distance from R136, is of particular interest, to determine whether feedback in the nebula is dominated by that cluster core, or whether individual hot stars scattered throughout the region are equally important. We have already seen that the latter is true, for example the hot eastern end of the bubble apparently excited by the WN6 star source "E". Within several tens of parsecs from R136, however, there does appear to be a global effect. The top panel of Figure 2.22 shows the radial dependence of the ionic line ratios and fitted T_{rad} and U. The bubble at $\sim$10pc radius is clearly evident in lowered

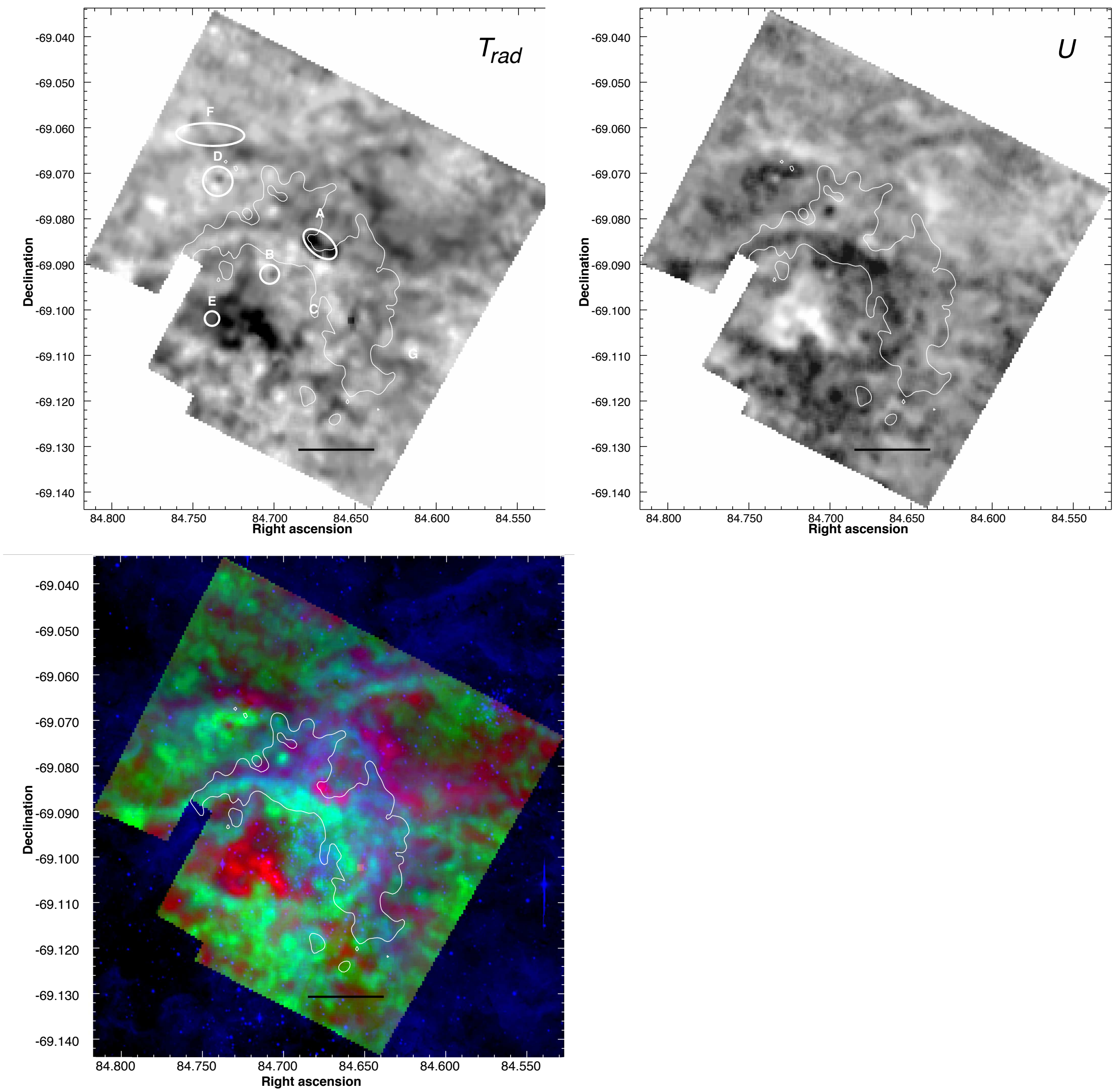

Fig. 2.21.— Top left: fitted T_{rad} based on the S and Ne line ratios. Top right: fitted U. Higher values are dark in both grayscale images. Bottom: fitted T_{rad} (red) and U (green), plus optical B band (blue). All images are in log space except for the B band map. White contours: a single level of 3cm radio emission (see Figure 2.2). The black lines indicate a scale of 1' or 15 pc. Sources of interest (see Table 2.2) are labeled on the T_{rad} map. The derived parameters, T_{rad} and U, should be compared with the ratio maps in Figure 2.15.

T_{rad} and raised U. Outside the bubble there is a modest gradient in the hardness of the fitted radiation field, but not much gradient in the ionization parameter U. This is sensible in a region which has the hottest stars in the center, but some ionizing sources distributed more widely. As R136 is apparently driving an off-center "blister" type H II region, it is interesting to separate the radial dependencies of the ionized gas parameters in the eastern and western direction. the second panel of Figure 2.22 shows this comparison, showing clearly the bubble wall at $\sim$5pc distance in the east, and the hot bubble between R136 and the $\sim$25pc distant bubble wall in the west. Unfortunately the effects of saturation make the measurements less reliable beyond the bubble wall in the west (see §2.3.2).

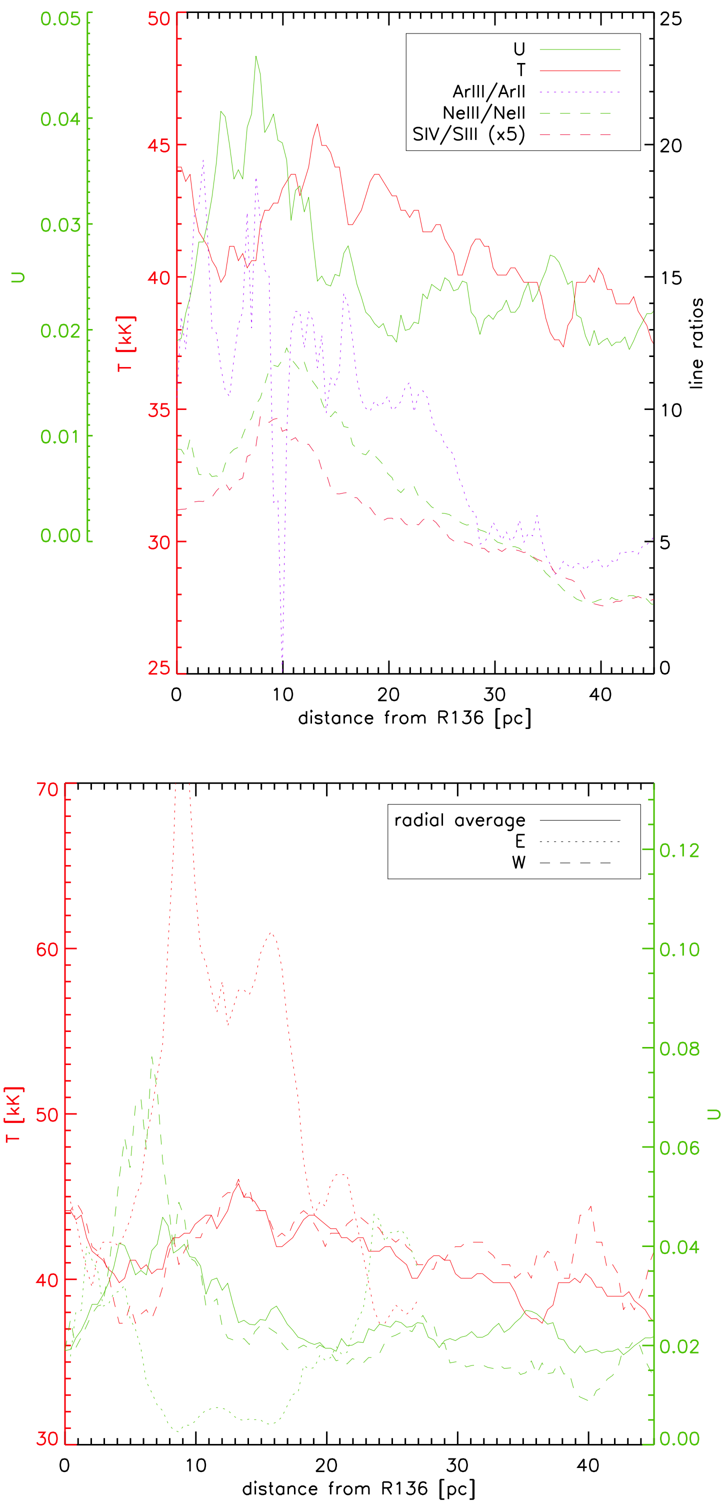

Fig. 2.22.— (top) Radial dependence of conditions in the ionized gas as a function of radial distance from R136. The different lines show azimuthal median values of the ionic line ratios and of the fitted T_{rad} and U from photoionization models. (bottom) Radial parameters in the eastern and western directions. R136 is an off-center blister H II region, much closer to the bubble wall in the eastern than western direction.

2.6.2 Shock Models

Protostellar shocks can also produce MIR fine-structure emission, but only if the excitation (shock velocity) is high enough. [Ne II] requires J-shocks with v$\gtrsim$60km s^{-1} (Hollenbach & McKee 1989) and [Ne III] velocities in excess of 100km s^{-1} (Molinari & Noriega-Crespo 2002). Lefloch et al. (2003) detect [Ne II]λ12.8 μm and [Ne III]λ15.5 μm in HH 2, but only from the highest excitation working surface. Similar results are being found with *Spitzer*, detecting [Ne II]λ12.8 μm but not [Ne III]λ15.5 μm, and [S III]λ33.4 μm but not [S IV]λ10.5 μm in HH46/47 (Noriega-Crespo et al. 2004b), Cep E (Noriega-Crespo et al. 2004a), and HH7-11 and 54 (Neufeld et al. 2006). Even the bow shock near a runaway O9.5 star (France et al. 2007) and the stronger shocks in SNR (Neufeld et al. 2007) show similar relatively low-excitation MIR emission.

The (few) MIR observations of regions containing both shocks and photoionization tend to show photoionization dominant. In [Ne II] and [S IV] maps of the massive star formation region W51 IRS2, high spectral resolution mapping with TEXES (Lacy et al. 2007) allows the high velocity emission to be separated from that at the velocity of the molecular cloud. The authors do not note dramatically different line ratios in the high velocity emission from that at the systemic velocity, but rather confirm earlier ground-based observations of MIR fine structure lines consistent with photoionization by late O-type stars (Okamoto et al. 2001). Lacy et al. (2007) interpret their observations as a neutral jet emerging from the molecular cloud and being subsequently photoionized.

More recent work with *Spitzer* in the Galactic center (Simpson et al. 2007) cannot produce the observed O^{+3} abundance with any reasonable photoionization model, even including hot supergiant atmospheres and 10$^{5-6}$K blackbodies representing diffuse X-ray emission. The proposed alternative of $\sim$100km s^{-1} shocks can match the observed [O IV] line emission. The authors do not *require* shock excitation to explain their Ne and S line ratios, but do note that the highest excitation gas is found between the two stellar clusters, which is indicative of shock excitation.

We ran a set of shock models using John Raymond's code (Raymond 1979; Cox & Raymond 1985; Hartigan et al. 1987) with a range of velocities and pre-shock densities. The ratios of relevant fine-structure lines are shown in Figure 2.23, along with the observed ranges in 30 Doradus. To first order, all three ratios can be matched with shocks on the order of a few hundred km s^{-1} in quite low-density gas ($n < 1\mathrm{cm}^{-3}$). However, we have significant nondetections of emission from the higher ionization species [O IV] and [Ne V], with 3-σ upper limits less than 10^{-2} relative to [S III]λ18.7 μm across the map. The predicted ratios for those two species relative to [S III] are also calculated, and shocks of this order should produce easily detectable [O IV]. Shocks can also produce [Ne V] (e.g. in supernova remnants Rakowski et al. 2007), but it is more usually used as an indicator of very hard radiation from AGN or WR stars (Abel & Satyapal 2008, and Table 2.1). Thus we conclude that in 30 Doradus as elsewhere, although shocks certainly exist, the ionization structure of the gas is dominated by photoionization and not shock activity. Furthermore, while the effects of hard radiation from WR stars affects the ionization balance in some parts of the nebula, the radiation field on ∼0.5pc scales is not apparently hard enough for very high ionization species to be very important.

It is particularly interesting to consider the "hot" region on the eastern side of the bubble where the photoionization models are driven to high T_{eff} and moderate U by low [S IV]/[S III] and moderate [Ne III]/[Ne II]. That low [S IV]/[S III] ratio makes this part of 30 Doradus more consistent with shock models than other parts, although the nondetections of [O IV] and [Ne V] are still problematic. We suggest

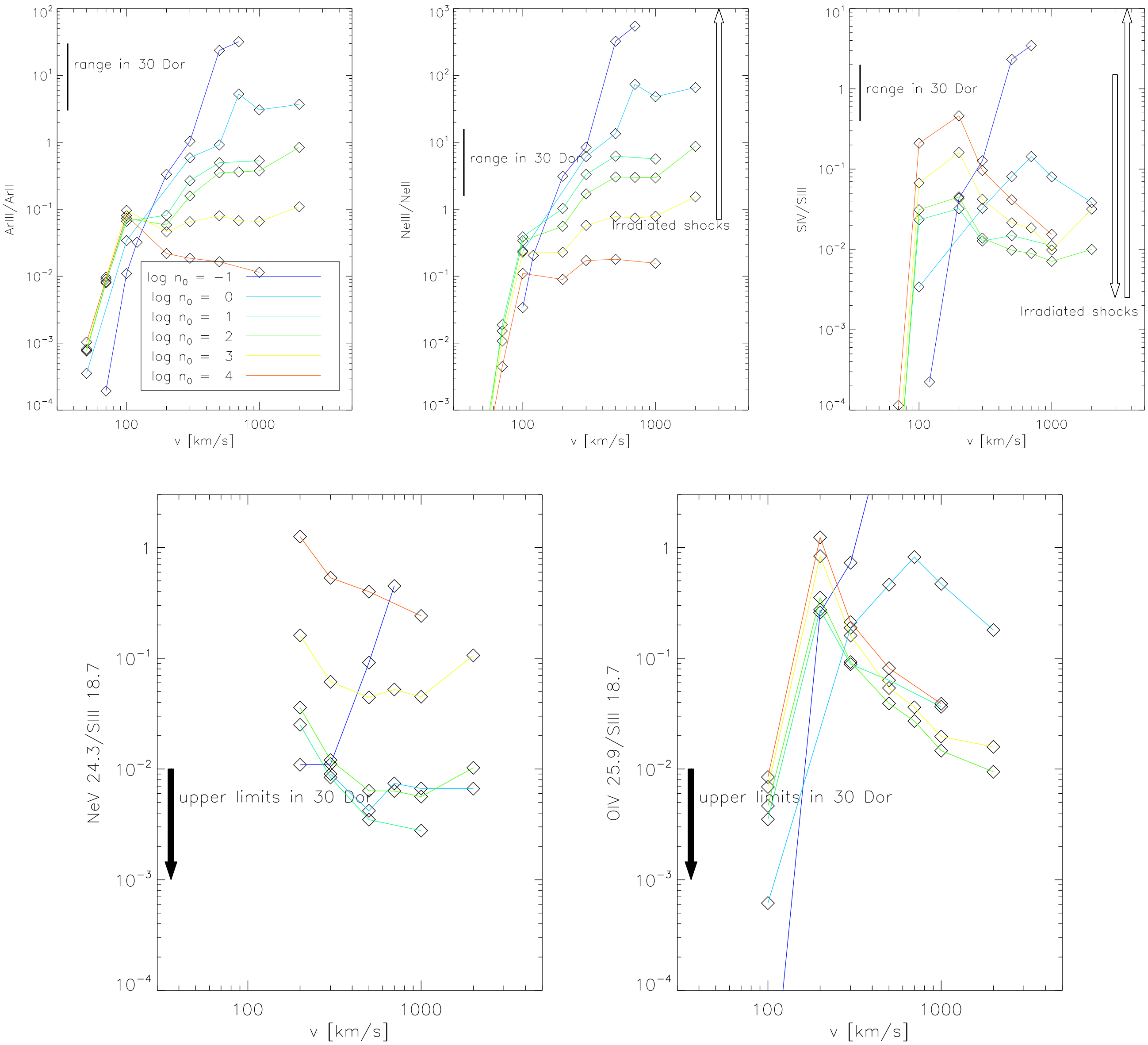

Fig. 2.23.— Ratios of line strengths calculated from plane-parallel shock models (the actual models that were run are diamonds, connected for clarity). Although the Ne, Ar, and S ratios can be produced by shocks of a few 100km s^{-1} in diffuse gas, those shocks should also produce [O IV] emission, which we do not detect in 30 Doradus.

that of anywhere in the nebula, the eastern end of the bubble may have the highest likelihood of excitation by shocks, as would be expected from winds of the WN6 star located there hitting the denser sides of an evacuated bubble.

2.7 Conclusions

We present an infrared data cube of 30 Doradus, observed with the InfraRed Spectrograph and Multiband Imaging Spectrometer on the *Spitzer* Space Telescope. Aromatic dust emission features are of modest strength in the 30 Doradus region, concentrated in the arc-like two-lobed ridge coincident with CO emission and partially encircling the central R136 cluster. Detailed analysis of the dust content of the region from these features will follow in a subsequent publication, although the high average dust temperature is immediately obvious from the shape of the MIPS/SED spectrum. Of the pure rotational lines of molecular hydrogen, only S(3)λ9.67 μm is detected with any significance, peaking on the bright "ridge" that dominates the morphology of the region at many wavelengths (see Fig 2.8). Low-ionization atomic lines are present but not particularly strong: [Si II] is detected in the outskirts of the mapped region, outside the region of strongest centimeter continuum (highest emission measure ionized gas). [Fe II] λ26.0 μm is only tentatively detected in two locations.

Two hydrogen recombination lines Huα (7-6) and Huγ (9-6) can be mapped over a large fraction of the observed area, and from these a relative measure of the extinction can be calculated. Independent estimates of the extinction are calculated from fitting the strength of the 10 μm silicate feature, and from the ratio of Hα to centimeter continuum. While none of the three extinction measures is extremely high signal-to-noise, the locations where all three show higher extinction should be quite secure - in particular three distinct locations in the west, southwest, and northeast, outside of the "ridge" (Fig 2.18).

The strongest atomic or molecular features in the data cube are the moderate-ionization ionic lines [Ar II]λ7.0 μm, [Ar III]λ9.0 μm, [Ne II]λ12.8 μm, [Ne III]λ15.5 μm, [S III]λ18.7 μm, [S III]λ33.4 μm, and [S IV]λ10.5 μm. These lines are most sensitive to physical conditions in the ionized gas: the ionization parameter U and hardness of the ionizing field, parametrized by the radiation temperature T_{rad}. We fit the Neon and Sulphur ratios with photoionization models to derive a 2-dimensional map of U and T_{rad}. We find that the excitation generally follows the "ridge and bubble" morphology, and that under the assumptions of pure photoionization, there are "hot spots" of hardened ionizing field in the east of the bubble and between the two lobes of the ridge (corresponding to two molecular clouds). We also compare the line ratios to shock models and find poorer agreement with the data. In particular the nondetections of emission from more highly ionized species [O IV] and [Ne V] suggest that photoionization dominates over collisional excitation by shocks. Overall, the local effects of hot stars in 30 Doradus (such as the single WR star on the eastern side of the bubble) appear to dominate over any large-scale trend with distance from the central cluster R136.

2.8 Flux calibration and adjustment (Appendix A)

2.8.1 Background subtraction

Our off-target background observations bracket the data set in time. We chose to take an average (with minima and maxima trimmed) of all the background records and subtract that from all of the data records. It was possible that the two sets of background records could be appreciably different, reflecting a gradual change in the instrument (e.g. electronic drift), and that a linear interpolation of the two sets over time would be more appropriate as the background for each data record. Indeed, the mean flux level of our background records tends to increase with time, varying by 8% between the first and last exposures. Therefore, the average of the second set of background records has a higher mean flux level than the average of the first set.

We tested three different background subtractions on several apertures from the SL1 module: using only the first background set, using only the second, and using the mean of the two sets. The difference between the resulting spectra was very small. Specifically, the difference in continuum levels between typical spectra using the different background subtractions was on the order of 2%. For very low signal-to-noise spectra extracted from faint areas of the map, the continuum difference could reach 10%. We emphasize that, even then, the shape of the spectrum and the strength of the emission line features did not appreciably change. For the highest signal-to-noise spectra, the continuum difference was reduced to about 0.1%. We conclude that using the mean of all background records is adequate.

2.8.2 Flux calibration

The IRS SL slit is approximately 3.6 arcseconds wide, and the LL is approximately 10.6 arcseconds wide (see Spitzer Science Center 2006, Table 7.5). Some fraction of the instrument point-spread function (PSF) falls outside of the slit, depending on wavelength. For example, the full width half max (FWHM) of the PSF at 14.5 μm, at the upper wavelength range of the SL first order, is about 3.74 arcseconds (see Spitzer Science Center 2006§8.1.2.1). Optimized for point sources, the Spitzer Space Center pipeline adjusts the data for this loss of flux. However, in the case of a spatially uniform extended source, there is no net loss of flux. CUBISM can apply a slit loss correction factor which re-corrected the data to the original levels. In the case of 30 Doradus, an extended sources, we opted to do so. However, it is important to note that in some areas of the map, there are bright features which are neither point sources nor uniformly extended emission, which have some net loss of flux. The magnitude of this loss is at most 36% (see Sheth 2006, Slide 13)[4] . This loss may be responsible for some of the mismatches we experienced between the flux densities in the four different modules at some points in the map.

2.8.3 Final adjustments to the spectra

The wavelength range of the spectra needs to be trimmed. The full range of the IRS in each of the four modules includes bins where the response is unreliable. In the LL modules, where the spectrum of 30 Doradus is generally smooth, the drop in response at the long-wave edge of the LL2 module and the increase in noise at the long-wave edge of the LL1 module are evident.We trimmed the LL modules based on these observations. The spectrum of 30 Doradus is more complex in the SL modules, however, with many emission lines and an unclear continuum. In order to determine the range of wavelengths which can be trusted in each SL module, we examined the IRS low resolution staring mode spectrum of α Lacertae, an A1 dwarf star whose smooth spectrum is well known. In each of the SL modules, the spectrum departs from its smooth curve at the margins. We trimmed our SL spectra to the wavelengths where the IRS spectrum of α Lac stayed faithful to the smooth curve. We also found, based on some spectra from 30 Doradus, that the limit at the long-wave edge of the SL1 module based on the spectrum of α Lac was not conservative

[4]Available at: ssc.spitzer.caltech.edu/sust/workshop/2006data2/talks/kartik.pdf

enough; consequently, we decreased the trusted upper limit on wavelength for the SL1. We could not use the spectrum of α Lac to determine the reliable wavelengths for the LL modules because the stellar spectrum has low signal-to-noise at such long wavelengths.

After extracting our spectra, we found that some of the SL spectra were suspiciously low, even negative for some counts. This may be a problem with background subtraction, and thus requires an additive correction. We raised both SL modules by the additive quantity necessary to make the floor of the SL2 spectrum (the median of the five lowest counts) non-negative. Over 72% of the map, this correction was unnecessary. Over the remaining 28%, mainly in areas of low signal, the SL spectrum was raised by a mean level of 5.5 MJy/sr, with standard deviation of 6.5 MJy/sr. For comparison, the mean level of the background spectrum in the SL is 3.2 MJy/sr and the mean level of the background-subtracted SL spectrum averaged across a large region of 30 Doradus is about 100 MJy/sr.

The different modules of an IRS spectrum do not always match up well in flux density. The mismatches between the SL1 and SL2 modules, and between the LL1 and LL2 modules, were rarely serious. However, we noticed more consistent mismatches between the SL1 and LL2 modules. The primary cause is probably that the emission in the 30 Doradus region is often best characterized as neither a point source nor as a uniform extended source, but instead as something in between. We have treated it as a uniform extended source (see §2.8.2), likely losing some flux. This would call for a multiplicative correction. We found logarithmic fits to the continuum emission close to the junction in each module and multiplied the SL spectra by the ratio of the fits in the overlapping wavelengths. The mean value of the multiplicative correction is 1.2 with a standard deviation of 1.2.

2.9 Quality Assurance (Appendix 2)

In order to check our work on reducing the spectral map, we compared our spectra, taken with the low resolution modules of the IRS in mapping mode, to spectra of several areas of the 30 Doradus nebula taken with both the low and high resolution modules of the IRS, in staring mode (private correspondence and Lebouteiller et al. 2008)[5]. These spectra will henceforth be referred to as the GTO spectra. The apertures they span are displayed in green in Figure 2.3. By selecting the subsets of our map that coincide with the GTO apertures, we can produce spectra which should be consistent with theirs. We applied PAHFIT, the same fitting algorithm that we use on our spectral map, to the GTO spectra. We made some adjustments to PAHFIT to allow for the much higher spectral resolution in the GTO spectra redward of about 10 μm, where there is coverage from the high resolution modules.

In Figure 2.24, the fitted spectra from two of these apertures are shown. The overall agreement in the shape of the spectrum is clear, with a notable exception in the continuum from 20 to 32 μm (likely the result of nonlinearity in the short-low detector response). In the upper panel, taken from an aperture toward the south of the 30 Doradusnebula, at around $05^h38^m50^s$ -69°06′41″, where the continuum emission at long wavelengths is relatively faint, the agreement between the GTO spectrum and ours is close, but the effect starts to become noticeable at higher flux densities. In the lower panel, taken from a brighter part of the 30 Doradus nebula at $05^h38^m48^s$ -69°04′10″ where the falling response in the LL1 is more severe, the difference between the GTO spectrum and ours is larger.

We are most concerned with whether we can obtain the same emission line strengths by fitting the GTO spectra in the same manner as ours. Figures 2.24 and 2.25 show

[5] IRS GTO program, ID#63, AOR keys 4382720, 12081152, and 12081408

that the PAHs have similar profiles, while the unresolved atomic lines are narrower with higher central intensities in the long-wave, high resolution part of the GTO spectra. The integrated strengths of several of the long-wave emission lines of interest are plotted in Figure 2.26, for twelve GTO spectra and the corresponding apertures in our map. Perfect agreement falls along the line of unity.

The fits to the PAH complex at 11.3 μm agree well only at low strength. This may be because of detailed fine structure that appears in the PAH complex at high resolution. In the low resolution spectrum, only a broad feature at 11.3 μm, with a shoulder at 11.0 μm, is apparent. A Drude profile is sufficient to fit that, and a more complex fitting profile would not be appropriate because of the lack of resolution. In high resolution such as in the GTO spectra, the shoulder at 11.0 μm resolves into a completely separate feature (see Figure 2.25), possibly another PAH feature. This might also be the Paschen-γ HI recombination line, although so significantly shifted from its rest wavelength at 10.95μm as to make such an identification questionable. The main PAH feature at 11.3 μm displays a different profile that would require a more complex fitting algorithm. Thus, we are not concerned about this disparity. The conclusion is that PAHFIT is adequate for fitting PAHs at low resolution, but may not sufficiently describe the same features at high resolution – not surprising, as the list of features used in PAHFIT was empirically tuned using low resolution spectra.

A systematic disparity is evident in the comparison of the Humphreys-α λ12.37 μm fitted line strength. Upon closer examination, two factors surfaced. Both support the trend that the fitted line strength at low resolution is higher than the line strength at high resolution. First, the fainter molecular hydrogen line, H_2 S(2) λ12.28 μm, is resolved in high resolution. The fit to the high resolution Humphreys-α line therefore does not include any of the flux from the molecular hydrogen line. Meanwhile, in the low resolution spectrum, the flux from both lines contributes to the same broad feature. We are confident that Humphreys-α contributes most of the flux we see in low resolution, in part because the line center more closely coincides with 12.37 than with 12.28 μm, and in part because, as we can see in the high resolution spectra, the Humphreys-α line is equal to or stronger than H_2 S(2) in all of the areas of our map covered by the high resolution spectra. However, the flux of both emission lines is contributing to the low-resolution fit, and so to some extent, our fits to the line strength of the Humphreys-α line are overestimated. Quantitative comparison between high- and low-resolution spectra and between fits with and without the molecular hydrogen line show that the contamination of the Humphreys-α line strength is at most $\sim$20% (see §2.5.1). This effect is weakest in the parts of 30 Doradus dominated by ionized gas that are the focus of this paper, but should be kept in mind for analysis of the outer parts of the region and PDR physics in future papers. The second factor that contributes to the disparity seen in the second panel of Figure 2.26 is the PAH feature at 12.6 μm. As discussed above in the context of the PAH complex at 11.3 μm, the fitting package PAHFIT is intended for the relatively smooth features seen in low resolution, and does not handle the complex morphology of PAHs seen at high resolution as well. In the case of the PAH at 12.6 μm, its line strength in the high resolution fit is generally overestimated. Its broad wings thus lead the strength of the Humphreys-α line to be underestimated in the high resolution fit. The slight overestimation of the line in the low resolution spectrum and the slight underestimation of the line in the high resolution spectrum both contribute to the disparity.

The results for the forbidden neon lines, as for most of the stronger lines, show a tighter correlation. The close agreement in the fits to the low and high resolution spectra for the weaker [Ne II]λ12.8 μm is particularly encouraging because one of our concerns in interpreting the neon ratio was the possible entanglement of the [Ne II] atomic emission line with the above-mentioned PAH at 12.6 μm. In the high resolution spectrum, the PAH (with its often-unusual shape) and the atomic line are resolved. As in the case of the Humphreys-α line, the strength of the [Ne II] line may be slightly underestimated because of the poor, overestimated fit to the PAH at 12.6 μm. The close agreement between the low resolution and high resolution fit, across almost all of the twelve apertures, regardless of PAH strength in each aperture, indicates that there are no systematic errors to the low resolution fit that do not also appear in the high resolution fit. Thus, our results may share the slight bias toward underestimating the [Ne II] strength, but we are generally able to decompose [Ne II] and the PAH at 12.6 μm despite the lack of spectral resolution.

Finally, the correlation for the fitted line strength of [Ne III]λ15.5 μm is similarly good, with the exception of two apertures where the high resolution fitted line strength is significantly higher than the low resolution fitted line strength. These two apertures (displayed with squares rather than diamonds in Figure 2.26) are located in a small region of the map that exemplifies the extreme of the trend shown in Figure 2.24, where the response in the LL1 module falls until the module finally saturates. In these cases, our fit to the continuum with thermal dust components is not very successful. The fitted continuum is dragged down in the area from 20 to 32 μm, which forces it up in the region of 15 μm. This causes our estimation of the strength of [Ne III] to be underestimated.

For these two anomalous apertures, we conducted a test by removing the faulty LL1 spectrum and fitting only the remaining spectrum, to get a better estimation of continuum in the region of [Ne III]. This increased the fitted strength of [Ne III], though not enough to get it to agree with the value we obtained by fitting the high-resolution spectrum.

The effect of long-wave line strengths being underestimated in our low resolution spectra compared to the high resolution GTO spectra is seen for [Ne III]λ15.5 μm and [S III]λ33.4 μm in some areas of the map. Empirically, the line strengths of [Ne II]λ12.8 μm and [S III]λ18.7 μm appear to be unaffected, as shown by their close agreement with the GTO spectra. It is crucial to note that this effect is restricted to the small areas of the map where we can see falling response in the LL1 module, as drawn in Figure 2.4. In that localized area, we can expect our values of [Ne III] and [S III]λ33.4 μm to be underestimated relative to the GTO results by perhaps 30%, as shown in Figure 2.26 (the effect is very similar for [S III]λ33.4 μm). Outside these small areas of the map, the agreement between our spectra and the high-resolution GTO spectra is excellent for these two emission lines.

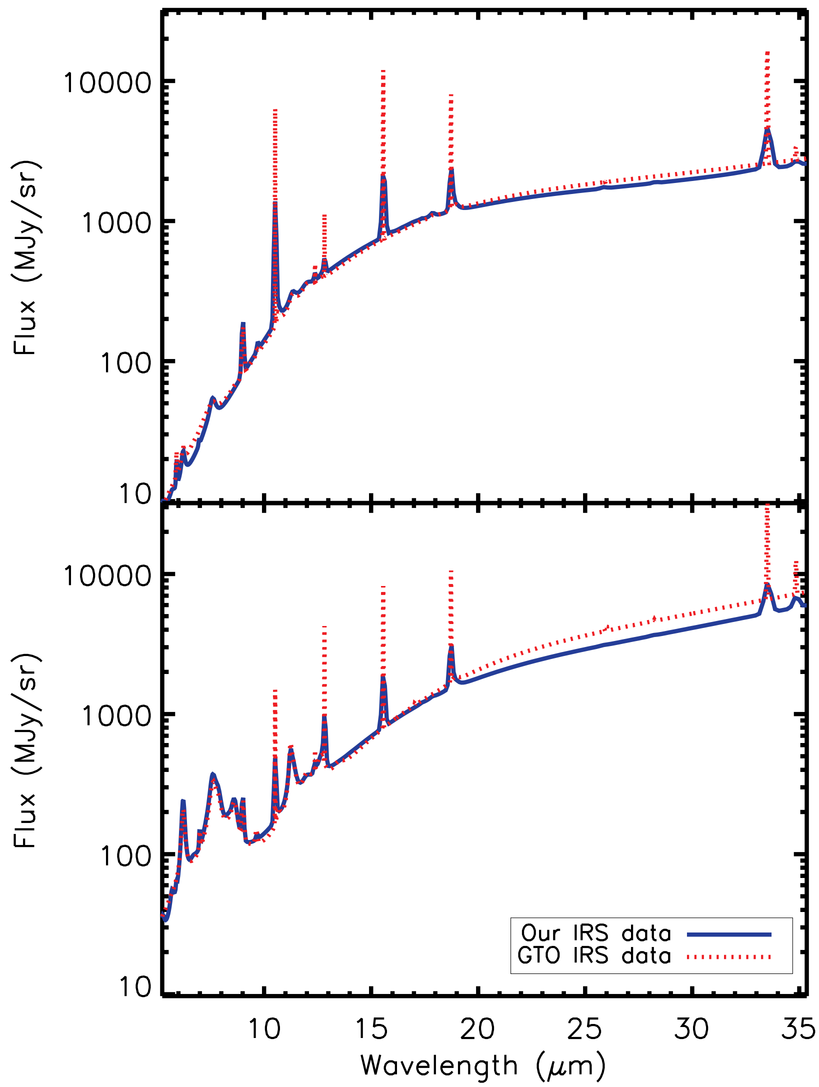

Fig. 2.24.— In blue, the fit to our low resolution spectra. In red, the same type of fit applied to the high resolution GTO spectra, with high resolution data at long wavelengths combined with low resolution data at short wavelengths (the transition is at about 10 μm). Top: a relatively faint area in the southern part of the 30 Doradus nebula. Bottom: a brighter area, where the low resolution spectrum suffers from partial saturation and falling response in the LL1 module.

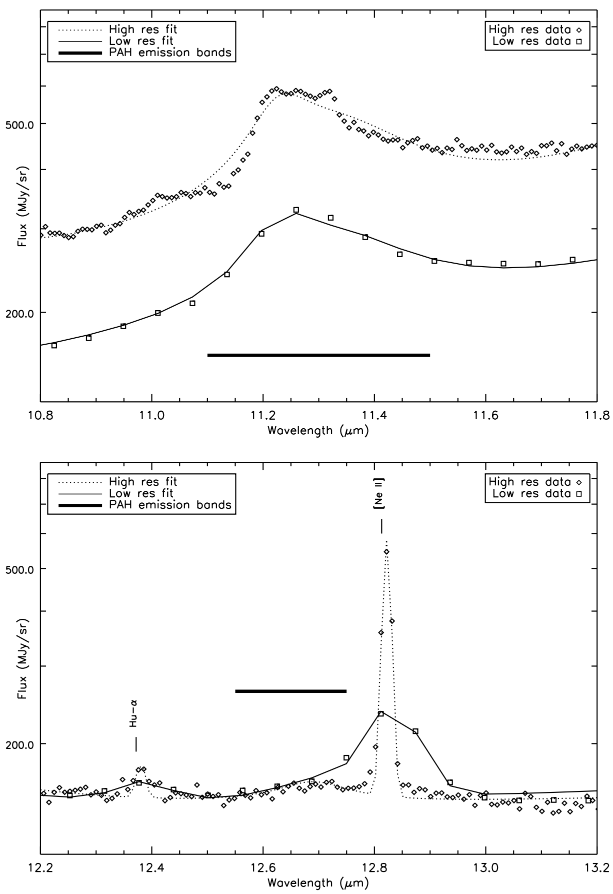

Fig. 2.25.— Two comparisons of our low-resolution IRS data to high-resolution IRS data from Lebouteiller et al. (2008). (The two panels are drawn from different regions on the sky, but for each panel the high and low resolution spectra are both extracted from the same aperture on the sky.) Both the measured spectra (symbols) and our fits made with PAHFIT (solid and dotted lines) are displayed. Note that while the high resolution spectrum has higher resolution for the lines, and the continuum strength may vary, the overall strength of the lines agree. Also note that the PAH has a fairly smooth appearance in the low-resolution plot and a more complex morphology in the high-resolution spectrum, which can cause problems when attempting to fit PAH strength in high-resolution. See §2.9.

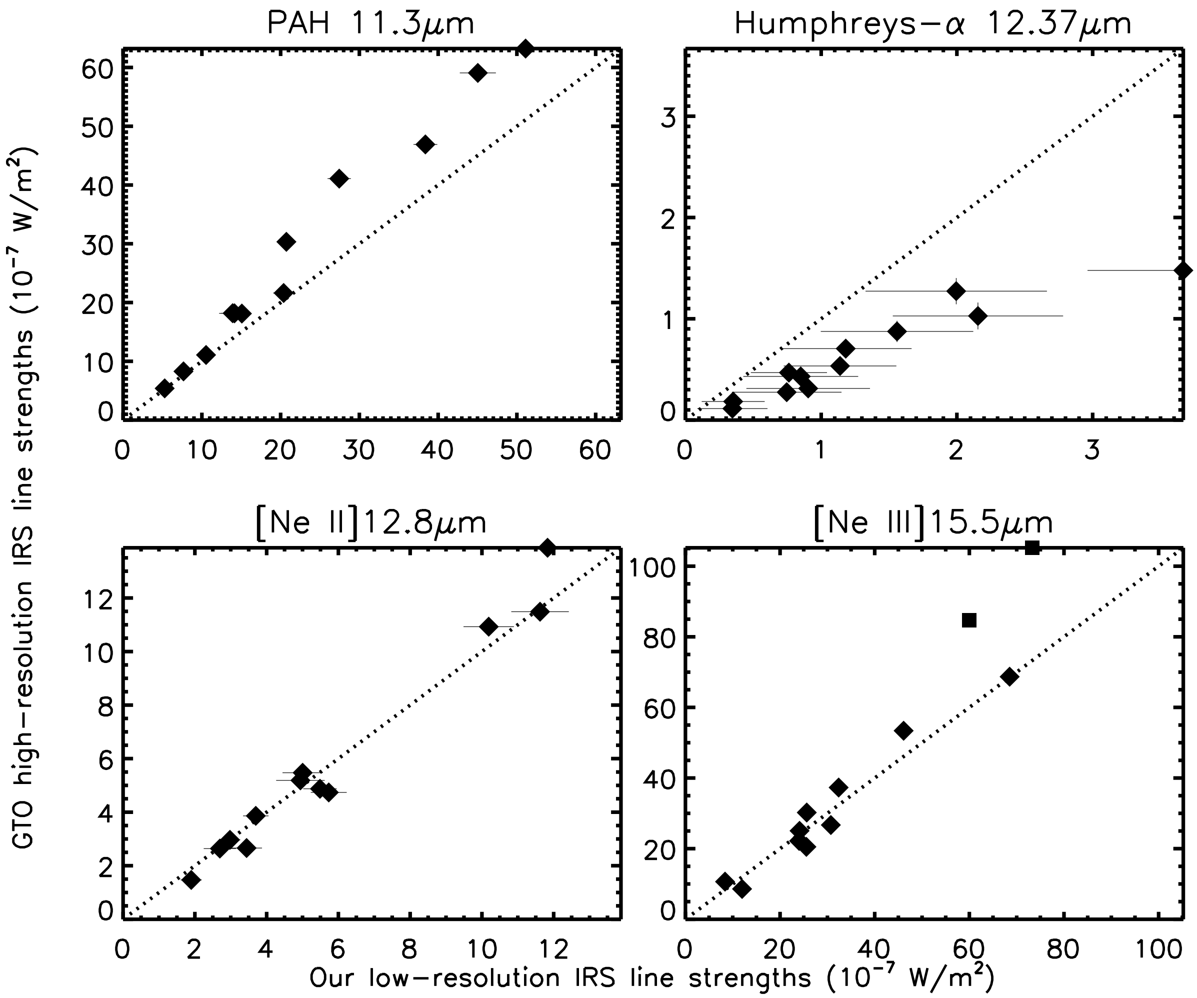

Fig. 2.26.— Comparison of the fitted integrated strengths of four emission lines. On the horizontal axis are the results from our low resolution spectra. On the vertical axis are the results of using the same type of fit on the GTO spectra, which are high resolution longward of about 10 μm. Each symbol represents one area of the 30 Doradus nebula, with horizontal and vertical error bars. The discrepancies from the line of unity are discussed in §2.9. Among those discrepancies, the fitting algorithm we used is not designed to fit the more complex structure of PAHs that is resolved in the high resolution spectrum. Another reason for the discrepancy in the Humphreys-α is that our fits to the line also include the fainter H_2 S(2) λ12.28 μm emission line, which is not well resolved at low resolution. The square symbols in the lower right plot call attention to two outlying points discussed in §2.9.

Chapter 3

Polycyclic Aromatic Hydrocarbons, Ionized Gas, and Molecular Hydrogen in Brightest Cluster Galaxies of Cool-core Clusters of Galaxies

3.1 Abstract

We present measurements of $5-25$ μm emission features of brightest cluster galaxies (BCGs) with strong optical emission lines in a sample of nine cool-core clusters of galaxies observed with the Infrared Spectrograph on board the *Spitzer* Space Telescope. These systems provide a view of dusty molecular gas and star formation, surrounded by dense, X-ray-emitting intracluster gas. Past work has shown that BCGs in cool-core clusters may host powerful radio sources, luminous optical emission-line systems, and excess UV, while BCGs in other clusters never show this activity. In this sample, we detect polycyclic aromatic hydrocarbons (PAHs), extremely luminous, rotationally excited molecular hydrogen line emission, forbidden line emission from ionized gas ([Ne II] and [Ne III]), and infrared continuum emission from warm dust and cool stars. We show here that these BCGs exhibit more luminous forbidden neon and H_2 rotational line emission than star-forming galaxies with similar total infrared luminosities, as well as somewhat higher ratios of 70 μm/24 μm luminosities. Our analysis suggests that while star formation processes dominate the heating of the dust and PAHs, a heating process consistent with suprathermal electron heating from the hot gas, distinct from star formation, is heating the molecular gas and contributing to the heating of the ionized gas in the galaxies. The survival of PAHs and dust suggests that dusty gas is somehow shielded from significant interaction with the X-ray gas.

3.2 Introduction

Infrared spectroscopy provides critical clues about the power sources of luminous galaxies whose energy sources are shielded from visual inspection by layers of dust and gas (Genzel et al. 1998; Kennicutt 1998a; Laurent et al. 2000), including star formation activity and AGN (e.g., Roussel et al. 2001). The Infrared Spectrograph (IRS) on board the Spitzer Space Telescope (Houck et al. 2004), exploiting the sensitivity and spatial resolution of *Spitzer*, delivered stunning infrared spectra from galaxies of many types. A key project, Spitzer Infrared Nearby Galaxy Survey (Kennicutt et al. 2003), as a survey of nearby galaxies ($D < 30$ Mpc), was limited to mainly spirals and a few ellipticals. Studies targeting the brightest infrared galaxies in the sky (e.g., Armus et al. 2009) included mainly the most luminous IR galaxies (LIRGs) and nearby IR-bright, star-forming galaxies. *Spitzer* programs such as these have produced a treasure of infrared spectra of galaxies as well as improved and standardized techniques for measuring infrared features (e.g., Dale et al. 2009). These recent theoretical and observational efforts have identified useful infrared diagnostics, which now allow a physical interpretation of the spectra based on models (Dale et al. 2006; Farrah et al. 2007; Smith et al. 2007b).

We explore here the infrared spectral signatures of Brightest Cluster Galaxies (BCGs). BCGs are not common even in large samples of galaxies, because massive clusters themselves are rare (of order a few in a box 100 Mpc on a side), so in general, to study an interestingly large and bright sample of BCGs, they must be specially targeted. Although most BCGs have red colors and are dust-free, suggesting little star formation, some 15-25% show evidence of significant star formation (rates up to $\sim 100\,\mathrm{M_{\odot}\ yr^{-1}}$) in their UV and optical continua (e.g., Johnstone et al. 1987; McNamara & O'Connell 1989; Fabian 1994; Crawford et al. 1999; Hicks & Mushotzky 2005; Rafferty et al. 2008; Bildfell et al. 2008; Hicks et al. 2010; Donahue et al. 2010).

Star-forming BCGs seem to be exclusively found in the centers of clusters whose hot intracluster medium (ICM) cores exhibit gas cooling times shorter than about

1 billion years or low hot gas entropies (K) where $K = kTn_e^{-2/3} < 30$ keV cm^{-2}, (e.g. Cavagnolo et al. 2008; Rafferty et al. 2008; Hudson et al. 2010) These clusters, once known as cooling flows, are called “cool-core” clusters. About half of the nearby X-ray luminous clusters fall into this category. This trend for cooling flow clusters to host BCGs with powerful emission line nebulae was first found by Hu et al. (1985), who noted a $\sim$ 14 billion year threshold, limited by the far cruder X-ray data available at the time. Then, astronomers suspected that gas cooling from the hot phase was somehow related to these nebular emission line systems although the emission lines themselves were too bright to be generated directly by cooling gas. Almost two decades later, X-ray Multi-Mirror (XMM) spectroscopy failed to show [Fe XVII] and [O VII] emission lines, conclusively demonstrating that very little X-ray emitting gas existed at temperatures 1/2-1/3 the temperature of most of the ICM (e.g., Peterson et al. 2003). However, the disproof of the simplest massive cooling flow model did not explain why BCGs in these systems frequently exhibited properties indicative of activity: extended emission line systems (Heckman et al. 1989), including vibrationally-excited molecular hydrogen at $1000-2000$ K (Elston & Maloney 1994; Jaffe & Bremer 1997; Donahue et al. 2000), CO masses indicating cold H_2 at $\sim$ 100 K (Edge 2001), UV excesses (most recently, O'Dea et al. 2010; Hicks et al. 2010; Donahue et al. 2010), radio sources (e.g., Burns 1990; Cavagnolo et al. 2008), IR emission from warm dust (Egami et al. 2006b; Donahue et al. 2007b; O'Dea et al. 2008). It is important to note that the XMM spectral results ruled out the enormous X-ray cooling rates inferred from the simple cooling flow model ($\sim$ 100s M$_\odot$ yr^{-1}), but do not provide limits near the cooling rates similar to the typical star formation rates estimated for these BCGs ($\sim 1-10$s M$_\odot$ yr^{-1}), with quantities an order of magnitude higher for the most extreme systems. Early Herschel results of a few

classic examples of these active brightest cluster galaxies in cool-core clusters reveal far-IR spectra of similar sources that are consistent with the short wavelength *Spitzer* observations: strong peaks in broadband photometry from dust warmed by recently formed stars and powerful interstellar coolant lines of OI (63 μm) and CII (153 μm) (Edge et al. 2010a,b), and *Spitzer* IRS measurements of individual BCGs reveal that some, like Zwicky 3146, have not only have powerful IR emission from warm dust but unusually luminous molecular hydrogen (Egami et al. 2006a), while others, like NGC4696, have luminous molecular hydrogen but only faint dust emission (Kaneda et al. 2008).

These brightest cluster galaxies also pose a challenge to galaxy formation models. The so-called "over-cooling" problem in galaxy formation simulations creates massive galaxies that are bluer, even more luminous, and with higher star formation rates than observed (see Balogh et al. 2001; Croton et al. 2006; Bower et al. 2006). To remedy this situation, models must include AGN feedback in the form of non-radiative energy in addition to stellar feedback to quench the formation of stars (e.g., Springel et al. 2005) and prevent the rapid cooling of hot intergalactic gas (e.g., Churazov et al. 2001; McNamara & Nulsen 2007). Furthermore, the accretion of hot gas has been proposed as the dominant mode for forming the most massive ($> 10^{11.4}$ $M_{\odot}$) galaxies (e.g., Kereš et al. 2005).

Conveniently, BCGs provide a laboratory for this type of galaxy formation. Chandra observations clearly show AGN interactions with the hot ICM in the form of cavities in the hot atmospheres of clusters and galaxies. The mechanical energy associated with these cavities is is sufficient to offset cooling (Bîrzan et al. 2004; Dunn & Fabian 2006), and to somehow regulate or quench star formation in most systems (Rafferty et al. 2006). However, energetic feedback from AGN is apparently unable to offset cooling entirely in all BCGs, and these systems that are struggling to offset rapid cooling are rich in cold gas and star formation (O'Dea et al. 2008). The correlation between star formation and short central cooling times in the hot gas shows that the gas fueling star formation may well have cooled from the hot ICM (Cavagnolo et al. 2008; Rafferty et al. 2008). Assessing and decoding the state of gas, dust, and stars in these galaxies, using *Spitzer* spectra, will yield clues about which physical processes are most relevant in determining a system's appearance and star formation rate during accretion of hot gas.

We present here Spitzer Infrared Spectrograph (IRS) (Houck et al. 2004) measurements of a sample of nine BCGs residing in cool-core clusters. We describe the measurement procedures, including the scaling we applied to the data to match aperture photometry, in §2. We present our results in §3. In §4, we compare the full spectra to a set of simulated time-averaged starburst spectral energy distributions (SEDs). In §5 we compare the emission line and polycyclic aromatic hydrocarbons (PAH) ratios and correlations seen in our sample to those seen in other types of galaxies. In §6 we discuss the correlation and lack of correlation in the various spectral components that suggest that at least two sources of heat must be considered in order to interpret the observations of these systems. We assume $H_0 = 70$ km s^{-1} Mpc^{-1}, and a flat, $\Omega_M = 0.3$ cosmology throughout.

3.3 Observations and Data Reductions

3.3.1 Observations

The *Spitzer* IRS observations took place in 2005 and 2006 (see Table 3.1), and the data were reprocessed in April 2009 (v18.7). Both short (SL) and long (LL) wavelength

Table 3.1. Observation Log.

Cluster BCG	Redshift[a]	*Spitzer* ID	IRS Mode	Obs Date	Duration (s) SL	LL	# of Slit Positions SL	LL
2A0335+096	0.0347	20345	Staring	2006 – 09 – 16	10156	1698	12	12
Abell 478	0.0860	20345	Staring	2006 – 03 – 17	10156	1698	12	12
Abell 1068	0.1386	3384	Mapping	2005 – 04 – 21	2925	234	6	2
Abell 1795	0.0633	3384	Mapping	2005 – 02 – 07	11701	1879	24	16
Abell 1835	0.2520	3384	Mapping	2005 – 02 – 13	2925	234	6	2
Abell 2597	0.0821	3384	Mapping	2005 – 06 – 30[b]	6826	704	14	6
Hydra A	0.0549	3384	Staring	2005 – 12 – 14	7313	1509	12	12
MS 0735.6+7421	0.216	20345	Staring	2006 – 04 – 25	21280	2768	4	4
PKS 0745-19	0.1028	20345	Staring	2006 – 05 – 16	10640	1384	4	4

[a]BCG redshift sources, from emission lines: 2A0335+096 (Donahue et al. 2007a), Hydra A (Smith et al. 2004), Abell 1795 (CGCG 162-010) (Hill & Oegerle 1993), Abell 2597 (PKS 2322-12) (Voit & Donahue 1997; Colless et al. 2003), see also http://www.mso.anu.edu.au/2dFGRS/, Abell 478 (NVSS J041325+102754) (Zabludoff et al. 1990), PKS 0745-19 (Hunstead et al. 1978), Abell 1068 (FIRST J104044.4+395712) (Allen et al. 1992), MS0735 (ZwCl 1370 or BCG 4C +74.12) (Stocke et al. 1991), Abell 1835 (SDSS J140102.07+025242.5) (SDSS DR2 ; see also Allen et al. (1992).

[b]Also 2005-07-05.

Table 3.2. Spitzer MIPS/IRAC Observation Log.

Cluster BCG	IRAC AOR	Obs Date	Duration (s)	MIPS AOR[a]	Obs Date	Duration[b] (s)
2A0335+096	18646528	$2006-09-26$	108	18636544	$2007-02-27$	400, 300
Abell 478	11579904	$2005-09-16$	1200	14944256 (1), 14944512 (2 & 3)	$2006-02-22, 2006-03-02$	550, 1500, 1200
Abell 1068	18650368	$2006-12-27$	108	18638336	$2006-12-08$	400, 320
Abell 1795	···	···	···	8788480	$2004-07-11$	36, 42
Abell 1835	4404480	$2004-01-16$	3600	4764160(1), 4744448(2 & 3)	$2004-02-20, 2005-06-28$	1800, 600, 150
Abell 2597	13372160	$2005-11-24$	3600	13371904	$2005-06-18$	140, 150, 60
Hydra A	26923008	$2008-06-09$	3600	4707584	$2004-05-04$	140, 120, 180
MS0735.6+7421	7858688	$2003-11-20$	500	···	···	···
PKS 0745-19	18667776	$2006-12-27$	108	18667520	$2006-12-08$	400, 300

[a]Channel (1) is the 24-μm channel, Channels (2 & 3) are the MIPS 70- and 160-μm channels respectively.

[b]Two durations indicate total exposure time in seconds for 24- and 70-μm MIPS observations, respectively. Three durations indicate exposure times for 24-, 70-, and 160-μm MIPS observation sequences, respectively.

observations were obtained, at low spectral resolution, $R \sim 60 - 130$. With two spectral orders each, we obtained a total of four spectral modules. We have sparse spectral maps of nine cool-core BCGs, though we analyze only the central region here. We used IRSCLEAN v1.7 to apply the bad pixel mask supplied by the *Spitzer* pipeline and to find additional rogue pixels using a WCLEAN formula with an aggressive level of 0.5 (suitable for relatively faint targets such as these). The LL pixels are $5.1''$ across, while the SL pixels are $1.8''$ across (Houck et al. 2004).

To cross-check our flux calibration of the IRS spectroscopy, we also analyzed photometry data from the *Spitzer* Infrared Array Camera (IRAC) (Fazio et al. 2004) and the from the Multiband Imaging Photometer for Spitzer (MIPS) (Rieke et al. 2004). We list the archival observations (known by their Astronomical Observation Requests or AORS) in Table 3.2. The aperture photometry is discussed in § 3.3.3.

3.3.2 Spectral Data Filtering and Extraction

This section discusses our choices regarding the IRS spectral extraction process, with particular attention to the treatment of extended sources compared to point sources. We used the software package CUBISM v1.7[1] (Smith et al. 2007a) to combine the exposures into a data cube, or spectral map. To reduce noise near the ends of the slit, we trimmed the exposures in the cross-dispersion direction by $3-5\%$. We confirmed that the off-target, paired observations for each spectrum were indeed source-free. These blank sky spectra were used for background subtraction.

To remove rogue pixels which were not caught by IRSCLEAN, we composed bad pixel lists using CUBISM's *autobadpix* algorithms, on both the global and individual record levels. At the global level, we flagged any pixel which deviated by more than

[1]http://ssc.spitzer.caltech.edu/dataanalysistools/tools/cubism/

Table 3.3. Parameters used in data reduction.

Cluster	Module	FWHM ($''$)	FWHM (kpc)	Type	Aperture center (J2000) RA	DEC	Aperture size ($''$)	θ[a] ($^\circ$)	Factor[b]
2A0335+096	SL2			Extended	3 : 38 : 40.5	9 : 58 : 12	10.8 × 10.8	17	1.16
	SL1	8.0	5.7		3 : 38 : 40.6	9 : 58 : 11	10.8 × 10.8	17	1.16
	LL2	10.5	7.5		3 : 38 : 40.4	9 : 58 : 9	30.6 × 15.3	−80	1.01
	LL1				3 : 38 : 40.5	9 : 58 : 10	30.6 × 15.3	−80	1.01
Abell 478	SL2			Extended	4 : 13 : 25.4	10 : 27 : 55	7.2 × 7.2	14	2.26
	SL1	7.0	12.3		4 : 13 : 25.4	10 : 27 : 56	7.2 × 7.2	14	2.26
	LL2	8.4	14.7		4 : 13 : 25.3	10 : 27 : 57	15.3 × 10.2	8	1.71
	LL1				4 : 13 : 25.3	10 : 27 : 56	15.3 × 10.2	8	1.71
Abell 1068	SL2			Point	10 : 40 : 44.5	39 : 57 : 11	12.6 × 5.4	−40	0.65
	SL1	3.7	10.6		10 : 40 : 44.4	39 : 57 : 11	19.8 × 3.6	−40	1.00
	LL2	9.0	25.6		10 : 40 : 44.7	39 : 57 : 9	35.7 × 10.2	43	1.00
	LL1				10 : 40 : 44.6	39 : 57 : 10	56.1 × 10.2	43	1.00
Abell 1795	SL2			Extended	13 : 48 : 52.5	26 : 35 : 33	12.6 × 3.6	−6	1.87
	SL1	8.1	10.5		13 : 48 : 52.5	26 : 35 : 34	12.6 × 3.6	−6	1.87
	LL2	12.7	16.5		13 : 48 : 52.2	26 : 35 : 35	20.4 × 10.2	78	1.33
	LL1				13 : 48 : 52.3	26 : 35 : 36	20.4 × 10.2	78	1.33
Abell 1835	SL2			Point	14 : 1 : 2.1	2 : 52 : 41	16.2 × 3.6	−11	1.20
	SL1	3.8	19.4		14 : 1 : 2.1	2 : 52 : 42	16.2 × 3.6	−11	1.20
	LL2	9.5	49.2		14 : 1 : 1.9	2 : 52 : 40	45.9 × 10.2	72	1.00
	LL1				14 : 1 : 2.0	2 : 52 : 39	45.9 × 10.2	72	1.00
Abell 2597	SL2			Extended	23 : 25 : 19.9	−12 : 7 : 27	9.0 × 3.6	27	3.42
	SL1	6.4	10.7		23 : 25 : 19.8	−12 : 7 : 27	9.0 × 3.6	27	3.42
	LL2	15.0	25.3		23 : 25 : 19.7	−12 : 7 : 26	15.3 × 10.2	21	1.87
	LL1				23 : 25 : 19.8	−12 : 7 : 26	10.2 × 10.2	21	1.87
Hydra A	SL2			Point	9 : 18 : 5.7	−12 : 5 : 43	14.4 × 3.6	−20	1.70
	SL1	4.7	5.3		9 : 18 : 5.7	−12 : 5 : 44	18.0 × 3.6	−20	1.70
	LL2	8.7	9.7		9 : 18 : 5.4	−12 : 5 : 43	35.7 × 10.2	63	1.70
	LL1				9 : 18 : 5.5	−12 : 5 : 44	35.7 × 10.2	63	1.00
MS 0735	SL2			Extended	7 : 41 : 44.6	74 : 14 : 39	5.4 × 3.6	−7	3.58
	SL1	6.2	27.5		7 : 41 : 44.6	74 : 14 : 39	3.6 × 3.6	−7	3.58
	LL2	10.4	46.0		7 : 41 : 44.2	74 : 14 : 39	10.2 × 10.2	−13	1.72
	LL1				7 : 41 : 43.8	74 : 14 : 39	10.2 × 10.2	−13	1.72
PKS 0745-19	SL2			Point	7 : 47 : 31.4	−19 : 17 : 39	12.6 × 3.6	−11	3.36
	SL1	4.9	10.3		7 : 47 : 31.4	−19 : 17 : 36	27.0 × 3.6	−11	1.29
	LL2	9.4	19.7		7 : 47 : 31.3	−19 : 17 : 37	25.5 × 10.2	72	1.00
	LL1				7 : 47 : 31.2	−19 : 17 : 36	25.5 × 10.2	72	1.00

(a) Angle of longer axis of aperture, in degrees east of north (CCW). (b) Factor applied to the extracted spectrum, to scale it up to the total light in a similar broadband aperture (only for extended-source spectra) and in a few cases to co-register modules and improve agreement with broadband measurements.

2.5σ from the median level in at least 50% of its appearances in the cube. This method flags only a few pixels, but each of these pixels has a relatively large effect on the spectral map. At the record level, we conservatively flagged any pixel which is a 5σ outlier in at least 75% of its appearances in the cube. This method flags more pixels, but only in individual exposures. We also manually removed obvious rogue pixels.

The *Spitzer* pipeline is optimized for single-slit observations of point sources, including a correction for the light lost from the slit, which can be as much as 36% (Smith et al. 2007a, Figure 4). However, CUBISM includes an option to remove this slit-loss correction factor, in order to extract spectra of extended sources. To determine which targets to treat as point sources, we used CUBISM to create a map combining all SL1 wavelengths, and averaged the two rows which covered the peak source emission. Using this light profile, we measured the FWHM along the slit (see Table 3.3). We did the same for the LL2. These modules were selected because their signal-to-noise is highest. *Spitzer's* PSF has an average FWHM of $2.6''$ in the SL and $6.6''$ in the LL [2]. Four of our nine galaxies have a FWHM in the SL1 of $\lesssim 5.5''$ and were considered to be point sources. The other five sources do not uniformly fill the *Spitzer* slit, but they are not well characterized as point sources.

For the point sources, we extracted spectra using an aperture that just spans the slit (2 pixels) and a length that captures most of the light along the slit (see Table 3.3). *Spitzer* data are calibrated for point sources and for this kind of aperture. Single-pointing software such as SMART[3] (Higdon et al. 2004; Lebouteiller et al. 2010) uses a similar aperture with its "tapered column" extraction, increasing the length of the aperture as the PSF broadens with wavelength, and further optimizing

[2] http://ssc.spitzer.caltech.edu/irs/irsinstrumenthandbook/

[3] http://ssc.spitzer.caltech.edu/dataanalysistools/tools/contributed/irs/smart/

the extraction by weighting each pixel by its signal-to-noise (Lebouteiller et al. 2010). In order to use the same software for all of our spectra, we used CUBISM to extract our point-source spectra, approximating the tapered column type of aperture. (For PKS 0745-19 SL2, we truncated the aperture to avoid a noisy region. For Abell 1068 SL2, CUBISM spreads the light from those two pixels across three rows.) To check our procedure, we also extracted the point-source spectra using SMART and found agreement to within about 10%, sometimes to within 2%.

For the extended targets, we removed the pipeline slit-loss correction factor. Our apertures include much of the available light with good signal-to-noise. However, our sparse spectral maps do not cover the full extent of the source.

After extraction, any noisy edges were trimmed from each order. In the observed frame, the four low-resolution IRS modules span the following wavelength ranges: SL2: $5.2 - 7.6$ μm; SL1: $7.5 - 14.5$ μm; LL2: $14.3 - 20.6$ μm; LL1: $20.5 - 37.5$ μm. Spectra extracted from CUBISM are reported in units of MJy sr^{-1}, so the size of the extraction aperture is used to convert spectra to units of flux density (mJy). We then corrected to the rest frame for each target (see Table 3.1) by dividing both the wavelength and fluxes by a factor of $(1 + z)$.

3.3.3 Aperture Photometry and Systematic Uncertainties

The light collected by the narrow *Spitzer* slit and our sparse spectral maps represents only a portion of the MIR light. Therefore, to obtain meaningful luminosities, we rely on IRAC and MIPS photometry (see Table 3.4) (as in Egami et al. (2006a)). The broadband aperture diameters are approximately three times the source's FWHM measured using the IRS (or equal to the FWHM of *Spitzer's* PSF for the 70 and 160 μm points) with subtraction of background computed from a larger annulus. We adjusted the aperture size to exclude unrelated foreground or background sources, and applied the suggested aperture corrections given by the MIPS Instrument Handbook. At 24 μm, the corrections are 1.17 (for apertures of 26″ and 30″) and 1.13 (for apertures 50″). For 70 and 160 μm the corrections are 1.22 and 1.752 respectively. The photometric uncertainty is 5% for IRAC, and 10, 20 and 20% for the MIPS 24, 70 and 160 μm points respectively.

Because the spectra within the cited IRAC and MIPS circular apertures may differ from the spectra obtained from within our smaller, rectangular IRS apertures, our analysis and conclusions rely most heavily on relative quantities, i.e., ratios, rather than absolute quantities. All correction factors for each module are listed in Table 3.3. The interested reader can recover the flux in the apertures listed in Table 3.3 by dividing the fluxes published here by this factor.

In three cases (Hydra A, A1795, MS0735), we do not have complete IRAC and MIPS coverage in the IRS wavelength range, and we needed a robust, standalone scaling procedure. For this purpose, we developed a scaling procedure that did not rely on IRAC or MIPS photometry. We validated this procedure, with scaled IRS spectra for sources with IRAC and MIPS photometry, by comparing the resulting spectrophotometry to IRAC and MIPS photometry. We now describe our scaling procedure.

For the sources we identified as extended, we fit Gaussian, azimuthally symmetric light profiles (and neglected the fainter extended haloes) to estimate how much of the source was included within a circle of the same area as our rectangular aperture. The spatial profile from the SL1 map was used as the reference to determine the scale for the SL1 and SL2 spectra for light from outside the rectangular aperture. The profile from the LL2 map was used for both LL orders. For point sources, this scaling has already been performed by the pipeline (See § 3.3.2).

An additional scale factor is needed to match the orders of the IRS spectrum. Flux mismatches are expected between the spectral orders extracted with CUBISM, because it is impossible to perform an exact tapered column extraction using CUBISM. Even tapered column extractions with SMART sometimes show mismatches. In our sample, three targets had mismatches between the first and second orders (SL1/SL2 or LL1/LL2), and three had mismatches between the SL and LL. Some spectra are plagued by noise or decreased signal at the module interface (e.g. 2A0335 near 7.1 μm). We selected the LL2 spectrum as the photometric reference point because of the good agreement between the LL spectrum and MIPS photometry in a similar aperture and because the LL is less vulnerable to slit loss due to pointing errors (because of its larger pixels) (Smith et al. 2007a). As mentioned above, the LL2 has superior signal-to-noise to the LL1. We used low-order polynomial continuum fits to match the modules when major features did not interfere.

In three cases an additional overall factor was needed (Hydra A (1.70), A478 (1.55), MS0735 (1.12)), probably because of extended halo light contained within the broadband aperture but not represented by our Gaussian profile. This procedure worked well, because agreement between the IRS spectra and broadband photometry was relatively good, almost always within 10%, and usually within 5% (see Figures 3.1-3.2). Therefore, while the IRS spectrum appears to exceed the IRAC value at 8 μm for Hydra A, the agreement between the integrated spectrum and the IRAC photometry point is actually excellent. Note that the comparison here is between the MIPS and IRAC photometry and the observer-frame IRS spectra integrated over appropriate bandpasses. These flux points should not be confused with the integrated IRS photometry in the rest-frame 24-μm MIPS bandpass reported in Table 3.5.

For analysis and plots, we combine the uncertainty calculated by the SSC pipeline in quadrature with a 15% systematic uncertainty to all fluxes to account for the uncertainty in scaling the IRS photometry relative to *Spitzer* broadband photometry. The systematic uncertainty dominates in almost all measurements. An additional 5% absolute photometric uncertainty is applied when making comparisons with data from other telescopes.[4].

3.3.4 PAHFIT Spectral Decomposition

We used the spectral-decomposition package PAHFIT v1.2 (Smith et al. 2007b) to make empirical fits to the IRS spectra and to facilitate direct comparison with results from other workers using the same method. The short-wavelength PAHFIT results are plotted in Figures 3.1-3.2 and the full-wavelength results are shown in Figure 3.3. PAHFIT fits the following components: a starlight continuum, several thermal dust continuum components, broad PAH emission bands, narrow atomic and molecular emission lines, and broad silicate absorption bands (Figures 3.1-3.2.) We customized the list of fitted emission features to a limited set, excluding those that were very weak. In the case of 2A0335, small parts of the spectrum (below 5.3μm and between 7.05 and 7.35μm) were excluded from the PAHFIT analysis because noise in those parts of the spectrum hindered a successful fit.

[4]http://ssc.spitzer.caltech.edu/spitzermission/missionoverview/spitzertelescopehandbook/

Table 3.4. Broadband Spitzer Photometry

Band	2A0335+096	Abell 478	Abell 1068	Abell 1795	Abell 1835	Abell 2597	Hydra A	MS 0735	PKS 0745-19
3.6	9.2 [12]	4.2 [20]	2.1 [10]		2.5 [14]	4.5 [20]		1.4 [20]	3.0 [14]
4.5	5.6 [12]	2.8 [20]	2.0 [10]		2.0 [14]	2.9 [20]	2.9 [14]	1.0 [20]	2.1 [14]
5.8	4.4 [12]	2.0 [20]	2.7 [10]		1.3 [14]	1.8 [20]		0.7 [20]	1.7 [14]
8.0	3.5 [12]	1.7 [20]	7.5 [10]		4.5 [14]	1.9 [20]	4.1 [14]	0.4 [20]	2.3 [14]
24.0	2.4 [26]	1.6 [30]	74.8 [30]	1.8 [40]	17.8 [30]	2.1 [50]	9.1 [30]		10.2 [30]
70.0	77.1 [70]	62.8 [70]	894.5 [70]	37.2 [70]	175.0 [70]	89.0 [70]	155.2 [70]		154.3 [70]
160.0		56.4 [80]			317.0 [80]	42.0 [80]	181.8 [80]		

Note. — IRAC and MIPS waveband centers are in units of μm. Observer-frame fluxes are in units of mJy, and aperture diameters in arcseconds are given in brackets. Photometric uncertainties are $\sim 5\%$ for IRAC and, for MIPS, 10, 20, 20% for 24, 70, and 160 μm respectively.

3.4 Results

Our BCG galaxies exhibit a number of emission features from PAHs, ions, and H_2 molecules. The H_2 features are unusually prominent. The BCG spectra qualitatively fall into two general categories. Four galaxies (A1835, A1068, PKS0745, and Hydra A) exhibit the strongly rising IR continuum at $> 25\,\mu$m and distinct PAH features characteristic of galaxies with strong signatures of star formation (e.g., Brandl et al. 2006; Smith et al. 2007b). In the remaining five cases, the 5-7μm continuum is dominated by cool stars, in contrast to the spectra of starbursts.

Several spectral features, which do not correspond to a known emission feature, are artifacts of noise or the data reduction process. For example, in the spectrum of A1835, there is noise on the red shoulder of the 11.3 μm PAH band where the SL and LL modules do not perfectly align; this is also responsible for noise near 13 μm in A478. The junction between the LL2 and LL1 accounts for some of the noise near 17 μm for A1835, and near 20 μm for 2A0335. A feature near 24 μm in the spectrum of A1068 may be attributed to [Ne V]24.3 μm, as discussed in § 3.6.5, but is probably spurious. An emission feature near 4.9 μm in A478, and possibly A1795, A2597, and PKS0745, might be ascribed to [Ar V]4.93 μm, or to an unidentified PAH. The feature at 20.7 μm in A478 is unidentified. The noise at 15.0 μm in the spectra of A2597 and A1795, and 18.0 μm in Hydra A, appears to be spurious. Note that noise increases dramatically past about 33 μm in the observed frame.

The features we will examine most closely in this paper are the relatively bright forbidden emission lines of [Ne II] at 12.8 μm, [Ne III] at 15.6 μm, and the PAH complexes at 7.7, 11.3, and 17 μm. We include an analysis of the correlation of the intensities of the brightest rotationally-excited molecular hydrogen transitions, S(2) and S(3), with those of other spectral features. A selection of line measurements and intrinsic luminosities including 1-σ statistical errors from PAHFIT are presented in Table 3.5. The continuum fluxes and luminosities (νL_ν) are found from the feature-free continuum (the stellar blackbody, thermal dust components, and silicate absorption). The continuum measurements were determined by averaging across bandpasses 1 μm in width at 6 and 15 μm, and weighting by the 24-μm MIPS response. All fluxes and luminosities in Table 3.5 are presented in the rest frame, at the rest wavelength. To recover observed fluxes, multiply by $(1+z)$. A more detailed analysis of the molecular hydrogen line ratios and excitation diagrams is deferred to a paper in preparation.

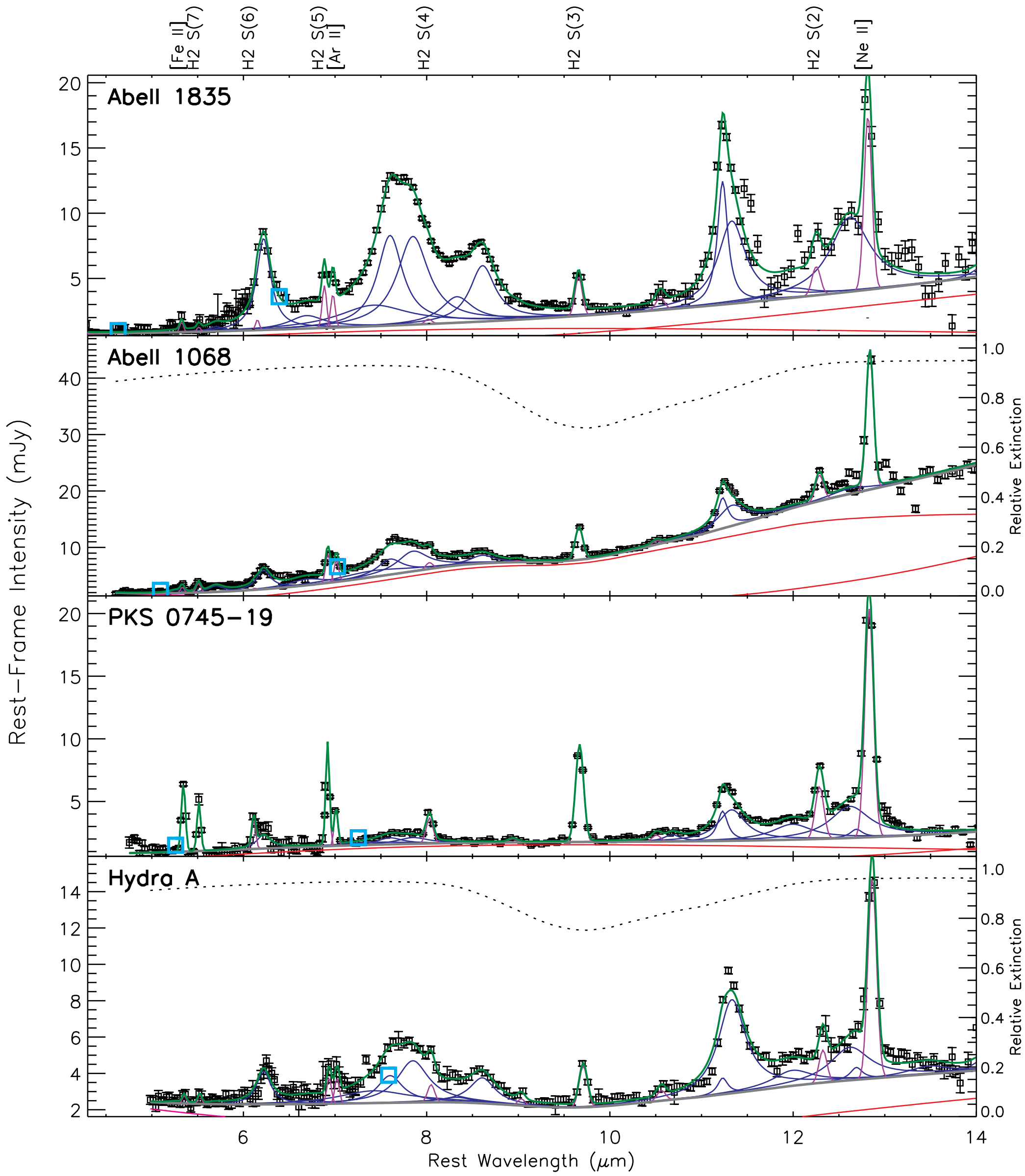

Fig. 3.1.— Detailed decompositions of nine cool-core galaxy clusters from 4.3 to 14 μm, utilizing PAHFIT (Smith et al. 2007a). Red lines represent thermal dust components; magenta, the stellar continuum. Their combination is a thick gray line. Broad PAH emission complexes are plotted in blue, and the unresolved emission lines arising from low-ionization or molecular hydrogen emission are plotted in violet and labeled at the top. The full spectral extraction is indicated by the green line, plotted over the rest-frame flux intensities and statistical uncertainties. In the two cases where the empirical PAHFIT detected silicate extinction, the extinction curve is represented with a dotted line using the axis at right; all components are diminished by the extinction. Appropriately transformed IRAC photometry is indicated by cyan squares (see Table 3.5).

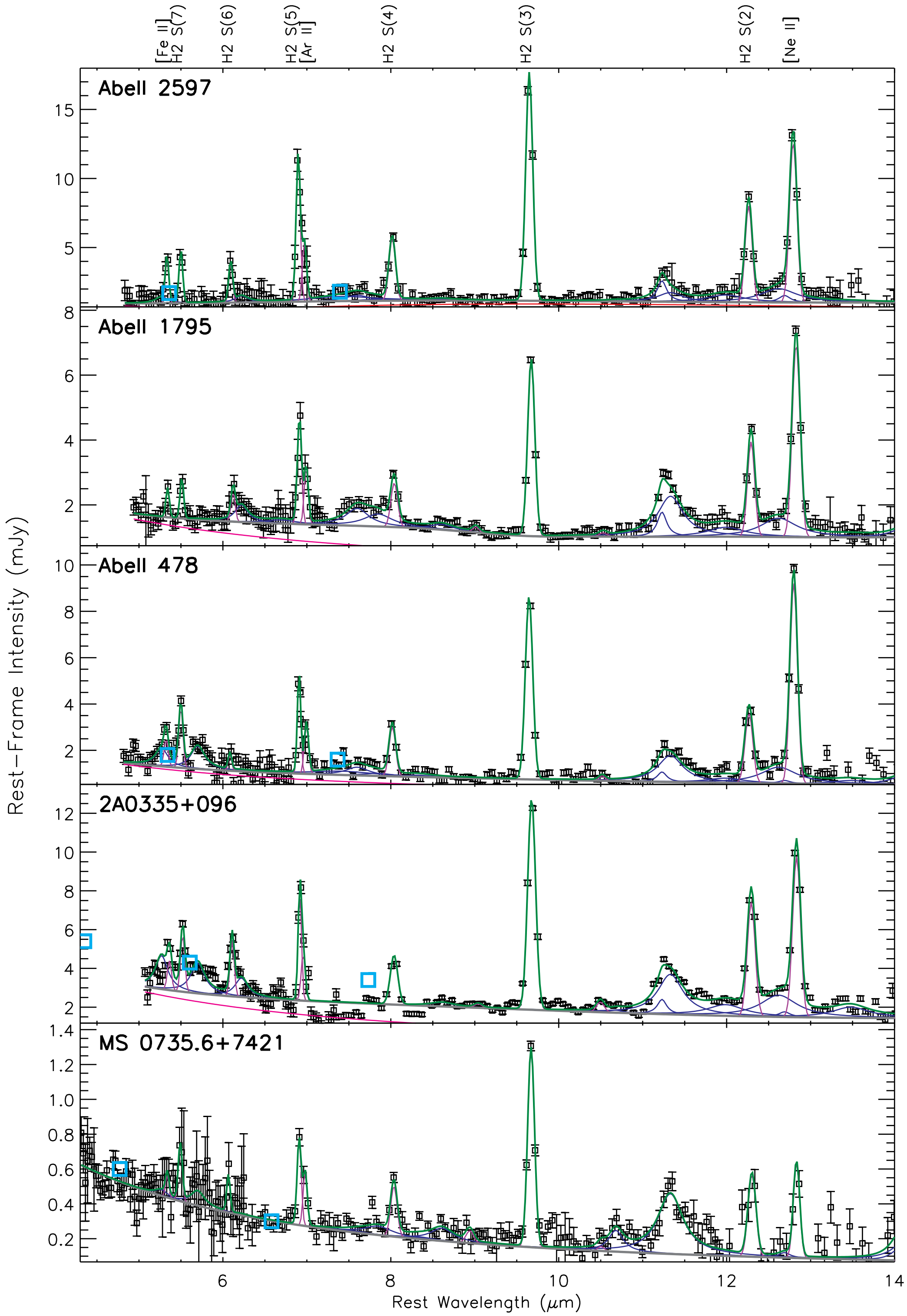

Fig. 3.2.— Figure 3.1 continued.

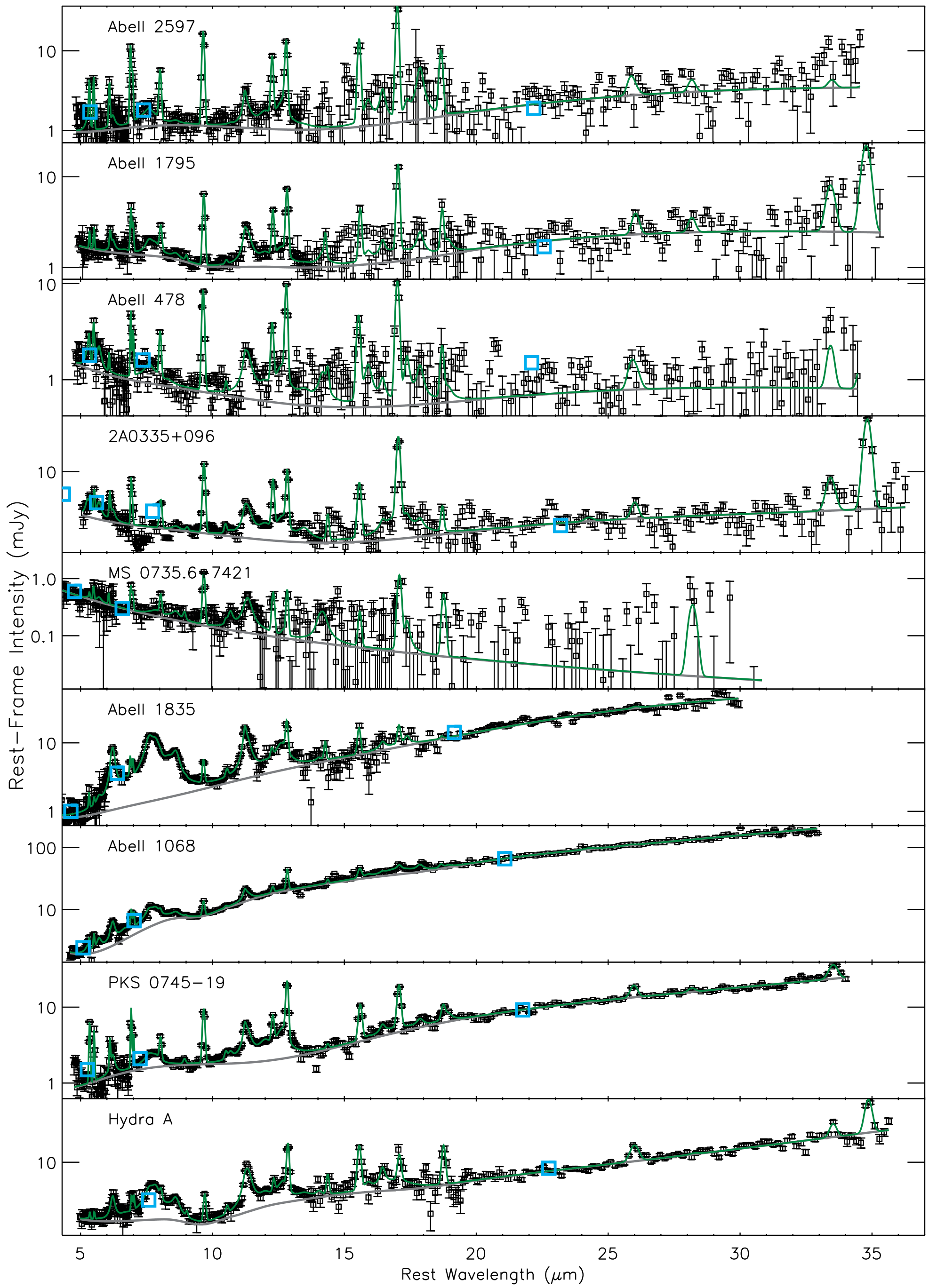

Fig. 3.3.— PAHFIT results over the full wavelength coverage. The continuum (stellar + thermal dust) is represented by a thick gray line, and the full spectral extraction by a green line. The rest-frame flux intensities are plotted with statistical uncertainties. Note the log scaling exaggerates the uncertainty of the faint, long-wavelength continua for several targets. Appropriately transformed IRAC and MIPS photometry points are indicated by cyan squares (see Table 3.5).

Table 3.5. Line and Continuum Measurements

Line	2A0335	A478	A1068	A1795	A1835	A2597	HydraA	MS0735	PKS0745
Ne II 12.8 μm Flux	17.7	17.4	47	13.0	26	23.2	24.6	0.95	38.9
Ne II 12.8 μm Flux Error	± 0.3	± 0.4	± 2	± 0.3	± 4.	± 0.9	± 0.6	± 0.2	± 0.3
Ne II 12.8 μm Lum	0.0499	0.319	2.4	0.126	5.0	0.386	0.176	0.129	1.05
Ne III 15.5 μm Flux	11.6	8.2	28	5.63	16	21	22	< 0.5	14.3
Ne III 15.5 μm Flux Error	± 0.7	± 0.6	± 1	± 0.7	± 2.	± 2.	± 1.	···	± 0.3
Ne III 15.5 μm Lum	0.0328	0.15	1.45	0.054	3.1	0.36	0.16	< 0.07	0.385
PAH 7.7 μm Flux	··· [a]	26	300.	28	532.	42	180	< 4	46
PAH 7.7 Flux Error	···	± 6	± 8	± 9	± 6	± 10	± 10	···	± 4
PAH 7.7 Lum	···	0.49	15.4	0.27	103.	0.71	1.3	< 0.6	1.2
PAH 11.3 μm Flux	31.2	17	91	22	132.	16	83	4.6	44.9
PAH 11.3 Flux Error	± 0.7	± 1	± 2	± 1	± 2	± 3	± 3	± 0.3	± 0.8
PAH 11.3 Lum	0.0881	0.32	4.7	0.21	25.5	0.27	0.60	0.63	1.21
PAH 17 μm Flux	32	< 14	260.	< 27	< 36	< 48	42	< 0.89	25
PAH 17 Flux Error	± 10	···	± 80	···	···	···	± 20	···	± 10
PAH 17 Lum	0.090	< 0.25	13	< 0.26	< 7.0	< 0.80	0.30	< 0.12	0.68
H2 S1 Flux	38.7	16.8	< 20	18.0	< 11	49	10.	1.8	23.6
H2 S1 Flux Error	± 0.9	± 0.7	···	± 1.	···	± 2	± 2	± 0.2	± 0.5
H2 S1 Lum	0.109	0.310	< 0.9	0.174	< 2.2	0.82	0.075	0.25	0.635
H2 S2 Flux	13.7	7.0	10.9	6.4	5.1	14.5	4.0	1.1	9.7
H2 S2 Flux Error	± 0.3	± 0.4	± 0.7	± 0.3	± 2.	± 0.8	± 1.	± 0.2	± 0.3
H2 S2 Lum	0.0386	0.13	0.56	0.062	0.99	0.242	0.029	0.15	0.26
H2 S3 Flux	40.8	27.8	28	22	9.6	56	11	3.73	27.0
H2 S3 Flux Error	± 0.4	± 0.5	± 1	± 2	± 0.6	± 1	± 1	± 0.09	± 0.3
H2 S3 Lum	0.115	0.511	1.4	0.21	1.9	0.93	0.077	0.509	0.726
Cont 24 μm Flux (mJy)	2.66	0.931	91.0	2.12	25.4	2.57	9.0	< 0.04	11.6
Cont 24 Flux Error	± 0.06	± 0.05	± 0.1	± 0.07	± 0.1	± 0.1	± 0.06	···	± 0.03
Cont 24 Lum	0.937	2.14	582.	2.56	614.	5.35	8.1	< 0.7	38.9
Cont 15 μm Flux (mJy)	1.45	0.520	28.4	1.04	6.13	1.07	4.49	< 0.1	3.13
Cont 15 Flux Error	± 0.1	± 0.1	± 0.2	± 0.1	± 0.3	± 0.3	± 0.2	···	± 0.06
Cont 15 Lum	0.817	1.91	291.	2.01	237.	3.57	6.43	< 2.73	16.8
Cont 6 μm Flux (mJy)	2.60	1.14	2.23	1.46	0.99	1.0	2.20	0.36	1.18
Cont 6 Flux Error	± 0.03	± 0.05	± 0.05	± 0.04	± 0.09	± 0.1	± 0.05	± 0.02	± 0.05
Cont 6 Lum	3.66	10.5	57.1	7.04	96.	8.4	7.8	25.	15.9

Note. — Emission line flux values are in rest-frame units of 10^{-18} W m^{-2}, while continuum ('Cont') fluxes are quoted in mJy. Luminosities are in units of 10^{42} erg s^{-1}. Fluxes, luminosities, and wavelengths are corrected to their rest-frame values (To recover the observed flux, multiply by $(1+z)$.) The 1σ flux errors are statistical only. A 15% systematic error (0.06 dex) is included in the plots and in the analysis, as discussed in § 3.3.3. Upper limits are 3σ.

[a]The fit to 2A0335's 7.7μm PAH complex failed because of decreased signal near the expected location of the feature. We were unable to set an upper limit in this case.

3.5 Best Fit Starburst and Old Stellar Population SED Models

We fit the IRS spectra of the BCGs with an ensemble of simulated spectral energy distributions (SEDs). These models allow us to estimate the total infrared luminosity and associated star formation rates and to identify differences between the SED of a star-forming galaxy and the observed SEDs. We use the suite of starburst models, including a wavelength-dependent attenuation template, described in Groves et al. (2008) together with an SED of a 10 billion year old stellar population, derived using Starburst99 (Leitherer et al. 1999). Groves et al. (2008) model the starburst SED as the time-integrated sum of distinct HII regions and the the photodissociation regions (PDRs) surrounding them, over a range of cluster ages and cluster masses. These models were used to reproduce the SEDs of typical template starbursts such as Arp 220 and NGC 6240. The models span 5 different metallicities (Z = 0.05, 0.2, 0.4, 1.0, and 2.0 solar). Metallicity affects the prominence of the PAH features and the dust-to-gas ratio. The models sample 6 compactness parameters $\mathcal{C}$ which characterize the intensity of the stellar radiation at the HII region/PDR interface. More compact HII regions result in hotter grains. $\mathcal{C}$ determines the location (the "temperature") of the dust peak and thus controls the mid-IR emission peak, a feature that is not well constrained by IRS spectral coverage.

Groves et al. (2008) provide models for five gas pressures ($P/k = 10^4, 10^5, 10^6, 10^7, 10^8$ K cm^{-3}), spanning the range of lower pressures in star-forming galaxies to the higher pressures in ULIRGs. However, the infrared SED between 5-25 μm is insensitive to the pressure, except, at a marginal level, the forbidden lines, and we checked that changing the gas pressure does not change the other parameters. Since the ICM pressure in cool-core clusters is $\sim 10^6 - 10^7$ K cm^{-3}, the fits reported in Table 3.7 sample the range of $10^6, 10^7, 10^8$ K cm^{-3}. Finally, the Groves et al. (2008) models were computed for unobscured HII regions and HII regions with PDRs. We opted here to fit only the PDR models, since the models with only HII regions had no PAHs. Models are normalized in luminosity to a star formation rate of 1 $M_{\odot}$ yr^{-1} sustained over the 10 Myr lifetime of the HII region. The spectra and the best-fit components are shown in Figures 3.4-3.5.

We compared the observed spectra with the full suite of theoretical spectra and quantitatively identified the spectrum that best fit the data, in L_ν units, by minimizing the sum of chi-squared. In addition to the quantized parameters described above, we fit the normalization for each starburst SED ($M_{\odot}$ yr^{-1}), the attenuation (A_V), and the normalization of the old stellar SED ($M_{\odot}$). The Groves et al. (2008) models include forbidden lines and PAH emission, but not molecular emission, so we added a two-component local thermodynamic equilibrium (LTE) H_2 spectrum, each component specified by T (K), and column density N (10^{18} cm^{-2}). We used molecular properties and A-values from Black & Dalgarno (1976); Huber & Herzberg (1979). The widths of the H_2 lines were fixed to 0.05 μm.

In this comparison, the compactness parameter ($\mathcal{C}$) seemed to divide BCGs with strong rising IR continuum from those with relatively flat IR continuum in the IRS spectral range. The fit quality was sensitive to $\mathcal{C}$, which mainly affects the steepness of the long-wavelength IR continuum. The BCGs with the best-fit $\mathcal{C} = 4$ are 2A0335, A1795, A2597, A478, and MS0735. The first four of these galaxies have the lowest four 24/70 μm MIPS photometry ratios in the sample ($= 0.03 \pm 0.01$); MS0735 lacks MIPS photometry. The signal to noise in the IRS spectrum of MS0735 at long wavelengths

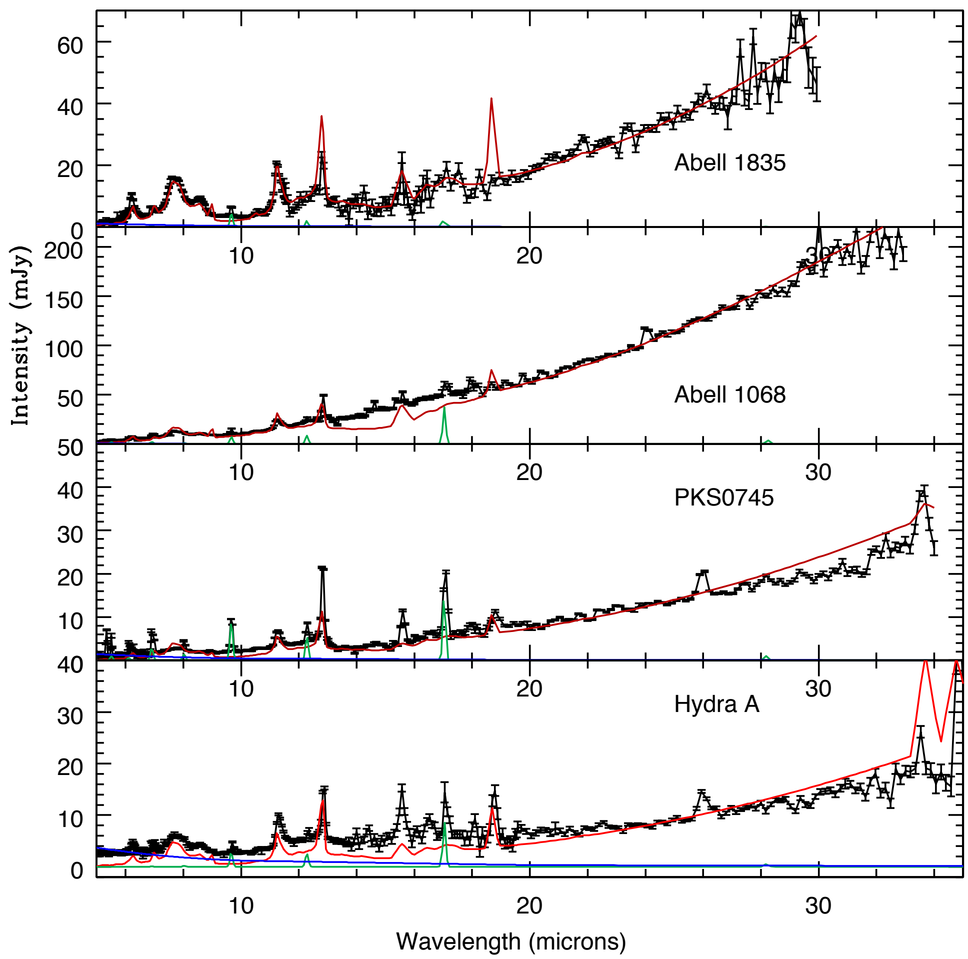

Fig. 3.4.— Rest wavelength 5-35 μm spectra, observed fluxes. (To convert to rest-frame flux, divide by (1+z).) Red line: Best fit constant star formation model from Groves et al. (2008). Blue line: Best fit old stellar population. Green line: Molecular hydrogen, two-temperature LTE model.

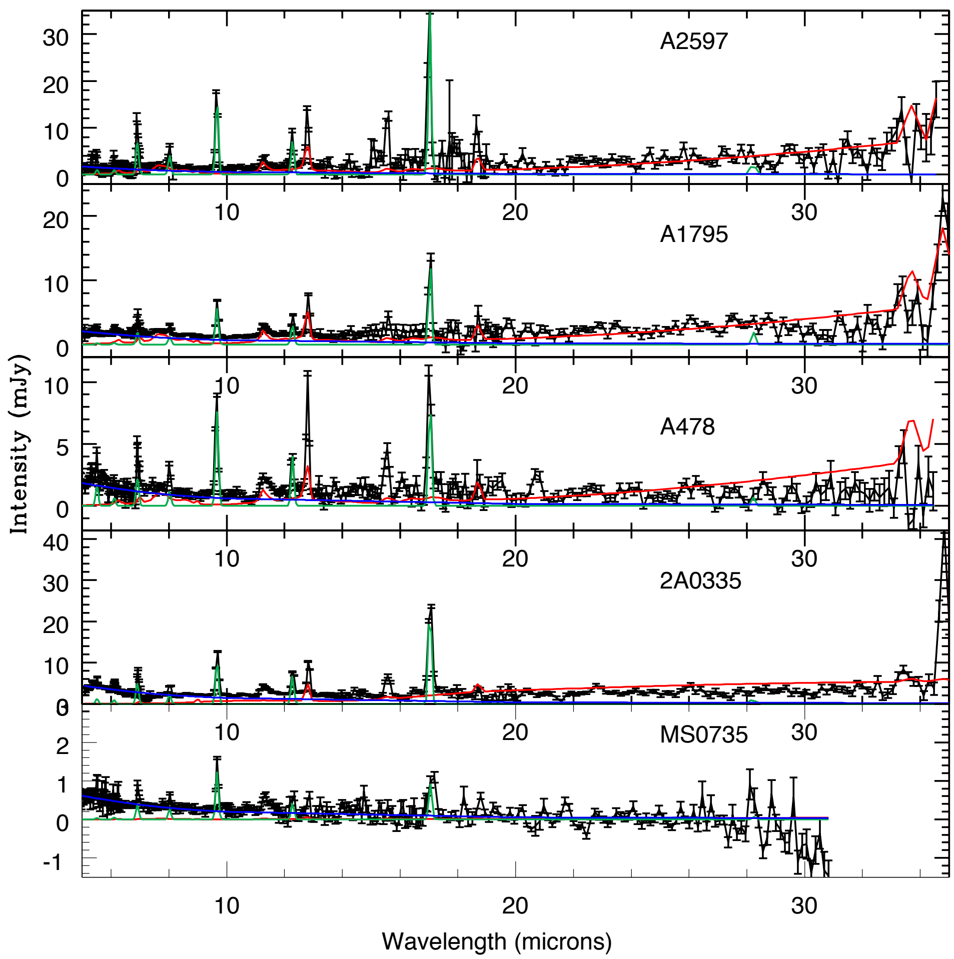

Fig. 3.5.— Figure 3.4 continued.

is so low that there are no strong preferences for any starburst SED over another. The other 4 BCGs in the sample have higher 24/70 μm ratios ($= 0.08 \pm 0.02$). This trend in flux ratios is consistent with the compactness parameter governing the peak in the dust spectrum, in the sense that more compact HII regions have PDRs with hotter dust.

The metallicity also affects the SED in this region, particularly the relative strength of the PAH feature to the infrared continuum. The preferred starburst SED metallicities for the BCGs were at the high end ($Z/Z_\odot = 1$ or 2). For all of the BCGs, the fit quality was very similar for $Z/Z_\odot = 1$ or 2, except for that of A1068, which preferred $Z/Z_\odot = 0.5$ or 1. That result is consistent with the fact that the BCG in A1068 has the lowest PAH to mid-IR continuum ratio of the sample (see § 3.6.1). We note these high metallicities are consistent with the metallicity of the ICM in the centers of these clusters. As expected, pressure did not affect the fit quality in any significant way. The spectral features, including the 7.7 and 11.3 μm PAH features, were often well-matched by models including the PDRs at rest wavelengths shortward of 10-11 μm. The two-temperature molecular hydrogen template matched the H_2 spectrum very well in most cases.

To check this process, we estimated the total infrared luminosity from the expression $L_{TIR} = 1.559 L_{24} + 2.1156 L_{70}$, adapted from Dale & Helou (2002). L_{24} is νL_ν at 24 μm and L_{70} is νL_ν at 70 μm. To adapt their equation 4 to this expression, we assume that νL_ν at 70 μm $\sim \nu L_\nu$ at 160 μm. Some assumption was necessary since the 160 μm flux is only available for 4 objects. This approximation may underestimate the TIR luminosity by about 30% compared to estimates using the 160 micron luminosities, but these 160 μm luminosity estimates are subject to large systematic uncertainties, and the detected sources may not be representative of the sources lack-ing photometry. (For MS0735+74, we have no MIPS photometry and only a 3-σ flux limit at 24 μm from the IRS spectrum. We do not include this source in plots of TIR.) We compared L_{TIR} estimated from this adaptation of Dale & Helou (2002) to L_{TIR} derived using the calibration of L_{24} in Equation 2 of Wu et al. (2010). To get rest-frame 70/24 μm ratios used in this calibration, we convert the observed MIPS luminosity 70 to 24 μm ratios to rest-frame ratios for 8 of the 9 galaxies in the sample with k-correction factors ($k_{70/24}$) based on the best-fit SEDs ($< 3 - 25\%$; Table 3.6). The derived total IR luminosities were consistent to better than 20% (Table 3.6). The relationship between either estimate of L_{TIR} and the SED-inferred SFR is consistent with the Kennicutt (1998) SFR relation for starbursts (Figure 3.6a). This consistency indicates the 24 and 70 μm MIPS data, not included in the fits, are consistent with the star formation rates inferred from the IRS data alone.

In Figure 3.6b, we plot the star formation rates based on the SED fits versus the Calzetti et al. (2010) mean relation for SFRs derived from the observed MIPS 70 μm luminosities (νL_ν) ($\mathrm{SFR(M_\odot)} = 0.059(\mathrm{L_{70}}/10^{42})\ \mathrm{ergs^{-1}}$). The dotted line shows the same relation, also from Calzetti et al. (2010), if a different Hα-based SFR from Kennicutt (1998) is used for calibration. Figure 3.6 demonstrates reasonable consistency between SFRs estimated based on SED fits to the IRS spectra and SFRs derived from MIPS photometry. One caveat to this comparison is that the IR continuum of galaxies with a significant old stellar population may have contributions from dust heated by these cool stars. The observed 70-μm luminosities of the BCGs are somewhat higher than what is predicted by the best-fit SEDs, by a factor of 1.3-2.4, which, if taken literally may indicate that dust heated by evolved stars may be contributing between 30-60% of the 70 μm luminosity. The 70 μm luminosities of these BCGs are in the valid domain for applying the relationships in Calzetti et al. (2010); the

160 μm luminosities are likely to be even more contaminated from cool dust emission unrelated to star formation.

It is interesting to note that the SFR estimates based on 24-μm luminosities, from Calzetti et al. (2010), are systematically lower compared to SFRs based on these SED fits or the 70-μm luminosities for the 4 galaxies with high 70/24 μm flux ratios (A478, 2A0335, A2597, and A1795) and low best-fit $\mathcal{C} = 4$, as well as MS0735 (which has no MIPS photometry). In Figure 3.7, we plot the rest-frame 70/24 μm luminosity ratio of the BCGs together with the local sample studied by Calzetti et al. (2010; Figure 17). The rest-frame 24 μm luminosity is calculated from the IRS spectra, but it is consistent with MIPS photometry. The rest-frame ratios are based on MIPS photometry alone, with small k-corrections ($< 10\%$ for $z < 0.1$, and $10 - 25\%$ for $z > 0.1$), based on the best-fit starburst SEDs. The 70/24 μm ratio varies by about factor of 10 for a given 24 μm luminosity in the full sample of Calzetti galaxies, and some of this scatter is due to metallicity, with the highest metallicity systems having the highest 70/24 μm luminosity ratios. The 70/24 μm ratios of BCGs are similar to, but somewhat higher than, those of high-metallicity star-forming galaxies. The two BCGs most like starbursts, A1835 and A1068, have ratios similar to the luminous infrared galaxies (LIRGs) of the Calzetti et al. (2010) sample.

We briefly discuss the results of the comparison to theoretical SEDs of star-forming galaxies for each source, ordered approximately by decreasing mid-IR luminosity. Note that all fluxes and luminosities in this paper are derived from PAHFIT, not these fits.

Abell 1835. The IRS spectrum of Abell 1835 shows a strong red continuum and PAH features whose shapes and intensities are well-fit by the model in Table 3.7. The most prominent residual is the overestimate of the flux of the [S III] 18.7 μm line.

Table 3.6. Total Infrared Luminosity Estimates

Name	L_{24} 10^{42} erg s^{-1}	L_{TIR} (DH) 10^{42} erg s^{-1}	L_{TIR} (W) 10^{42} erg s^{-1}	$k_{70/24}$	$\log L_{70}/L_{24}$ (rest)
2A0335	0.94	21.2	25.8	0.97	1.07
A478	2.14	108.	76.2	0.92	1.09
A1068	582.	5060.	4120	0.73	0.48
A1795	2.56	36.6	40.9	0.94	0.82
A1835	614.	4028.	4210.	0.83	0.45
A2597	5.35	143.	177.	0.92	1.13
HydraA	7.32	112.	94.3	0.94	0.74
PKS0745	38.9	437.	389.	0.84	0.64

Note. — All luminosities are in units 10^{42} erg s^{-1}. L_{24} is rest-frame νL_ν at 24 μm from the IRS spectra. L_{TIR} (DH) is the TIR derived from a relation adapted from (Dale & Helou 2002). L_{TIR} (W) is based on L_{24} and the observed ratio L_{70}/L_{24} luminosities based on MIPS photometry, from Equation 2 in Wu et al. (2010). The k-correction for the 70/24 μm luminosity ratio is based on rest- and observer-frame MIPS response functions convolved with the best-fit SED shapes. The last column is the $\log_1 0$ ratio of the k-corrected, rest-frame L_{70}/L_{24} luminosities.

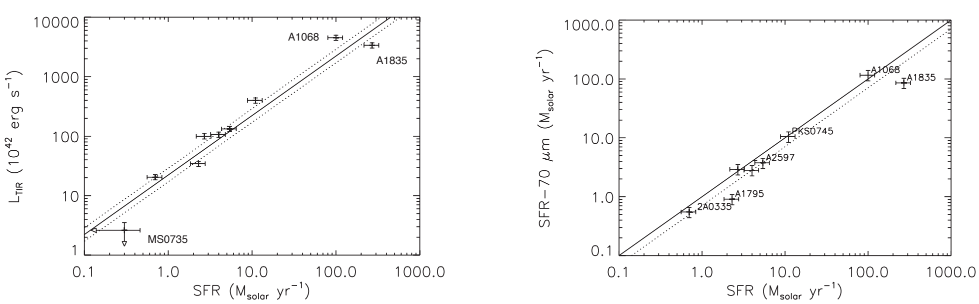

Fig. 3.6.— A comparison of infrared Brightest Cluster Galaxy (BCG) star formation rates (SFRs) from the best-fit starburst models of Groves et al. (2008) and total infrared luminosity (L_{TIR}) and the SFRs inferred from L_{TIR}. On left, we show these inferred SFRs are highly correlated with the total infrared luminosity (L_{TIR} DH; Table 3.6). For comparison, the solid line shows the Kennicutt (1998) relation for starbursts ($\mathrm{SFR}(M_\odot\ \mathrm{yr}^{-1}) = 0.045(L_{\mathrm{TIR}}/10^{42})$ erg s^{-1}), along with $\pm 30\%$ typical calibration scatter (dotted lines). On right, the same SFRs are plotted against the SFRs based on 70 μm luminosities, using the mean relation in Calzetti et al. (2010) ($\mathrm{SFR}(M_\odot) = 0.059(L_{70}/10^{42})$ ergs^{-1}). The solid line shows the line of equality; the dotted line shows how the predicted SFR from L_{70} would change, from Calzetti et al. (2010), if a different Hα-based SFR from Kennicutt (1998) is used for calibration.

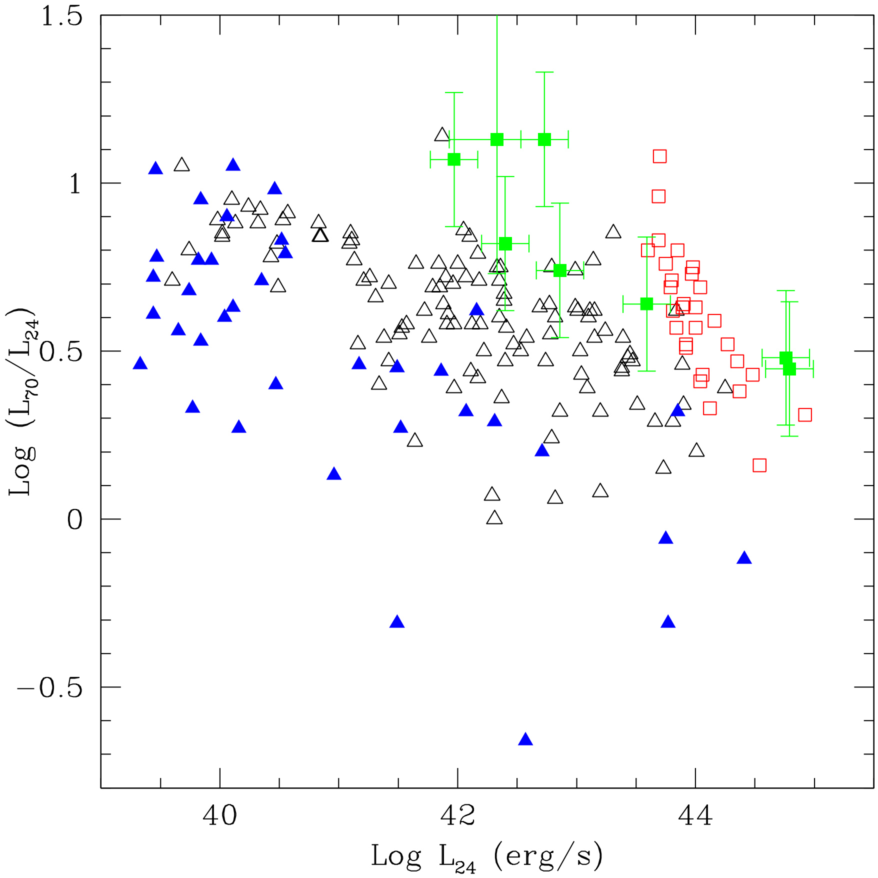

Fig. 3.7.— The L_{70}/L_{24} ratio as a function of the 24 μm luminosity L_{24}.The open black triangles are higher-metallicity star forming galaxies; the closed blue triangles are lower-metallicity star-forming galaxies; and the open red squares are luminous infrared galaxies (LIRGs), all from Calzetti et al. (2010). The green symbols with error bars are the rest-frame 24 μm luminosities and rest-frame (k-corrected) 70 to 24 μm luminosity ratios for the 8 BCGs in our sample with MIPS photometry.

Abell 1068. The IRS spectrum of Abell 1068 is similar to that of Abell 1835 in that it has a strong red continuum, but its emission features are weaker. All features are well matched except for a 24 μm feature that is likely spurious but could be associated with [Ne V]24.3 μm. (The deficiency in the model spectrum between 13-18 μm is a shortcoming of the Groves et al. (2008) models compared to many starburst spectra.)

PKS0745-19. The IRS spectrum of PKS0745-19 also has a strong red continuum but fainter PAHs than Abell 1835. The observed long wavelength slope is flatter than the model. The observed blend of [Fe II] + [O IV] at 26 μm is bright. For this source, the [Ne II]12.8 μm and [Ne III]15.6 μm features are underpredicted by our simulated SED. The H_2 S(1) transition is quite bright.

Hydra A. The fit to the IRS spectrum of Hydra A overpredicts the [S III] 33 μm line somewhat, while the [S III] 18.7 μm line is underpredicted. The ratio of this line pair is set by gas density. Shortward of 20 μm, the spectrum resembles the best fit starburst model fairly well, except for the previously noted deficiency in the model spectra between 10-19 μm. As in other systems, the [FeII] + [OIV] blend is not modeled.

Abell 2597. The IRS spectrum of Abell 2597 is fairly flat. Most features seem to be represented. There are small excesses of [Ne II] and [Ne III] emission visible in the residuals.

Abell 1795. The IRS spectrum of Abell 1795 is fairly well represented by the starburst models.

Abell 478. The IRS spectrum of Abell 478 is faint. The data exhibit stronger lines of [Ne II] and [Ne III] and a flatter long-wave spectral slope.

2A0335+096. The IRS spectrum of 2A0335+096 has a flat red continuum, and molecular hydrogen and neon lines are well fit by the model. The most prominent feature in the residual spectrum is the strong [Si II] 34.8 μm line. 2A0335 is the lowest redshift source, so we have no other sources for context, and it does sit near the edge of the spectrum where noise spikes are not uncommon. The [Ne III]/[Ne II] ratio is higher than predicted in the best fit model.

MS0735+74. The IRS spectrum of MS0735+74 has a flat red continuum with very weak emission line features, and to the limits of the data, fit but not tightly constrained in this exercise.

In summary, the starburst models of time-averaged HII regions and PDRs, based on fits to the IRS data, do a surprisingly good job at qualitatively representing the continuum, PAH, and nebular features of the IRS spectra of BCGs, but far from perfectly. On the other hand, the star formation rates derived are consistent with estimates based on the 70μm continuum or PAH features. We will discuss this further in § 3.6.3, where we show that the H_2 and [Ne II] luminosities are significantly higher than those of star-forming galaxies with similar infrared luminosities. While the PAHs and the IR continuum are usually well represented, the models do not match the nebular [Ne II] (and [Ne III]) emission relative to the continuum, and the slope of the continuum through the longest wavelengths of the IRS spectra is not consistently fit for spectra with faint IR continuua. We note that the metric for a best-fit for a given starburst model is dominated by the continuum since most of the points are continuum-dominated.

Table 3.7. Best Fit Starburst PDR + HII Model Parameters and Stellar Masses

Name	$Z/Z_\odot$	$\mathcal{C}$	Log P/k ($\mathrm{K\ cm^{-3}}$)	HII or PDR	A_V (mag)	Old Star $10^{11}\ \mathrm{M_\odot}$	SFR $\mathrm{M_\odot\ yr^{-1}}$	T1 (K)	N1 (H_2) ($10^{18}\ \mathrm{cm^{-2}}$)	T2 (K)	N2 (H_2) ($10^{18}\ \mathrm{cm^{-2}}$)
2A0335	1	4	8	PDR	0	1.5	0.7	350 (5)	52 (0.2)	1200 (30)	0.8 (0.1)
A478	2	4	8	PDR	0	4.4	2.7	460 (10)	13 (0.7)	1920 (200)	0.12 (0.02)
A1068	1	6.5	8	PDR	2.5	8.6	100	320 (4)	98 (7)	2000*	0.120 (0.007)
A1795	2	4	8	PDR	0	2.6	2.3	260 (13)	48 (0.6)	760 (40)	1.7 (0.2)
A1835	2	5.5	6	PDR	0	26	270	530 (40)	4.7 (1.5)	1300 (750)	0.03 (0.02)
A2597	2	4	8	PDR	0	4.1	5.4	240 (4)	160 (8)	810 (17)	4.9 (0.3)
HydraA	2	5	7	PDR	0	3.3	4.3	380 (25)	15 (0.3)	–	–
MS0735	2	4	6	PDR	0	9.7	0.3 (0.12)	300 (240)	4.4 (7)	730 (70)	0.5 (0.2)
PKS0745	2	6.0	8	PDR	0	5	11	390 (20)	26 (1)	1200 (65)	0.48 (0.05)

Note. — *Value pegged at extreme temperature. Uncertainties are quoted in parentheses. Component normalizations for the old stellar population SED and the starburst SED had statistical uncertainties of less than 1-3%, with the exception of MS0735. However, the photometric calibration and scaling uncertainties were $\sim 15-20\%$, so at minimum, uncertainties at that level apply to the stellar masses and SFRs estimated here.

3.6 Discussion

In typical star-forming galaxies, the luminosities of dust, PAHs, [Ne II] lines, and even the rotationally-excited molecular hydrogen lines are linearly correlated with each other and with the star formation rate (SFR). There is a significant uncertainty in the SFR inferred for any individual galaxy, a factor of 5-10, because of the dispersion, but these quantities are highly correlated in star-forming galaxies. Therefore we compare the correlations we see for the BCGs in our sample with those of star-forming galaxies. We will show here, based on the correlations and ratios that we observe for BCGs, that the infrared continuum and PAH features are consistent with being powered primarily by star formation in BCGs. In contrast, the emission lines from rotational transitions of hydrogen are uncorrelated with the dust and PAH features, and are primarily powered by a second process. The forbidden lines of neon are correlated with the IR emission, but not linearly. This pattern is consistent with these lines being powered by star formation and a second process that does not provide much heat to the PAHs and dust but is very effective at producing H_2 emission. This second heating mechanism is consistent with heating by a population of suprathermal electrons, either from the hot gas or perhaps associated with the radio source.

All linear correlation coefficients (r) in the analysis below are based on the measurements in *logarithmic* quantities unless stated otherwise. For reference, a correlation of $r > 0.66 (r > 0.86)$ might be considered significant at the 2σ (3σ) level for $N = 9$ points (e.g. Bevington 1969; Bevington & Robinson 2003). In general, if two quantities are correlated linearly (i.e., the log-log slope is unity), they may have common origins. But if they are correlated, but not linearly, there may be something more interesting going on. For that reason, we plot dotted lines with unity slope in our correlation graphs.

3.6.1 Dust and PAH Luminosity Correlations

The smallest dust grains are the polycyclic aromatic hydrocarbons (PAHs), composed of only a hundred atoms or so. These structures generate emission from C-H or C-C-C bending modes (Leger & Puget 1984; Boulanger et al. 1998; Van Kerckhoven et al. 2000), excited by the absorption of UV photons (Allamandola et al. 1985; Sloan et al. 1999). Such photons can heat these tiny grains stochastically, causing them to suddenly increase in temperature then cool (e.g., Li & Draine 2001). PAH features at 3.3, 6.2, 7.7, 8.6, and 11.3 μm in spectra are thought to be an excellent tracer of B stars, or of relatively recent star formation (Peeters et al. 2004; Brandl et al. 2006; Förster Schreiber et al. 2004). The continuum IR luminosity, which traces star formation, and PAH luminosity is strongly correlated in normal star-forming galaxies (Wu et al. 2010). Studies of low metallicity star-forming dwarf galaxies by Rosenberg et al. (2008) and of star forming regions in irregular galaxies by Hunter & Kaufman (2007) show the PAH emission decreases as metallicity decreases, so metallicity is one factor that can lead to scatter in the correlation between PAH emission and IR luminosity from dust.

The brightest features from the polyaromatic hydrocarbons (PAHs) are the complexes at 11.3 μm and 7.7 μm. The sum of those lines in our BCG sample is strongly correlated with the 24 μm continuum in both flux and luminosity (Figure 3.8). The correlation coefficient $r = 0.93$ for both. Excluding MS0735 does not affect the correlation. The relationship is very close to linear: $L_{11.3+7.7} \propto L_{24}^{0.90\pm0.03}$, where $L_{24} = \nu L_\nu$ at 24 μm rest frame. ($L_{11.3} \propto L_{TIR}^{0.96\pm0.05}$.)

The ratio of the 11.3 μm luminosity to L_{TIR} is $\sim 0.0039\pm0.0020$ (omitting MS0735 from the sample for lack of MIPS data), plotted in Figure 3.8b, to compare to the mean of $\sim 0.0066^{+0.0045}_{-0.0042} L_{11.3\mu\mathrm{m}}^{0.02\pm0.03}$ from 123 starburst dominated galaxies from a 24-μm flux-limited sample of 330 galaxies in Wu et al. (2010). The best-fit power law relating $L_{11.3\mu\mathrm{m}}$ and L_{TIR}^{α} is $\alpha = 1.05 \pm 0.05$, also similar to that seen for starburst galaxies (Wu et al. 2010). Given the uncertainties in converting from L_{70} and L_{24} to L_{TIR}, this comparison shows that these galaxies have PAH/IR luminosity ratios that are only somewhat lower than normal star-forming galaxies, with the exception of A1068 and possibly A2597. The PAHs in Abell 1835 are about 4 times brighter compared to L_{24} than the nearly equally IR luminous Abell 1068, so we detect significant intrinsic scatter in this ratio. There is no correlation in the ratio of PAH/IR luminosities to IR luminosity (see Figure 3.8b).

The 11.3 μm PAH luminosity is highly correlated with the 24 μm and the TIR luminosity, which makes sense if the dust and PAHs are heated by the same process. The 15 and 24 μm continuum luminosities are strongly correlated with each other ($r = 0.96$) and nearly linearly correlated ($L_{24} \propto L_{15}^{1.042\pm0.006}$), as expected since both quantities are usually produced by dust grains.

In contrast, 24 μm continuum and 11.3 μm PAH luminosities are not correlated with 6 μm continuum luminosity. In fact, when MS0735 is excluded, there is no correlation between 24 μm and 6 μm luminosities, $r = 0.17$. Similarly excluding MS0735, there is no correlation between the 6 μm and PAH flux at 11.3 μm ($r = 0.23$) or [Ne II] ($r = 0.004$). (Including MS0735 in the tests increases the correlations to ~ 0.6, under the 2σ threshold, but because the computed significance relies on the inclusion of a single source, it must be considered spurious.) The 6 μm light in these BCGs is produced primarily by old (cool) stars, and therefore is a metric for the stellar mass. The lack of correlation between dust and stellar continua luminosities suggests that dust, PAH, and gas heating is not determined by cool stars. The systems where the dust luminosity well exceeds the 6 μm luminosity from stars, A1068 and

A1835, exhibit higher PAH 7.7 to 11.3 μm ratios, consistent with the hypothesis that these are like starburst galaxies with levels of PAH ionization similar to those seen in starbursts (Figure 3.9). We will consider these ratios more fully in § 3.6.4.

For the rest of this discussion, we will assume that the long wavelength IR continuum is powered primarily by obscured recent star formation. However, even though dust heating by evolved stars does not seem to dominate these systems at 24-70 μm, evolved stars may be the dominant source of heat for cooler dust emitting at longer wavelengths, and this dust therefore could *contribute* to emission at shorter wavelengths (see § 3.5). Furthermore, processes of interest such as suprathermal electron heating and weak AGN may also supply energy to these systems. Since the observed global quantities are galaxy-wide averages, they suffer from the same interpretation ambiguitiy as high redshift, unresolved sources. Even if we could interpret these spectra in the context of star formation alone, it is impossible to unambiguously distinguish between a star formation episode of a single age and stellar mass and a time-averaged star formation history of "constant" star formation. Physically, signatures of star formation in normal galaxies include cold, dusty molecular gas, excess UV continuum, Hα, PAH emission, and infrared dust emission. We will discuss these data in a framework where obscured star formation is tracked by the infrared and PAH emission. However, we will show that star formation alone is inadequate to explain the full set of infrared spectral features in these systems.

3.6.2 Forbidden Neon Line Correlations

The luminosities of forbidden lines of neon, which are channels for radiative cooling, are sensitive to the thermal energy input into the ionized gas. They therefore have also been shown to be good tracers of star formation rates in normal star-forming galaxies. Ho & Keto (2007) showed that the sum of the fine structure lines of Ne II (12.8 μm) and Ne III (15.6 μm) correlates strongly with IR luminosity in normal star-forming galaxies over 5 orders of magnitude in luminosity. The sums of [Ne II] and [Ne III] luminosities in our BCG sample also correlate strongly with L_{24} ($r = 0.95$, fluxes correlate with $r = 0.90$). [Ne II] alone is just as correlated ($r = 0.94$, fluxes correlate with $r = 0.91$). The relationship, however, deviates even more from linearity than the PAH-IR luminosity relationship, with $L([Ne\ II])$ scaling as $L_{24}^{0.58\pm0.03}$ (or $L_{TIR}^{0.79\pm0.04}$). We suspect that while the dust and the PAHs are heated primarily by star formation, this lack of linearity in the [Ne II]-IR correlation suggests that star formation may not be the sole process producing [Ne II] emission.

The ratio of [Ne II] to total infrared luminosity (L_{TIR} (W); Table 3.6) decreases somewhat with increasing IR luminosity (Figure 3.10). The Ho & Keto (2007) mean relationship between [Ne II] and L_{TIR} for star-forming galaxies is $\log(\mathrm{[Ne\ II]}/\mathrm{L_{TIR}}) = -3.44 \pm 0.56$, nearly independent of L_{TIR}. Excluding MS0735, the [Ne II] luminosity in BCGs is about $1.6 - 12$ times higher than the mean [Ne II] luminosities of normal star-forming galaxies of similar infrared luminosities. The largest differences are found for the BCGs with lower IR luminosities ($< 11^{10}$ $\mathrm{L_{\odot}}$). MS0735+74, for which there is only an upper limit continuum estimate, is particularly bright in [Ne II] compared to its infrared luminosity ($\gtrsim 0.009$), $> 25\times$ the mean. The observed scatter of this ratio for normal star-forming galaxies in Ho & Keto (2007) is large, ± 0.5 dex; nevertheless, the BCG ratios sit consistently on the high side of the scatter for normal star-forming galaxies, indicating that another process beyond star formation is also contributing to the heating of the ionized gas, particularly in the low-luminosity systems. In summary, the [Ne II] luminosities seen in the low IR-luminosity BCGs exceed what would be expected from a star-forming galaxy with the same IR luminosity, but the two quantities are strongly correlated.

The [Ne III]/[Ne II] ratio is not at all correlated with the mid-IR luminosity (Figure 3.11). It is possible that the [Ne III]/[Ne II] ratio indicates an approximate starburst age, with BCGs having the highest [Ne III]/[Ne II] also having the youngest starburst populations, but not necessarily the largest numbers of young stars (Thornley et al. 2000; Rigby & Rieke 2004; Snijders et al. 2007).

3.6.3 Molecular Hydrogen Correlations

Extremely luminous pure rotational H_2 lines, usually S(3) 9.67 μm, S(2) 12.28 μm, S(1) 17.04 μm, are detected in all nine galaxies. S(0) 28.22 μm was not detected in any of these sources. Rotational transitions from S(5) - S(7) (5.51 μm) are seen in a majority of these spectra. While the luminosities of rotationally-excited molecular hydrogen lines are correlated with IR luminosities of star-forming galaxies (Treyer et al. 2010), that is certainly not the case with our BCG sample. The line luminosities from rotational molecular hydrogen transitions from these BCGs are much greater than expected from the level of star formation heating the warm dust. H_2 emission is also uncorrelated with the continuum at 15 or 24 μm, $r = 0.4 - 0.5$.

Rotational emission from molecular hydrogen is commonly detected in ULIRGs (Higdon et al. 2006) and in star-forming normal galaxies (Roussel et al. 2007). In such galaxies, the luminosities of these lines are only about 4×10^{-4} of the total infrared power between 8-1000 μm. However, the ratio of H_2 luminosity to L_{24} for the BCGs in this sample, ranging from 0.004-0.3, is about 5-100 times more than one would expect from a photodissociation region. The most extreme object is MS0735, owing to its faint (and uncertain) IR continuum. The large H_2 luminosity from off-nuclear regions in the BCG NGC1275 (Johnstone et al. 2007) led Ferland et al. (2008, 2009) to propose that much of the H_2 luminosity in BCGs located in X-ray cool-core clusters can be generated by cosmic ray heating, or by non-radiative processes such as plasma waves.

Brightest cluster galaxies are not the only galaxies to exhibit unusually large luminosities of rotational molecular hydrogen. Ogle et al. (2007) find the FR II radio galaxies have strong H_2 lines, but these galaxies are dissimilar to the BCGs in our sample. For example, 3C 326 exhibits high ionization [Ne V] and [O IV] emission, indicating AGN or LINER-like lines, very tiny star formation rates ($< 0.1 M_\odot$ yr^{-1}), and the H_2 line transitions are primarily S(0) and S(1), indicative of cooler molecular gas than in our sample. These transitions are also seen in IRS mapping of the nearby group of galaxies, Stephan's Quintet, which exhibits bright H_2 (Cluver et al. 2010). Similarly, H_2 S(0) and S(1) emission lines have been reported from IRS mapping of edge-on spiral galaxies (Laine et al. 2010). An archival study of ULIRGs by Zakamska (2010) suggests that their H_2 emission is not associated with star formation. While many of these studies speculate that shocks might be a source of energy (e.g. Ogle et al. 2010), and might be quite common, the unifying thread to all of their discussions is that the molecular hydrogen rotational lines are surprisingly bright and their source of energy is still unidentified. The situation is not much different here, except the BCGs tend to also exhibit rotational lines characteristic of warmer molecular gas than the groups or radio galaxies (S(2), S(3), to S(7)).

The mid-IR luminosity is not significantly correlated with the summed luminosity of the molecular hydrogen lines, here represented by the sum of S(2) and S(3) lines, which were reliably detected in all 9 systems (Figure 3.12a). While we showed in § 3.6.2 that [Ne II] emission is correlated with dust continuum emission, here we see that dust continuum is not significantly correlated with molecular hydrogen emission (for fluxes, $r = 0.5$; for luminosities $r = 0.68$). We plot the ratio of H_2 sum to mid-IR luminosity (Figure 3.12b). These ratios decrease for the systems with the highest mid-IR luminosities. This trend appears because the H_2 luminosities are limited in range (factor of 20) while the IR luminosity spans a large range (> 1000). We interpret the trend to mean that the H_2 heat source is more important and in fact dominates the IR emission features in systems with low mid-IR luminosities.

The rather insignificant correlation between H_2 and L_{24} utterly vanishes once MS0735 is omitted from the sample. A similar effect happens when [Ne II] flux is compared with H_2 flux: dropping MS0735 from the sample causes a very weak (less than 2σ) correlation to completely vanish. On the other hand, the luminosity of [Ne II] is correlated with the luminosity of the H_2 S(2) + S(3) lines ($r = 0.92$). The presence or absence of MS0735 has little effect on the inferred strong correlations between Ne II, PAHs, and mid-IR continuum flux and luminosity correlations. This correlation analysis suggests that while there is some relationship between the heat sources for the ionized gas and the dust, there appears to be a much weaker relationship between the heating sources for the molecular hydrogen and the dust. The ratio of molecular hydrogen to IR luminosity (Figure 3.12b) decreases with increasing IR luminosity, however, and suggests that the H_2 heating process becomes less important to the total luminosity budget as star formation increases.

The strong luminosity correlation between [Ne II] and H_2 required further investigation, since the lack of correlations in the flux quantities suggested the luminosity correlation may be a simple "bigger is bigger" luminosity-luminosity comparison. (See Kennicutt (1990) for an infamous description of this type of error, involving a cigar.) Intriguingly, we find that the ratio of [Ne II] to L_{24} correlates even more strongly with the ratio of H_2 S(2)+S(3) summed luminosity to L_{24} ($r = 0.98$). The best power-law fit to this relationship is H_2/IR $\sim$ ([Ne II]/IR)$^{1.49\pm0.12}$ (Figure 3.13). The correlation of these ratios suggests that whatever process heats the molecular hydrogen is likely to be the culprit that boosts the forbidden line luminosity (heating the ionized gas) as well.

To explore this idea further, we investigated how much more luminous the neon and molecular hydrogen lines are than one would expect from a star forming galaxy, if the dust luminosity were a reliable indicator of the level of star formation. In Figure 3.14, we estimated the star formation rates inferred from the IR continuum (the best fits to the Groves et al. 2008 models, which are consistent with Kennicutt (1998) estimates), from the [Ne II]+[Ne III] luminosity (Ho & Keto 2007), and from the H_2 luminosity (Treyer et al. 2010). For the latter estimate, we assumed that the $Ne^+/Ne = 0.75$ and $Ne^{++}/Ne = 0.15$. The H_2-based star formation rate in Treyer et al. (2010) relies on the sum of the S(0), S(1), and S(2) transitions, which were not all detected in our systems. The sums plotted are based only on luminosities of the detected lines. These plots show that for most of the BCGs, while [Ne II] is moderately over-luminous for the inferred IR-based star formation rate (a factor of 2-5 above the upper end of the scatter exhibited by the galaxy sample of Ho & Keto 2007, and a factor of ~ 10 over the mean), the H_2 luminosity is a factor of 5-15 over-luminous based on the IR-based star formation rates. The BCGs in A1068, A1835, and Hydra A have ratios typical of starbursts.

It is interesting that the best fit for the points in Figure 3.13 is nearly linear. The slightly steeper than linear fit might be explained in the context of heating by suprathermal particles if the luminosity of the ionized gas ([Ne II]) is limited by the finite column density of ionized gas, while the luminosity of the rotational line emission from the molecular gas is limited by the penetration depth of the suprathermal particles into the molecular gas, not the total column density of molecular hydrogen.

We defer a full discussion of the excitation analysis of the individual molecular hydrogen lines to a future paper. The more approximate dual temperature fit that we have done here, however, shows very similar trends to those seen in NGC1275 filaments: the H_2 rotational line intensities cannot be fit by a single temperature. This trend is consistent with any model with a non-radiative energy source (Ferland et al. 2008).

In summary, as we examined correlations of continuum, PAH, and emission lines of [Ne II] and H_2, and compared them to correlations and infrared line ratios in other types of galaxies, it emerged that a single heating process cannot explain the range of infrared properties we see in these BCGs. Star formation seems to play a role, albeit with varying levels of dominance, in producing the emission from these systems, but other processes unrelated to star formation must also contribute, particularly in systems with apparently low rates of star formation but high fluxes from rotationally-excited transitions of molecular hydrogen.

3.6.4 PAHs and Dust Grain Survival and Processing

If the dust in these BCGs spent much time in contact with the hot, X-ray emitting gas (or more generally, suprathermal electrons), one might expect the dust properties, such as its size distribution or ionization fraction, to be different from dust that has not undergone such a traumatic experience. PAH survival alone is problematic if suprathermal particles alone provide heat: radiation and collisions make PAH lifetimes in the harsh environment of the center of a cool-core cluster of galaxies quite short. Using order of magnitude cross sections from Voit (1992a), and 0.5 keV photon fluxes of about 10^6 cm^{-2} s^{-1} we estimate lifetimes of order one million years. The damage from particle collisions may be even more dire. From the analysis of Micelotta et al. (2010), the lifetime of PAH molecules embedded in $\sim$ 1 keV gas with a density of $\sim$ 0.1 cm^{-3} is limited to hundreds of years by collisions with the hot electrons and ions. Any processing along these lines causes the PAHs and small grains to evaporate preferentially compared to large grains. The presence of PAHs requires the dusty gas to be shielded from the hot gas and its radiation.

As in other galaxies observed with the *Spitzer* IRS (Smith et al. 2007b; Kaneda et al. 2008), the fluxes and luminosities of the PAH complex at 7.7 μm and at 11.3 μm are strongly and linearly correlated. The 7.7 and 11.3 μm PAH complex luminosities are strongly correlated ($r = 0.98$, fluxes at $r = 0.94$) for all 7 systems in which both are detected. 2A0335 and MS0735 lack PAH 7.7 μm detections.

The ratio of 7.7 to 11.3 μm PAH complexes is relatively insensitive to the sizes of the PAHs (Schutte et al. 1993), but sensitive to the ratio of ionized to neutral PAHs (Allamandola et al. 1989; Draine & Li 2007). For example, the ratio of the PAH complex at 7.7 to the PAH complex at 11.3 μm is lower in galaxy centers that are AGN-dominated compared with those which are HII-dominated (Smith et al. 2007b). The mean range for seven ratios of the PAH complexes at 7.7 and 11.3 μm in our sample is 2.7 ± 0.2 (Figure 3.15). The mean sample ratio is intermediate between that of HII/starburst galaxies (4.2, Smith et al. (2007b)) and diffuse Galactic emission (2-3.3, Sakon et al. (2004)). The BCGs with classic indicators of starburst activity (Abell 1068 and Abell 1835) have ratios typical of starbursts; the others are closer to that of Galactic ISM. In elliptical galaxies, the PAH 7.7/11.3 ratio is unusually weak ($\sim 1 - 2$) (Kaneda et al. 2008); the lowest ratios seen in dusty ellipticals are lower than the ratios detected in our BCG sample. For BCGs with a low PAH 7.7 μm to 11.3 μm ratio, the incident spectrum on the PAHs may be dominated by evolved stars, compared to a harder, ionizing spectrum with contributions from young massive stars. Our result suggests that the radiation fields in BCGs are intermediate in their hardness between those of dusty elliptical galaxies and star-forming galaxies, which is consistent with what one might expect in the ISM of galaxies with enormous old stellar populations, together with small numbers of recently formed stars.

The ratio of PAH complexes at 17 and 11.3 μm is thought to be regulated by PAH sizes with large PAHs contributing more to the longer wavelength complex (e.g., Draine & Li 2007). The broad PAH feature at 17 μm was detected with confidence in 4 BCGs (2A0335, A1068, Hydra A, and PKS0745), while the others have 3σ upper limits (Figure 3.16). With the single exception of Abell 1068, the detections and upper limits are consistent with the ratio of PAH 17 μm to PAH 11.3 μm fluxes typical of normal star-forming galaxies (~ 0.5) (Smith et al. 2007b). The consistency of the observed ratios and limits in nearly all of these BCGs compared with those with normal galaxies suggests that the PAH size distribution may be normal. The exception of Abell 1068, with a ratio > 2, indicates it may have deficit of small PAHs compared to large PAHs. This BCG also has a smaller PAH to L_{TIR} ratio. In the BCG of Abell 1068, PAHs, and particularly the small PAHs, may have been preferentially destroyed by collisions with particles or photons.

Since both [Ne III]/[Ne II] and the ratio of PAH 7.7 μm to 11.3 μm flux are related to the hardness of radiation, we compared these quantities to see whether they are correlated (Figure 3.17) and whether the BCG points cover similar parameter space as other galaxies. We see no correlation between the PAH ratios and the neon forbidden line ratios, but that is not surprising since the gas producing the forbidden lines is different from the gas hosting the PAHs; similarly, the photons ionizing neon are not the same photons setting the ionization level of PAHs. As shown in Figure 3.17, the seven BCGs with detections in all 4 quantities exhibit ratios rather similar to SINGS galaxies (Smith et al. 2007b). There are spiral galaxies in the SINGS sample in Figure 3.17 with very high [Ne III]/[Ne II] ratios (> 10); the explanation may be that these galaxies (about 15% of the SINGS sample) are dominated by very recent star formation, and therefore hotter O stars (Thornley et al. 2000; Rigby & Rieke 2004; Snijders et al. 2007), compared to the BCGs. LINERs in the Smith et al. (2007b) sample do not exhibit [Ne III]/[Ne II] $< 0.7 - 0.8$ together with low PAH 7.7/11.3 μm fractions (< 2), so a few of the BCGs in our sample with low [Ne III]/[Ne II] ratios (A1795, A478, and PKS0745) also have lower PAH 7.7/11.3 μm ratios than seen in the SINGS sample, more similar to those of dusty ellipticals (Kaneda et al. 2008) or diffuse Galactic ISM (Sakon et al. 2004). The two systems with the highest IR and PAH luminosities of the sample (Abell 1068 and Abell 1835) also exhibit the largest PAH 7.7/11.3 μm ratios, indicating the PAHs in the most luminous BCG systems are more ionized than those in the other BCGs.

We arrive at the following conclusions about the PAHs and dust in these systems.

- The presence of PAHs, and the similarity of the PAH emission ratios to those in star-forming galaxies, mean that these tiny grains must be protected from the ICM and shocks. PAHs are easily destroyed by ionizing UV and X-rays, by collisions with hot thermal particles, and by shocks.

- The emissivities of the PAHs and the ionized gas are correlated with the mid-IR continuum emitted by dust grains. Therefore there is a common source of heat for these components, consistent with being star formation. However, the excess luminosity of [Ne II] and H_2 in the less luminous systems suggests that another component is contributing to the heating of the ionized gas in addition to star formation.

- The emissivity of the PAHs is not correlated with the stellar (6 μm) IR continuum. Correlation is expected if the stars were the main agent heating the dust.

We speculate that the evolved stars in the BCGs are the main production source of dust. The dust, except in a couple of cases, shows little indication that it may have been processed by hot, X-ray emitting plasma or AGN. The source of the cool BCG gas may be the hot intracluster medium, but it seems unlikely that the dust came with the gas. Dust, however, is an extremely effective coolant, and if mixed with the hot gas, could precipitate the cooling necessary to fuel the formation of dusty molecular star-forming clouds.

3.6.5 AGN Contributions

Synchrotron radiation from a jet could contribute some of the infrared continuum. Cleary et al. (2007) find in their survey of an unbiased set of 3CR and quasars that only the quasars have a nonthermal contribution at 15 μm of $> 20\%$. About half of the 15-μm emission from nucleus of M87 is synchrotron emission, based on analysis of its IRS spectrum (Buson et al. 2009). Of the 9 sources in our sample, only Hydra A has a radio synchrotron source that is luminous enough to contribute more than $\sim 10\%$ to the IRS continuum at 24 μm, if its power law extends unbroken into the infrared.

High ionization lines in the infrared could indicate a buried AGN or the presence of very hot stars. [Ne V] 14.3 μm and 24.3 μm, with an ionization potential of 97.1 eV, would be an unambiguous AGN indicator (Voit 1992b). We did not detect this emission line in any of our sources at a level $\gtrsim 10^{-17}$ W m^{-2}), although a a weak [Ne V]14.3 μm feature is detected in Abell 1835 and Hydra A, and a suspicious (possibly spurious) feature appears near 24 μm in the spectrum of Abell 1068, which is known to have some AGN contribution in the infrared (Quillen et al. 2008). The lack of [Ne V] does not rule out some AGN contribution, since this line can be faint compared to [Ne II]. [O IV] at 25.9 μm would also be an unambiguous sign of AGN photoionization, since O III has an ionization potential just above that of He I (to He II), 54.4 eV, and is therefore rare in regions ionized by stars. However, [O IV] 25.9 μm is blended with [Fe II] at 26 μm. We detected this blend unambiguously only in PKS0745-19 and Hydra A. Puzzlingly (if this blend is an indication of the presence of O IV), the [Ne III]/[Ne II] ratio in PKS0745-19 is one of the lowest in the sample. The [O IV]-[Fe II] blend does not appear at all in the spectrum of Abell 1068, however, nor does [Ne V] 14.3 μm. The lack of these features casts further doubt on the candidate [Ne V] feature in that spectrum.

The presence of high ionization lines such as [S IV] (10.51 μm) and [Ne III] indicate the presence of young hot stars in these galaxies. The ionization parameters consistent with the [NeIII]/[NeII] ratios in the ionized gas are similar to those seen in star-forming galaxies. The energy required to ionize neon once to Ne II is 21.6 eV, compared to 41 eV for reaching Ne III. [Ne II] was easily detected in every galaxy in our sample, and only MS0735+74 lacked detectable [Ne III]. Although S III to S IV has an ionization potential (34.8 eV) similar to Ne II to Ne III, it has a very low photoionization cross-section. So a significant detection of [S IV] not only indicates hot stars, but a high density of them. In contrast to [Ne III], [S IV] was not detected in any of the systems. PAHFIT results for 2A0335+096, Abell 1835, Abell 1068, and Hydra A indicate faint formal detections at $\sim 3 - 7\sigma$, but inspection of the fits and data causes us to regard these detections as extremely marginal.

Based on the lack of [Ne V] emission lines from the gas, we have no conclusive evidence in favor of the gas being photoionized by an AGN, consistent with conclusions based on spatially-resolved optical emission-line studies of these and similar galaxies (e.g., Heckman et al. 1989).

The detection of spatially extended UV continuum in a number of cases is unambiguous evidence of the importance of recent star formation over AGN contributions in this sample of BCGs (McNamara & O'Connell 1993; Martel et al. 2002; O'Dea et al. 2004; Hicks & Mushotzky 2005; Hicks et al. 2010; Donahue et al. 2010). Since lack of evidence is not the same as evidence of lack, we keep in mind that some of the spectra may have contributions from a low-luminosity AGN since none of these spectra exclude the nucleus. However, Occam's Razor prefers the simplest explanation for heating these systems, and as such, no need for AGN excitation or heating is required by these observations.

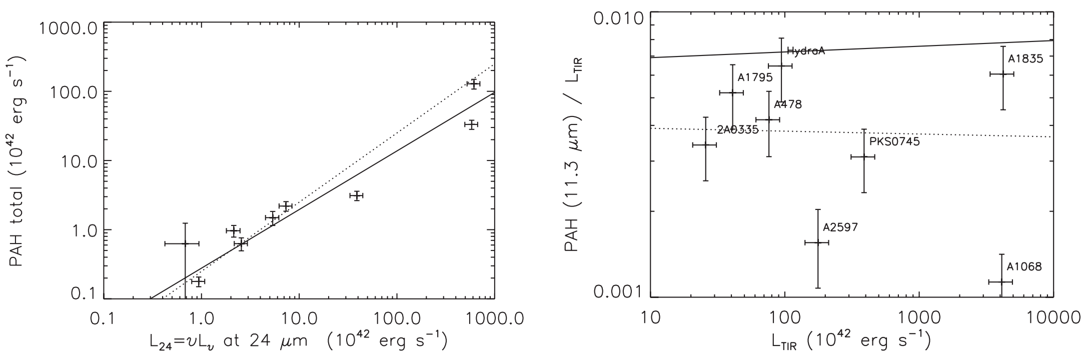

Fig. 3.8.— PAH and infrared continuum properties compared. The 24 μm continuum luminosity (L_{24}) is strongly correlated with the sum of the luminosities of the PAH complexes at 11.3 μm and 7.7 μm. The slope of the best-fit power law (plotted as a solid line) is 0.90 ± 0.03. For comparison, a dotted line of slope unity is shown. On the right, we show that the ratio of PAH (11.3 μm) to L_{TIR} (W; Table 3.6) is $\sim 0.0039 \pm 0.0020$. The solid line is the mean $\sim 0.0066^{+0.0045}_{-0.0042}$ from Wu et al. (2010); the dashed line is the lower limit of the range of their best-fit to the mean for starburst galaxies. Given the uncertainties in converting from L_{70} and L_{24} to L_{TIR}, this plot shows that these galaxies have PAH/IR luminosity ratios that are only somewhat lower than normal star-forming galaxies, with the exception of A1068 and A2597.

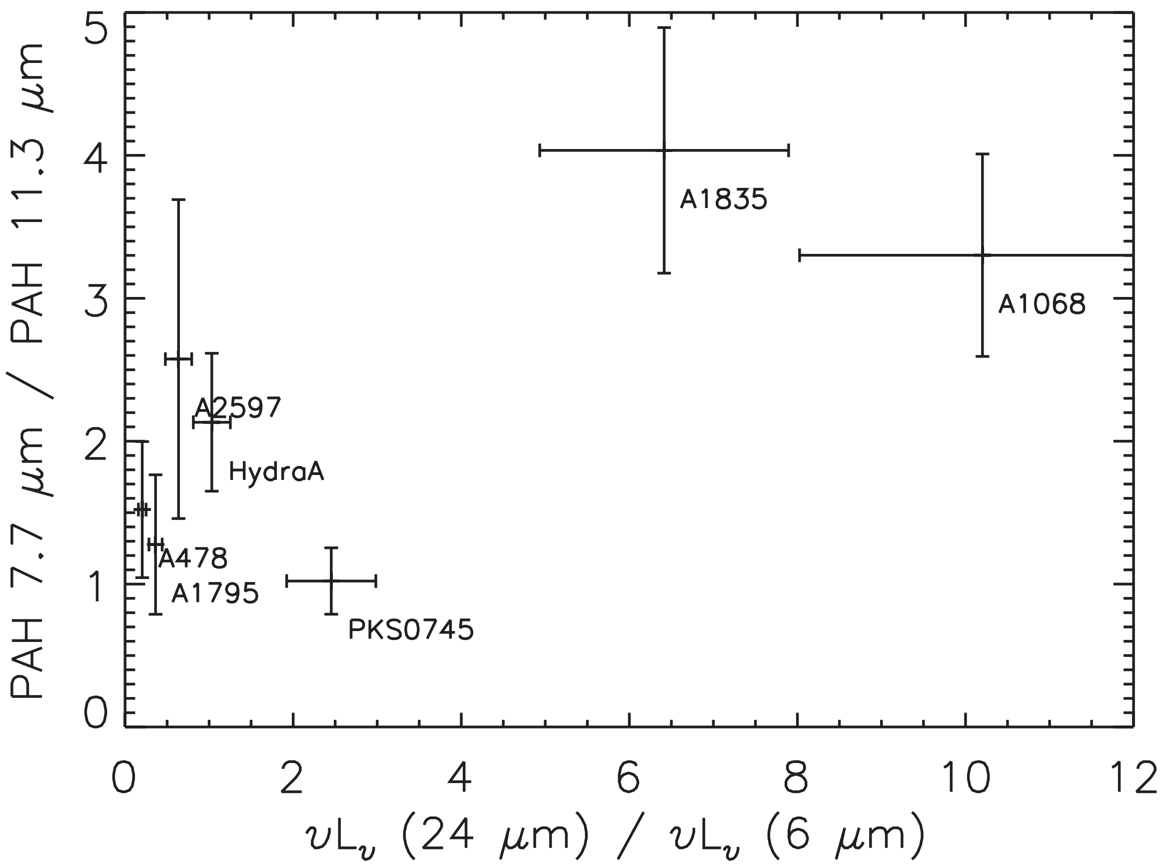

Fig. 3.9.— A plot of the PAH 7.7 to 11.3 μm ratio vs. the ratio of the 24/6 μm continuum luminosities, The PAH ratio indicates the ionization level of PAHs, and this ratio is higher in systems in which the 24 μm luminosity from dust exceeds the 6 μm stellar continuum. This trend is consistent with the PAHs in the BCG systems most like starbursts experiencing a harder incident radiation spectrum.

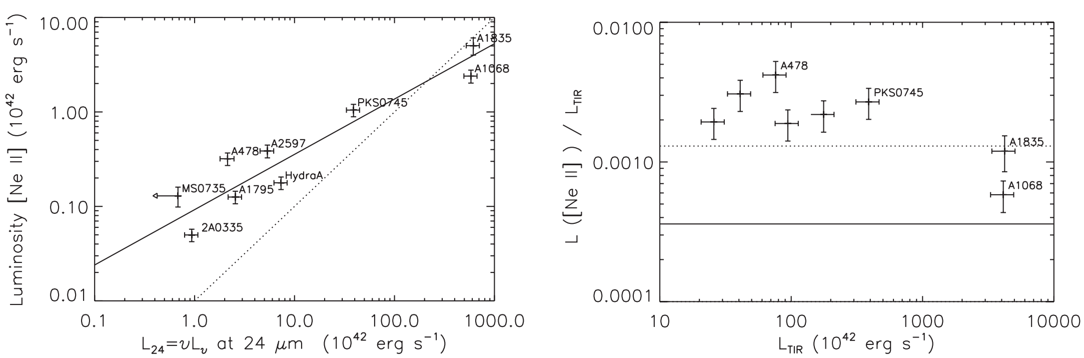

Fig. 3.10.— [Ne II] and infrared continuum properties compared. On the left, [Ne II] luminosity is strongly correlated with L_{24} luminosity, but the best-fit power-law (solid) is flatter than linear, with a index of 0.59 ± 0.03. A dotted line with slope unity is plotted for comparison. On the right, the ratio of [Ne II] luminosity to L_{TIR} (L_{TIR} (W); Table 3.6) continuum luminosity decreases with increasing L_{TIR}. The ratio for typical star-forming galaxies, $\log([\mathrm{Ne\ II}]/\mathrm{L_{TIR}}) = -3.44 \pm 0.56$, from Ho & Keto (2007) is plotted. The dotted line is the approximate upper bound of the intrinsic scatter.

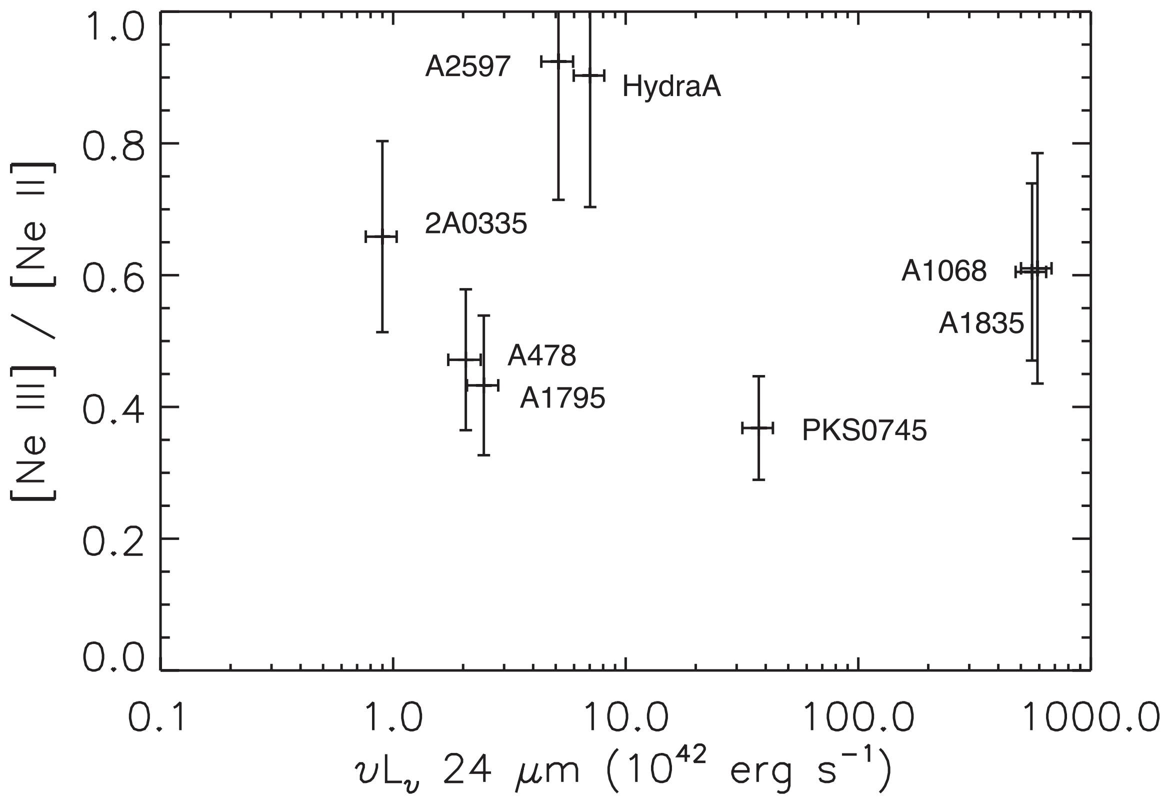

Fig. 3.11.— [Ne III] / [Ne II] ratios, indicators of the hardness of the incident UV spectrum for the ionized gas, are plotted against the 24 μm luminosity, a surrogate for star formation rate. The ionization level of the gas shows no correlation with the mid-IR continuum. The neon line ratios exhibit intrinsic scatter, possibly evidence that either the ages of the youngest stars vary from system to system (which would mean a constant star formation rate is not a good assumption), or the mix of heating mechanisms (between star formation and energetic particles) differs from galaxy to galaxy.

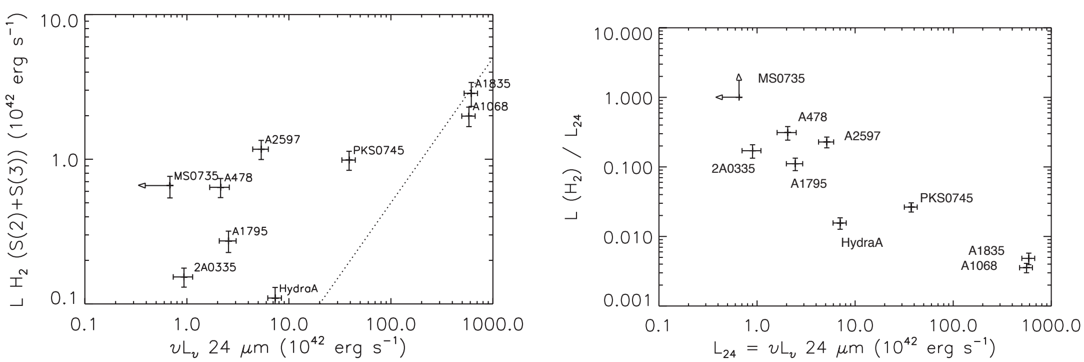

Fig. 3.12.— Rotational H_2 and infrared continuum properties compared. On left, the summed luminosity of the two most prominent rotational hydrogen lines (S(2), S(3)) is very weakly correlated ($< 2\sigma$ significance) with the L_{24} as might be expected if the sample is (approximately) flux-limited; if plotted as a flux-flux diagram all correlation disappears. A dotted line of slope unity is shown. On right, the ratio of molecular hydrogen to L_{24} decreases with increasing L_{24}, which suggests that the source of energy powering H_2 is unrelated to star formation in most of this sample. At the highest IR luminosities (A1068 and A1835), the H_2 might be generated by star formation processes.

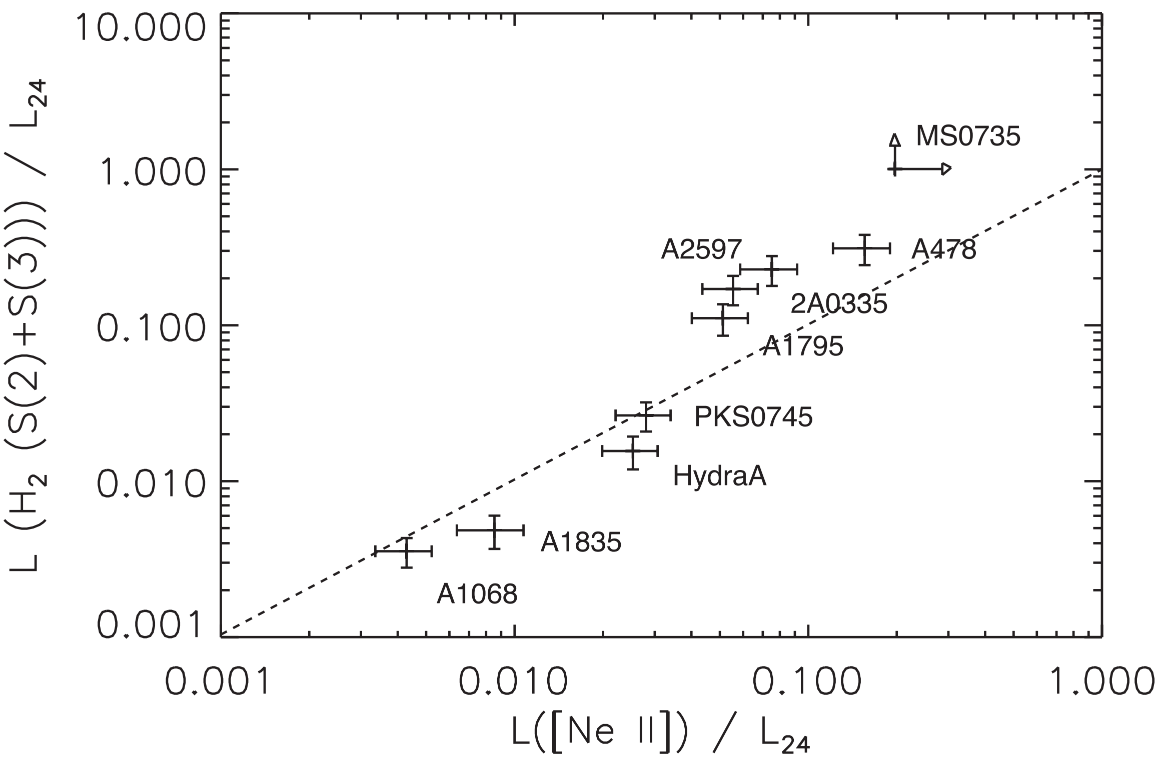

Fig. 3.13.— [NeII]/IR ratio correlates with H_2/IR, which might be expected if the heating source that powers the molecular hydrogen well over that expected from star formation also elevates the [Ne II] emissivity of the ionized gas over that expected from star formation. This additional heating source might simultaneously explain the H_2 luminosity and the excess [Ne II] luminosity. The dashed line indicates a slope of unity.

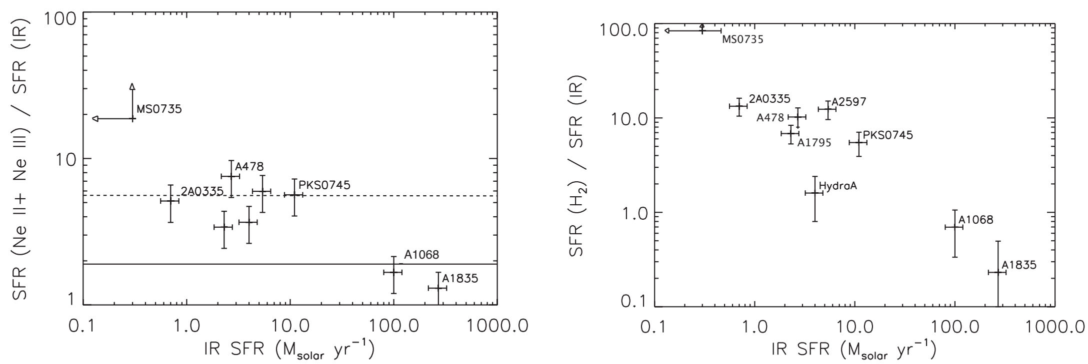

Fig. 3.14.— Ratios of inferred star formation rates demonstrate that both the forbidden neon lines and the molecular rotational lines are being emitted in excess of what would be expected of a star-forming galaxy where the star formation rate is tracked by the IR luminosity. The left plot shows the ratio of the star formation rates from the sum of [Ne II]+[Ne III] (Ho & Keto 2007) compared to our estimated IR star formation rates, based on fits to the infrared continuum. The lower line shows the average of the Ho & Keto rate compared to the IR rate based on Kennicutt (1998) quantities for their sample. The higher line shows the upper limit of their scatter. Therefore [Ne II] in BCGs is moderately over-luminous, by a factor of ~ 3 over the mean for star-forming galaxies. The rotational transitions in H_2 are overluminous by a factor of 5-15. In both these relations, MS0735 is an extreme example.

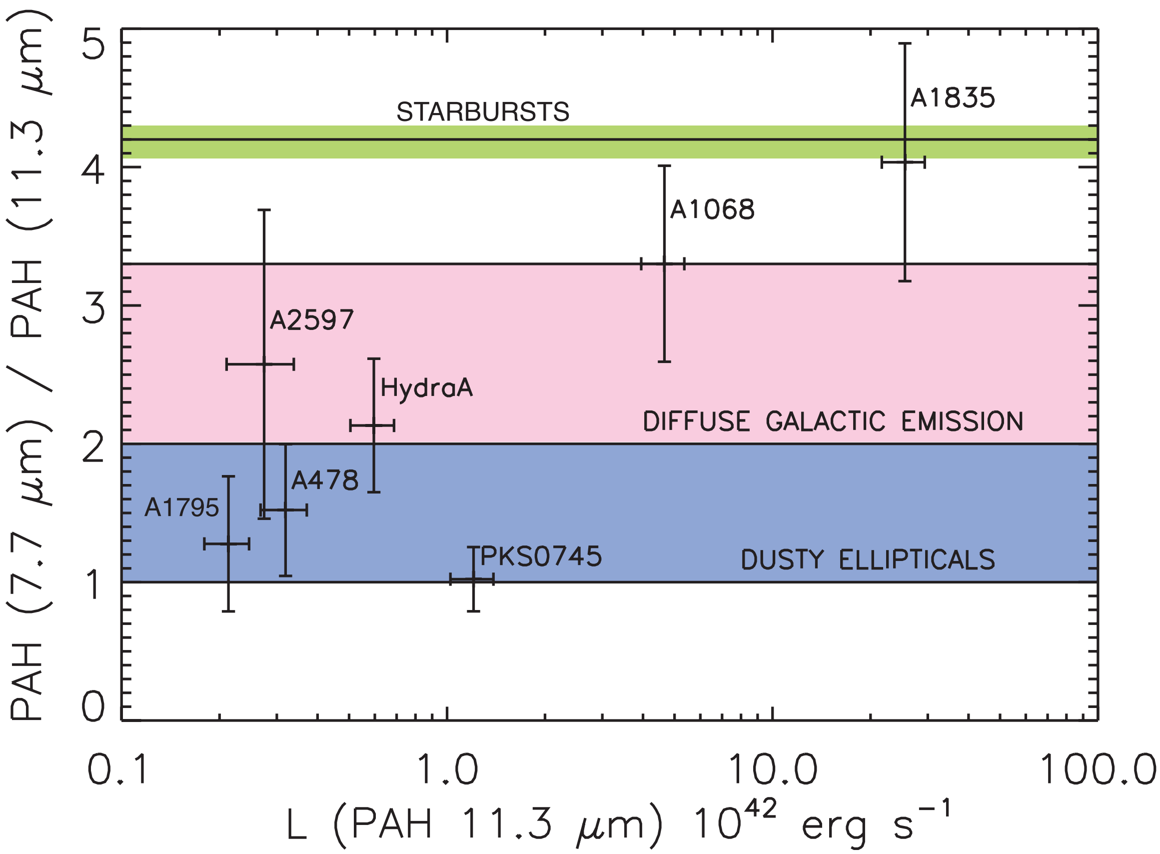

Fig. 3.15.— The PAH complex at 7.7 μm is strongly correlated with the PAH complex at 11.3 μm. The mean ratio for starbursts, indicated with a single horizontal line at the top of the plot, is ~ 4. Diffuse Galactic ISM generates ratios from $2-3.3$, shaded pink (light grey), and the ratio in dusty ellipticals ranges from $1-2$, shaded blue (darker grey). The weighted mean for seven BCGs with PAH 7.7 μm detections in our sample is 2.7 ± 0.2, indicating radiation fields intermediate in hardness between dusty elliptical and normal star-forming galaxies.

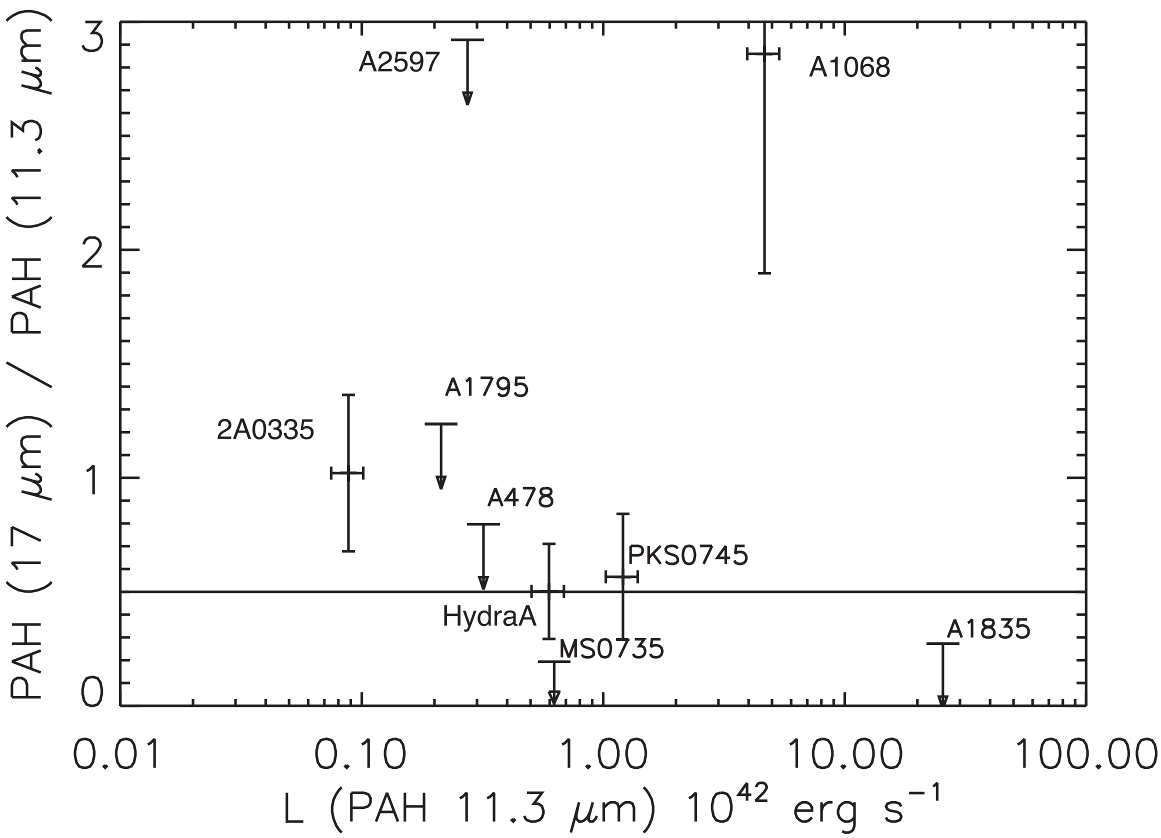

Fig. 3.16.— The luminosity ratios and upper limits for the PAH complexes at 17 and 11.3 μm. The line indicates the mean value of the ratio between the 17 and 11.3 μm PAH complexes (0.5) for normal star-forming galaxies (Smith et al. 2007b). Only A1068 has a ratio that is distinctly atypical, suggesting some processing of the smaller PAHs have occurred in that system.

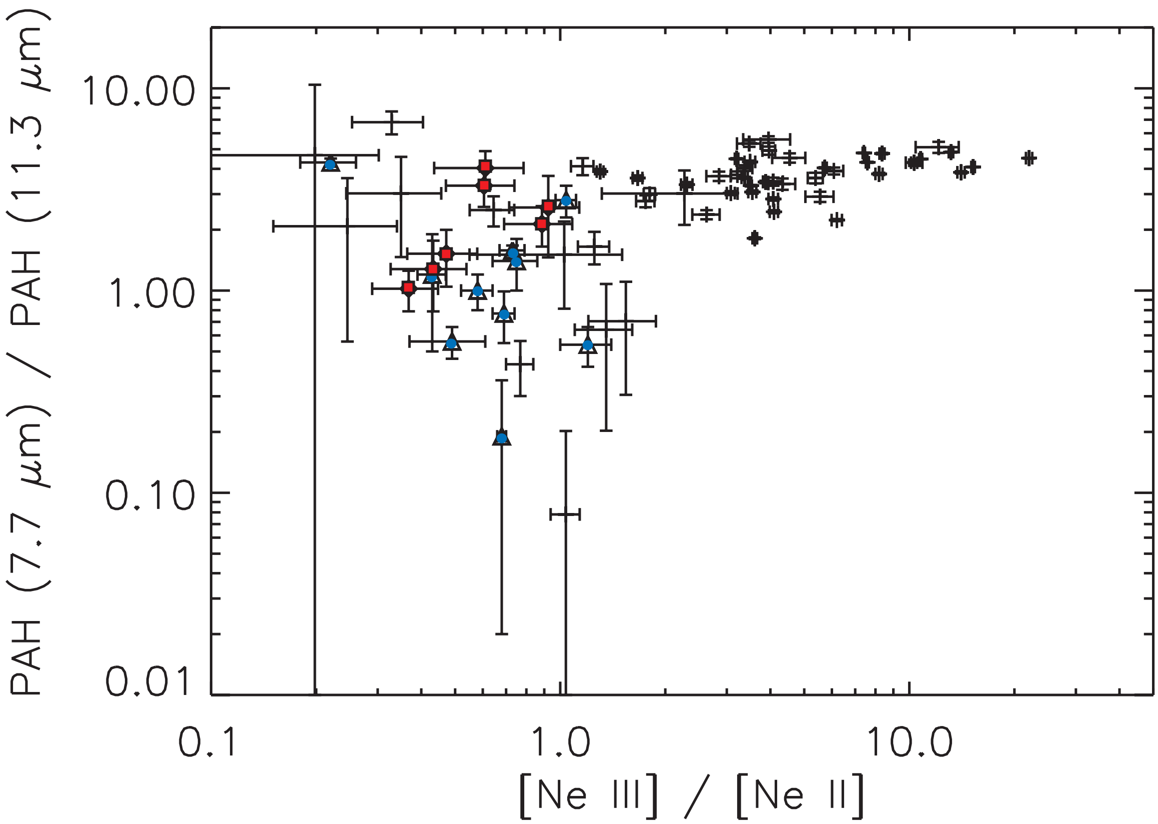

Fig. 3.17.— The [Ne III]/[Ne II] and PAH 7.7 μm and 11.3 μm ratios for 55 SINGS galaxies (Smith et al. 2007b, using on-line data from their Table 4) with black points, elliptical galaxies (Kaneda et al. 2008) with blue filled circles inside triangles, and our sample (red, filled square points). The [Ne III]/[Ne II] line ratios of BCGs are similar to those seen in star-forming galaxies with low [Ne III]/[Ne II] ratios, LINERS, and dusty ellipticals. Three of the red (filled square) points (A478, A1795, PKS0745) have somewhat lower PAH 7.7 to 11.3 μm ratios than seen in SINGS galaxies with similarly low [Ne III]/[Ne II] ratios, but are rather similar to the ratios seen in ellipticals in Kaneda et al. (2008). 2A0335 and MS0735 are not plotted here.

3.7 Conclusions

In our *Spitzer* IRS spectroscopic study of 9 brightest cluster galaxies residing in cool-core X-ray clusters, we have detected very bright molecular hydrogen rotational transitions, PAH features, and forbidden lines from ionized gas (Ne II, Ne III), in addition to dust continuum at 15-25 μm. These galaxies were known previously to have prominent optical forbidden and Balmer emission line nebulae (e.g. Heckman et al. 1989). Photometric MIPS and IRAC studies of similar BCGs have shown prominent mid-infrared dust emission, together with UV and blue signatures of star formation (e.g. O'Dea et al. 2008). The low resolution *Spitzer* 5-25 μm IRS spectra reveal that BCGs host PAHs, and the ratios of these features indicate that the PAHs in such BCGs are similar to PAHs in other types of galaxies. The emission from PAHs and dust are highly correlated, nearly linearly, as might be expected if the PAHs and dust are heated by star formation. The ratios of the 11.3 μm PAH luminosities to total IR luminosities are similar to or slightly lower than those of normal star-forming galaxies, with the exception of MS0735 whose PAH 11.3 μm feature is well-detected, and its IR continuum is very weak. Fits of simulated starburst models published in Groves et al. (2008) show that the star formation rates inferred from the 5-25 μm spectra are consistent with star formation rates inferred from our 70 μm MIPS photometry using relations from Kennicutt (1998) and Calzetti et al (2010). These simulated starburst SEDs also provide reasonable fits to the PAH features in the spectra, again consistent with the strong, nearly linear correlation between PAH luminosity and dust continuum luminosities.

The luminosity of the warm ionized gas, traced by the [Ne II]12.6 μm emission line, is also correlated with the dust luminosity, so it is likely that the star formation powering the dust luminosity is also contributing to the heating of the warm ISM.

However, the relation is distinctly non-linear, in the sense that the systems with lower IR luminosities have larger [Ne II]/IR ratios. All of the systems are over-luminous in [Ne II] compared with PAH or dust emission, as most lie at or above the top end of the scatter of this luminosity relation as seen in star-forming galaxies (Smith et al. 2007b).

Even more strikingly, the molecular hydrogen luminosities of BCGs are very high compared to that expected from star-forming galaxies of similar infrared luminosities. The H_2 luminosities are only weakly correlated with the mid IR or PAH luminosities, suggesting that the H_2 emission line power source is nearly independent of that powering the dust. The strong correlation of the molecular hydrogen line luminosity scaled by L_{24} with [Ne II] scaled in the same way suggests that the warm gas has a second heat source that may be related to the primary power source for the molecular hydrogen emission lines, a scenario consistent with excess heating by energetic particles and/or conduction from the hot intracluster gas (Sparks et al. 1989; Ferland et al. 2008, 2009).

The existence of dusty gas and, in particular, PAHs, along with the fact that PAH feature ratios are similar to those found in star-forming galaxies, suggests that (a) the dust and PAHs are similar in ionization and size distributions as in spiral galaxies and that (b) the PAHs and dust are shielded from the destructive X-ray radiation and fast-moving thermal particles in the ICM. On the other hand, the ionized and molecular gas may indeed receive a noticeable energy dose from thermal particles from the hot ICM, boosting the forbidden line radiation from the ionized gas and the rotational line emission from molecular hydrogen.

The fits with starburst SEDs from Groves et al. (2008) give a consistent story to our empirical comparisons: we can simultaneously fit the mid-IR continuum and

PAH features and some of the ISM emission lines, and the fits give SFRs which are consistent with Kennicutt (1998) relations for the 24-70 μm photometry measured with *Spitzer* MIPS and with Calzetti et al. (2010) relations for 70 μm. However, the models do not reliably predict the neon line spectrum, which we suggest may be partially generated by the same physical mechanism that generates the majority of the molecular H_2 emission.

Furthermore, our results are in agreement with the Johnstone et al. (2007) analysis of IRS spectra of NGC1275 and NGC4696. Our sample further demonstrates that there is no correlation between the star-formation signatures in these galaxies and the strength of the molecular hydrogen luminosities, and that molecular hydrogen luminosities are more extreme than produced by typical star formation-related processes. The neon forbidden lines and rotational lines of molecular hydrogen can be enhanced without significantly modifying the luminosities of dust if the ionized gas and some of the molecular gas is heated by non-radiative agents that can penetrate the molecular gas clouds, such as cosmic rays, hot electrons, and MHD waves.

Chapter 4

Star Formation in Cool Core Galaxy Clusters: Mid-Infrared and Optical Evidence

4.1 Abstract

This second paper in a series on IRS spectra of brightest cluster galaxies (BCGs) in nine massive cool-core clusters examines the mid-infrared evidence for star formation. We compare to optical/UV evidence, which unambiguously indicates that all but one of the sample are active star-formers, with star formation progressing in some cases in extended filaments or at regions associated with the edges of the radio lobes. Weak emission in the small dust grain continuum and PAH bands compared against relatively strong optical/UV star formation evidence indicates that the star formation is progressing in an unusually exposed environment, consistent with a model of extended, delicate, magnetically supported filaments of star-forming material describing another cool-core BCG (NGC 1275). Two galaxies in the sample have strong MIR dust continua and PAH emission consistent with the presence of vigorous star formation in a normal disk or nuclear starburst, probably in addition to the extended star formation seen in the other six galaxies.

4.2 Introduction

Brightest cluster galaxies (BCGs) are the most massive and luminous galaxies in the universe. They are embedded in the deep gravitational potential wells of galaxy clusters, which are dominated in mass by dark matter ($\sim 90\%$). The baryonic mass is dominated by a diffuse halo of X-ray-emitting intracluster gas at tens to hundreds of millions of degrees K (~ 4 keV) with electron densities of $n_e \sim 10^{-5} - 10^{-2}$ cm^{-3}, extending to several hundreds of kiloparsecs (Fabian 1994; McNamara 2002; Fabian et al. 2011a). In gas-rich clusters, the gas mass is about $5 \times 10^{13} - 5 \times 10^{14}$ M$_{\odot}$. BCGs contain an exotic mixture of stellar populations formed by multiple processes:

infall of primordial gas, aggregation of stars and gas from other galaxies, compression of circumgalactic gas by radio-emitting jets, and inflow of cooled intracluster gas (Fabian 1994). They have elliptical morphologies, but about 15% of BCGs exhibit strong nebular optical line emission indicative of star formation or nuclear activity. Star formation is rare among normal quiescent ellipticals (Sauvage et al. 2005).

About half of nearby galaxy clusters feature cusps of cool, dense X-ray-emitting gas near their BCGs. Among these clusters, the fraction with observed optical line emission rises dramatically, to 70% (Crawford et al. 1999; Edwards et al. 2007). In these clusters, the hot intracluster medium (ICM) has a short cooling time ($\lesssim$ 1 billion years) and low entropy ($K = kTn_e^{-2/3} < 30$ keV cm^{-2}) (Fabian 1994; Cavagnolo et al. 2008). Under those circumstances, the cooler gas ($\sim$ half of virial temperature, or $\sim$ 1 keV) inside the cooling radius exerts less pressure to support the overlying gas, and is forced to flow inward (in a "cooling flow") to increase in density (with central electron densities of $\sim 10^{-2} - 10^{-1}$ cm^{-3}, Hudson et al. 2010) and to exert more pressure. Central ICM pressures in these clusters fall in the range of $10^6 - 10^7$ K cm^{-3} (Rafferty et al. 2008). Unchecked, the inner mass of the ICM would quickly condense onto the BCG in a cooling catastrophe, radiating away its heat and depositing massive quantities of cold gas that would be expected to fuel major episodes of star formation. The gas has been processed by earlier generations of stars and has a metallicity of $\sim 0.3 - 0.5$ Z$_\odot$ (Fabian 1994; Hudson et al. 2010).

Many such BCGs have blue continua and stellar absorption features within several to tens of kpc of the nucleus indicative of recent star formation at rates of $\sim 10 - 100\,\mathrm{M_\odot\,yr^{-1}}$ (McNamara 2002). Star formation in BCGs is conclusively linked to the cooling flow (Johnstone et al. 1987; McNamara & O'Connell 1989; Fabian 1994; McDonald et al. 2011b). Star formation and Hα emission are observed when the central cooling time of the hot gas falls below $\sim$ 500 million years (Rafferty et al. 2008; Cavagnolo et al. 2008). However, the cooling rates were initially estimated to be $\sim 50 - 1000\,\mathrm{M}_{\odot}\,\mathrm{yr}^{-1}$, far in excess of the observed star formation (Fabian 1994).

Recent X-ray spectroscopy with the XMM-*Newton* and *Chandra* X-ray Observatories demonstrates that simple cooling is not the dominant process in most clusters. Rather, radiative losses from the hot ICM are for the most part offset by a remarkably efficient heating mechanism, probably stable feedback associated with nuclear activity, with perhaps some assistance from thermal conduction or mergers (Fabian et al. 2002; Gómez et al. 2002; Bîrzan et al. 2004; McNamara & Nulsen 2007; Rafferty et al. 2008; Guo et al. 2008; Conroy & Ostriker 2008; ZuHone 2011). Recent estimates of the cooling rate based upon X-ray spectroscopy demonstrate that the majority ($\sim$ 90%) of the inner hot intracluster medium concentrated on the cluster core is sustained by this heating mechanism, while $\sim$ 10% is able to cool down below 1 keV and deposit onto the BCG (McNamara & Nulsen 2007). The activity may be episodic, with periods of quiescent deposition of cooling gas or conductive heating of the inner region of the ICM by the hot outer layers punctuated by outbursts from the active galactic nucleus (AGN), which is fueled by accretion of the cooled gas (Guo et al. 2008). The revised net cooling rates rates are now comparable to the estimated star formation rates (SFR) (Rafferty et al. 2006; O'Dea et al. 2008).

These results greatly strengthen the case that continuing star formation in BCGs results from condensation of intracluster gas (e.g. McDonald et al. 2011a), which is itself regulated by AGN feedback. Cluster cooling flows are therefore among the few environments in which models for the fundamental cooling and energy feedback mechanisms that are thought to dominate early galaxy formation can be directly tested. In this work, the term "cooling flow" is used to describe the regulated deposition of gas onto the center of the galaxy cluster (sometimes termed a "moderate cooling flow", Soker 2008) and not to the catastrophic cooling event absent any source of heating that was hypothesized in early cooling flow theory.

Improved radio and infrared (IR) instrumentation has recently permitted identification of other tracers of star formation in cool-core BCGs (CC BCGs) (Genzel & Cesarsky 2000; Brandl et al. 2006). Substantial reservoirs ($< 10^8$ M$_\odot$ to $\sim 10^{11}$ M$_\odot$) of cool molecular hydrogen are now found in many cooling flows, mainly through detection of emission from CO (Edge 2001; Salomé & Combes 2003; Salomé et al. 2008a) or the near-IR ro-vibrational transitions of H_2 (Jaffe & Bremer 1997; Donahue et al. 2000; Jaffe et al. 2001; Edge et al. 2002; Hatch et al. 2005).

Photometry with the *Spitzer* Space Telescope reveals far-IR (FIR) excesses characteristic of cool dust with $T_d \lesssim 100$ K in some BCGs in cool-core clusters (Egami et al. 2006a; Quillen et al. 2008; O'Dea et al. 2008). The dust mainly forms in the stellar winds of low-to-medium mass stars in the AGB phase. While the majority of the hot ICM is expected to be dust-free, the cooling inner region is injected with dust either dredged up from the pre-existing population in the BCG or generated from stars forming from the cooling material (Hansen et al. 1995).

Spatially resolved spectroscopy and imaging of the environment of nearby cool-core BCGs has uncovered complex morphologies including Hα-bright filaments of star formation that may be associated with the interface between the AGN jet and the hot ICM (see §4.2.1 and §4.4). The geometry of the star-forming regions has major differences from the morphology seen in normal star-forming galaxies.

Despite this considerable progress, many questions about the gas deposition, star formation, and feedback processes in BCGs remain unresolved. This is the second of a series of three papers.

In Paper 1, Donahue et al. (2011), we introduced our *Spitzer* Infrared Spectrograph (IRS) and broadband IRAC and MIPS data of a sample of nine cool-core BCGs (see §4.3), greatly increasing the available library of MIR spectra of the category. Star formation activity has previously been detected in eight of the nine galaxies.

In Donahue et al. (2011), we focused on the character of the polycyclic aromatic hydrocarbons (PAHs) in the BCGs, and found that the PAH emission is well correlated with the warm dust emission (as expected in a star-forming environment). PAH diagnostics indicate that these large molecules have a similar size and ionization profile in the cool-core BCGs (with a few exceptions) to the relatively undisturbed ISM in spiral galaxies, and thus that the PAHs are generally shielded from radiative or collisional trauma from the hot ICM. The exceptions include the two BCGs that are forming stars at a more vigorous rate, where the PAHs indicate a higher ionization fraction and possible destruction of the smaller molecules.

We found that the luminosity of the warm ionized gas, traced by forbidden neon emission lines, is also correlated with the warm dust continuum, but the ionized gas appears to have an additional heating source. This suggests either that the ionized gas has a major heating source other than star formation (probably a non-radiative energy source related to the hot ICM or AGN jet, such as cosmic rays or magnetohydrodynamic waves) or that star formation is not heating the warm dust as consistently as the gas. The ionized gas also appears to share a heating source with the remarkably strong pure rotational H_2 emission found in all of the BCGs.

In this paper, we analyze the MIR spectra with the particular goal of discovering what conclusions can be drawn about the character, environment, and amount of star formation in CC BCGs. From the literature, we include estimates of exposed star formation rates derived from optical and ultraviolet data. We examine several MIR indicators of star formation estimate the total amount of star formation, and discuss the fraction of obscured star formation. We compare to the cooling rate derived from X-ray data to find the efficiency of star formation from the fuel of the cooling flow. We contrast with various surveys of galaxies and other classic examples of star formation.

In Paper 3, we will expand upon the analysis and interpretation of the strong H_2 emission in the cool-core BCGs. This emission is much stronger than expected in a normal star-forming environment.

Analyses of IRS spectra of two other star-forming BCG systems have already appeared: the nearby archetypal system Perseus (Johnstone et al. 2007) and the distant but very luminous system ZwCl 3146 (Egami et al. 2006a). Four cool-core clusters (Perseus, Hydra A, Abell 2052, and Abell 2199) are also included in the IRS survey of warm H_2 emission in radio galaxies of Ogle et al. (2010).

All computations in this paper assume a Hubble constant of 70 km s^{-1}Mpc^{-1} and the cosmological parameters $\Omega_M = 0.3$ and $\Omega_\Lambda = 0.7$.

4.2.1 Environment of star formation

In this work, we consider the morphology of star formation in the BCGs of cool-core galaxy clusters. We consider three possible environments of star formation: normal star formation in a disk or other massive star-forming region; star formation in magnetically supported filaments of material dredged from the BCG by AGN jet activity; and knots of jet-induced star formation where the jet impacts the overlying ICM.

Normal star formation

Normal star formation, for the purposes of this work, refers to star formation in a giant molecular cloud (GMC) complex (20-50 pc in size or larger, with a gas mass of $\sim 10^5$ $M_\odot$) in a spiral disk, nuclear starburst, or similar environment where a considerable fraction of the emitted UV light is reprocessed into the IR via absorption by gas and dust. The energy re-emerges as a strong thermal continuum from small dust grains beyond ~ 15 μm, as well as a suite of other MIR features including aromatic emission from large molecules (Peeters et al. 2004; Indebetouw et al. 2009). This generalization of normal star formation encompasses a broad range of scales, morphologies and environments.

In the inner part of a spiral disk (such as the Milky Way), there tends to be a self-regulating population of GMCs with a moderate mean gas density of $\sim 2-50$ $M_\odot$ pc^{-2} and steady star formation (Kennicutt 1998b). At this level of extinction, star formation can be approximated from optical features such as Hα emission by making reasonable assumptions about the degree of extinction, but approximately two-thirds of the optical light is internally absorbed (Kennicutt 1998b). Characterizations of the star formation rate based on dust emission features must take into account sources of heating from other sources such as cirrus heated by older stars (Kennicutt et al. 2003). We note that in the outer part of a disk (such as the outer reaches of M33), there is a low density of GMCs, a low fraction of dust to gas, and a low fraction of H_2 to H I, compared to the inner disk (Bigiel et al. 2010a). In these environments, optical-FUV extinction is low and star formation is relatively exposed, but star formation is also comparatively inefficient in the outer disk and usually represents only a small part of the total star formation in the galaxy (Bigiel et al. 2010b). Therefore, when we discuss star formation in a normal disk, we primarily refer to star formation in the inner or nuclear regions of a disk.

In the nuclear regions of normal spiral galaxies, or the nucleus or circumnuclear disks of starburst galaxies (such as M82), the gas densities are much higher, to the point where GMCs can be packed in close enough to effectively form one enormous complex or super star cluster (Kennicutt 1998b; Brandl et al. 2006). A smaller-scale, nearby and well-studied laboratory for this environment of intense star formation is the H II region and super star cluster analogue 30 Doradus in the Large Magellanic Cloud ($\sim$ 50 kpc away, $\sim$ 200 pc in diameter, and with a gas mass of several $\sim 10^5$ $M_\odot$) (Indebetouw et al. 2009). Though there is a considerable range of extinction, the optical-FUV light of young stars can be completely obscured. Among the strongest star-formers, star formation can be estimated just from measures of the reprocessed infrared light, such as $L_{24\mu m}$ (Rieke et al. 2009; Calzetti et al. 2010). Star formation in starbursts is often stimulated by interacting systems or other morphological disturbances of galaxies. Other major hosts of obscured star formation include starburst-associated luminous infrared galaxies (LIRGs) and, mainly at $z > 2$, ultraluminous infrared galaxies (ULIRGs) where vigorous star formation (or sometimes nuclear activity) is driven by violent merger activity (Armus et al. 2009). In these dusty environments, $\sim$ 90% of the UV light is absorbed and re-radiated in the infrared, and $L_{24\mu m}$ or PAH luminosity are good indicators of star formation activity (Alonso-Herrero et al. 2006; Farrah et al. 2007). Submillimeter galaxies (SMGs) are another category of high-redshift, highly obscured sites of star formation (Chapman et al. 2005).

Jet-induced star formation

Jet-induced star formation occurs where the jet from an AGN plows into the dense inner ICM, triggering a shock front at the interface between the jet and the ICM (van Breugel et al. 2004). A related radio-triggered mode of star formation is stimulated by shocks at the collision between the radio plasma and cool gas clouds, rather than along the path of the jet (McNamara 2002). These types of star formation are detected when indicators such as a blue continuum excess or Hα emission from 10^4 K gas are mapped in extended knots or lobes, often resolved into more complex filaments, that correlate with the edges of radio-bright structures or the footprint of the jet upon the ICM. Candidate sites have been detected in many radio galaxies (van Breugel et al. 2004) including many of the nearest cool-core galaxy clusters such as A1795 and A2597 (van Breugel et al. 1984; McNamara & O'Connell 1993; Koekemoer et al. 1999; O'Dea et al. 2004), 2A0335 (Donahue et al. 2007a), Hydra A, A2052 (McDonald et al. 2010), and NGC 1275 (McNamara et al. 1996; Conselice et al. 2001). There is tentative evidence in support of radio-triggered star formation in A1068, but high-resolution analysis is needed (McNamara 2002). In the well-resolved candidate sites of jet-induced or radio-triggered star formation, the blue color, distance from the nucleus ($\sim 6-20$ kpc), and resolved spatial structure rule out a source such as old stars within the BCG or non-stellar heating such as an AGN. Scattered light from an obscured AGN is also ruled out for A1795 and A2597 (McNamara et al. 1999; McNamara 2002).

A problem with the environment of jet-induced star formation is that the radio structures have a lifetime of only $10^6 - 10^8$ yr, while star formation is likely to last $10^8 - 10^9$ yr (McNamara & O'Connell 1993). In most cases, one would expect the two structures to have decoupled unless they happen to be observed in the early stages.

Ghost cavities (cavities in the X-ray emission from previous outbursts where the radio emission has faded) have been detected in several cases including A2597 and NGC 1275, and possibly 2A0335 (McNamara et al. 2001; Fabian et al. 2006; Mazzotta et al. 2003). Continuing star formation kinematically associated with the edges of the ghost cavities may provide support for the model of jet-induced star formation.

Filamentary star formation

Extended filaments or knots of blue continuum or Hα emission, which often correspond to complex X-ray structures but are unassociated with radio structures, have been detected in cool-core BCGs including A2597 (Koekemoer et al. 1999), A1835 (O'Dea et al. 2010), A1795 (especially its long entwined filaments), A0478, A0496, A4059, A1644, Sérsic 159-03 (McDonald et al. 2010), 2A0335 (Donahue et al. 2007a), and A2052 (Martel et al. 2002).

The nearest cool-core BCG, NGC 1275 in the Perseus cluster has a spectacular filamentary structure, detected in optical continuum and ionized emission (Conselice et al. 2001; Fabian et al. 2008), cold and warm molecular filaments (Salomé et al. 2008b; Johnstone et al. 2007), and detailed X-ray maps (Fabian et al. 2006, 2011b). Star formation is progressing in the "Blue Loop" extended region of NGC 1275 at a rate of 20 $M_\odot\,yr^{-1}$ (Canning et al. 2010). Many other cool-core BCGs also display powerful molecular gas emission (see Chapter 5) and a comparison of a degraded-resolution image of NGC 1275 to cool-core BCGs at higher redshifts shows similar optical structures; NGC 1275 may have a typical morphology for cool-core BCGs, making it a valuable source of high-resolution, detailed information (McDonald et al. 2010).

Filaments in cool-core BCGs are unambiguously linked to the cooling flow (located within the cooling radius and at sites of heightened cooling, McDonald et al. 2010) and optical-UV continuum analysis in many of the references cited above demonstrates that many of the filaments are the sites of current star formation.

However, some Hα filaments are unassociated with continuum emission and cannot be ionized by young stars (Martel et al. 2002; Canning et al. 2010). Furthermore, recent work demonstrates that photoionization by young stars is generally inadequate to energize the observed luminous Hα and molecular emission in the filaments even in targets with filamentary star formation (McDonald et al. 2010).

McDonald et al. (2010) discuss other mechanisms capable of ionizing Hα filaments, including radiation from the AGN, X-ray heating from the hot ICM, conduction from the ICM into the filaments, shocks, and cosmic ray heating. The penetration of energetic particles from the surrounding hot plasma into the magnetically supported cold gas (where the particles are suprathermal) is a prime candidate for producing the Hα and molecular emission (McDonald et al. 2010; Fabian et al. 2011a). Other potential sources of non-radiative heating are cosmic rays and kinetic sources such as dissipative magnetohydrodynamic (MHD) waves (Ferland et al. 2008).

While some of the filamentary structures are associated with mergers (Martel et al. 2002; Donahue et al. 2007a), in general there is no spatial association between the filaments and nearby cluster galaxies (McDonald et al. 2010). The filaments probably form as part of the cooling flow, when gas at about the cooling radius collapses into filaments and into smaller clump structures as it falls inward along magnetic field lines toward the BCG, interacting with buoyant radio bubbles on their way up (Canning et al. 2010; McDonald et al. 2010, 2011a). These bubbles may also drag cold gas and dust from the BCG to inject into the cooling gas, possibly on short enough timescales to mix with the ICM within the cooling radius; this is an important source of dust for star formation (Churazov et al. 2000; Canning et al. 2010). An alternate theory describes filaments that are formed in the wake of the buoyant bubbles, rather than by the cooling flow (Churazov et al. 2000). There is as of yet no consensus on whether the filaments are kinematically on their way out or in.

Substructures to the filaments are observed, often in the form of knots of H II regions within the filamentary halo (Martel et al. 2002). The observed optical filaments have kiloparsec length scales and may extend to 50 kpc, as in the intertwined chains of resolved HII regions in the wake of the BCG in A1795 as the BCG moves through the ICM, but are typically ~ 100 pc in diameter (Martel et al. 2002; McDonald et al. 2010). The large axial ratios (length/thickness ~ 30) imply that magnetic support is likely (McDonald et al. 2010).

In the nearby target NGC 1275, the filaments themselves start to be resolved into complex structures of smaller threads, smaller than 70 pc in diameter, with an estimated mean density of ~ 2 cm^{-3} (Ferland et al. 2008; Fabian et al. 2008). They appear to be supported in a stable state by magnetic pressure. Models of certain filaments in NGC 1275 suggest that the magnetically supported filaments have a low volume filling factor ($\sim 10^{-5}$) and extraordinarily delicate structure, composed of hundreds to thousands of sub-threads of star-forming material (dense molecular cores at $\sim 10^3$ K with a density of $\sim 10^5$ cm^{-3}) enveloped in lower-density halos of ionized gas), each molecular thread about a third of a parsec in size and separated from its neighbors by ~ 10 pc (Ferland et al. 2008, 2009; Fabian et al. 2011a). The most likely source of ionization is energetic particles from the surrounding ICM (Fabian et al. 2011a). The application of this model to other cool-core BCGs may be difficult because of lack of resolution, but as noted above, NGC 1275 may be a good local template for other cool-core BCGs.

As demonstrated by the overlap in the targets discussed here and in the previous subsection on jet-induced star formation, evidence suggests that the complex environment of a cool-core BCG can easily host both types of extended star formation.

An important question is how much optical-FUV extinction is expected in these extended star-forming environments. If a geometry like that modeled for NGC 1275 applies for filamentary star formation in cool-core BCGs in general, the molecular cores are only ~ 0.3 pc in diameter, and the light of young stars may escape much more readily than in the giant molecular clouds of normal star formation.

4.3 Sample

Our sample consists of nine BCGs which have been well studied in the X-ray and optical/ultraviolet bands. The sample selection goal was to target major examples of cool-core BCGs which were observable with the *Spitzer* IRS but had not yet been observed. Initial presentation of these data, as well as analysis of the polycyclic aromatic hydrocarbons (PAHs) and other features, appears in Donahue et al. (2011). Basic data on the sample are given in Table 4.1. The index numbers in that table are used in some figures throughout the paper. We typically refer to individual systems by an abbreviation of the name of the cluster, though our IRS data is restricted to the environs of the BCG.

The redshifts are derived from optical emission lines from a variety of sources, as follows: 2A0335: Donahue et al. (2007a). Hydra A (also Abell 780): Smith et al. (2004). A1795 (CGCG 162-010): Hill & Oegerle (1993). A2597 (PKS 2322-12): Voit & Donahue (1997); Colless et al. (2003); see also http://www.mso.anu.edu.au/2dFGRS/. A478 (NVSS J041325+102754): Zabludoff et al. (1990). PKS0745: Hunstead et al. (1978). A1068 (FIRST J104044.4+395712): Allen et al. (1992). MS0735 (ZwCl 1370 or BCG 4C +74.12): Stocke et al. (1991). A1835 (SDSS J140102.07+025242.5): SDSS DR2 ; see also Allen et al. (1992).

The luminosity distance D_L is based upon these redshifts and the cosmology mentioned above.

The cooling rates given in Table 4.1, $\dot{M}_{XS}$, are derived from *Chandra* and *XMM-Newton* spectra and are based on intermediate-temperature X-ray-emitting gas. The cooling rate for MS0735 comes from observations with a low number of counts and should be considered less reliable. Rafferty et al. (2006) also have observations for 2A0335, PKS0745 and A1068 which are generally consistent with the results from O'Dea et al. (2008). The rates for Hydra A, A478, A1795 and A2597 in McDonald et al. (2010, 2011b) are also generally consistent with Rafferty et al. (2008), though somewhat lower.

All of the clusters have central cooling times t_{cool} in the range 100–500 Myr (Rafferty et al. 2008), though these timescales should be regarded as an upper limit on the true central cooling time, particularly for the more distant, less well-resolved sources. The radius or semi-major axis, r_{cool}, within which the cooling time is less than 7.7 Gyr, based on *Chandra* data, is also given (Rafferty et al. 2006). 7.7 Gyr is the time since $z = 1$, or approximately the timescale over which the cluster has been relaxed. The cavity power, P_{cav}, is a measurement of the mechanical energy output of the AGN jets (Rafferty et al. 2006). It is a lower limit on the total AGN power, though it may trace older rather than current activity. It is derived from *Chandra* observations except for A1068, where it is estimated from the 1.4 GHz radio flux.

Table 4.1. Basic Characteristics of Cool-Core BCGs.

#	Cluster	BCG[a]	BCG position (J2000.0)[a] R.A.	Decl.	z	D_L (Mpc)	Scale[b] (kpc/")	$\dot{M}_{XS}$[c] ($M_\odot$ yr^{-1})	r_{cool}[d] (kpc)	t_{cool} (10^8 yr)	P_{cav}[d] (10^{42} erg s^{-1})
1	2A0335+096	PGC 013424	03:38:40.6	09:58:12	0.0347	153	0.691	17^{+5}_{-3}	135	1.4	24^{+23}_{-6}
2	Hydra A	PGC 026269	09:18:05.7	-12:05:44	0.0549	245	1.07	16 ± 5	109	2.0	430^{+200}_{-50}
3	Abell 1795	PGC 049005	13:48:52.5	26:35:34	0.0633	284	1.22	8^{+13}_{-7}	135	3.7	160^{+230}_{-50}
4	Abell 2597	PGC 071390	23:25:19.7	-12:7:27	0.0821	373	1.55	30^{+30}_{-20}	128	2.6	67^{+87}_{-29}
5	Abell 478	PGC 014685	04:13:25.3	10:27:55	0.0860	392	1.61	40^{+40}_{-20}	150	1.3	100^{+80}_{-20}
6	PKS 0745-19	PGC 021813	07:47:31.4	-19:17:39.7	0.1028	474	1.89	200^{+40}_{-30}	176	2.1	1700^{+1400}_{-300}
7	Abell 1068	PGC 093944	10:40:44.4	39:57:12	0.1386	654	2.45	30^{+20}_{-10}	152	1.4	20
8	MS 0735.6+7421	PGC 2760958	07:41:44.7	74:14:38	0.216	1070	3.50	20^{+20}_{-10}	141	4.7	6900^{+7600}_{-2600}
9	Abell 1835	2MASX J14010204+0252423	14:01:02.0	02:52:45	0.2520	1270	3.93	< 200	156	3.0	1800^{+1900}_{-600}

(a) Crawford et al. (1999); Rafferty et al. (2008); Quillen et al. (2008); Hicks et al. (2010). (b) The angular diameter distance D_A. (c) ICM cooling rates from X-ray spectroscopy. Rafferty et al. (2006) except for 2A0335+096, PKS 0745-19 and Abell 1068 (O'Dea et al. 2008), and Abell 1835 (Peterson et al. 2003). (d) Rafferty et al. (2006).

4.4 Optical/UV Evidence for Star Formation

All the BCGs in this sample have good star formation rate estimates derived from the optical/UV continuum. MS0735 is the only target in the sample with no optical or ultraviolet evidence of recent star formation (McNamara et al. 2009). Estimates for the others are in the range of $\sim 5 - 20$ $M_\odot\,yr^{-1}$, with a star formation rate of 100 $M_\odot\,yr^{-1}$ in one target (see Table 4.2). The detection of spatially extended optical or UV continuum or Hα line emission in a number of cases is unambiguous evidence of recent star formation in extended knots and filaments around the BCG (McNamara & O'Connell 1993; Koekemoer et al. 1999; Conselice et al. 2001; Martel et al. 2002; O'Dea et al. 2004; Bildfell et al. 2008; McDonald et al. 2011b); also, see §4.2.1. Nuclear star formation is also found, well-distinguished from emission caused by shocks or older stellar populations (McNamara et al. 2006; McDonald et al. 2011b).

Unfortunately, we do not have a homogeneous source of optical or ultraviolet evidence for star formation for our entire sample. In Table 4.2, we have compiled estimates of the SFR from a variety of targets. The BCGs of our sample are not adequately resolved to obtain separate estimates of extended and nuclear star formation. We sought to standardize our discussion by finding estimates of SFR which utilize similar data and assumptions.

For simplicity in this work, we refer to these values as SFR_{opt}, and we refer to this evidence, both optical and near-ultraviolet, as "optical" evidence.

4.4.1 Hα evidence for star formation

Star formation is often correlated with the luminosity of optical line emission from Hα (Kennicutt 1998b) and there is a plethora of such data for our sample, associated with star formation rates between ~ 1 $M_\odot\,yr^{-1}$ (for A1795 and Hydra A, McNamara

1995; Rafferty et al. 2006) up to $\sim$ 40 $M_\odot\,yr^{-1}$ (A1835, McNamara et al. 2006). Intermediate levels are estimated for some of the other targets in our sample: 2A0335 (Donahue et al. 2007a), A2597 (Donahue et al. 2007b), and A1068 and PKS0745 (Rafferty et al. 2006).

In a normal star-forming galaxy where the only expected source of hydrogen ionization is recent star formation, Hα is a reliable signature of star formation. However, in the complex environment of a cool-core galaxy cluster BCG, where the Hα may be ionized by many high-energy processes, we cannot rely on Hα from a general aperture as a metric of star formation. In fact, while imaging has conclusively demonstrated that the filamentary Hα structures mapped out in some cool-core BCGs are associated with star formation (Conselice et al. 2001; McDonald et al. 2010), many of the Hα filaments in the cool-core BCG NGC 1275 are not associated with recent star formation (Canning et al. 2010) and a non-radiative heating mechanism such as energetic particles from the hot ICM probably ionizes much of the gas (McDonald et al. 2010; Fabian et al. 2011a).

Therefore, we cite Hα evidence for star formation only to corroborate optical-UV evidence, instead of relying on it as the primary indicator of exposed star formation.

4.4.2 Assumptions inherent in optical SFRs

The SFR_{opt} column in Table 4.2 represents star formation rates derived from a variety of optical or near-ultraviolet continuum observations (U through I band), in the apertures listed, assuming steady, continuous star formation of long duration (listed in the table as well).

These SFRs all utilize the same cosmology as this work. Several of the older observations have been converted to this cosmology by Rafferty et al. (2006) or in this work (Hydra A).

The SFRs have been corrected for Galactic extinction but - with the exception of 2A0335 - have not been corrected for internal dust extinction, which can be considerable for massive star-forming galaxies. Therefore, they are a measure of only the *exposed* star formation: the light of newly formed stars that escapes without being reprocessed into the mid-infrared by dust. We expect the total SFR to be higher in all cases. Estimates of total star formation typically use measurements from both exposed and reprocessed sources (Calzetti et al. 2010), as discussed in §4.8.5 and Table 4.11.

When modeling star formation, a worker's choice of duration impacts the resulting SFR. An assumption of a longer duration yields a lower SFR. However, SFRs derived over a long duration ($\gtrsim$ 100 Myr) are relatively insensitive to the choice of duration, to within about a factor of 2 (Leitherer et al. 1999; Calzetti et al. 2010), which is at least the uncertainty on this heterogeneous set of observations. The durations are comparable to the central cooling times in these BCGs (see Table 4.1), which is a realistic estimate of the timescale of star formation in cool-core galaxy cluster cores. Some of the durations are longer than the cooling time, but as noted above, the SFRs become less sensitive to duration at longer durations.

$t_{\rm cool}$ is the timescale during which a mass of hot gas will radiate away all of its heat, absent a source of heating (McNamara & Nulsen 2007). While there evidently is a remarkably efficient source of heating in cool-core galaxy clusters, the cooling time for a CC cluster also gives the general timescale since the last major heating event; if the cooling time were longer, the cooling flow would not have had time to develop (McNamara & Nulsen 2007). Therefore, fuel for star formation, in the form of cold gas condensing onto the BCG at a feedback-regulated rate, has been supplied on a timescale approximately equal to the cooling timescale.

There are still many unknowns in this process. It is unknown whether star formation in cool-core clusters proceeds cyclically or in a steady state (Romanishin 1987; Allen 1995; Guo & Oh 2009). Furthermore, it is likely that when star formation occurs, it proceeds sporadically, with any given molecular cloud forming stars in a self-governed burst perhaps no longer than 10 Myr. It is entirely possible that the star formation has been progressing for a shorter duration than the central cooling time, and indeed even t_{cool} should be regarded as an upper limit on the true central cooling time (especially for targets at higher redshift).

Overall, however, it is a reasonable assumption that the integrated star formation in the BCG is proceeding in a relatively continuous fashion over a timescale comparable to the cooling time. In several cases, there is a choice of star formation models in the literature with different durations, and while there is some evidence supporting longer durations (on the order of 10 - 100 Myr) over shorter durations (Schmitt et al. 1999; McNamara et al. 2006), in other cases the various models fit the data equally well. We selected durations which are conservative with regards to the conclusions of this work. To this end, the modeled duration of star formation is frequently longer than the estimate of cooling time, except for A1068 and A1835, where the two timescales are in close agreement.

We will demonstrate that the star formation in A1068 and A1835 is relatively obscured: star formation measured via reprocessed light (i.e., thermal dust emitting at 24 μm) equals or exceeds exposed star formation, as is the case in many starbursts (Sargsyan & Weedman 2009). If we selected exposed star formation rate estimates for those two targets that assume longer durations, the SFRs would decrease (e.g. the hard lower limit to the SFR in A1835 of $\geq 50\,\mathrm{M}_{\odot}\,\mathrm{yr}^{-1}$ for a duration of 900 Myr, McNamara et al. 2006), and strengthen further the conclusion that the star formation in those targets is relatively obscured. It is possible that even shorter star formation durations, with correspondingly higher estimates of the exposed SFR, would be appropriate for these two targets. For this reason, among others, our conclusions with regards to A1068 and A1835 are tentative.

On the other hand, we argue below that in several of the cool-core BCGs, especially A1795, A2597, and A478, the star formation is abnormally exposed: star formation measured via reprocessed IR light falls far short of optical measures of star formation. For these targets, we conservatively selected optical or UV-based measures of exposed star formation that assume long durations of star formation, typically $\sim 10\times$ longer than the central cooling time in those targets. If we selected exposed star formation rates with shorter durations when available, the exposed SFR will only increase (not necessarily by much, due to the general insensitivity of SFR to duration for durations longer than $\sim$ 100 Myr), rendering the discrepancy with measures of obscured SF even more extreme.

Some literature on the optical and ultraviolet evidence for star formation in these BCGs cites "burst" models of star formation, with a given mass of stars all formed in a theoretically instantaneous moment at a certain age, or continuous star formation over a very short duration ($\sim$ 10 Myr) which may be recent or at a given epoch. While this may represent the star formation history in any of these BCGs, the fuel for star formation has been supplied over a long timescale, approximately equal to the cooling time.

The star formation history may be complex, and the continuous star formation rates expressed in Table 4.2 are heterogeneous, but they provide a comparative measure of the degree of exposed star formation. They are conservatively low for most of the sample, and conservatively high for A1068 and A1835, to emphasize that even under those assumptions, the exposed star formation is stronger than expected (compared to MIR diagnostics of obscured star formation calculated in §4.8) for most of the sample. A1068 and A1835 do not appear to be abnormal, but fall toward the obscured end of the range of star formation.

For the purposes of comparison to MIR data, we assign uncertainties of a factor of 3× to $\mathrm{SFR_{opt}}$.

4.4.3 Aperture selection in the MIR and optical bands

Aperture mismatches between the optical and IR measurements are a potential source of uncertainty. The apertures we use in the mid-infrared (see Table 4.3) have diameters generally $\sim 5-10\times$ the full width, half max (FWHM) of the core of the diffraction disk for a diffraction-limited point source observed with *Spitzer* at those wavelengths (2" at 8 μm and 6" at 24 μm). Many of our targets are partially extended in the MIR, as discussed below; our apertures are selected based on the observed extent of the source in the MIR. Thus, our apertures are large enough to capture nearly all of the MIR continuum emission for point source or slightly extended sources. In most cases, we are able to adjust the aperture size to avoid nearby sources.

At optical and ultraviolet wavelengths, the diffraction disk is much smaller, but detector blur limits the resolution of telescopes like GALEX to about 5". The optical and ultraviolet apertures in question tend to be about 3× the point spread function. We attempt to select similar apertures to our MIR observations when possible, to capture emission from a similar region. We consider the apertures a good match if neither the optical nor MIR apertures overlap unnecessarily with extraneous sources, and if they are both large enough to capture most of the light of a point source or moderately extended source.

The optical apertures from Table 4.2 may be compared to the IRAC and MIPS apertures from Table 4.3. Our IRS apertures were drawn from generally smaller apertures, but are scaled appropriately to the IRAC and MIPS photometry (see §4.5.3), so the IRAC and MIPS apertures are the relevant MIR aperture. Specific cases of note are discussed here:

2A0335: The optical aperture is 46" across, considerably larger than the IRAC aperture, and – like the MIPS aperture – easily large enough to encompass an interacting companion galaxy 5.6" away to the northwest, within the BCG's extended halo (Donahue et al. 2007a). The IRAC aperture may capture some of the blue light from this companion. Romanishin & Hintzen (1988) find that the companion has a red core which is bright in Hα emission, consistent with the profile of an elliptical galaxy dominated by an older population of stars, perhaps containing some dust as well (Donahue et al. 2007a). This is consistent with the IRS spectrum we extracted of this companion galaxy, which is weak at longer wavelengths and rises strongly to the blue, with few MIR emission features. The companion is bright in Hα and in the R band, but not as bright as the BCG. Because it has a red optical continuum profile, it does not contribute significantly to the blue excess measured by Romanishin & Hintzen (1988), despite being included within the aperture.

As demonstrated by the imaging in Romanishin & Hintzen (1988), no other targets of note are included within a 46" diameter aperture. To obtain the SFR reported in Table 4.2, they measure the blue excess (effectively the B-I color) and also find that the H-α emission of the BCG in the same aperture yields a consistent SFR.

Abell 1795: We have no IRAC apertures to compare to the U and I apertures in this case, but the optical aperture is intermediate in size between a typical IRAC aperture for this sample and the MIPS aperture for Abell 1795. As optical (McNamara & O'Connell 1993) and ultraviolet (O'Dea et al. 2004) imaging demonstrate, a rectangular aperture of these dimensions captures most of the light of the blue lobes of recent star formation at these wavelengths.

Abell 2597 is an extended source in the MIR, and the optical aperture is somewhat smaller than the MIR apertures. It is possible that the star formation rate is a lower limit.

Abell 478: While the length of the optical slit (corresponding approximately to the B or V band) is consistent with the MIR apertures, the slit is quite narrow. We regard the star formation rate reported in Table 4.2 as a lower limit, both in the sense that it has not been corrected for intrinsic extinction and also that the slit may be missing some of the emission arising from star formation.

Abell 1068: The U and R-band apertures are slightly smaller than the infrared apertures, but are close enough to capture a similar light profile, especially considering that Abell 1068 is a point source in the MIR.

Table 4.2. Optical and ultraviolet continuum-based star formation rates

Cluster	SFR_{opt} ($M_\odot\ yr^{-1}$)	Aperture[a] (")	Duration (10^8 yr)	Source
2A0335	4.2[b]	46	1	Romanishin & Hintzen (1988)[c]
Hydra A	11	20x10	25	Hansen et al. (1997)
Abell 1795	6.3	22x11	40	McNamara & O'Connell (1993)[c]
Abell 2597	6.4	15	40	McNamara & O'Connell (1993)[c]
Abell 478	10	1.7x25	10	Rafferty et al. (2006)[d]
PKS0745	17	18	10	Romanishin (1987)[c]
Abell 1068	16	8	1	McNamara et al. (2004)
MS0735	< 0.25	10	1	McNamara et al. (2009)
Abell 1835	100	18	3.2	McNamara et al. (2006)

(a) Diameter unless two dimensions are given. (b) Corrected for internal extinction. (c) via Rafferty et al. (2006). (d) based on data from Cardiel et al. (1998).

4.5 MIR Observations and Data Reduction

4.5.1 Observations

We obtained sparse spectral maps of the nine BCGs in the 5–38 μm range with the four low-resolution ($R \sim 50 - 100$) modules of the *Spitzer* IRS. We also utilize photometry based on available observations with *Spitzer*'s IRAC and MIPS cameras (see Table 4.3). The IRS, IRAC and MIPS observations and data reduction are discussed in detail in Donahue et al. (2011). A summary with some additional detail is included here.

We use the most recent version (v18.7) of the IRS data. The low-resolution modules of the IRS include two short-wavelength and two long-wavelength spectral orders, with the following observed wavelength ranges: SL2 (5.2 - 7.6 μm), SL1 (7.5 - 14.3 μm), LL2 (14.3 - 20.6 μm), and LL1 (20.5 - 37.5 μm). The SL pixels are 1.8" in size; the LL pixels are 5.1". Our earliest observations were taken in *Spitzer*'s mapping mode. When we realized that the staring mode can also be used to create spectral maps and offers additional tools for point sources, we switched to staring mode for the remaining targets.

4.5.2 Spectral extraction

After applying the *Spitzer* package IRSCLEAN v1.7 to remove rogue pixels, we used the spectral extraction tool CUBISM v1.7 (Smith et al. 2007a) to assemble the spectral maps and prepare the IRS spectra. Using CUBISM, we removed background light, the noisy margins in the cross-dispersion direction, and additional rogue pixels. CUBISM is designed to extract IRS spectral maps of extended targets, but can handle spectra of point sources as well.

We evaluated the spatial extent of each target by combining all wavelengths in the SL1 module into a single map and measuring the light profile along the slit, and repeating the process for the LL2 (these two modules suffer from the least noise). While most of our targets are intermediate between true point sources and uniform extended sources, we used these light profiles to determine that four are point sources (Hydra A, PKS 0745-19, Abell 1068, and Abell 1835), and the other five are best treated as extended sources. The physical sizes of the sources range from 5 kpc (the FWHM of Hydra A in the SL1) to 50 kpc (the FWHM of Abell 1835 in the LL2).

While software packages designed for IRS point sources exist, such as SMART (Higdon et al. 2004), in the interest of consistency we used CUBISM to extract all of our spectra. However, to check our method, we also extracted the point source spectra using SMART, finding agreement within 10%, and 2% in the best cases.

In order to obtain a true spectrum of a point source from CUBISM, the user may turn off the option to remove the "slit loss correction factor" (SLCF), and select a slit-shaped aperture only two pixels wide but as long as necessary to capture most of the target's light at that wavelength. Using CUBISM's feature to remove the SLCF for extended sources, we chose apertures which covered most of the target's light while maintaining good signal-to-noise. Because our slits did not densely cover the core emission area, we could not capture all of the emission in a given aperture.

After spectral extraction, we trimmed the noisy edges of each spectral module. In our notation, $\mathrm{f}_\nu(\lambda_{\mathrm{obs}})$ is the observer-frame flux observed at the given wavelength, and for a redshift of z, $\mathrm{F}_\nu(\lambda_{\mathrm{rest}})$ is the rest-frame flux emitted at the given wavelength. They are related as follows:

$$\mathrm{F}_\nu(\lambda_{\mathrm{rest}}) = \frac{\mathrm{f}_\nu(\lambda_{\mathrm{obs}}/(1+\mathrm{z}))}{1+z} \tag{4.1}$$

In other words, we convert to the rest frame by dividing both wavelength and flux by a factor of $(1 + z)$.

4.5.3 IRS photometric levels

To address the photometric shortfall for extended sources, and to correct gaps between the four modules in both point and extended sources (which can appear even when using SMART to extract point source spectra, and are caused in part by the larger LL pixels which make it impossible to extract SL and LL spectra from identical apertures), we used IRAC and MIPS broadband photometry, where available (see §4.5.4), as a guide in scaling the modules of our IRS spectra. The scaling is detailed in Donahue et al. (2011, Table 3). Therefore, the effective aperture of our IRS observations is equal to that of the nearest-wavelength IRAC or MIPS observation (see Table 4.3). In physical units, these apertures correspond to $\sim 8 - 70$ kpc for the SL modules, and $\sim 20 - 120$ kpc for the LL modules. This assumes that the spectral shape is the same across the various source regions.

For extended sources, we attempted to make the scaling process partially independent of the IRAC and MIPS photometry (because we do not have full photometry coverage of our sample) by measuring the light profile along the slit and estimating the scale factor assuming an azimuthally symmetric emission profile. The SL and LL were treated separately, and after this scaling, any discrepancies between the two were generally resolved. Because of the sparse nature of our spectral maps, this scale factor is the dominant part of the overall scale factor for each module, and is required only for extended sources (because the SLCF provides the same function for the point sources).

Additional corrections, generally small, were required in some cases for both point and extended sources to correct gaps between modules (sometimes caused by the necessity of selecting a smaller aperture for one module because of a nearby source of contamination) or to bring the overall spectrum into agreement with the IRAC and MIPS SED. Agreement between the final rest-frame IRS spectra and the rest-frame broadband photometry is within $\sim 15\%$ (see Figs. 4.4 - 4.6 and the discussion in §4.5.7, and compare Tables 4.8 and 4.3).

We acknowledge the risks of the assumptions of this scaling. The continuum light is relatively smooth, as seen in the light profile along the slit, but it may not be azimuthally symmetric, and it may not have a uniform SED everywhere in the IRAC and MIPS apertures. The interested reader may recover the emission in the original IRS aperture by dividing by the relevant scale factor listed in Donahue et al. (2011, Table 2).

4.5.4 Broadband photometry

The IRAC and MIPS apertures were chosen to be approximately three times the FWHM of the source as measured with the IRS spectra. We based the IRAC apertures on the FWHM measured in the SL1, the MIPS 24 μm apertures on the FWHM in the LL2, and the MIPS 70 and 160 μm apertures on the FWHM of a point source at those wavelengths. For more discussion of aperture selection, see §4.4.3. Background is subtracted from a larger annulus. The aperture corrections are described in Donahue et al. (2011). Rest-frame IRAC and MIPS photometry is reported in Table 4.3; it was obtained by dividing the observed flux densities by a factor of $1 + z$. These values are not k-corrected; therefore, this is the rest-frame emission which is observed at the listed wavelengths, rather than emitted at those wavelengths.

4.5.5 Uncertainty

The uncertainties for the IRS spectra are a combination of the uncertainties provided by the *Spitzer* pipeline (hereafter termed "statistical uncertainty") and a 15% systematic uncertainty to account for scaling the IRS spectra relative to the broadband photometry. The systematic uncertainty typically dominates in the case of strong emission features and elevated continuum.

The uncertainties for the broadband photometry are 5% for IRAC and 10, 20, and 20% for MIPS24, 70, and 160 μm respectively.

When comparing *Spitzer* data to data from other telescopes, we include an additional 5% absolute photometric uncertainty.

The median signal-to-noise for our extracted spectra in the SL modules (bins of width 0.028 μm) and LL modules (bins of width 0.056 μm) is 16 and 6.3, respectively. Signal-to-noise is considerably higher for the strong emission features and for broadband measures of the continuum.

Features and continuum which are not detected with 3σ confidence are instead reported as 3σ upper limits (which are then combined with the systematic uncertainty mentioned above) or left out of the discussion.

A potential source of error which we have not accounted for is the assumption that the source is centered in the IRS slit. Small pointing errors cause the light to be lost asymmetrically from the slit in a wavelength-dependent manner. We minimize this effect by assuming that the photometric levels of the LL modules are more accurate than the SL modules, because any pointing error is smaller relative to the large size of the LL pixels, and by using broadband photometry as a photometric guide as discussed above. However, any pointing errors may introduce small differences in the shape of the spectrum (private discussion, J. Leisenring).

4.5.6 Feature strength extraction

To extract feature strengths, we applied the spectral-decomposition package PAHFIT v1.2 (Smith et al. 2007b), which empirically fits the following components: a starlight continuum, several thermal dust continuum components, broad silicate absorption features, broad PAH emission complexes, and unresolved emission lines (mainly low-ionization forbidden atomic emission and molecular hydrogen emission).

The observed fluxes are reproduced in Table 4.4. A subset of these data, in the rest frame, appear in Donahue et al. (2011, Table 5), or Table 3.5. The central rest wavelength of each feature is reported in the second column. Uncertainties are 1σ, and represent a combination of the empirical uncertainties found by PAHFIT (based on the statistical uncertainties provided by the *Spitzer* pipeline) and the photometric uncertainty. The uncertainties are at least 15%, as mentioned above, and frequently higher. Upper limits are 3σ. In cases where PAHFIT was unable to determine an upper limit, typically in cases of very weak features, lower signal-to-noise, or a problematic juncture between spectrum modules, the failed fit is represented with an ellipsis (...).

The equivalent widths (EQW) of the same features, in μm, are listed in Table 4.6. Features with failed fits, those beyond the wavelength range for the target, or those with only an upper limit to the flux are represented with ellipses. In principle an upper limit to the EQW could be found in the case of the latter examples, but the uncertainties on feature flux and continuum are too compounded to give meaningful results. The uncertainties for EQW are based on the uncertainty in the feature strength and the uncertainty in the local continuum level, and are somewhat overestimated because the same statistical uncertainties are used to estimate both. Upper limits are 3σ and can be extremely high in cases of very low continuum level, notably for the H_2 S(1) feature for MS0735 and A2597.

Integrated feature luminosities, in rest-frame units of 10^{41} erg s^{-1}, are presented in Table 4.7, in the same format as Table 4.4. To recover the observed luminosity, multiply by $(1 + z)$.

Weak unresolved emission lines

We attempted to fit an inclusive set of emission features with PAHFIT, but not all appeared in our sample in sufficient strength to achieve well-determined fluxes. The high-ionization [Ne V] features at 14.3 and 24.3 μm are weak (particularly the 24.3 μm line), but are of sufficient interest that they are reported in the table. The upper limits to the [Ne V] feature at 14.3 μm for 2A0335 and A1068 appear to be affected by an unknown feature at 14.65 μm. [S IV] 10.5 μm only has one potentially firm detection in our sample, in Hydra A, but the upper limits may still be of interest. Similarly, the H_2 (S0) emission line at 28.2 μm is not detected with significance in any of our targets, but is important enough in the study of the pure rotational series that we included the upper limits.

The emission lines of [O IV]25.9 μm (a hallmark of AGN activity) and [Fe II]26.0 μm are not resolved by the *Spitzer* low-resolution spectrograph, nor can we universally conclude that one is more likely to dominate the other in these BCGs. PAHFIT attempts to fit them separately, and in the case of our sample, typically finds that the centroid favors [Fe II]. This is not conclusive, however. We present the combined line fluxes in Table 4.4. The complex is securely detected in two targets.

Meanwhile, the [Ar III]8.99 μm was also not significantly detected. We exclude it from Table 4.4, but note that its maximum strength appears in PKS0745, where its upper limit is 50% the flux of the [Ar II]6.99 μm line, in the case of PKS0745.

Polycyclic aromatic hydrocarbons

The fluxes of the major PAH emission bands are reported in Table 4.4. The complex suite of PAH features is described in detail in Smith et al. (2007b). See §4.7.3 for discussion of the background and importance of these large molecules. The PAH features between 7.3 and 7.9 μm are combined into a single complex reported at 7.7 μm, as are the pair of features near 11.3 μm and another pair near 12.6 μm. All of the PAH features between 16.4 and 17.9 μm are combined into one complex reported at 17.0 μm, though the reader should note that because of the extremely low, broad nature of this complex, the larger uncertainties in the LL module, and the difficulty in pinning down the exact continuum level, this detection should be regarded with caution. We assign an uncertainty of 30% to this complex, and 50% in the case of PKS0745.

Smith et al. (2007b) have discussed the systematic difference in PAH strengths as measured by PAHFIT and by other methods. While other methods vary, they are typically based on selecting two or more points flanking a PAH feature, assuming that the continuum level passes through those points, and fitting a spline between them to determine the continuum level beneath the PAH. This assumption is frequently not valid, particularly for the unisolated PAHs near 8 μm, where the broad wings of the PAH features can easily blend into each other. Non-PAHFIT estimates of PAH strength often set the local continuum level at a point which realistically has significant contribution from the PAH feature itself.

On the other hand, PAHFIT uses a more physical (though still empirical) estimate of the continuum strength, by combining a series of blackbody curves to represent thermal dust emission at a variety of temperatures. Compared to other methods, PAHFIT tends to estimate a lower continuum and a higher feature flux for PAHs.

Examination of star-forming spectra near 8 μm (Smith et al. 2007b; Donahue et al. 2011) demonstrates that the PAHFIT assumptions are more reliable than methods that fix a local continuum around each PAH feature. (For unresolved emission lines, including the atomic and H_2 features, the choice of fitting algorithm will make little difference.)

Smith et al. (2007b) have also attempted to characterize the offset between PAHFIT and other methods, in their Table 6. Several important datasets and calibrations are not based on PAHFIT methods, so we are interested in converting results based on other methods to PAHFIT equivalents. Such conversions are extremely rough (Smith et al. 2007b). While they may be applied to samples in general, the conversion is unlikely to hold up under individual examination. Therefore, when we apply such a conversion in order to compare other datasets to our sample, we are careful to not rest our conclusions upon it.

Major PAH complexes in these targets are analyzed in detail in Donahue et al. (2011).

The observed fluxes of the minor PAH features are relegated to Table 4.5. There are only a handful of well-determined fits among them. Each of those was manually verified and found to be convincing, though it is likely that the statistical PAHFIT uncertainties (even after combination with the photometric uncertainty) are underestimated. For example, the 8.33 μm feature in A1835 is flanked by much stronger features at 7.7 and 8.6 μm, rendering its fit necessarily uncertain. Most of the minor PAH features are fit with only upper limits, if at all. A fit to the PAH at 33.1 μm was not attempted.

4.5.7 Continuum Strength Extraction

Table 4.8 lists various measures of continuum strength drawn from the rest-frame IRS spectrum.

The first three rows give the average rest-frame flux density in 1 μm wide bins at the given rest wavelengths, for only the continuum components of PAHFIT (stellar light, thermal dust emission, and silicate absorption). The difference between the continuum-only spectrum and the full spectrum is negligible at 24 μm (see below), but can be considerable at 6 μm, where PAH emission bands can be very strong compared to the continuum.

The next three rows give each spectrum's average rest-frame flux density weighted by the bandpasses corresponding to the IRAC and MIPS bandpasses observed at 5.8, 8, and 24 μm. For example, $F_{\nu \frac{24}{1+z}}$ yields the average flux density in the bandpass centered on a rest wavelength of $\frac{24}{1+z}$, or ~ 19 μm for A1835. These fluxes appear in Figs. 4.4-4.6 as green diamonds. They are suitable for comparison to actual IRAC and MIPS observations, reported in Table 4.3 (note that the broadband photometry reported there has been corrected to the rest frame by a factor of $\frac{1}{1+z}$, but has not been k-corrected). Where the IRAC and MIPS photometry is present, the IRS photometry is typically within 15% agreement. The instances where the fractional disagreement is greater are typically cases of low signal-to-noise, and the absolute difference between the fluxes is low. The only instance where the IRS differs by more than 0.4 mJy from the IRAC or MIPS value is for 2A0335 at an observed wavelength of 8 μm. In this case, the IRAC observation should be regarded as more reliable than the corresponding IRS value, because the IRS signal is affected by the SL1/SL2 interface in that spectrum (see Fig. 4.4 and §4.6.2).

The last four rows of Table 4.8 report the rest-frame IRS flux density or luminosity averaged across the same IRAC and MIPS bandpasses, using rest wavelengths. For example, F_ν 24 represents the average flux density of the source emitted in the MIPS24 bandpass. νL_ν 24 is the luminosity in the same bandpass. These flux densities and luminosities, are applicable for relations that are calibrated in the local universe where redshift has little impact, such as estimates of star formation rate based on the 24 μm continuum like Rieke et al. (2009, Eq. 10, 11) or Calzetti et al. (2010, Eq. 17).

Note the good agreement between $F_{\nu,c}$ 24 and F_ν 24, indicating that the thermal dust components as fitted by PAHFIT are responsible for virtually all emission near 24 μm. A comparison between $F_{\nu,c}$ 6 and F_ν 5.8 demonstrates that the same is certainly not true at the short-wavelength end of the MIR spectrum.

Table 4.3. Rest-frame Broadband Photometry

Band	2A0335	Hydra A	A1795	A2597	A0478	PKS0745	A1068	MS0735	A1835
3.6	8.9 [12]			4.2 [20]	3.9 [20]	2.7 [14]	1.8 [10]	1.2 [20]	2.0 [14]
4.5	5.4 [12]	2.7 [14]		2.7 [20]	2.6 [20]	1.9 [14]	1.8 [10]	0.82 [20]	1.6 [14]
5.8	4.3 [12]			1.7 [20]	1.8 [20]	1.5 [14]	2.4 [10]	0.58 [20]	1.0 [14]
8.0	3.4 [12]	3.9 [14]		1.8 [20]	1.6 [20]	2.1 [14]	6.6 [10]	0.33 [20]	3.6 [14]
24	2.3 [26]	8.6 [30]	1.7 [40]	1.9 [50]	1.5 [30]	9.2 [30]	66 [30]		14 [30]
70	75 [70]	150 [70]	35 [70]	82 [70]	58 [70]	140 [70]	790 [70]		140 [70]
160		170 [80]		39 [80]	52 [80]				250 [80]

Note. — IRAC and MIPS observed waveband centers are in units of μm. Rest-frame fluxes are in units of mJy, and aperture diameters in arcseconds are given in brackets. Photometric uncertainties are $\sim 5\%$ for IRAC and, for MIPS, 10, 20, 20% for 24, 70, and 160 μm respectively.

Table 4.4. Observed line fluxes (10^{-18} W m^{-2}).

Feature	Rest μm	2A0335	Hydra A	A1795	A2597	A0478	PKS0745	A1068	MS0735	A1835
[Fe II]	5.34	10.2 ± 2.0	< 5.00	5.41 ± 1.38	18.6 ± 3.9	8.31 ± 1.93	35.2 ± 5.4	7.26 ± 1.65	< 2.21	< 6.83
H_2 S(7)	5.51	18.7 ± 3.0	< 4.84	7.31 ± 1.80	22.2 ± 4.9	17.3 ± 2.9	21.3 ± 3.5	12.7 ± 2.3	< 3.08	< 6.78
H_2 S(6)	6.11	14.9 ± 2.4	...	4.90 ± 1.52	14.4 ± 4.0	< 4.48	10.9 ± 2.2	< 4.82	< 1.75	< 7.29
PAH	6.22	23.1 ± 4.7	47.0 ± 8.4	13.4 ± 4.3	< 29.3	< 11.2	27.2 ± 5.4	95.9 ± 15.2	< 3.41	$199. \pm 30.$
H_2 S(5)	6.91	18.7 ± 3.7	6.30 ± 2.09	13.8 ± 2.8	44.9 ± 7.4	14.8 ± 2.4	28.7 ± 4.4	24.8 ± 4.0	< 3.58	15.9 ± 2.6
[Ar II]	6.99	< 15.6	5.96 ± 1.78	7.10 ± 1.87	17.7 ± 3.9	8.86 ± 1.72	9.99 ± 1.69	17.9 ± 3.2	< 22.4	12.1 ± 2.0
PAH	7.70	...	$187. \pm 31.$	29.9 ± 10.4	45.8 ± 16.7	28.7 ± 7.7	50.5 ± 8.6	$342. \pm 52.$	< 6.08	666.
H_2 S(4)	8.03	13.5 ± 2.2	< 9.16	7.00 ± 1.27	21.7 ± 3.6	10.5 ± 1.7	9.94 ± 1.65	< 9.99	1.56 ± 0.28	< 2.39
PAH	8.61	4.56 ± 1.28	35.4 ± 6.1	< 6.30	< 13.8	...	...	40.6 ± 6.7	1.90 ± 0.53	$114. \pm 17.$
H_2 S(3)	9.67	42.2 ± 6.4	11.3 ± 2.1	23.2 ± 4.2	60.4 ± 9.1	30.2 ± 4.6	29.8 ± 4.5	31.8 ± 4.9	4.54 ± 0.69	12.1 ± 2.0
[S IV]	10.5	< 2.82	2.30 ± 0.71	< 1.43	...	< 1.27	< 2.86	< 6.11	< 0.433	< 5.72
PAH	11.3	32.3 ± 4.9	87.7 ± 13.4	23.5 ± 3.7	17.8 ± 4.2	18.8 ± 3.1	49.5 ± 7.5	$104. \pm 16.$	5.58 ± 0.91	$165. \pm 25.$
PAH	12.0	10.5 ± 1.9	16.9 ± 3.8	< 6.86	< 12.6	< 5.75	24.0 ± 3.8	...	< 1.87	< 25.1
H_2 S(2)	12.3	14.1 ± 2.1	4.21 ± 1.28	6.78 ± 1.07	15.7 ± 2.5	7.57 ± 1.22	10.7 ± 1.6	12.4 ± 2.0	1.32 ± 0.33	6.40 ± 2.19
PAH	12.7	19.5 ± 3.2	34.9 ± 6.1	10.1 ± 2.3	19.5 ± 4.8	12.7 ± 2.5	47.2 ± 7.2	18.6 ± 4.3	< 1.27	$112. \pm 18.$
[Ne II]	12.8	18.3 ± 2.8	25.9 ± 3.9	13.8 ± 2.1	25.1 ± 3.9	18.9 ± 2.9	42.9 ± 6.4	53.3 ± 8.4	1.15 ± 0.27	32.6 ± 6.7
[Ne V]	14.3	< 5.77	5.46 ± 1.30	< 3.69	...	< 2.10	< 1.09	< 12.6	...	8.72 ± 2.90
[Ne III]	15.6	12.0 ± 1.9	23.0 ± 3.7	5.99 ± 1.15	23.2 ± 3.9	8.89 ± 1.50	15.8 ± 2.4	32.2 ± 5.1	< 0.715	19.9 ± 3.9
PAH	17.0	33.1 ± 9.9	43.7 ± 13.1	< 33.0	< 59.7	< 18.1	27.6 ± 13.8	$292. \pm 88.$	< 1.24	< 52.3
H_2 S(1)	17.1	40.0 ± 6.1	11.0 ± 2.7	19.2 ± 3.1	52.9 ± 8.2	18.3 ± 2.8	26.0 ± 3.9	< 25.4	2.23 ± 0.44	< 16.5
[S III]	18.7	2.32 ± 0.70	15.5 ± 2.8	3.62 ± 1.13	12.5 ± 3.5	< 5.74	5.32 ± 1.00	10.7 ± 2.8	0.840 ± 0.176	< 9.87
[Ne V]	24.3	< 2.17	...	...	...	...	< 1.82	< 15.3	...	...
[O IV]+[Fe II]	26.0	< 4.69	9.42 ± 1.49	< 4.48	< 6.60	< 3.15	9.44 ± 1.43	< 6.95	...	< 12.0
H_2 S(0)	28.2	...	< 1.97	< 3.30	< 2.97	...	< 3.81	...	< 1.10	...
[S III]	33.5	5.56 ± 1.22	6.67 ± 1.42	6.34 ± 1.64	0.905	< 3.23	14.7 ± 2.4	...	...	...
[Si II]	34.8	32.7 ± 5.1	22.8 ± 3.7	20.5 ± 3.6	...	...	...	...	...	...

Uncertainties are 1σ. If not given, they are 15%. Upper limits are 3σ. An ellipsis represents a failed fit. Machine-readable version available in the published journal paper based on this work.

Table 4.5. Minor PAH features: observed line fluxes (10^{-18} W m^{-2}).

Center (rest μm)	2A0335	Hydra A	A1795	A2597	A0478	PKS0745	A1068	MS0735	A1835
5.27	< 88.6	< 19.5	...	< 39.3	25.9 ± 6.6	...	20.6 ± 5.4	< 6.84	< 22.8
5.70	< 65.9	< 15.8	< 12.0	...	31.0 ± 5.9	...	< 60.3	< 6.99	< 27.5
6.69	...	< 32.3	< 25.1	...	...	...	$< 101.$	...	< 88.9
8.33	...	< 19.4	...	...	< 6.81	...	< 16.1	< 2.15	70.6 ± 11.0
10.7	< 1.98	...	...	< 5.84	...	< 7.80	...	< 2.50	< 5.42
13.5	7.97 ± 1.45	< 9.81	< 5.69	< 13.0	< 6.58	< 5.44	...	...	...
14.0	...	< 8.52	...	...	...	...	...	< 2.27	< 15.4
14.2	...	...	< 9.36	...	< 12.5	...	< 16.1	< 2.84	...
15.9	...	< 9.04	< 6.41	< 12.9	< 11.1	< 2.81	< 37.6	...	...
18.9	...	...	< 8.28	...	< 6.11	< 15.9	< 43.8	...	...

Uncertainties are 1σ. Upper limits are 3σ. An ellipsis represents a failed fit. Machine-readable version available in the published journal paper based on this work.

Table 4.6. Observed feature equivalent widths (μm).

Feature	Rest μm	2A0335	Hydra A	A1795	A2597	A0478	PKS0745	A1068	MS0735	A1835
[Fe II]	5.34	0.033 ± 0.007	...	0.030 ± 0.008	0.17 ± 0.04	0.056 ± 0.013	0.31 ± 0.05	0.031 ± 0.007	...	...
H_2 S(7)	5.51	0.066 ± 0.011	...	0.044 ± 0.011	0.21 ± 0.05	0.13 ± 0.02	0.19 ± 0.03	0.056 ± 0.011	...	...
H_2 S(6)	6.11	0.070 ± 0.012	...	0.039 ± 0.012	0.16 ± 0.05	...	0.10 ± 0.02	...	...	...
PAH	6.22	0.077 ± 0.016	0.17 ± 0.03	0.075 ± 0.024	...	...	0.17 ± 0.04	0.28 ± 0.05	...	1.3 ± 0.2
H_2 S(5)	6.91	0.12 ± 0.03	< 0.041	0.15 ± 0.03	0.61 ± 0.13	0.22 ± 0.04	0.29 ± 0.05	0.094 ± 0.016	...	0.17 ± 0.03
[Ar II]	6.99	...	0.040 ± 0.012	0.078 ± 0.021	0.24 ± 0.06	0.14 ± 0.03	0.10 ± 0.02	0.066 ± 0.012	...	0.13 ± 0.02
PAH	7.70	...	0.98 ± 0.17	< 0.30	< 0.54	0.37 ± 0.10	0.38 ± 0.07	0.75 ± 0.12	...	5.0 ± 0.8
H_2 S(4)	8.03	0.13 ± 0.02	...	0.11 ± 0.02	0.37 ± 0.07	0.23 ± 0.04	0.12 ± 0.02	...	0.13 ± 0.02	...
PAH	8.61	0.036 ± 0.010	0.24 ± 0.04	...	...	...	...	0.083 ± 0.014	0.14 ± 0.04	0.90 ± 0.14
H_2 S(3)	9.67	0.68 ± 0.11	0.16 ± 0.03	0.66 ± 0.12	1.5 ± 0.2	1.2 ± 0.2	0.48 ± 0.08	0.11 ± 0.02	0.77 ± 0.13	0.14 ± 0.02
[S IV]	10.5	...	0.032 ± 0.010	...	...	...	...	...	...	...
PAH	11.3	0.56 ± 0.09	0.83 ± 0.13	0.63 ± 0.10	0.44 ± 0.11	0.79 ± 0.14	0.70 ± 0.11	0.19 ± 0.03	1.2 ± 0.2	1.3 ± 0.2
PAH	12.0	0.21 ± 0.04	0.16 ± 0.04	...	...	...	0.36 ± 0.06	...	...	...
H_2 S(2)	12.3	0.45 ± 0.07	0.058 ± 0.018	0.32 ± 0.05	0.70 ± 0.13	0.60 ± 0.11	0.24 ± 0.04	0.030 ± 0.005	0.57 ± 0.18	< 0.072
PAH	12.7	0.45 ± 0.08	0.33 ± 0.06	0.34 ± 0.08	0.63 ± 0.17	0.74 ± 0.16	0.74 ± 0.12	0.030 ± 0.007	...	0.81 ± 0.14
[Ne II]	12.8	0.65 ± 0.11	0.36 ± 0.06	0.71 ± 0.11	1.2 ± 0.2	1.7 ± 0.3	1.00 ± 0.16	0.13 ± 0.02	< 0.59	0.34 ± 0.07
[Ne V]	14.3	...	0.083 ± 0.020	...	...	...	...	...	...	< 0.089
[Ne III]	15.6	0.64 ± 0.11	0.38 ± 0.06	0.43 ± 0.10	1.6 ± 0.5	1.3 ± 0.3	0.33 ± 0.05	0.074 ± 0.012	...	0.19 ± 0.04
PAH	17.0	1.3 ± 0.4	0.53 ± 0.16	...	...	...	< 0.53	0.46 ± 0.14	...	...
H_2 S(1)	17.1	2.3 ± 0.4	0.20 ± 0.05	1.5 ± 0.3	3.8 ± 1.2	3.0 ± 0.8	0.49 ± 0.08	...	< 8.6	...
[S III]	18.7	0.15 ± 0.05	0.31 ± 0.06	< 0.30	< 1.1	...	0.091 ± 0.018	0.024 ± 0.006	< 5.0	...
[Ne V]	24.3	...	...	...	...	...	...	...	...	...
[O IV]+[Fe II]	26.0	...	0.20 ± 0.03	...	...	...	0.14 ± 0.02	...	...	...
H_2 S(0)	28.2	...	...	...	...	...	...	...	...	...
[S III]	33.5	0.58 ± 0.15	0.13 ± 0.03	< 0.97	0.091 ± 0.028	...	0.21 ± 0.04	...	...	...
[Si II]	34.8	3.6 ± 1.0	0.42 ± 0.07	< 4.1	...	...	...	...	...	...

Uncertainties are 1σ. Upper limits are 3σ. An ellipsis represents a feature with an undetermined flux level. Machine-readable version available in the published journal paper based on this work.

Table 4.7. Rest-frame line luminosities (10^{41} erg s^{-1}).

Feature	Rest μm	2A0335	Hydra A	A1795	A2597	A0478	PKS0745	A1068	MS0735	A1835
[Fe II]	5.34	0.275 ± 0.056	< 0.359	0.491 ± 0.133	2.87 ± 0.65	1.41 ± 0.36	8.58 ± 1.45	3.27 ± 0.85	< 3.02	< 13.2
H_2 S(7)	5.51	0.504 ± 0.084	< 0.347	0.664 ± 0.174	3.42 ± 0.82	2.93 ± 0.53	5.19 ± 0.94	5.71 ± 1.18	< 4.21	< 13.1
H_2 S(6)	6.11	0.401 ± 0.067	...	0.445 ± 0.147	2.22 ± 0.67	< 0.824	2.66 ± 0.59	< 2.47	< 2.39	< 14.1
PAH	6.22	0.622 ± 0.131	3.19 ± 0.60	1.22 ± 0.42	< 4.89	< 2.06	6.63 ± 1.45	43.1 ± 7.8	< 4.66	$308. \pm 58.$
H_2 S(5)	6.91	0.504 ± 0.103	0.428 ± 0.150	1.25 ± 0.27	6.92 ± 1.23	2.51 ± 0.44	7.00 ± 1.18	11.2 ± 2.0	< 4.89	24.6 ± 5.0
[Ar II]	6.99	< 0.435	0.405 ± 0.128	0.645 ± 0.181	2.73 ± 0.65	1.50 ± 0.32	2.44 ± 0.45	8.05 ± 1.64	< 30.6	18.7 ± 3.9
PAH	7.70	...	12.7 ± 2.2	2.72 ± 1.00	7.06 ± 2.78	4.86 ± 1.42	12.3 ± 2.3	$154. \pm 27.$	< 8.30	$1029. \pm 193.$
H_2 S(4)	8.03	0.364 ± 0.061	< 0.657	0.636 ± 0.123	3.34 ± 0.60	1.78 ± 0.31	2.42 ± 0.44	< 5.12	1.75 ± 0.38	< 4.62
PAH	8.61	0.123 ± 0.036	2.41 ± 0.44	< 0.608	< 2.30	...	...	18.3 ± 3.4	2.13 ± 0.72	$176. \pm 33.$
H_2 S(3)	9.67	1.14 ± 0.18	0.768 ± 0.151	2.11 ± 0.41	9.31 ± 1.52	5.12 ± 0.85	7.27 ± 1.21	14.3 ± 2.5	5.10 ± 0.94	18.7 ± 3.9
[S IV]	10.5	< 0.0786	0.156 ± 0.051	< 0.138	...	< 0.234	< 0.769	< 3.13	< 0.591	< 11.1
PAH	11.3	0.870 ± 0.137	5.96 ± 0.96	2.13 ± 0.36	2.74 ± 0.70	3.18 ± 0.57	12.1 ± 2.0	46.8 ± 8.2	6.27 ± 1.24	$255. \pm 48.$
PAH	12.0	0.283 ± 0.053	1.15 ± 0.27	< 0.662	< 2.10	< 1.06	5.85 ± 1.02	...	< 2.55	< 48.6
H_2 S(2)	12.3	0.380 ± 0.059	0.286 ± 0.092	0.616 ± 0.103	2.42 ± 0.42	1.28 ± 0.22	2.61 ± 0.43	5.58 ± 1.02	1.48 ± 0.45	9.89 ± 4.24
PAH	12.7	0.525 ± 0.089	2.37 ± 0.44	0.917 ± 0.222	3.00 ± 0.80	2.15 ± 0.46	11.5 ± 1.9	8.37 ± 2.20	< 1.73	$173. \pm 35.$
[Ne II]	12.8	0.493 ± 0.078	1.76 ± 0.28	1.25 ± 0.20	3.87 ± 0.65	3.20 ± 0.53	10.5 ± 1.7	24.0 ± 4.3	1.29 ± 0.37	50.4 ± 13.0
[Ne V]	14.3	< 0.161	0.371 ± 0.093	< 0.356	...	< 0.386	< 0.293	< 6.45	...	13.5 ± 5.6
[Ne III]	15.6	0.323 ± 0.053	1.56 ± 0.27	0.544 ± 0.111	3.57 ± 0.65	1.51 ± 0.28	3.85 ± 0.65	14.5 ± 2.6	< 0.976	30.8 ± 7.5
PAH	17.0	0.891 ± 0.276	2.97 ± 0.94	< 3.19	< 9.95	< 3.33	6.73 ± 3.71	$131. \pm 45.$	< 1.69	$< 101.$
H_2 S(1)	17.1	1.08 ± 0.17	0.748 ± 0.194	1.74 ± 0.30	8.15 ± 1.37	3.10 ± 0.52	6.34 ± 1.05	< 13.0	2.50 ± 0.60	< 31.9
[S III]	18.7	0.0625 ± 0.0195	1.05 ± 0.20	0.329 ± 0.109	1.93 ± 0.58	< 1.06	1.30 ± 0.27	4.81 ± 1.43	0.943 ± 0.240	< 19.1
[Ne V]	24.3	< 0.0605	...	...	...	...	< 0.489	< 7.84	...	...
[O IV]+[Fe II]	26.0	< 0.131	0.640 ± 0.107	< 0.433	< 1.10	< 0.579	2.30 ± 0.38	< 3.56	...	< 23.2
H_2 S(0)	28.2	...	< 0.141	< 0.319	< 0.495	...	< 1.02	...	< 1.50	...
[S III]	33.5	0.150 ± 0.034	0.453 ± 0.102	0.576 ± 0.158	0.139 ± 0.023	< 0.594	3.58 ± 0.65	...	...	...
[Si II]	34.8	0.881 ± 0.142	1.55 ± 0.27	1.86 ± 0.35	...	...	...	...	...	...
[Fe II]	5.34	0.275 ± 0.056	< 0.359	0.491 ± 0.133	2.87 ± 0.65	1.41 ± 0.36	8.58 ± 1.45	3.27 ± 0.85	< 3.02	< 13.2

Uncertainties are 1σ. If not given, they are 15%. Upper limits are 3σ. An ellipsis represents a failed fit. Machine-readable version available in the published journal paper based on this work.

Table 4.8. IRS-based continuum measurements

	2A0335	Hydra A	A1795	A2597	A0478	PKS0745	A1068	MS0735	A1835
$F_{\nu,c}$ 6[a]	2.6 ± 0.4	2.2 ± 0.3	1.5 ± 0.2	1.0 ± 0.2	1.1 ± 0.2	1.2 ± 0.2	2.2 ± 0.3	0.36 ± 0.06	0.99 ± 0.17
$F_{\nu,c}$ 15[a]	1.5 ± 0.2	4.5 ± 0.7	1.0 ± 0.2	1.1 ± 0.3	0.52 ± 0.13	3.1 ± 0.5	$28. \pm 4.$	< 0.10	6.1 ± 1.0
$F_{\nu,c}$ 24[a]	2.5 ± 0.4	8.8 ± 1.3	2.1 ± 0.4	2.5 ± 0.5	0.74 ± 0.16	$11. \pm 2.$	$92. \pm 14.$	< 0.14	$25. \pm 4.$
$F_{\nu}\,\frac{5.8}{1+z}$[b]	4.0 ± 0.6	2.5 ± 0.4	1.7 ± 0.3	1.4 ± 0.2	1.9 ± 0.3	1.5 ± 0.2	2.4 ± 0.4	0.53 ± 0.08	0.89 ± 0.14
$F_{\nu}\,\frac{8}{1+z}$[b]	2.5 ± 0.4	4.1 ± 0.6	1.9 ± 0.3	2.0 ± 0.3	1.4 ± 0.2	2.2 ± 0.3	6.7 ± 1.0	0.41 ± 0.06	3.6 ± 0.5
$F_{\nu}\,\frac{24}{1+z}$[b]	2.6 ± 0.4	8.2 ± 1.2	2.0 ± 0.3	2.2 ± 0.4	1.0 ± 0.2	9.3 ± 1.4	$66. \pm 10.$	0.13 ± 0.03	$14. \pm 2.$
F_{ν} 5.8[b]	4.0 ± 0.6	2.8 ± 0.4	1.8 ± 0.3	1.6 ± 0.3	1.8 ± 0.3	1.7 ± 0.3	3.5 ± 0.5	0.47 ± 0.07	2.6 ± 0.4
F_{ν} 8[b]	2.4 ± 0.4	4.1 ± 0.6	1.8 ± 0.3	1.9 ± 0.3	1.3 ± 0.2	2.3 ± 0.3	8.4 ± 1.3	0.31 ± 0.05	6.7 ± 1.0
F_{ν} 24[b]	2.7 ± 0.4	9.0 ± 1.4	2.1 ± 0.3	2.6 ± 0.4	0.93 ± 0.15	$12. \pm 2.$	$91. \pm 14.$	< 0.049	$25. \pm 4.$
νL_{ν} 24[b]	9.4 ± 1.4	81 ± 13	25 ± 4	54 ± 8	21 ± 3	400 ± 70	5800 ± 900	< 8.4	6000 ± 1000

Uncertainties are 1σ. Upper limits are 3σ. Units of flux density are mJy; units of luminosity are 10^{41} erg s^{-1}. All are in the rest frame (divided by 1+z). A machine-readable transpose of this table is available in the published journal paper based on this work. (a) Averaged across 1 μm-wide bands, for continuum components only. (b) Weighted by the corresponding IRAC or MIPS response.

4.6 Mid-IR Spectra of Cool-Core BCGs

4.6.1 Catalog of Spectral Plots

The resulting rest-frame spectra for the nine BCGs are tabulated online, with a fragment available in Table 4.9 for guidance regarding form and content. Note that all spectra are included sequentially, distinguished by the BCG name in the first column, for ease of machine readability. Also note that the spectra are presented wavelength order, with the module number corresponding to each bin flagged in the final column. The modules overlap slightly in places.

The spectra are presented in Figs. 4.1 through 4.7. In the first set of figures, the region between 5 and 16 μm is plotted in linear flux-wavelength space, to focus on the most important region of the IRS spectra. The spectra are organized by redshift. The stronger and more significant unresolved features are labeled at the top of the plot, and major PAH bands are marked with bold black lines. Rest-frame flux intensities per unit wavelength are plotted with blue crosses, and the PAHFIT extraction with a bold black line. For a more detailed plot of the PAHFIT extraction, including statistical uncertainties on the data points, plots of the fits to individual features, and curves of silicate extinction in the two cases where it was detected by PAHFIT, see Donahue et al. (2011, Fig. 1), or Figs. 3.1 - 3.2. We include this version of the plot, with less details included, in this work for ease of reference.

In the second set of figures, Figures 4.4 through 4.6, the entire IRS spectrum is plotted along with the IRAC and MIPS broadband photometry, in the rest wavelength range (2.8 to 67 μm) corresponding to the observed IRAC and MIPS bands from 3.6 μm through 70 μm throughout the sample. To accommodate this broad range, both wavelength and intensity are plotted in logarithmic space. Note that for those IRS

Table 4.9. IRS spectra of BCGs.

BCG	Rest wavelength (μm)	Rest F_ν (mJy)	PAHFIT fit (mJy)	Module #
Hydra A	7.104	3.60 ± 0.39	3.21	1
Hydra A	7.134	3.33 ± 0.41	3.26	1
Hydra A	7.161	3.25 ± 0.27	3.32	2
Hydra A	7.163	3.11 ± 0.42	3.32	1
Hydra A	7.193	3.01 ± 0.44	3.39	1
Hydra A	7.220	3.11 ± 0.27	3.46	2
Hydra A	7.222	3.28 ± 0.49	3.46	1
Hydra A	7.279	3.52 ± 0.26	3.63	2
Hydra A	7.338	4.76 ± 0.24	3.84	2
Hydra A	7.397	3.99 ± 0.22	4.11	2

Uncertainties are statistical only. An empirical fit to the spectrum is given in the PAHFIT column. The IRS modules in which each bin appear are indexed as follows: SL2=1, SL1=2, LL2=3, LL1=4. The full table, including spectra of all nine BCGs, is available in the published journal paper based on this work. A portion is shown here for guidance regarding its form and content.

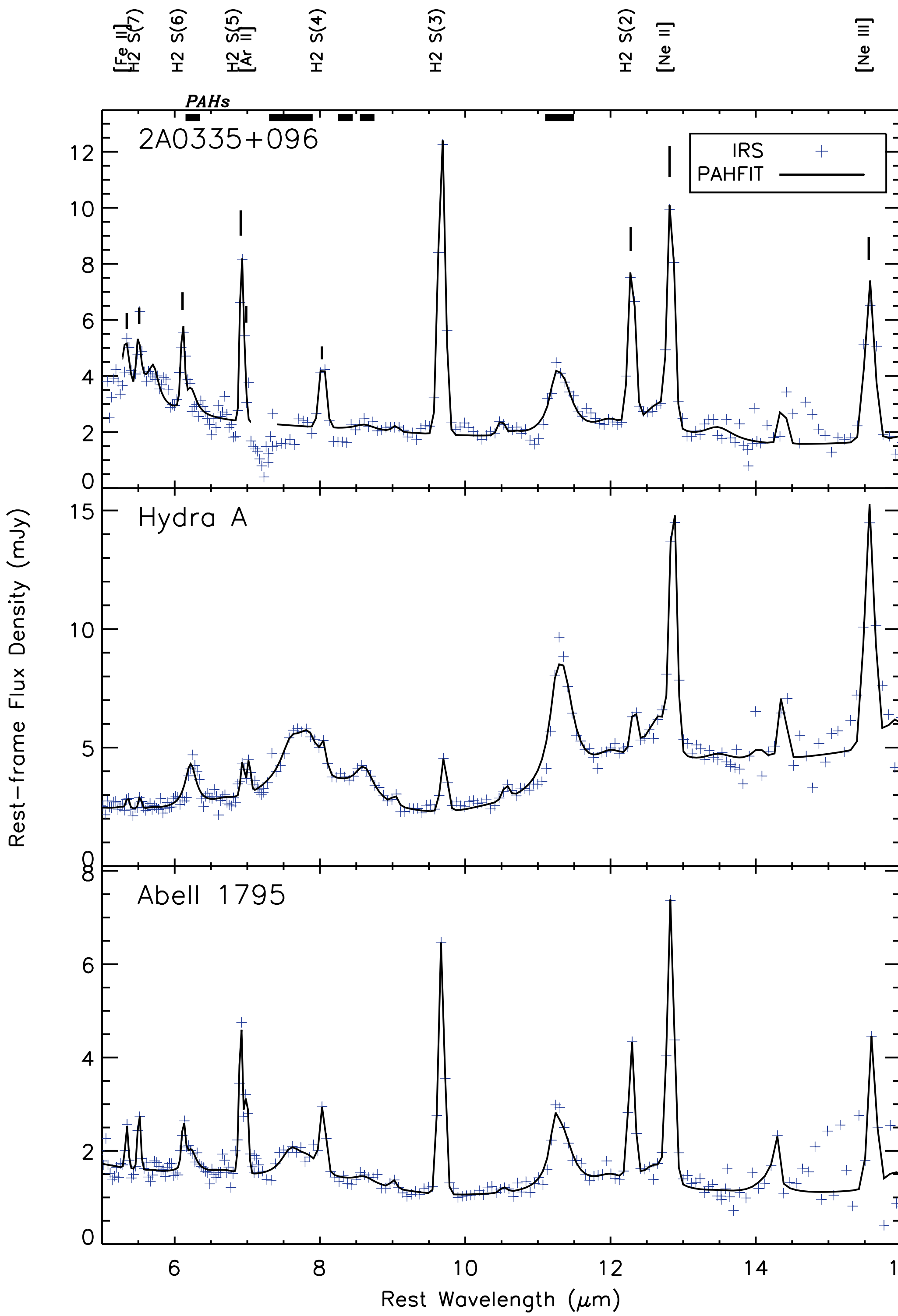

Fig. 4.1.— Rest-frame IRS spectra of the nine BCGs (blue crosses), in the wavelength range between 5 and 16 μm. Energy distributions are plotted in units of intensity per unit frequency (mJy). The PAHFIT extraction of the spectrum is represented with a solid black line. Unresolved emission lines and major PAH bands are identified at the top.

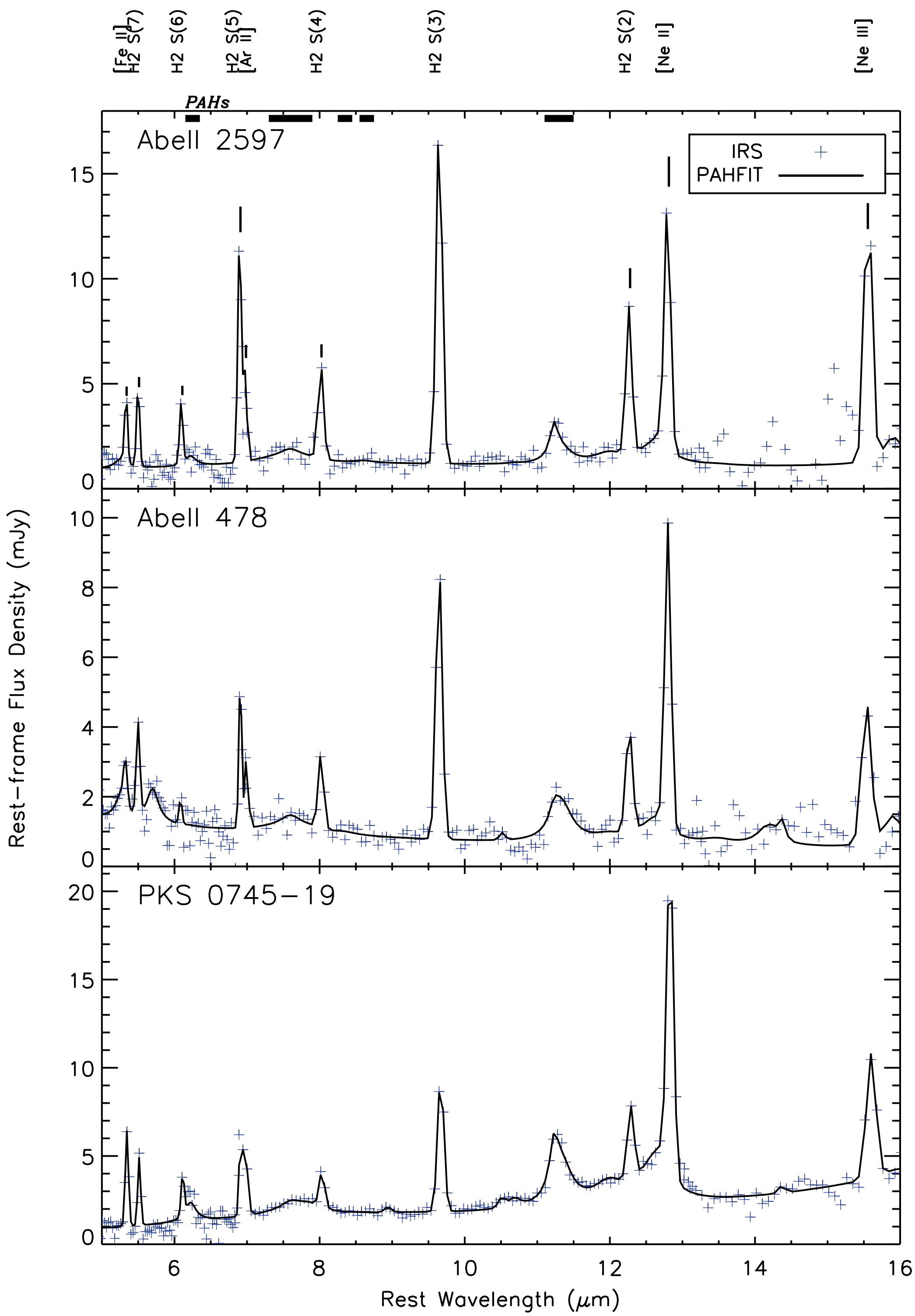

Fig. 4.2.— Figure 4.1 continued.

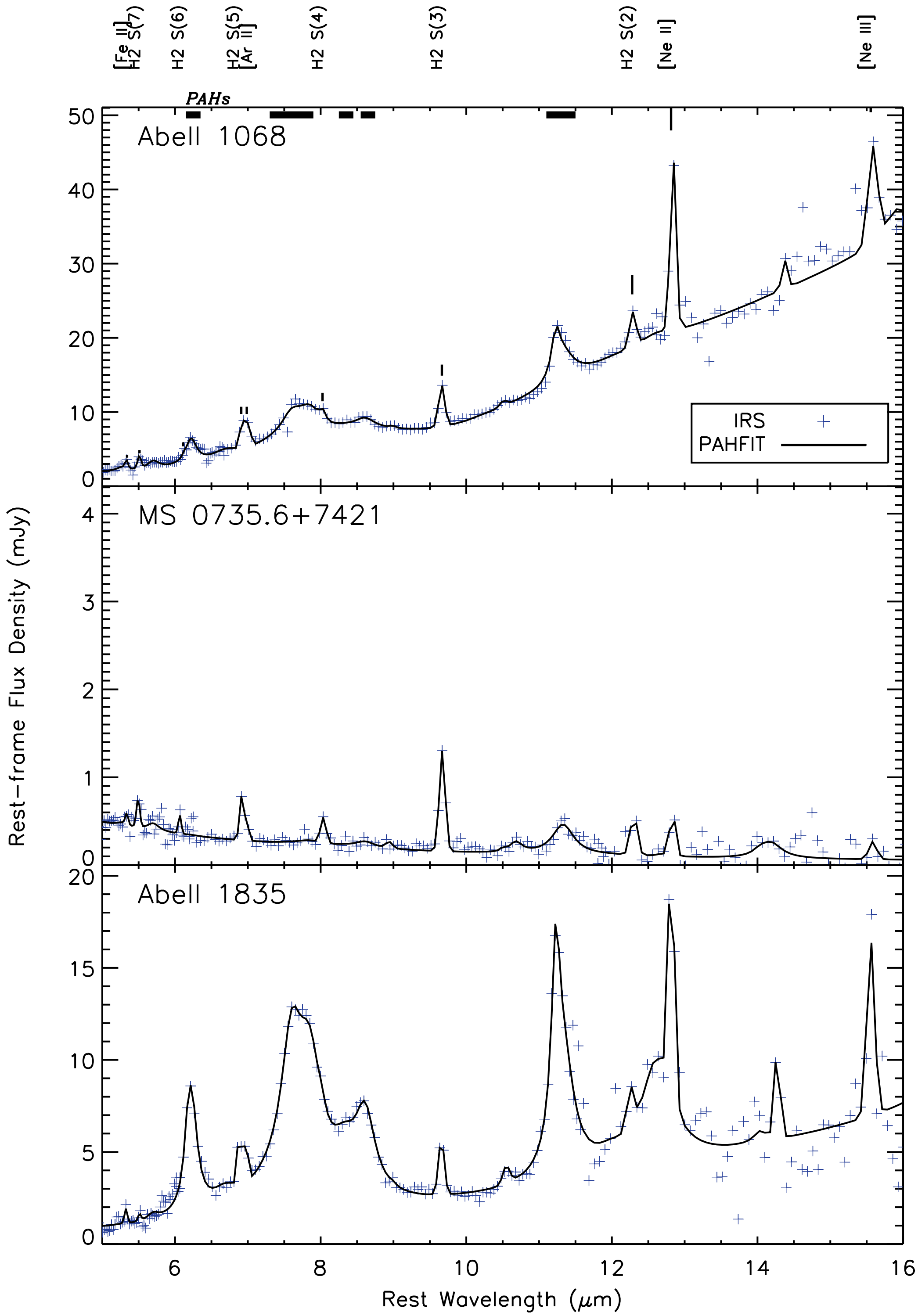

Fig. 4.3.— Figure 4.1 continued.

spectra with extremely faint continua and relatively low signal-to-noise, the log scale exaggerates the scatter. The IRS data points are indicated with blue crosses, and the PAHFIT extraction of the spectrum is represented with a bold black line. Certain areas where the signal was so low that PAHFIT was unable to securely detect the continuum are excluded: namely for 2A0335 below 5.3 μm and between 7.05 and 7.35 μm, and the spectrum beyond 19 μm for MS0735. Note that, although we regard the continuum beyond 19 μm for MS0735 as too weak to meaningfully fit with PAHFIT, we were able to obtain an upper limit to the H_2 S(0) feature at 28.2 μm (see Table 4.4). [S III] 18.7 μm is the reddest feature which can be securely detected in MS0735.

The PAHFIT fit line displays the best fit to each emission feature, even in cases where the feature is not detected to better than 3σ, and is thus reported as an upper limit (see Table 4.4, and §4.5.6). In instances where a feature fit appears in Figs. 4.1 - 4.6, but seems to be suspicious due to low signal-to-noise, the reader may consult Table 4.4 to discover whether it is regarded as a trustworthy strength determination in this analysis. These weak features sometimes appear to have disproportionate importance in the log scaling of Figs. 4.4 - 4.6.

IRAC and MIPS rest-frame broadband photometry points (see Table 4.3) are plotted with red squares, with the FWHM of each band represented with a horizontal line. The IRS photometry convolved across the IRAC and MIPS bands (at the observed wavelengths of 5.8, 8, and 24 μm) (see Table 4.8) are plotted with green diamonds; note that agreement with the IRAC and MIPS values is generally within 15%. Features of interest that were not labeled in Figs. 4.1 through 4.3 are labeled at the top of these plots. A legend is only included in Fig. 4.3 to reduce confusion in the other plots.

In Figure 4.7, the IRS spectra are grouped by gross spectral morphology and

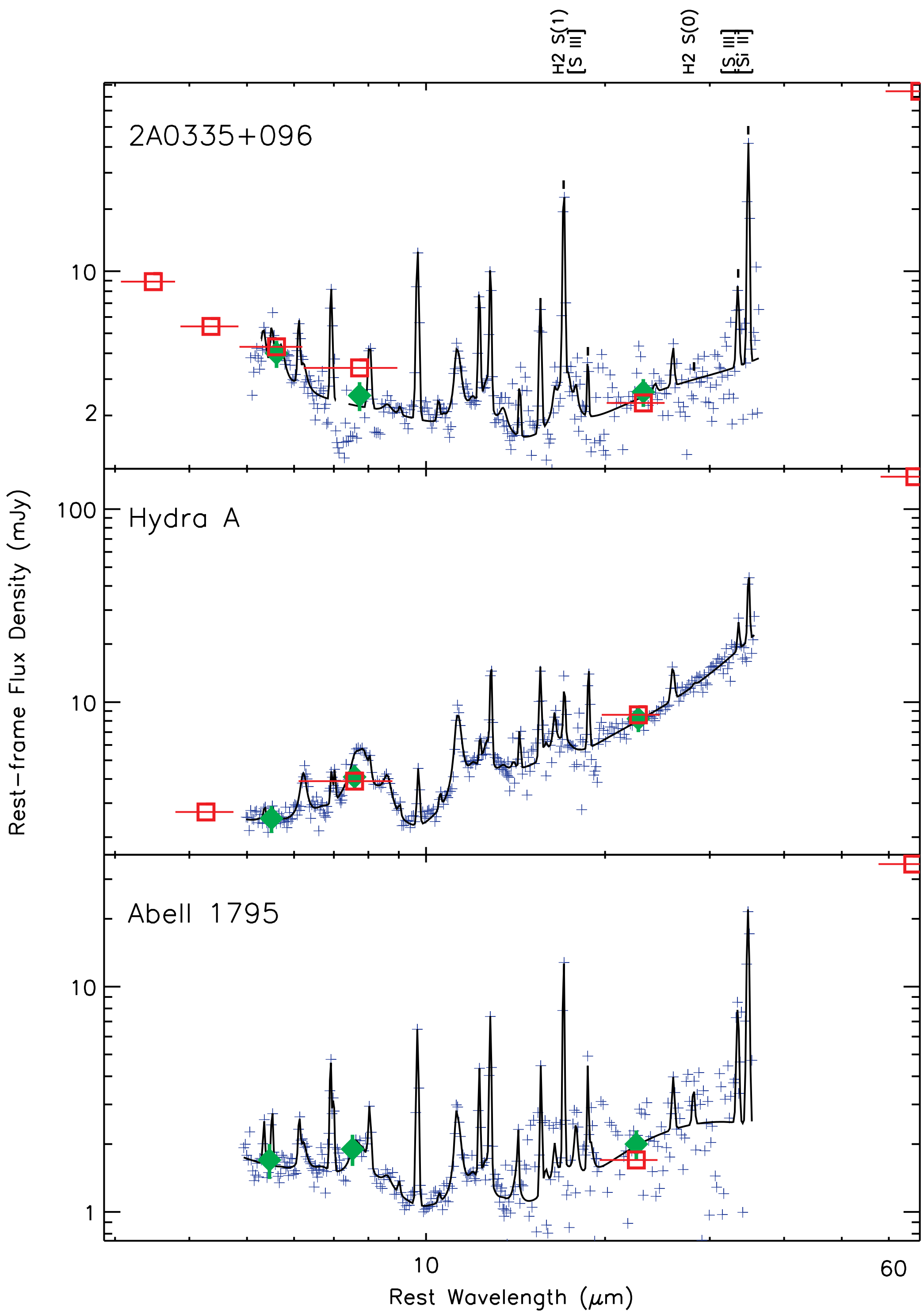

Fig. 4.4.— Log-scale rest-frame IRS spectra of the nine BCGs (blue crosses), across the full wavelength range. Black line: PAHFIT extraction. Red boxes: IRAC and MIPS rest-frame photometry between 3.6 and 70 μm; horizontal errorbars represent the FWHM of the band. Green diamonds: IRS fluxes in the same rest-frame wavebands. Features that are not identified in Figures 4.1 through 4.3 are identified at the top.

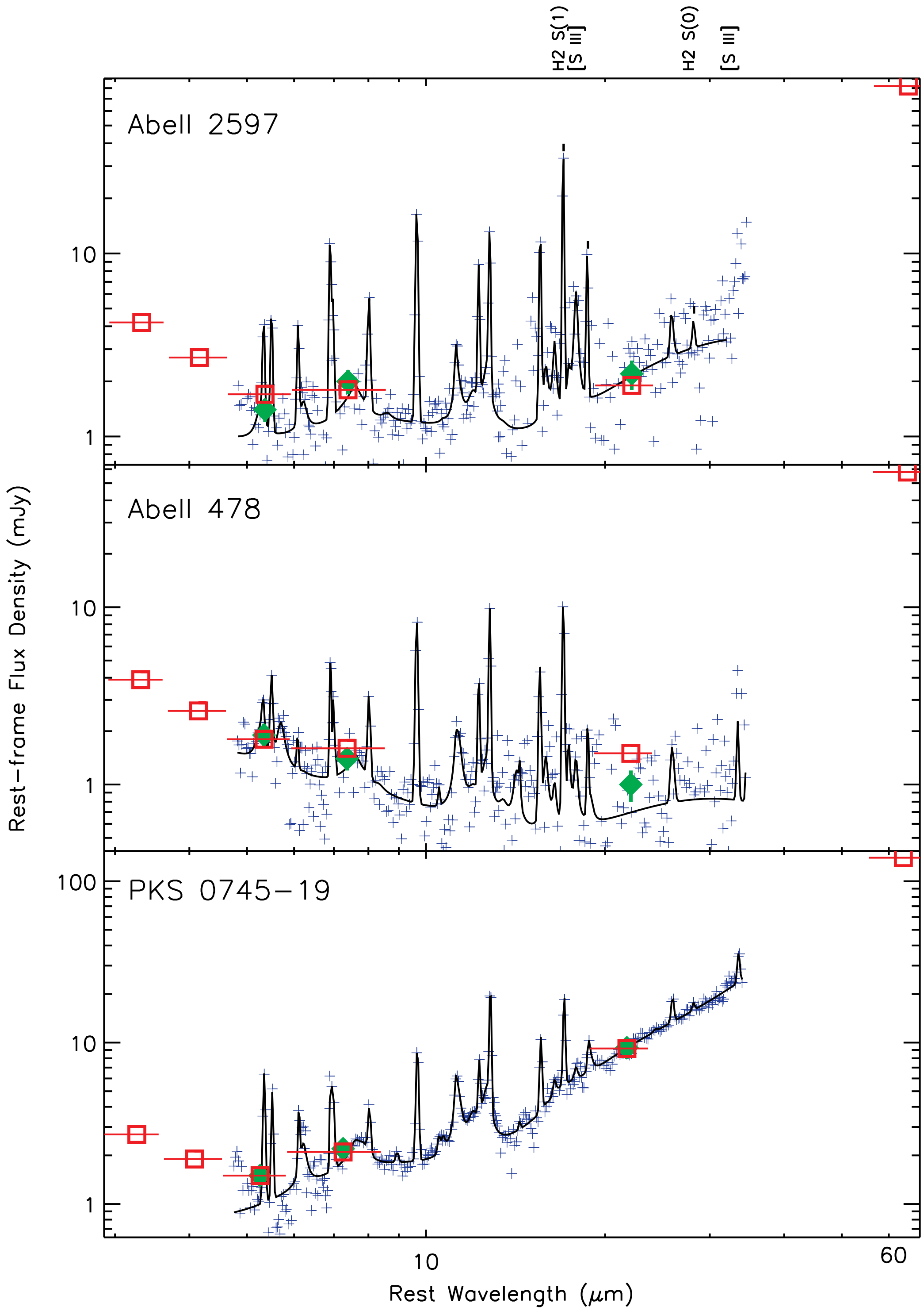

Fig. 4.5.— Figure 4.4 continued.

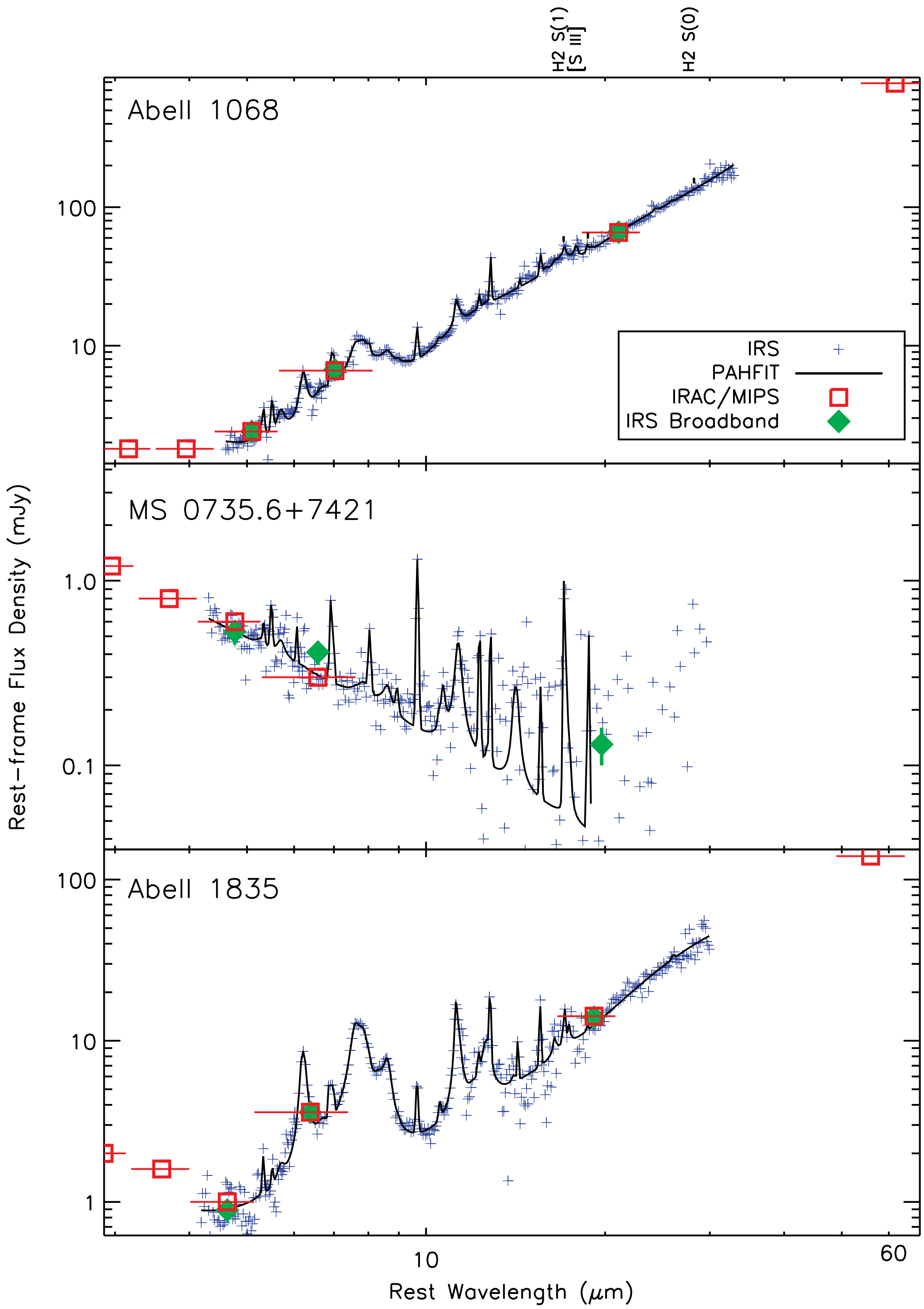

Fig. 4.6.— Figure 4.4 continued.

compared to a template of a typical starburst (Brandl et al. 2006) to differentiate the classes of continuum strength. The spectra are normalized at their highest point shortward of 30 μm. The vertical scale of this image is highly compressed and many features including low, broad PAHs tend to vanish. However, the overall continuum morphology is readily apparent. We note that the top two targets, which are also among the highest-redshift, have a morphology readily comparable to the starburst template. Distinguishing features include a powerful thermal dust continuum rising to the red, without the characteristic break at around $15-20$ μm seen in some AGN-dominated spectra (Weedman et al. 2005). PAHs are strong (though, in the case of A1068, not relative to the continuum). Low ionization and H_2 lines are detected.

The next two targets may be considered intermediate. They feature a strong red continuum and (especially in the case of Hydra A) strong PAH emission. However, the low ionization and H_2 lines have higher equivalent width than in the previous two cases. The blended feature of [O IV] and [Fe II] at 26 μm is strong in both cases. As we will discuss, there are other senses in which these targets are intermediate as well, in that their thermal dust continuum is strong, but not as strong as expected for a normal star-forming system with their level of star formation as measured in optical and ultraviolet light.

Finally, the last five BCGs in the figure all exhibit an extremely flat, faint thermal dust continuum. Some have a weak blue continuum associated with old stars. The PAHs are detected in all cases, at least at 11.3 μm, but are generally weak. The spectra are dominated by powerful narrow (spectrally unresolved) line emission, notably the H_2 lines of 0-0 S(1) and S(3) and the [Ne II] and [Ne III] atomic lines.

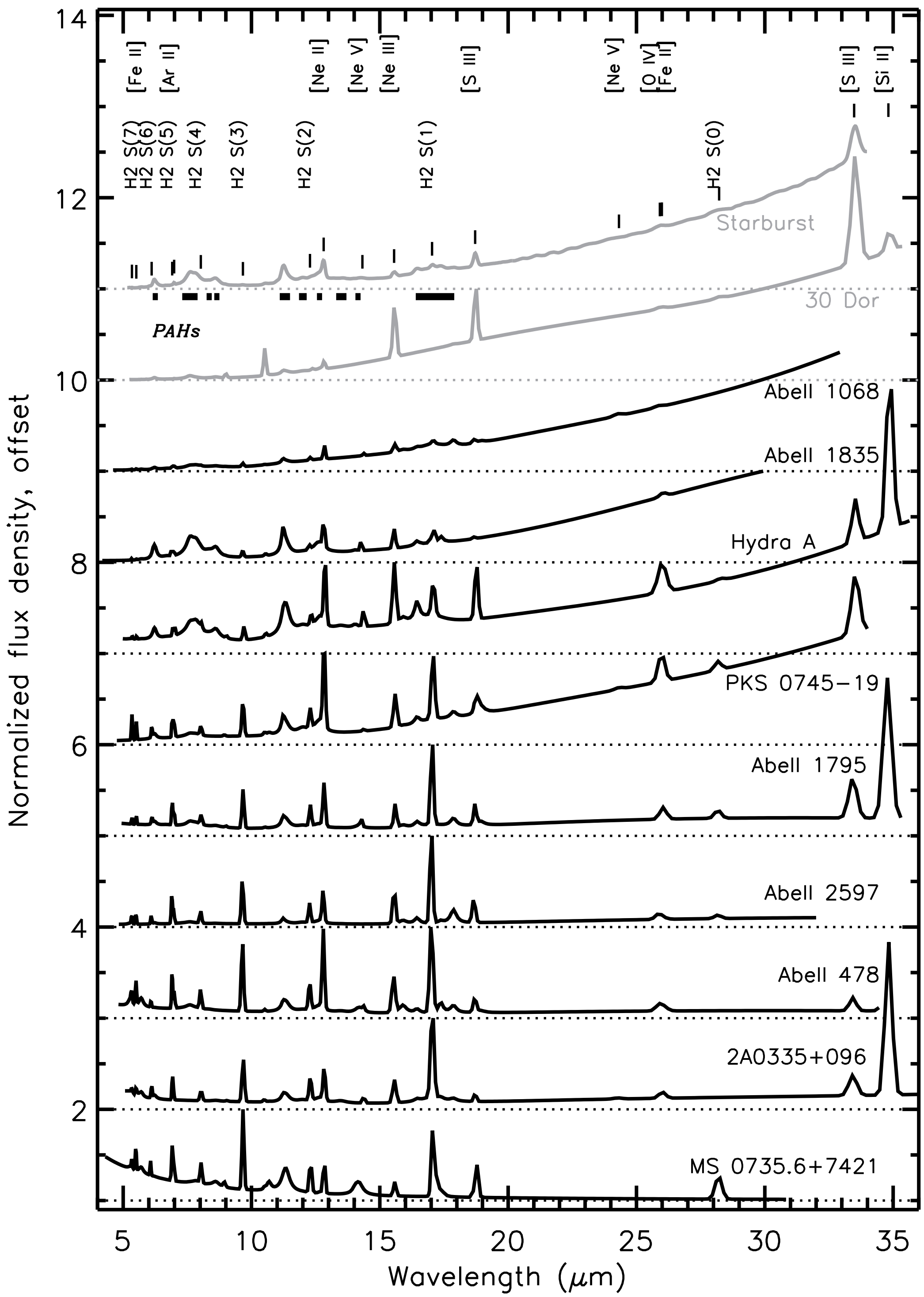

Fig. 4.7.— The PAHFIT extractions of the nine BCG spectra, grouped by gross spectral morphology. At the top, a template of a typical starburst (Brandl et al. 2006) is included.

4.6.2 Individual spectra and their PAHFIT quality

PAHFIT is an empirical code and thus has every reason to track spectral continuum and features very closely except in cases where the spectrum varies on narrow wavelength ranges beyond the scope of the continuum and emission feature curves utilized by PAHFIT, or in cases where there are emission features – potentially genuine, or otherwise noise-related – which are not included in PAHFIT. The more significant discrepancies among these are discussed below. Otherwise, the performance of PAHFIT is excellent, and feature strengths and continuum levels used in this analysis accurately represent the levels seen in the IRS spectra, within the limits of the photometric accuracy of the data reduction process.

For a set of theoretical models for the IRS spectra, based on simulated starburst SEDs described in Groves et al. (2008), the SED of an old stellar population, and a separate H_2 component, see Donahue et al. (2011); the resulting SFRs are included in Table 4.11 as SFR_{Groves}. While these models encompass the overall MIR emission of our sample, they do not predict the strength of individual features or particular continuum levels as well as PAHFIT.

2A0335+096 displays one of the strongest blue continua of the set, probably arising from stellar emission, coupled with a relatively weak longwave continuum. It is dominated by unresolved emission features. The PAH complex at 11.3 μm is strong as well.

The junction between the SL1 and SL2, near 7.2 μm, is a site of increased noise and decreased signal, to the extent that we were forced to exclude a small section of the continuum in that region from PAHFIT. Because of this area of reduced signal, 2A0335 is the only target for which we were unable to obtain even an upper limit to the major PAH complex at 7.7 μm. It is possible that this spectral artifact masks true emission from this complex in 2A0335, and in fact the IRAC flux at 8 μm is elevated above the IRS (see Figure 4.4). We took no great lengths to bring the IRS into agreement with IRAC here, because of the good agreement in other bands. It is also possible that the H_2 S(4) feature at 8.03 μm is underestimated for the same reasons; note from Table 4.7 that it numbers among the least luminous detections of this line in the sample.

The junction between the LL1 and LL2 is responsible for the noise near 20 μm.

Hydra A is an "intermediate" spectrum in our sample, with considerable PAH emission and a rising red continuum with strong unresolved emission lines. The noise near 18.0 μm appears to be spurious.

Abell 1795 strongly resembles Abell 2597 and Abell 478 in the MIR. They all demonstrate a very weak MIR continuum, detected but weak PAHs, and a strong suite of low-ionization and molecular hydrogen emission lines, with correspondingly large equivalent widths.

In the spectrum of Abell 1795, there are slight features, probably spurious, at about 6.7 and 15.0 μm. Noise at the blue end of the LL module is responsible for the slight emission near 20 μm.

Abell 2597: The SL/LL junction at about 13.2 μm is a source of slight noise. The noise near 15.0 μm appears to be spurious. Some of the emission beyond about 33 μm probably originates in [S III]33.5 μm, but we were unable to fit this feature using PAHFIT because of a single, probably anomalously low count near the center of the feature.

Abell 478: An unidentified feature near 4.9 μm in A478, and also possibly appearing in A1795, A2597, and PKS0745, could be ascribed to either [Ar V]4.93um or to an unidentified PAH.

Near 13 μm, there is noise where the SL and LL modules do not perfectly align. An unidentified and probably spurious feature appears at 20.7 μm.

PKS 0745-19 is another intermediate example, similar to Hydra A. The PAH feature at 6.2um may be underpredicted by PAHFIT.

Abell 1068 is dominated in the MIR by a powerful warm dust continuum. Though the PAHs and unresolved emission lines are present and strong, they are dwarfed by the continuum. The spectrum contains a few elevated counts, including one near 14.6 μm and another at 30.0 μm, which are probably stray rogue pixels.

A feature near 24.0 μm is probably spurious, but may be partially contributed by the [Ne V]24.3 μm feature. The feature could even be [Fe I]24.04 μm.

MS 0735.6+7421 is one of the most distant targets in our sample, and has very weak continuum emission. Many of its features are determined only as upper limits (see Table 4.4), and the continuum beyond 19 μm is so faint that its level is also an upper limit in this region.

However, a number of features are strong enough to firmly detect, including four H_2 lines, the unresolved emission lines of [Ne II]12.8 μm and [S III]18.7 μm, and the PAH bands at 8.61 and 11.3 μm.

Abell 1835 is dominated in the MIR by its warm dust continuum and by powerful PAH emission complexes. The broad complex at 7.7 μm is fitted with a remarkable equivalent width of 5 μm.

On the red shoulder of the 11.3 μm PAH complex, there is noise where the SL and LL modules do not perfectly align. Another slight discontinuity between the modules, LL2 and LL1 in this case, is responsible for some of the noise near 17 μm. There is considerable noise in the LL1, and no well-determined line strengths in this longest-wavelength module.

4.6.3 Overview of features

The BCGs exhibit strong emission lines, notably [Ne II] at 12.8 μm and the 0-0 S(1) through S(7) pure rotation series of H_2. The PAH emission bands at 6.2 μm, 7.7 μm, and 11.3 μm are detectable in most cases. The low-ionization [Si II] emission line at 34.8 μm is strong in all targets which are at low enough redshift for the IRS to cover that wavelength. It is a strong coolant for X-ray-emitting gas (Cluver et al. 2010). Extracted feature strengths are reported in Tables 4.4 through 4.7.

None of our spectra resemble normal, quiescent (i.e. non-star-forming) elliptical galaxies. Those lack strong emission features, are dominated shortward of 15 μm by a stellar continuum declining to longer wavelengths, and at 10 μm have a broad excess attributed to emission from circumstellar silicates in asymptotic giant branch (AGB) stars (Bressan et al. 2006; Smith et al. 2007b; Clemens et al. 2009). Ellipticals with even small episodes of recent star formation are readily identified by mid-IR signatures (Panuzzo et al. 2007; Clemens et al. 2009). However, certain similarities may be found between the star-forming cool-core BCGs and the category of quiescent ellipticals that contain large amounts of dust. PAH features and some of the other lines seen in our targets are often present in dusty ellipticals (Kaneda et al. 2005, 2008). The PAHs can be associated with a weakly rising red continuum, similar to cirrus in the diffuse ISM of our galaxy heated by old stars, though the stellar continuum dominates (Bregman et al. 2008; Kaneda et al. 2010). Dusty ellipticals are also sometimes significant sources of warm H_2 emission (Ogle et al. 2010; Kaneda et al. 2010). However, dusty elliptical galaxies do not demonstrate the ionized PAH emission seen in most of our sample (see §4.7.3, and Kaneda et al. 2005, 2010).

Because all but one of our BCGs are known star-formers, it is expected that their mid-IR spectra should not resemble quiescent galaxies. Surprisingly, however,

Table 4.10. Mid-IR Continuum Diagnostics in Cool Core BCGs.

Cluster	$\frac{F_{\nu,c}15}{F_{\nu,c}6}$ a	$\frac{F_{\nu,c}24}{F_{\nu,c}6}$ a	$\frac{\nu L_\nu(70\mu m)}{\nu L_\nu(24\mu m)}$ b
2A0335	0.58 ± 0.31	0.96 ± 0.55	12
Hydra A	2.0 ± 0.9	4.0 ± 1.8	5.5
A1795	0.67 ± 0.24	1.4 ± 0.5	6.6
A2597	1.1 ± 0.4	2.5 ± 0.7	13
A0478	0.47 ± 0.16	0.67 ± 0.21	12
PKS0745	2.6 ± 0.7	9.2 ± 2.7	4.4
A1068	13 ± 6	42 ± 19	3.0
MS0735	< 0.28	< 0.39	–
A1835	6.2 ± 1.4	25 ± 6	2.8

A machine-readable version is available in the published journal paper based on this work. (a) Ratios of IRS continuum flux densities (see Table 4.8). (b) Ratio of the K-corrected MIPS luminosities at 70 and 24 μm; uncertainty is 22% (Donahue et al. 2011).

most also do not closely resemble classic star-forming galaxies observed with *Spitzer*. They exhibit distinct behavior in one or more of the following characteristics: weaker long-wave continua, weaker PAH features, and stronger H_2 features.

To illustrate the differences, we include in Fig. 4.7 a template spectrum from Brandl et al. (2006), based on the average of 13 nearby starburst galaxies with SFR $\sim 10\,M_\odot\,yr^{-1}$. This template is characteristic of most star-forming galaxies, including those in the SINGS sample of nuclear observations of a variety of local galaxy types (Kennicutt et al. 2003; Smith et al. 2007b) and the Rieke et al. (2009) sample of LIRGS, though there is considerable scatter of spectral morphology within those samples. The starburst template has conspicuous emission features from PAHs and low ionization metals.

The template also exhibits a strong, red-rising continuum above 15 μm produced by very small (15-40 Å, Draine & Li 2007), warm dust grains heated by young stars. We detect the mid-IR continuum longward of 15 μm in all our BCGs, but in most of our sample, it is much fainter than in normal star-forming galaxies. Table 4.10 contains continuum diagnostics including the continuum (excluding emission features) flux ratios $F_{\nu,c}$ 15 / $F_{\nu,c}$ 6 and $F_{\nu,c}$ 24 / $F_{\nu,c}$ 6 (see Table 4.8) and the ratio of the k-corrected MIPS observations at 70 and 24 μm (Donahue et al. 2011).

The ratio $F_{\nu,c}$ 24 / $F_{\nu,c}$ 6 $= 29 \pm 1$ for the starburst template. This ratio is close to the starburst for only the two topmost BCGs in Fig. 4.7. As discussed above, PKS0745 is an intermediate case, which is also evident from this ratio. For the other six BCGs (including Hydra A, which might be considered an intermediate case as well), the mean ratio is 1.6, which is 18 times smaller than for the starburst template. The short-wave continuum is flat in three cases, but three BCGs (2A0335, A0478 and MS0735) have *blueward*-rising continua below 15 μm, with ratios of $F_{\nu,c}$ 15 /

$F_{\nu,c}6 < 1$. This is normally seen only where the cool stellar population dominates the interstellar component in the mid-IR (Smith et al. 2007b).

In general, an AGN may contribute significantly to the MIR continuum (see §4.9). In cases of intermediate AGN and starburst power, an AGN can confuse the interpretation of a MIR spectrum, which may have significant small warm dust grain continuum emission powered by both star formation and the AGN.

While cool-core BCGs have been known to exhibit the MIR spectral morphology of a classical AGN, e.g. the nuclear region of Perseus A (Weedman et al. 2005), none of our targets have an AGN-dominated spectrum. For more discussion, see §4.9. Our spectra are remarkable because of the surprisingly weak MIR continuum in the majority of the sample. If there is a non-stellar source of heating contributing to the MIR continuum, the relative paucity of small dust grains heated by star formation becomes even more extreme.

The rotational H_2 lines, particularly H_2 0-0 S(1) at 17.04 μm and S(3) at 9.7 μm, are extremely strong in our spectra. These features are weak or absent in normal star-forming systems, but have been detected in cool-core galaxy cluster BCGs (Egami et al. 2006a; Johnstone et al. 2007; Ogle et al. 2010). In our sample, they have especially large equivalent widths in the five lowermost systems in Fig. 4.7; in Abell 2597, the H_2 S(1) feature has $EW = 3.8$ μm. In the analysis of Donahue et al. (2011), we found the H_2 to have a separate power source than the star formation in these cool-core BCGs, and we found that the atomic line emission may share power sources with both. We will discuss the quantitative interpretation of the H_2 lines in Chapter 5, but we infer a wide range of temperatures for the H_2 gas, similar to results obtained by Ferland et al. (2008) for NGC 1275.

Broad PAH emission features are generally associated with star formation activity.

The major complexes at 6.2, 7.7, 11.3, and sometimes 17 μm are used to parameterize the character of PAHs in the source (Donahue et al. 2011). Among most of the cool-core BCG sample, the PAH features at 6.2 and 7.7 μm are unusually weak for star-forming systems, in terms of equivalent width (see Fig. 4.10) or relative to low-ionization emission line power (see Fig. 4.13). The feature at 11.3 μm is well-detected throughout the sample, but several targets do not have secure detections at 6.2 or 7.7 μm (see Table 4.4). The latter two features are also depressed relative to the 11.3 μm feature in several targets of our sample relative to the normal nearby star-forming galaxies of SINGS, as discussed in Donahue et al. (2011) and §4.7.3. While the PAH complexes associated with star formation are present in all the BCGs, it is only in Abell 1835 and Hydra A that we see a 5–8 μm PAH spectral morphology typical of the SINGS or starburst samples.

Comparison to the SINGS sample may be vulnerable to aperture effects. The nearby SINGS galaxies are typically studied with apertures only $\sim 0.3 - 4$ kpc in diameter (Smith et al. 2007b), tightly focused on nuclear star-forming regions. By comparison, our effective apertures range from 8 to 120 kpc. In our analysis, we note aperture effects when they arise. Also, the gas in the inner cooling flow has a relatively low metallicity ($\sim 0.3 - 0.5$ $Z_{\odot}$, Fabian 1994; Hudson et al. 2010) while SINGS has a wide range (Dale et al. 2009).

Of our nine galaxies, only the spectra of Abell 1835 and Abell 1068 meet most expectations for normal star-forming galaxies. The spectrum of Abell 1068 is nearly identical to that of NGC 7569, a Seyfert 1 galaxy with a circumnuclear starburst (Weedman et al. 2005). Hydra A and PKS 0745-19 also exhibit a red continuum but have abnormal emission features. The spectrum of PKS 0745-19 is very similar to the BCG in the cooling flow cluster ZwCl 3146 (Egami et al. 2006a), exhibiting weaker

PAH and stronger H_2 features than normal. The off-nuclear filamentary structures of NGC 1275 (Johnstone et al. 2007) also share some of these characteristics. Cool core BCGs in general appear to share the properties of strong H_2 emission (see Chapter 5 and Ogle et al. 2010). Mid-IR spectral discrepancies from normal star-forming systems are common among star-forming BCGs.

4.7 Feature Analysis

4.7.1 Infrared extinction

We do not find evidence of significant extinction of MIR light in most of the cool-core BCGs. Using PAHFIT, we fit the infrared extinction by dust fully mixed with the emitting stars and grains as a power-law profile with the addition of silicate absorption features peaking at 9.7 μm, based on the Galactic profile done by Kemper et al. (2004), and 18 μm, based on a Drude profile (Smith et al. 2007b). We found formal detections of extinction in only two of our nine targets, A1068 and Hydra A (Donahue et al. 2011, Figure 1). Their optical depths at 9.7 μm are 0.83 ± 0.03 and 0.60 ± 0.16 respectively. Among the other targets, we found 3σ upper limits to $\tau_{9.7}$ of 0.59 for A1795 and 0.03 for A1835, and no fit at all to the extinction levels in the others.

For comparison, we fit the average starburst template from Brandl et al. (2006) in the same manner and found $\tau_{9.7} = 1.4$. There are no formal uncertainties, but we estimate that the detection of the extinction feature is marginal. Brandl et al. (2006) found $\tau_{9.7}$ to be $0.24{\pm}0.10$, also a sub-3σ detection; the differences may indicate systematic differences when fitting with PAHFIT compared to other methods, though this is not conclusive since both are marginal fits. Sturm et al. (2000) find that M82 shows no evidence for strong silicate absorption.

In typical star-forming regions of nearby disk galaxies, as in the SINGS sample, silicate extinction is not detected at a high confidence level, but the absorption can be strong in the cases of deeply embedded infrared sources like ULIRGs. Smith et al. (2007b) find an extreme level of silicate absorption in the case of the LINER NGC 3198, with an optical depth of 4.9 (Smith et al. 2007b).

The PAH feature at 11.3 μm tends to be more affected by extinction than those at 6.2 and 7.7 μm (Brandl et al. 2006). The fact that the latter two tend to be depressed relative to feature at 11.3 μm in our sample (see §4.7.3) supports the argument that infrared extinction does not play a major role in these targets.

Infrared extinction may also be measured by comparing hydrogen recombination line strengths, but we do not detect Humphreys-α 12.37 μm or Humphreys-γ 5.90 μm in our sample.

4.7.2 Excitation

The line ratios of [Ne III]15.55 μm/ [Ne II]12.81 μm and [S IV]10.51 μm/ [S III]18.71 μm each provide a measure of the hardness of the UV radiation field that is incident upon the ionized gas, though the latter is more vulnerable to extinction effects (Thornley et al. 2000). The relatively high ionization line of [S IV] has an ionization potential of 34.8 eV, similar to that of [Ne III] (41.0 eV), while the lower ionization lines of [S III] and [Ne II] require similar ionization energies (23.3 and 21.6 eV respectively). Higher ratios indicate a harder radiation field on the ionized gas, indicating either the proximity of very hot (and thus young) stars or the presence of an AGN.

Because indicators of AGN activity are weak or inconclusive in our sample (see §4.9), and because of the optical evidence for ongoing star formation in these targets (see §4.4), the moderately ionized [Ne III] and [S IV] emission could easily arise from young hot stars. The hardest radiation comes from the most massive stars, so the ratios may also track the age of the youngest stars present (Thornley et al. 2000).

Figure 4.8 recreates the "excitation plane" represented in Farrah et al. (2007, Figure 11), with the addition of data from the Veilleux et al. (2009) QUEST sample of ULIRGs and QSOs, and classical AGN from Weedman et al. (2005). For those ULIRGs included in both the Farrah et al. (2007) and Veilleux et al. (2009) samples, or AGN included in both the Sturm et al. (2002) and Weedman et al. (2005) samples, only the Veilleux et al. (2009) and Sturm et al. (2002) data are plotted.

The starburst template of Brandl et al. (2006) is also plotted. Because of the lack of formal uncertainties, it has no errorbars. The fit to the [S IV] emission line for the starburst template should be considered highly uncertain, while the other three are firm detections.

All four emission lines are frequently detected in an even wider array of targets; both species are Galactically abundant, and their ionization energies can be accessed in star-forming regions or by non-stellar heating sources such as an AGN.

In our sample of cool-core BCGs, both neon lines are detected with ease throughout most of our sample (see Table 4.4). However, [S IV] is only formally detected in Hydra A. The six BCGs with limits on their line ratios are overplotted. The relative strengths of moderately high to low ionization lines in our sample fall within the expected scatter for galaxy-scale sources of neon and sulfur emission.

The [S IV] and H_2 S(3) emission lines lie in a part of the MIR spectrum vulnerable to silicate extinction at 10 μm. We securely detect H_2 S(3) in all nine cool-core galaxy clusters. The disparity with the weak [S IV] line is sometimes explained by postulating that the ionized line emission arises in dusty, highly-extincted regions associated with

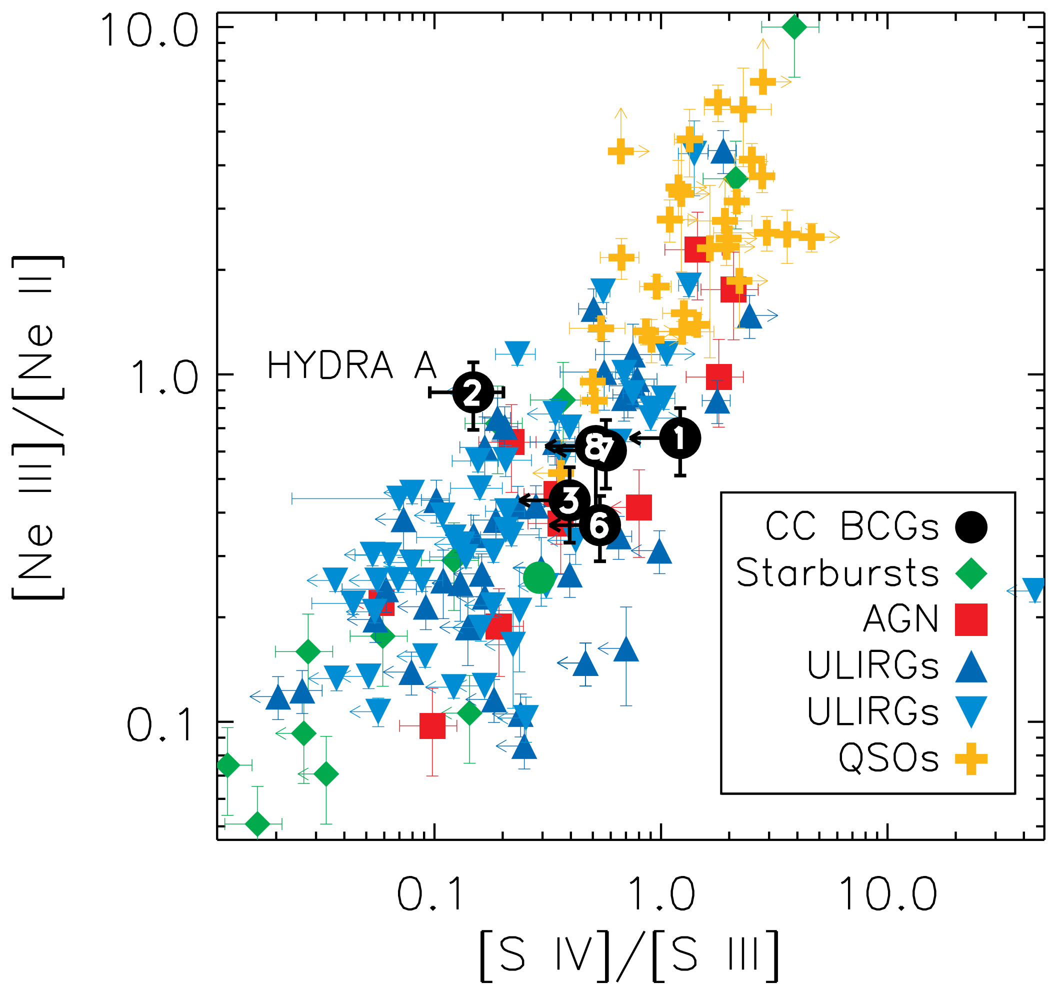

Fig. 4.8.— An excitation diagnostic diagram. The black points represent our cool-core BCGs (numbers correspond to those in Table 4.1). Other symbols correspond to observations of starbursts (Verma et al. 2003) (green circle is the starburst template of Brandl et al. 2006), AGN (Sturm et al. 2002; Weedman et al. 2005), ULIRGs (Farrah et al. (2007); Veilleux et al. (2009) respectively), and PG QSOs (Veilleux et al. 2009).

star formation while the heated H_2 lies outside those regions (Higdon et al. 2006; Farrah et al. 2007). However, that may not explain the disparity in the case of our cool-core galaxy cluster BCGs, because we find low levels of silicate extinction; indeed, we only securely detect silicate extinction in A1068 and in Hydra A, the only source with a firm detection of [S IV] (Donahue et al. 2011).

We consider the ratio of [Ne III] / [Ne II] further in Fig. 4.9. The histogram plots the ratio for a compilation of sources including the cool-core BCGs and samples of starbursts, normal star-forming galaxies, ULIRGs, AGN and QSOs. The area that each subset occupies within the histogram is plotted in color (with no subset hidden behind any others). Only results with solid detections in both neon lines are plotted, with the exception of our own sample: the upper limit to the ratio for MS0735 is plotted in black hatches. The neon ratio of the starburst template (Brandl et al. 2006) is indicated with an arrow. Fig. 4.9 has significant overlap with the data plotted in Fig. 4.8. However, the latter figure excludes samples for which the sulfur ratio is not available (e.g., the SINGS sample).

The radiation field incident upon the ionized gas is hardest or most intense for the SINGS sample of normal star-forming galaxies (where the relevant volume of ionized gas is comprised of HII regions), though there is a broad range (Smith et al. 2007b). The lowest-metallicity systems can have log([Ne III]/[Ne II]) up to 1.3, but the median is 0.54. The radiation field is also hard among the PG QSOs (median of 0.37) (Veilleux et al. 2009). Meanwhile, the AGN (Sturm et al. 2002; Weedman et al. 2005) are intermediate, with a median ratio of -0.18.

Starbursts have a broad range, perhaps inversely correlated with metallicity or affected by aging of the starburst, but tend to be associated with weaker radiation fields than the star-forming regions of SINGS (Thornley et al. 2000; Verma et al.

2003). The cause may be that the apertures cover a larger volume and include gas more distant from the forming stars, with the effect of reducing the average measured radiation field. The median ratio for the Verma et al. (2003) sample is only -0.75. The ULIRGs are mainly powered by starbursts, with a significant contribution from AGN, so it makes sense that they fall between the two categories (with a median ratio of -0.48) (Farrah et al. 2007; Veilleux et al. 2009).

The nine cool-core BCGs are relatively tightly clustered in the ratio of log([Ne III]/[Ne II]), with a median value (excluding the upper limit) of -0.21. They exhibit approximately the same hardness of radiation field as typical starbursts or ULIRGs, though with considerably less scatter. In the case of all three samples, the ratio may reflect a radiation field arising mainly from newly formed stars (and some AGN contributions in the case of the ULIRGs), with a reduced value relative to SINGS because of an aperture covering a larger spatial volume (see §4.6.3).

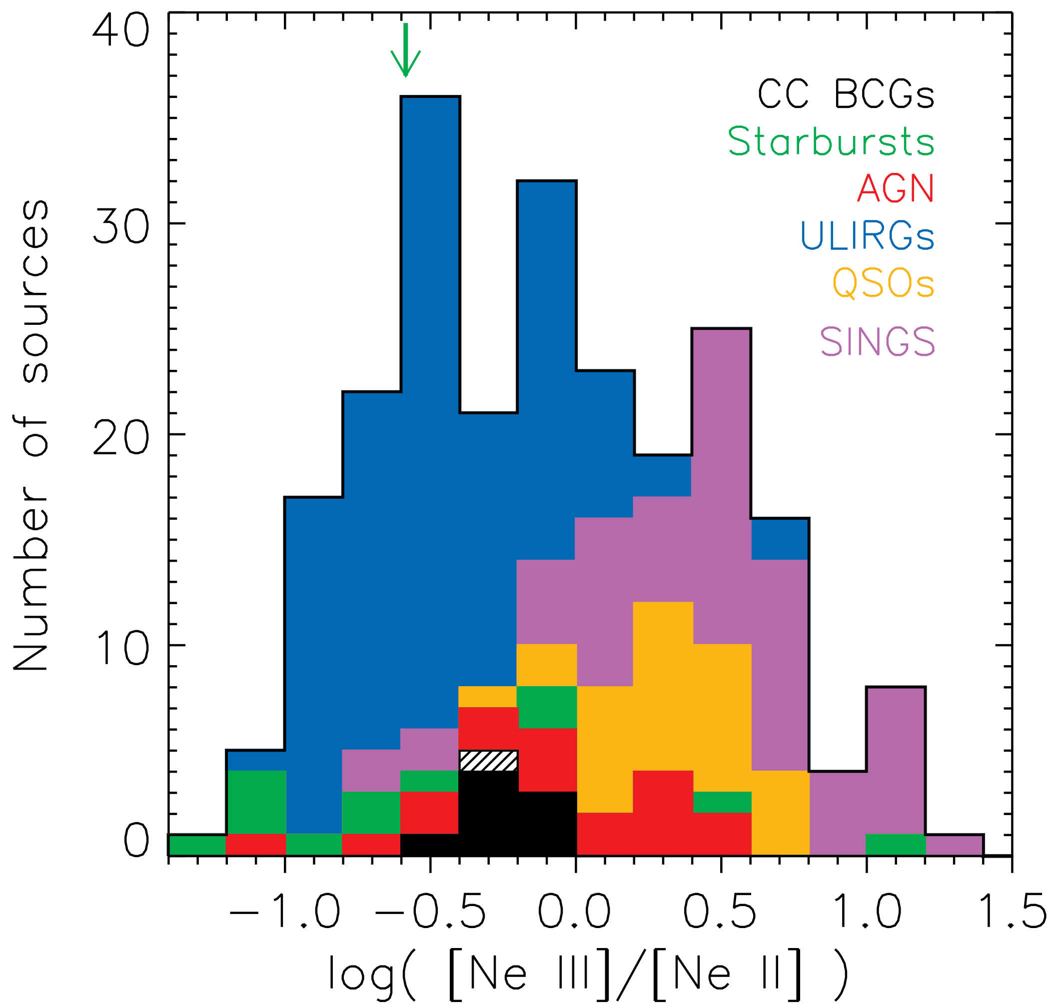

Fig. 4.9.— Black line: Histogram of [Ne III] / [Ne II] for a compilation of samples including our own; bin width is 0.2. Additive contributions to the total histogram from each sample subset are designated by color. Black: Cool-core BCGs (an upper limit is in hatched black and white). Green: starbursts (Verma et al. 2003). Arrow: starburst template (Brandl et al. 2006). Red: AGN (Sturm et al. 2002; Weedman et al. 2005). Blue: ULIRGs (Farrah et al. 2007; Veilleux et al. 2009). Orange: PG QSOs (Veilleux et al. 2009). Purple: SINGS (Smith et al. 2007b).

4.7.3 PAHs

Polycyclic aromatic hydrocarbons (PAHs) are large molecules (or ultra-small dust grains) made up of tens to thousands of carbon atoms (Draine & Li 2007). PAHs are abundant in the interstellar medium (ISM). They may be created in the ejecta of AGB stars or in the destruction of larger dust grains in interstellar shocks (Tielens 2008). If the dust in cool-core BCGs is dredged from the neighborhood of the AGN by jet activity, the PAHs may be created when dust grains are damaged by sputtering upon exposure to the hot ICM. PAH emission processes are the subject of active debate, but the general consensus is that single photons of optical to far-ultraviolet light excite each PAH molecule. The molecules then fluoresce to produce a suite of broad, complex and varying emission bands between 3 and 19 μm (Smith et al. 2007b; Tielens 2008). The stimulating emission may be ambient interstellar light from old stellar populations or the hard UV radiation from young hot stars; in principle the light of an AGN will also excite PAH molecules, but no PAH emission conclusively linked to AGN radiation has been observed (Peeters et al. 2004; Farrah et al. 2007; Bendo et al. 2008; Kaneda et al. 2010).

PAH emission is therefore closely linked with star formation activity, and it can comprise up to 20% of the total infrared luminosity in vigorously star-forming systems. The exact strength of the PAH features is notoriously difficult to determine, considering that the broad PAH features are often intermingled with each other and with other emission lines and silicate features, and that the features are located in a region of the MIR spectrum where stellar and thermal small dust grain continua tend to interact in a complex manner. The importance of PAHs in the study of star-forming systems motivated the development of the powerful empirical spectral decomposition package PAHFIT (Smith et al. 2007b), which is capable of simultaneously fitting all of the MIR spectral features discussed in this work (see §4.5.6).

Analysis of the different PAH emission bands can uncover the properties of this important component of the ISM, including abundance, molecule size, neutral fraction, and the history of radiative or collisional trauma that these delicate molecules may have experienced. Extinction may also play a role and tends to affect the feature at 11.3 μm more than those at 6.2 and 7.7 μm (see §4.7.1). In this work, we focus on those three features, all products of the bending and stretching vibrational modes of emission of intermediately sized molecules (Draine & Li 2007; Tielens 2008).

While the feature at 11.3 μm is generally thought to arise mainly from neutral PAHs about $5 - 20$ Å in size, smaller ($4 - 12$ Å) and ionized PAHs tend to be the primary contributors to the broad complex at 7.7 μm, and similar but slightly smaller molecules give rise to the feature at 6.2 μm. For comparison, the very small dust grains that produce the continuum around 24 μm are about $15 - 40$ Å in size (Draine & Li 2007).

Optical light from old stars can stimulate the emission modes of neutral PAH molecules, but only a harder radiation field can ionize PAHs. Therefore, the 11.3 μm feature dominates over the 6.2 and 7.7 μm features when PAHs are present but star formation is not ongoing (Kaneda et al. 2005, 2010). This is probably the explanation for the PAH morphology seen in the spectrum of MS0735, where of these three, only the 11.3 μm PAH is detected with significance. The PAH at 8.61 μm is typically associated with star formation, and it is detected in MS0735, but it is relatively faint.

EQW at 6.2 μm

While all of these PAH complexes are of significance, the PAH feature at 6.2 μm is heavily used as an indicator of star formation activity. It has the advantage over

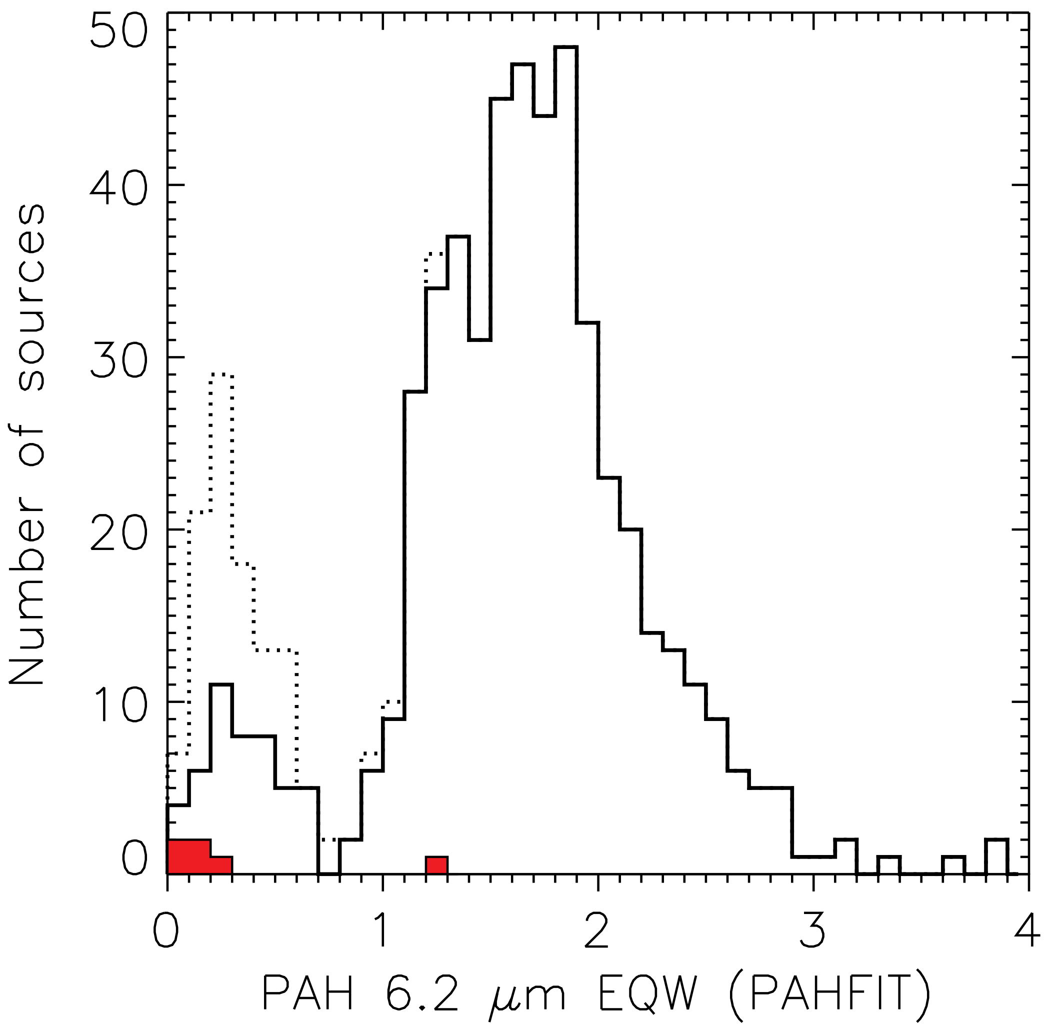

Fig. 4.10.— Histogram of equivalent widths of the 6.2 μm PAH feature. The six cool-core BCGs with known EQWs, fit with PAHFIT, are plotted in solid red. The other data, including the 5MUSES sample (Wu et al. 2010), starbursts (Sargsyan & Weedman 2009), nearby galaxies (Houck et al. 2007), and SMGs (Menéndez-Delmestre et al. 2009), are added together. Those PAHs were fit with local continuum methods, and have been corrected to their estimated value if fit with PAHFIT. The solid line represents secure detections, and the dotted line also includes upper limits.

the 7.7 μm feature of being more isolated from lesser PAH emission features. The broad 7.7 μm feature also often straddles the intersection between the SL1 and SL2 modules, while the 6.2 μm feature is located in the SL2 module in all targets in our sample except for MS0735 (where the feature is absent or weak) and A1835 (where it is fully in the SL1 module).

Most of the BCGs in our sample have PAHs at 6.2 μm with low equivalent width (see Table 4.6). Figure 4.10 is an adaptation of Wu et al. (2010, Fig 10), a histogram of the bimodal PAH 6.2 μm EQW for 280 sources with known redshifts in 5MUSES, a 24 μm flux-limited sample of galaxies. We have also included EQWs of this feature from Sargsyan & Weedman (2009) (a sample of 287 starbursts compiled from several sources including the ULIRGs from Farrah et al. (2007)); Houck et al. (2007) (the subset of a 24 μm flux-limited sample of nearby galaxies which are PAH sources); and submillimeter galaxies (SMGs) from Menéndez-Delmestre et al. (2009).

The PAHs in all of these spectra, aside from our own, were measured using various methods that subtract the local continuum before finding the PAH strength. These methods will generally underestimate the PAH strength of the 6.2 μm PAH by a factor of about 1.7 relative to PAHFIT (see §4.5.6). The difference in EQW is even higher, because PAHFIT tends to find both a higher feature flux and a lower continuum level relative to other methods.

In order to compare the other data to our work, we crudely correct the EQWs to their estimated values if fit by PAHFIT. All of the data plotted in Figure 4.10, except for our own, have been increased by a factor of 3. This correction is extremely uncertain. For instance, we fit the starburst template of Brandl et al. (2006) with PAHFIT and found an EQW to the 6.2 μm feature of 0.68 μm, which is lower than expected in comparison to the 5MUSES sample but is consistent with the SINGS results. Brandl et al. (2006) find an EQW to the same feature of the template (using a local continuum method) of 0.53 μm, which according to our method would scale to a PAHFIT estimate of 1.6 μm, more than twice our fitted value. It is certainly possible that we overestimate the degree of correction between PAHFIT and other methods. However, the discrepancies discussed below are large enough that even if no correction at all were applied, the same conclusions would generally hold.

As discussed in Wu et al. (2010) and in Veilleux et al. (2009), there is a correlation between the wavelength of the far-infrared thermal peak and the equivalent width of the 6.2 μm PAH. Cold MIR sources (for example, those with $f_{70}/f_{24} > 0.73$) have a median EQW of ~ 1.8 μm (PAHFIT estimate), and are associated with starburst activity. Similarly, most of the star-forming galaxies in the SINGS sample, when fit with PAHFIT, have EQWs for this PAH in the range 0.3 - 4 μm (Smith et al. 2007b, Fig 8). The starburst template also falls in this regime (Brandl et al. 2006). Meanwhile, warm MIR sources, with the comparatively featureless power-law spectra of AGN-dominated systems, typically have EQWs no greater than ~ 0.6 μm (PAHFIT estimate) (Wu et al. 2010).

The bimodal distribution of 6.2 μm EQW seen in Figure 4.10 reflects this duality. Most of the targets in the samples plotted here are associated with star formation or starburst activity, and have strong 6.2 μm EQWs. Meanwhile, the targets from the Wu et al. (2010); Houck et al. (2007); Menéndez-Delmestre et al. (2009) samples that have the mid-IR characteristics of an AGN also tend to have weaker features at 6.2 μm. The upper limits to the EQW shown in Figure 4.10 come mostly from AGN-dominated targets in the Wu et al. (2010) sample. A composite spectrum of the SMGs from Menéndez-Delmestre et al. (2009) with mid-IR signatures of AGN activity has an EQW at 6.2 μm of no more than 0.57 μm (PAHFIT estimate).

The measurements for our sample of BCGs are overplotted. Most of our BCGs have weak PAHs at 6.2 μm. For three of our nine targets, the feature flux is an upper limit and therefore we have opted not to set an upper limit on the EQW (see §4.5.6), but in these cases (A2597, A478, and MS0735), the feature is certainly weak, and the equivalent width low. Only A1835 has a 6.2 μm PAH as strong as typical star-formers.

We emphasize that although the other results plotted in Figure 4.10 have been corrected upwards by a factor of 3 to their estimated values if fit by PAHFIT, most of our targets would still have weak PAHs relative to normal star-formers even if we did no correction at all. In that case, A1835's PAH at 6.2 μm would no longer be considered typical, but would instead fall into the regime of the strongest PAH 6.2 μm EQWs plotted here (arising from a few of the SMGs).

While the suppression of PAH 6.2 μm equivalent width in most cool-core BCGs is interesting, this does not indicate that they are AGN-dominated systems such as those in the Veilleux et al. (2009); Wu et al. (2010); Houck et al. (2007); Menéndez-Delmestre et al. (2009) samples which share extremely low PAH 6.2 μm EQWs. The strong (though usually flat) power-law continuum seen in AGN-dominated targets is missing in all of these BCGs (see §4.9). Abell 1068, the only BCG whose intrinsically luminous 6.2 μm PAH is masked by a strong dust continuum, has moderate AGN activity but also many indicators of starburst activity (see §4.9). The other targets with low 6.2 μm equivalent widths simply have weak PAH emission over a weak or stellar-dominated local continuum.

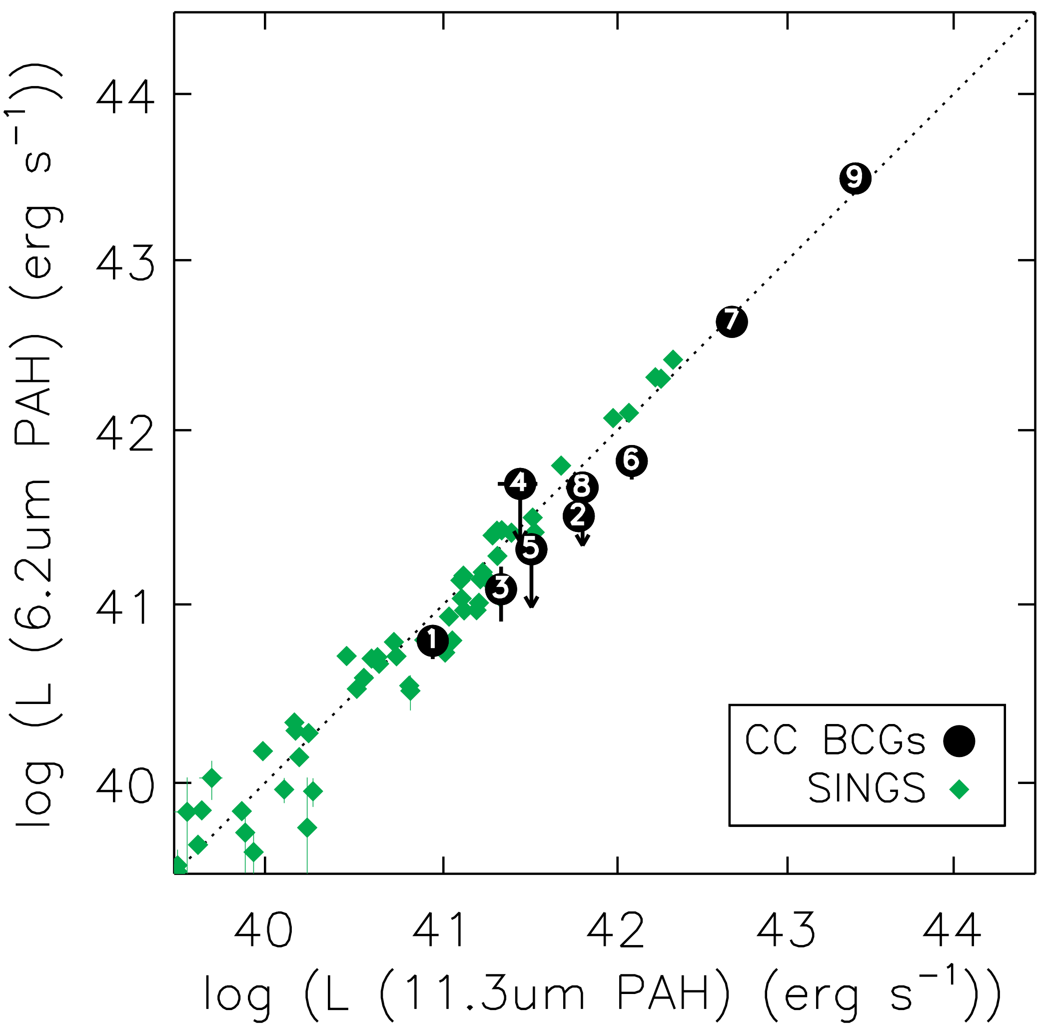

Fig. 4.11.— Rest-frame luminosities of the 6.2 μm and 11.3 μm PAHs. The dotted line is unity. The black points represent our cool-core BCGs (numbers correspond to those in Table 4.1). Green diamonds represent data from the SINGS sample.

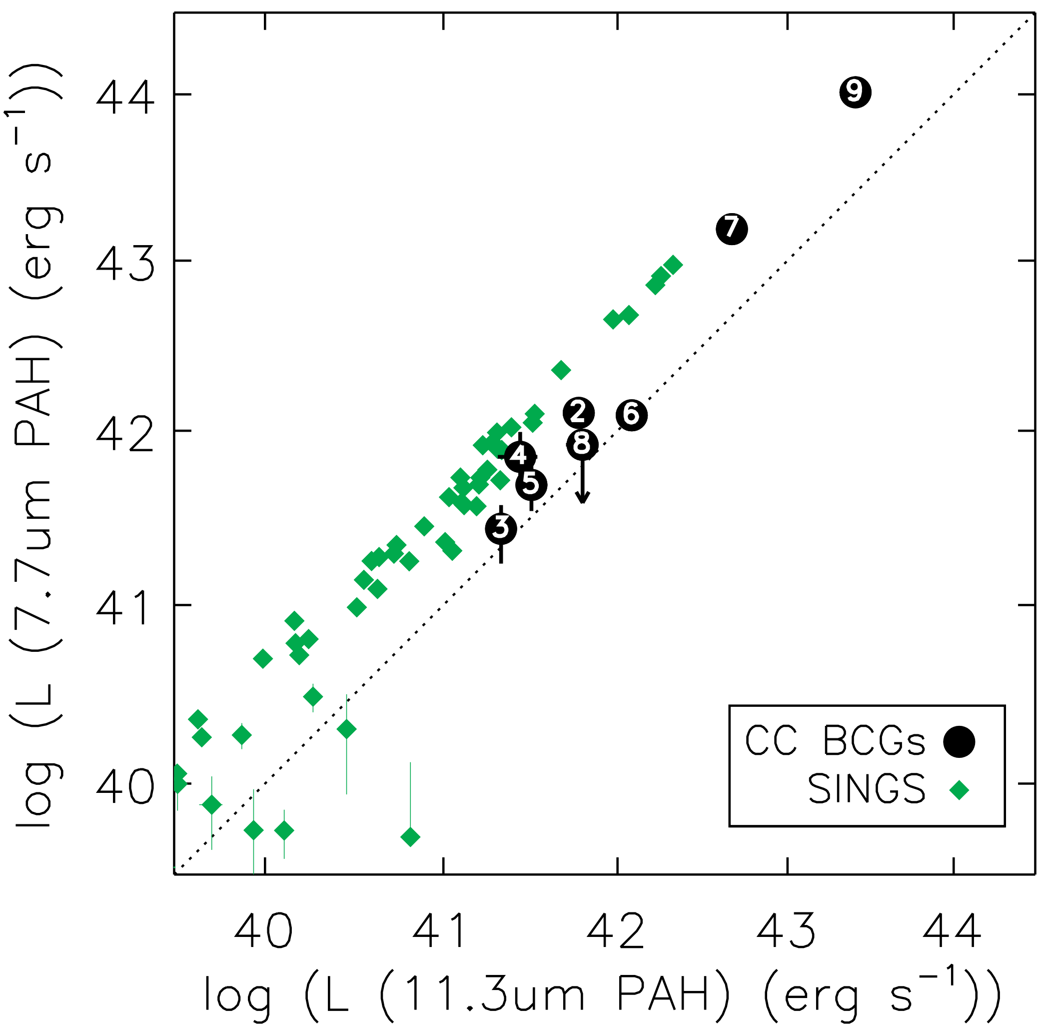

Fig. 4.12.— Rest-frame luminosities of the 7.7 μm and 11.3 μm PAHs. Format is the same as Fig. 4.11.

PAH luminosity

In Figures 4.11 and 4.12, the rest-frame luminosities of the PAHs at 6.2 and 7.7 μm, respectively, are plotted against that of the 11.3 μm PAH, and compared with the star-forming galaxies of the SINGS sample (Smith et al. 2007b). Both samples were fit with PAHFIT. The linear correlation of the PAHs is clear (unsurprisingly; bigger is bigger). While the PAH luminosities for most of our sample are typical compared to the SINGS sample, Abell 1835 has extraordinarily luminous PAHs.

Note that while the IRS spectrum of 2A0335 does not display a PAH complex at 7.7 μm, and thus does not have a fitted strength for this feature, that portion of the spectrum is artificially depressed by a poor junction between the SL1 and SL2 modules. IRAC photometry at 8 μm indicates the possible presence of a significant 7.7 μm PAH (see Figure 4.4).

Our cool-core BCGs are much larger objects than the smaller galaxies comprising SINGs, and our apertures cover a larger spatial region (see §4.6.3). Considering those factors, it is not surprising that A1068 and A1835 have more luminous PAHs than anything in the SINGS sample. Rather, it is interesting to note that the other targets do not exceed SINGS luminosities.

The scatter of SINGS measurements maps out a track of typical PAH ratios for normal star-forming galaxies, for both 6.2 vs 11.3 μm and 7.7 vs 11.3 μm. An examination of the position of our sample relative to this track in Fig. 4.11 indicates that the cool-core BCGs tend to have slightly weak emission at 6.2 μm compared to the 11.3 μm emission (Hydra A, PKS0745, MS0735, and perhaps A0478). The distinction is more clear in Fig. 4.12, where A1795, A0478, PKS0745 and MS0735 are all clearly subluminous at 7.7 μm relative to 11.3 μm. These discrepancies were analyzed in Donahue et al. (2011), as summarized below.

PAH ratios

In Donahue et al. (2011), we examined the ratio of the fluxes of the PAH complexes at 7.7 μm and 11.3 μm. As noted above, the former is mainly generated by fairly small, ionized PAHs while the latter is generated by slightly larger, neutral PAHs. The ratio of these features yields information about the ionization fraction of the PAHs, or about conditions under which the smaller grains that contribute most of the light at 7.7 μm tend to be preferentially destroyed (Smith et al. 2007b).

Among normal star-formers, the PAH ratio is insensitive to the hardness of the radiation field as measured by the ratio of the [Ne III] and [Ne II] atomic emission lines (see §4.7.2) for a given type of interstellar radiation field (ISRF). The level of the ratio is set by the type of ISRF and the lower cutoff of the distribution of PAH grain sizes, and can help to determine the age, IMF, and geometry of a star-forming region (Galliano et al. 2008b). For example, the ratio is expected to be $\sim 20 - 30\%$ higher for a hard interstellar radiation field corresponding to a young burst of star formation than for the Galactic interstellar radiation field (Galliano et al. 2008b, Fig 13). The ratio is also $\sim 50\%$ higher when the smallest PAH grains are only 20 carbon atoms in size, compared to a distribution that cuts off at about 1000 carbon atoms.

The ratio is constant at a level of about 4.2 for the SINGS sample of nearby normal star-forming galaxies when fit with PAHFIT (Smith et al. 2007b), corresponding to a ISRF even harder than in young bursts. The ratio is also constant at about 2 for a sample of starburst nuclei after fitting with a local continuum method and correcting for extinction (Brandl et al. 2006). Note that the underestimation of the 7.7 μm feature using a local continuum method instead of PAHFIT tends to be greater than it is for the 11.3 μm feature (Smith et al. 2007b) (see §4.5.6), so one would expect the ratio for the starburst sample to increase if PAHFIT were used instead. We find a ratio of 2.3 when applying PAHFIT to the average starburst template from Brandl et al. (2006). This is consistent with the young burst model with a larger PAH grain size distribution discussed by Galliano et al. (2008b), suggesting that the starburst template traces an environment where smaller PAH molecules are destroyed. However, variations in the PAH fitting method may impede the comparison between the two works.

Among the more distant submillimeter galaxies (SMGs) observed by Menéndez-Delmestre et al. (2009), the composite spectrum of the targets with the MIR signatures of starburst activity also has a ratio (when fit with a local continuum method) of 2.4 ± 0.4.

The ratio of the PAH features at 7.7 and 11.3 μm in the diffuse Galactic ISM is expected to be about the same as the starburst template (because the ISRF is lower, but smaller PAH molecules may survive; the two effects roughly cancel out) (Galliano et al. 2008b). The ratio is lower still ($\sim 1 - 2$) for spectra of dusty elliptical galaxies fit with PAHFIT (Kaneda et al. 2008). That extremely low ratio seems to indicate an unusually high fraction of neutral PAHs.

AGN-dominated targets have a broad scatter in PAH 7.7 / 11.3 ratios. At low levels of [Ne III]/[Ne II], the PAH ratio for AGN can be similar to star-forming galaxies, but in harder radiation fields, the PAH ratio declines sharply, to levels as low as ~ 0.4, possibly because of selective destruction of small grains (Smith et al. 2007b).

In Donahue et al. (2011), we found that the mean 7.7 μm/11.3 μm ratio for our seven sources with well-determined 7.7 μm fluxes is 2.7 ± 0.2. A1835 falls firmly in the regime of the SINGS star-formers with A1068 only slightly lower, and PKS0745 has an extremely low ratio of ~ 1. Most of the targets fall into an ambiguous region, with a somewhat lower ratio than SINGS. Hydra A, A1795, A0478, PKS0745 and MS0735 have ratios lower than the starburst template.

When plotted against the [Ne III]/[Ne II] ratio (Donahue et al. 2011, Fig. 15, or see Fig. 3.17), we found no distinct pattern except that A1068 and A1835 belong among normal star-forming galaxies. As demonstrated by Fig. 4.9, the hardness of the radiation field in our targets is relatively uniform among our sample, at a value that is typical for starbursts or ULIRGs but low compared to the H II regions of SINGS (probably because the apertures of the latter cover a tight nuclear area).

The analysis of the PAHs at 17 and 11.3 μm in Donahue et al. (2011) also indicates that the size distribution of PAH molecules in cool-core BCGs is normal (or is at least consistent with normality) relative to the normal star-forming galaxies of the SINGS sample. (The exception is A1068 and perhaps A2597, in which the small grains may be preferentially destroyed, perhaps by AGN activity. See §4.9.)

Therefore, the PAH 7.7 / 11.3 ratio indicates that the ISRF in A1068 and A1835 is as intense as in the SINGS sample, but considerably weaker in the rest of the sample. There is no indication that small grains have been preferentially destroyed in our sample, except in A1068 and perhaps A2597 (Donahue et al. 2011, Fig. 14), so in general the cool-core BCGs with low PAH ratios are more consistent with quiescent ISM than a starburst-like environment where small grains are preferentially destroyed. This supports the conclusion that the PAHs in most of the cool-core BCGs have not been exposed to any significant trauma.

In general, most of the cool-core systems appear to have a size and ionization distribution of PAHs that has not been seriously affected by one of the following sources: a hard UV field from hot stars or from an AGN, shocks, or collisions with hot thermal particles in the ICM. The PAHs may be protected because of distance from the sources of energy or other protection (such as a magnetic shield).

PAH luminosity compared to neon luminosity

Both neon emission and PAH emission have been linked to star formation. The correlation between the two types of emission has been characterized for star-forming regions and ULIRGs (Ho & Keto 2007; Farrah et al. 2007).

We examine whether the same relations hold for our sample of cool-core BCGs. To illustrate the relationship between the Ne and PAH strengths in our sample, we have plotted them in Figure 4.13, as in Farrah et al. (2007, Fig 15). The total luminosity in the [Ne III] and [Ne II] emission lines is plotted, in units of solar luminosity, against the total PAH luminosity in the 6.2 and 11.3 μm bands.

Our data points (black dots with index numbers) are plotted along with those from the SINGS sample (Smith et al. 2007b). Like our sample, but unlike the Farrah et al. (2007) sample, the SINGS data are fit using PAHFIT. Our targets are more luminous than most of the SINGS sample, and fall in approximately the same regime as the Farrah et al. (2007, Fig. 15) ULIRGs. As noted above, the SINGS measurements employ nuclear apertures, so it is not surprising that our targets tend to have higher luminosity.

The PAH features in the Farrah et al. (2007) sample of ULIRGs are fit using a spline between local assumed continuum points, which underestimates PAH strengths relative to PAHFIT (see §4.5.6). According to calibrations done with the SINGS sample, the PAH feature at 6.2 μm is underestimated by non-PAHFIT fits by a factor of approximately 1.70, and the PAH feature at 11.3 μm is underestimated by a factor of 1.86 (Smith et al. 2007b). Using these rough corrections, we can convert the mean neon-PAH correlation for ULIRGs obtained by Farrah et al. (2007, Eq. 3) to the PAHFIT measurement scale. This conversion is given in Eq. 4.2, where L_{Ne} is the sum of the [Ne II]12.81 μm and [Ne III]15.56 μm emission line luminosities. The luminosities may be in any units so long as they are the same.

$$L_{Ne} = 0.17^{+0.46}_{-0.12} \times \left(\frac{L_{PAH6.2}}{1.70} + \frac{L_{PAH11.3}}{1.86} \right)^{1.02\pm0.05} \tag{4.2}$$

An approximation of this curve (averaging the contributions of the two PAH features, which tend to be the same order of magnitude of strength) is plotted as a dotted line in Figure 4.13. Relative to the Farrah et al. (2007) ULIRGs, the SINGS targets tend to have stronger PAHs, perhaps by a factor of two.

The BCGs are significantly offset in Ne-vs-PAH space from both the SINGS and the Farrah et al. (2007) ULIRG sample. They appear to have stronger neon emission relative to their PAH strength than either comparison sample. This may be partially ascribed to a non-stellar source of heating that works upon the neon in the BCGs (Donahue et al. 2011). Meanwhile, PAH emission arises from stellar heating, both in general (Helou 1999) and in this sample (Donahue et al. 2011). In fact, exposure to non-stellar sources of heating like an AGN or energetic ICM processes can destroy PAHs (Voit 1992a; Weedman et al. 2006; Spoon et al. 2007).

This analysis does not determine how much of this difference is because of the effects of non-stellar sources of heating and how much is caused by unusually faint PAH emission arising from an exposed mode of star formation.

4.8 Mid-Infrared Measures of Star Formation Rate

There is no ready explanation for the differences between the mid-IR spectra of most of our cool-core BCGs and normal star-forming galaxies. However, three easily measured

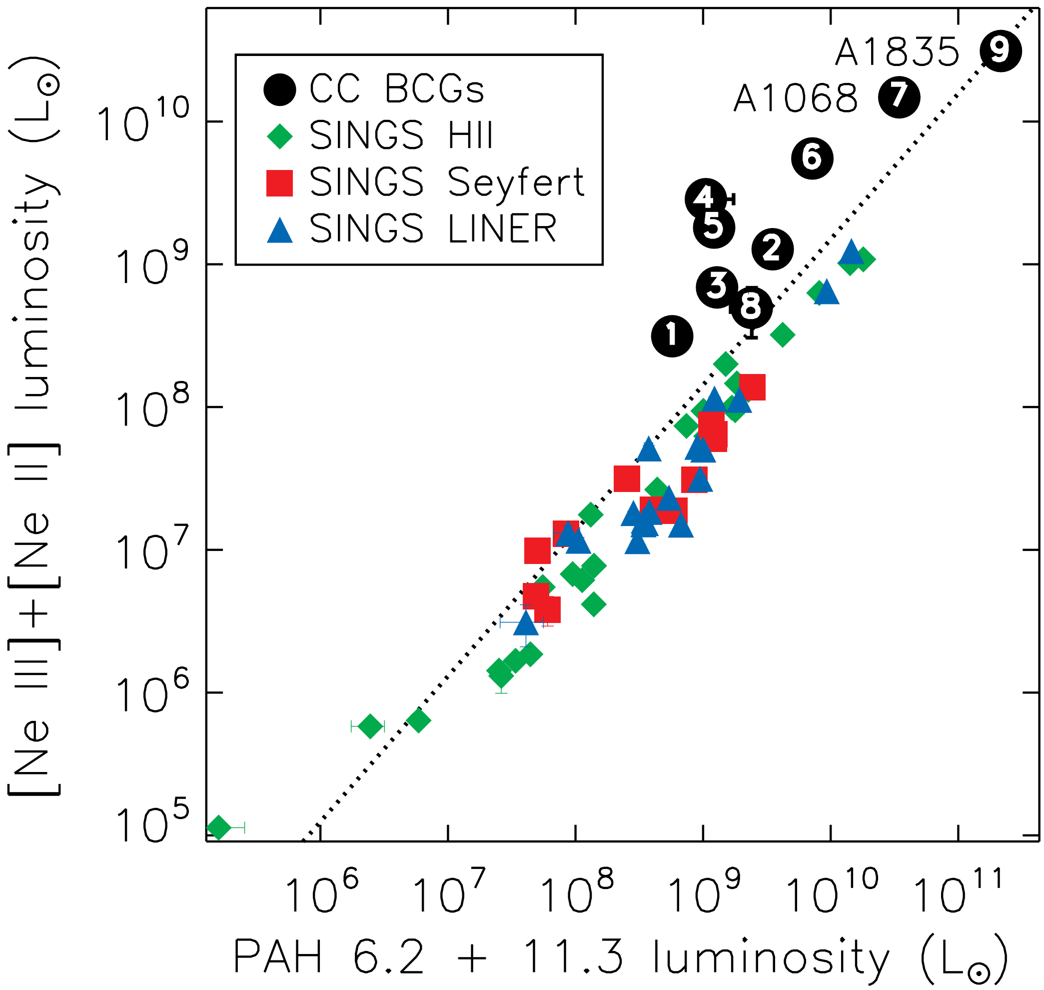

Fig. 4.13.— PAH and neon luminosities. The black points represent our cool-core BCGs (numbers correspond to those in Table 4.1). The other data points are from the SINGS sample of local galaxies (Smith et al. 2007b). Errorbars are generally smaller than the symbol size. The dotted line is Eq. 4.2: the best fit to a sample of ULIRGs.

properties of the MIR spectrum can assist in quantifying the discrepancies between the UV-MIR energy distributions of the BCGs and those of normal star-forming systems.

Neon emission, PAH features, and the luminosity at 24 μm are generally considered to be good diagnostics of the interstellar medium (ISM) enveloping star-forming regions. There are good baseline studies of their behavior as a function of star formation rate in the SINGS and other samples of star-forming galaxies.

Warm molecular hydrogen emission is also associated with star formation (Roussel et al. 2007; Treyer et al. 2010), and most of our targets have both luminous H_2 and indicators of star formation. However, in Donahue et al. (2011) we demonstrated that the strength of the H_2 is not correlated with the strength of the thermal warm dust continuum, indicating that the H_2 is probably not powered by star formation. The H_2 is discussed further in Chapter 5.

We can assess abnormalities in the UV-to-IR energy distributions of the BCGs by comparing estimates of SFR drawn from various spectral features. Even when we do not consider the estimate to be a particularly reliable estimate of SFR, it can still provide a useful metric of the relative strength of those emission features. The normal expectation is that the mid-IR estimates of obscured SFR (correlated with PAH or 24 μm luminosity) will be larger than the optical-UV SFR estimates because of the smaller effects of internal extinction in the mid-IR. The strength of this pattern correlates with IR luminosity, with the most 24 μm-luminous sources expected to host deeply buried star forming regions with almost no optical signature of star formation. Active star-formers tend to have a different relationship between the two wavelength regimes than quiescent targets (Salim et al. 2009).

We may also combine the measures of exposed star formation ($\mathrm{SFR_{opt}}$) with the estimate of obscured SFR based on the 24 μm continuum to yield a rough estimate of the total rate of star formation in these targets. This can be compared to the cooling rate estimated from X-ray observations of the ICM to yield an "efficiency" for accreted mass conversion. We also discuss the starburst models that we applied to the spectra in Donahue et al. (2011).

Table 4.11 presents a set of star formation rate estimates based on these IRS features and based on the starburst fits to the IRS spectra, as well as a comparison with the SFRs based on optical or ultraviolet continuum, an estimate of the total SFR, and a comparison with the cooling rate.

We emphasize that none of the IRS-based SFRs can stand alone as an estimate of the total star formation rate. We do assume that SFR_{24} represents the obscured star formation rate, and that it can be combined with $\mathrm{SFR}_{\mathrm{opt}}$ to estimate the total star formation rate. The same does not necessarily apply for $\mathrm{SFR}_{\mathrm{Ne}}$ and $\mathrm{SFR}_{\mathrm{PAH}}$ (see below). We present them here as a means of quantifying the discrepancy between the expected luminosity of the several MIR features among star-forming targets and the observed luminosity in our sample.

Table 4.11. IRS-based estimates of SFR, and comparisons.

BCG	SFR_{Ne} [a] ($M_{\odot}\,yr^{-1}$)	SFR_{PAH} [b] ($M_{\odot}\,yr^{-1}$)	SFR_{Groves} [c] ($M_{\odot}\,yr^{-1}$)	SFR_{24} [d] ($M_{\odot}\,yr^{-1}$)	SFR_{opt} [e] ($M_{\odot}\,yr^{-1}$)	SFR_{I} [f] ($M_{\odot}\,yr^{-1}$)	$\dot{M}_{XS}$ [g] ($M_{\odot}\,yr^{-1}$)	SFR_{PAH} / SFR_{24}	SFR_{Ne} / SFR_{24}	SFR_{Ne} / SFR_{I}
2A0335	4.0	0.66	0.70	0.19	4.2	4.4	17^{+5}_{-3}	3.4	21	0.91
Hydra A	16	4.0	4.3	1.6	11	13	16 ± 5	2.4	9.9	1.3
A1795	8.8	1.5	2.3	0.51	6.3	6.8	8^{+13}_{-7}	2.9	17	1.3
A2597	36	1.2	5.4	1.1	6.4	7.5	30^{+30}_{-20}	1.1	33	4.9
A0478	23	1.3	2.7	0.43	10	10	40^{+40}_{-20}	3.2	54	2.2
PKS0745	70	8.2	11	8.1	17	25	200^{+40}_{-30}	1.0	8.6	2.8
A1068	190	40	100	130	16	150	30^{+20}_{-10}	0.30	1.4	1.3
MS0735	6.3	2.7	0.30	< 0.17	< 0.25	< 0.42	20^{+20}_{-10}	> 16	> 37	> 15
A1835	400	250	270	140	100	240	< 200	1.8	2.9	1.7

Based on rest-frame luminosities. Uncertainties are a factor of about $1.7x$. A machine-readable version is available in the published journal paper based on this work. (a) SFR based on [Ne II]+[Ne III] (Farrah et al. 2007, Eq. 4). (b) SFR based on PAH 6.2+11.3 (Eq. 4.2). (c) SFR based on the best fit to a starburst PDR (Donahue et al. 2011; Groves et al. 2008). (d) SFR based on νL_{ν} 24 (Rieke et al. 2009, Eq. 10, 11). (e) SFR_{opt} from Table 4.2. (f) SFR_{24} + SFR_{opt}. (g) $\dot{M}_{XS}$ from Table 4.1.

4.8.1 SFR based on neon

SFR_{Ne} is a star formation estimator based on the combined luminosities of the [Ne II]12.81 μm and [Ne III]15.56 μm emission lines (Farrah et al. 2007, Eq. 4). It is an update to the relationship from Ho & Keto (2007), which is calibrated on star-forming galaxies and applied, in Farrah et al. (2007), to a sample of ULIRGs. Adopting the same assumptions as Ho & Keto (2007) and Farrah et al. (2007), namely that the fraction of photons that help to ionize the gas is $f_{\rm ion} = 0.6$ and the fractional abundances of [Ne II] and [Ne III] are, respectively, $f_{\rm Ne^{+}} = 0.75$ and $f_{\rm Ne^{++}} = 0.1$, we use the following form of Farrah et al. (2007, Eq. 4), where $L_{\rm Ne}$ is the combined luminosity of the two neon lines:

$$\frac{\rm SFR_{Ne}}{\rm M_{\odot}\ yr^{-1}} = 4.89 \times \frac{L_{\rm Ne}}{10^{41}\ \rm erg\ s^{-1}} \tag{4.3}$$

This estimate of SF has the advantage that the Ne lines are strong and easily detected and not very vulnerable to extinction effects. As a measure of the total ionizing luminosity, it has the potential to track total star formation, in contrast to SFR_{opt} from Table 4.2 or SFR_{24} (see below) which depend on the properties and distribution of dust clouds. However, the neon may be subject to non-stellar ionization (Farrah et al. 2007). Indeed, we have demonstrated that the neon in this sample of BCGs is correlated with L_{24} but not linearly, with $L_{\rm [NeII]} \propto L_{24}^{0.58}$ (Donahue et al. 2011). The implication is that star formation heating the 24 μm continuum is not the only source of heat stimulating the neon emission. Therefore, SFR_{Ne}, especially for MS0735, should be regarded as an upper limit on total star formation.

4.8.2 SFR based on PAHs

There is growing interest in using the association between PAH strength and star formation to estimate a star formation rate. Efforts to quantify this relation usually rest on the correlation between PAH luminosity and either L_{FIR} (Elbaz et al. 2002; Houck et al. 2007; Menéndez-Delmestre et al. 2009; Hiner et al. 2009), Hα (Roussel et al. 2001; Zhu et al. 2008), or neon line emission (Farrah et al. 2007). These efforts are hindered, especially on kiloparsec scales, by the complex, variable nature of the PAH emission. There is even some evidence that PAH emission may be associated more with cold, diffuse dust than the dust heated by star formation (Bendo et al. 2008), that stars of intermediate age may influence the $10 - 18$ μm emission spectrum as much or more than active star formation (Salim et al. 2009), and that the broad PAH band at 7.7 μm, frequently used for calibrations, may be subject to contamination from as-yet-unknown sources of emission (private communication, D. Calzetti and A. Crocker).

As demonstrated in §4.7.3, the PAH emission in the cool-core BCGs is subluminous relative to the neon emission. Here, we estimate a star formation rate based upon PAH emission in order to quantify the strength of the PAH emission relative to the thermal dust continuum emission measured at 24 μm (see §4.8.3). To that end, we have adapted the linear correlation of Farrah et al. (2007), based upon a sample of ULIRGs, which combines the emission from the PAH bands at 6.2 and 11.3 μm. No single method is likely to be very accurate, especially considering the wide scatter in PAH fitting methods (see §4.5.6), so we also perform the calculation presented in Menéndez-Delmestre et al. (2009), calibrated using submillimeter galaxies, for comparison.

The PAH-based SFR estimate of Farrah et al. (2007, Eq. 5) rests upon PAH fluxes measured with local continuum methods. We use our Eq. 4.2 instead of their Eq. 3, making it appropriate for PAH luminosities found using PAHFIT. Also, while Farrah et al. (2007) assume star formation in their ULIRGs occurs in bursts, and roughly account for that by scaling the star formation rate upward by 50%, we expect the star formation in our BCGs to transpire over durations of at least 10^8 yr (see §4.4.2). Therefore, we do not apply the 50% upward scaling. Otherwise, we use the same assumptions on fractional abundances as cited in §4.8.1. Our version of Farrah et al. (2007) Eq. 5 appears in Eq. 4.4, where the PAH luminosities are given in units of 10^{41} erg s^{-1}.

$$\frac{\mathrm{SFR_{PAH}}}{\mathrm{M_{\odot}\ yr^{-1}}} = 0.79 \left(\frac{\mathrm{L_{PAH6.2}}}{1.70} + \frac{\mathrm{L_{PAH11.3}}}{1.86} \right) \tag{4.4}$$

We present $\mathrm{SFR_{PAH}}$ in Table 4.11. We also estimated the SFR using the 7.7 μm PAH, as calibrated on a sample of submillimeter galaxies by Menéndez-Delmestre et al. (2009). That relationship employed PAH strengths based on localized power-law continuum fits, which probably underestimate the PAH strength relative to PAHFIT. Therefore, applying that relationship to PAHs fit with PAHFIT may somewhat overestimate the SFR. We found the SFRs estimated using Menéndez-Delmestre et al. (2009) to be about twice the values based on Eq. 4.4. We do not have a luminosity for the 7.7 μm feature for 2A0335, and only an upper limit for MS0735.

In Table 4.11, $\mathrm{SFR_{Ne}}$ exceeds $\mathrm{SFR_{PAH}}$ throughout our sample, by more than a factor of 4 except in the cases of MS0735 and A1835. This is expected from Fig. 4.13. Note that the PAH emission in MS0735 is dominated by the 11.3 μm feature, associated with neutral emission which may be stimulated by an old population of stars rather than current star formation.

4.8.3 SFR based on 24 μm continuum

The distinctive MIR thermal dust continuum arising from small dust grains reprocessing the light of hot young stars into the infrared is a hallmark of star formation. Classic star-forming systems and starbursts usually have infrared spectra dominated by the combination of this continuum and a powerful PAH emission spectrum. There is a host of factors that complicate any calibration of SFR based on the 24 μm continuum, but the wide availability of MIPS observations of a broad range of star-forming systems, as well as the tight correlation between extinction-corrected Pα emission (a reliable indicator of star formation activity) and L_{24} (Alonso-Herrero et al. 2006; Rieke et al. 2009), have motivated the development of estimates of SFR_{24}.

We adopt the SFR-L_{24} correlation of Rieke et al. (2009, Eqs. 10, 11), where L_{24} is in units of 10^{10} $L_\odot$:

$$\frac{\mathrm{SFR}_{24}}{\mathrm{M}_\odot\ \mathrm{yr}^{-1}} = \begin{cases} 7.8\ \mathrm{L}_{24} & \text{if } 6 \times 10^8\ \mathrm{L}_\odot \leq \mathrm{L}_{24} \leq 1.3 \times 10^{10}\ \mathrm{L}_\odot \\ 7.8\ \mathrm{L}_{24} \times (0.76\ \mathrm{L}_{24})^{0.048} & \text{if } 1.3 \times 10^{10}\ \mathrm{L}_\odot < \mathrm{L}_{24} < 2 \times 10^{12}\ \mathrm{L}_\odot \end{cases} \tag{4.5}$$

Among our sample, three BCGs (2A0335, A0478, and MS0735) are less luminous than the lower limit on those ranges. For MS0735, $L_{24} < 2.2 \times 10^8$ $L_\odot$. Below this limit, the scatter in the Pα - L_{24} relation increases significantly (Rieke et al. 2009, Fig. 7) but is still broadly applicable to L_{24} as low as 8×10^7 $L_\odot$. The other targets fall into the first category, except for A1068 and A1835, which belong to the latter category.

The values of SFR_{24} appear in Table 4.11 and are estimates of the rate of obscured star formation.

A1068 and A1835 have very strong continua (> 15 μm) from warm dust grains, yielding a rate of star formation in rough agreement with other IRS-based measures (within a factor of $\sim 2-3$). Obscured measures of star formation consistently exceed $\mathrm{SFR_{opt}}$, as expected in IR-luminous, starburst-like targets.

However, in the other cases (excluding MS0735, for which there is no optical-UV evidence for star formation) the optical-UV star formation rates systematically exceed those derived from the 24 μm continuum by factors of $\sim$ 10. We would have readily detected the mid-IR continuum associated with normal star formation if it were present in these galaxies. By comparison to normal star-forming galaxies, the BCGs are subluminous in the mid-IR continuum, possibly indicating a relatively exposed mode of star formation.

Furthermore, in several of those cases, the estimate of $\mathrm{SFR_{24}}$ falls short of $\mathrm{SFR_{PAH}}$ by factors of $2-3$ (see ratios in Table 4.11). While we do not trust the measure of $\mathrm{SFR_{PAH}}$ as an absolute indicator of star formation, we do conclude that this systematic discrepancy, while not severe, may indicate that the warm dust grains are subluminous relative to the PAH strength in these targets, compared to their distribution in the normal star-forming systems on which these relationships were calibrated. Recall that other analysis in this work indicated that the PAHs themselves (particularly the emission at 6.2 and 7.7 μm) tend to be weak in these targets relative to normal star-formers, whether measured against local continuum (see Fig. 4.10), the feature at 11.3 μm (see Figs. 4.11 and 4.12), or the neon emission (see Fig. 4.13).

The 24 μm continuum is especially weak when compared to the neon (see Table 4.11). It is capable of tracking total star formation, while the 24 μm continuum is sensitive only to light reprocessed into the infrared, thus obscured star formation. High ratios of $\mathrm{SFR_{Ne}/SFR_{24}}$ for most of the star-formers in the sample, $\sim 10-50$ (excluding A1068 and A1835), indicate that the dust may be capturing a remarkably small fraction of the light of young stars. However, the neon emission has a separate heating source than the 24 μm continuum (Donahue et al. 2011), so this ratio should be considered an upper limit on the ratio of exposed to total star formation.

In the event that non-stellar heating such as an AGN contributes significantly to the thermal dust profile, SFR_{24} must be taken as an upper limit of obscured star formation. Note that calibrations of star formation using 24 μm light are based on samples that purposefully exclude AGN (Rieke et al. 2009; Calzetti et al. 2010). However, these targets do not demonstrate the MIR signatures of an AGN-dominated target, and extended structures of star formation are too far from the core for nuclear radiation to play a major role (see §4.9).

4.8.4 SFR based on starburst models

In Donahue et al. (2011), we applied a physical model to the IRS spectra of the cool-core BCGs, composed of a set of simulated starburst models from Groves et al. (2008) (spanning a range of physical parameters: metallicity, pressure, compactness, and the presence of a PDR surrounding H II regions) as well as a 10 Gyr old stellar population and a two-temperature H_2 model. The purpose of the H_2 model was mainly to subtract the luminous rotational H_2 from the spectrum so it would not interfere with the other components of the fit; in Chapter 5, we apply a more careful model and get similar but slightly more refined results.

The physical model of Donahue et al. (2011) is relatively rough, frequently underpredicting the luminosity at ~ 15 μm and (in the case of the six targets which we conclude in this work to have unusually exposed star formation, namely 2A0335, Hydra A, A1795, A2597, A0478, and PKS0745) overpredicting the slope of the MIR continuum at > 18 μm. The fits to the models were made in consideration of the

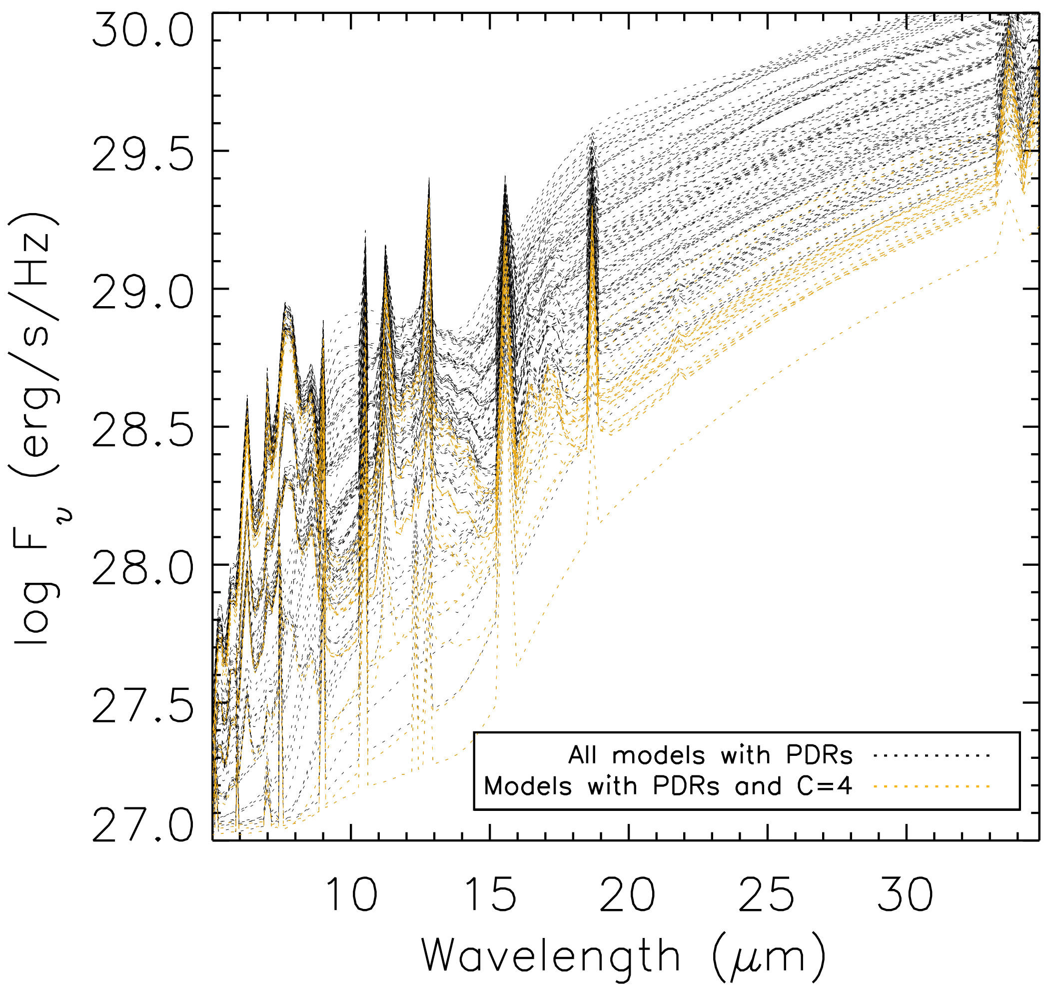

Fig. 4.14.— The 150 starburst models of Groves et al. (2008) that include a PDR are plotted as black dotted lines. Each model represents the SED for 1 $M_\odot\,yr^{-1}$ of star formation for a certain set of physical parameters. The subset of models with a PDR and the minimum concentration parameter ($C = 4$) are overplotted in orange.

entire spectrum, so the dominant components in each spectrum tend to have the greatest impact on the result; once H_2 is subtracted off, it is usually the long-wave continuum or the bright neon emission lines that tend to set the fit parameters. See Donahue et al. (2011) for a thorough discussion of each fit, a plot of the fits and spectra, and analysis of the models.

In brief, we found that the compactness parameter C is the feature that distinguishes the targets listed above (and MS0735 which also has a weak MIR continuum, but excluding PKS0745 which is an intermediate case) from A1068 and A1835. C characterizes the intensity of the radiation field at the H II / PDR interface; it is generally a measurement of how close the dust is to the young stars. More compact H II regions have hotter dust grains, a steeper MIR thermal dust continuum, and (as we established in Donahue et al. (2011)) lower ratios of L_{70} / L_{24} (see Table 4.10 and discussion in §4.10). A1068, A1835, and PKS0745 were fit with high C, while the other targets were fit with the lowest possible C in the range of models (Hydra A, also an intermediate case, was fit with a low but not the lowest C).

To illustrate, in Fig. 4.14 we have plotted the 150 Groves SEDs which include a PDR (as all of our models in Donahue et al. (2011) do, in order to account for the observed PAHs). Each model simulates the SED caused by 1 $M_\odot\,yr^{-1}$ of star formation, for a certain set of parameters. We have highlighted the models with the lowest values of C in orange. These are the SEDs which tend to be the best fits for the cool-core BCGs with exposed star formation. (Note that these plots do not include the other components of the model used in Donahue et al. (2011), namely the old stellar continuum and the two-temperature H_2 spectrum; the missing former element accounts for why all of the models shown in Fig. 4.14 seem to have steeper MIR continua than the spectra in Figs. 4.4 - 4.6.)

Since C is correlated to the steepness of the MIR continuum, and the models in Donahue et al. (2011) consistently overpredict the continuum slope for these targets, we speculate that an even lower compactness than available in the range of the Groves et al. (2008) models, with a flatter MIR continuum, may be appropriate.

The models support the result that the targets with higher optical-UV measures of star formation than SFR_{24} tend to have unusually exposed star formation, with a low compactness parameter (the dust is farther from the young stars than in most starburst-like environments) and cool dust peaks (measured with L_{70} / L_{24}).

The star formation rates derived from the models in Donahue et al. (2011) (SFR_{Groves} in Table 4.11) arise from the scaling of the selected Groves SEDs: how many SEDs (each providing 1 $M_{\odot}\,yr^{-1}$) are required to produce the observed MIR spectrum. We note that SFR_{Groves} consistently falls short of SFR_{Ne} and (except for A1068) consistently exceeds SFR_{24}. Agreement with SFR_{PAH} is generally good. We examine whether SFR_{Groves} is realistic as an estimate of obscured star formation in the cool-core BCGs.

Considering the model from an statistical point of view, it makes sense that SFR_{Groves} tends to cut the difference between SFR_{Ne} and SFR_{24}, because once the H_2 is subtracted away, those two components dominate most of the spectra, and the model compromises between them.

The SFR_{Groves} may exceed SFR_{24} because of the influence of the neon lines on the fit, which suggests that SFR_{24} may be a more reliable indicator of obscured star formation. We have established that neon has an extra heating source beyond that heating the dust that generates the 24 μm continuum (Donahue et al. 2011). However, we note that the models tend to underpredict the neon lines at 12.8 and 15.5 μm (which is not surprising from a physical point of view, since the models do not account for the extra source of heating that acts upon the neon) but do not systematically overpredict the 24 μm continuum. The slope at 24 μm is often overpredicted (probably a consequence of the limited range of compactness parameters) but the models are remarkably effective at fitting the flux. Any offset between the model and the spectra at 24 μm certainly does not account for the systematic discrepancy of $\sim 4\times$ seen in the first five targets listed in Table 4.11.

The puzzling discrepancy between $\mathrm{SFR_{Groves}}$ and $\mathrm{SFR_{24}}$ may be considered as a discrepancy between the assumptions of the Groves models and the standard calibration of SFR based on the 24 μm continuum that we used to obtain $\mathrm{SFR_{24}}$. In Fig. 4.15, we plot all 300 of the Groves et al. (2008) models. Recall that our targets with relatively flat MIR continua, associated with exposed star formation, are best fit by the Groves models with low compactness, which populate the bottom of the range of SEDs in Fig. 4.15.

We have also included the standard calibrations of SFR based upon the 24 μm continuum, from Rieke et al. (2009); Calzetti et al. (2010). Rieke et al. (2009) applied their calibration to a wide range of MIR luminosities (with a break between the high and low luminosity regime at $\mathrm{L_{24}} = 5 \times 10^43$ erg s^{-1}) in an effort to make a widely accessible measure of star formation. Meanwhile, Calzetti et al. (2010) estimated total star formation, which is only predicted by $\mathrm{L_{24}}$ alone in the highly obscured high-MIR-luminosity regime ($\mathrm{L_{24}} > 5 \times 10^43$ erg s^{-1}). At lower luminosities, they include Hα to estimate the exposed component of star formation.

The three calibrations are represented with symbols in Fig. 4.15, at the 24 μm spectral luminosity density predicted by 1 $\mathrm{M_\odot\,yr^{-1}}$ of star formation. Clearly, the two calibrations, and the high and low luminosity regimes for Rieke et al. (2009), are all in close agreement. We have also included the starburst template of Brandl et al.

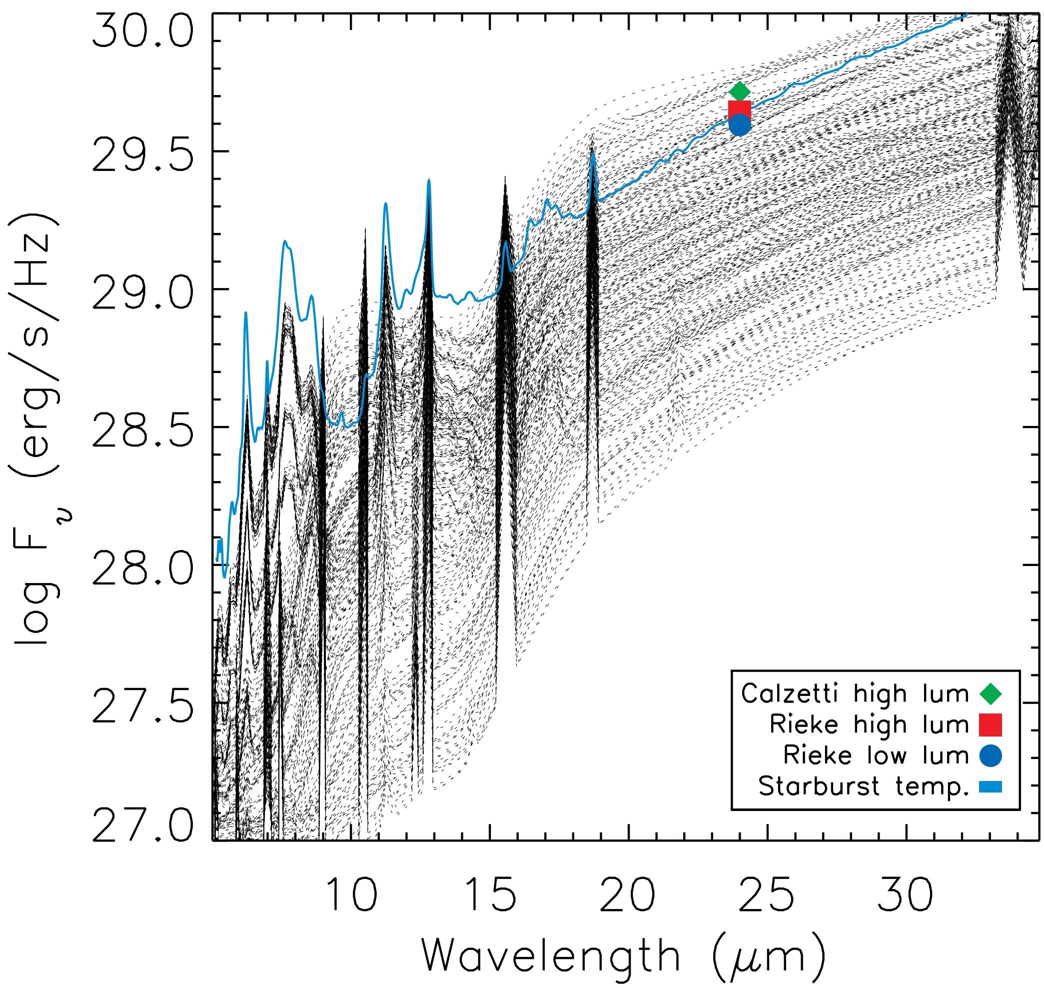

Fig. 4.15.— The 300 starburst models of Groves et al. (2008) are plotted as black dotted lines. Each model represents the SED for 1 $M_\odot\,yr^{-1}$ of star formation for a certain set of physical parameters. The standard star formation calibrations of Rieke et al. (2009); Calzetti et al. (2010) are overplotted (for $L_{24} > 5 \times 10^{43}$ erg s^{-1}, "high lum", or below that threshhold, "low lum"). The Brandl et al. (2006) starburst template (normalized to the Rieke et al. (2009) high-L_{24} calibration) is overplotted in cyan.

(2006), normalized to pass through the Rieke et al. (2009) “high lum” point.

It is a source of concern that the standard star formation calibrations based upon the 24 μm luminosity are clearly not representative of the majority of the starburst models of Groves et al. (2008), and specifically that the low-C models which comprise the best fits to many of the cool-core BCG spectra are very poorly represented by the 24 μm calibrations. This is a fundamental discrepancy between the physical (Groves et al. 2008) models and the empirical calibrations of SFR from 24 μm.

It remains to be decided whether the Groves et al. (2008) models or Rieke et al. (2009); Calzetti et al. (2010) calibrations are more representative of the environment of star formation in cool-core BCGs, and particularly of the mode of exposed star formation that we discuss in most of the cool-core BCGs. We must choose which is a more realistic estimate of obscured star formation in our targets. The ability of the Groves models applied in Donahue et al. (2011) to distinguish physically between low- and high-compactness environments of star formation is consistent with several other avenues of analysis discussed in that work and here (such as the temperature of the cool dust peak and the ratios of optical-UV estimates of exposed star formation to MIR dust-based estimates of obscured star formation), which disposes us to select $\mathrm{SFR}_{\mathrm{Groves}}$ as the estimate of obscured star formation. On the other hand, the Groves models are preliminary and do not cover a very wide range of parameter space, while the 24 μm calibrations are empirically determined using a broad range of star-forming targets, and there is no hazard of contamination from the extra source of heating which applies to the neon gas.

We tentatively elect to use SFR_{24} as the estimate of obscured star formation, but we will continue to investigate. Though there is a systematic offset of $\sim 4\times$ between the two estimates of SFR in the case of the star-forming cool-core BCGs with the weakest MIR continua, the discrepancy between SFR_{24} and the estimate of exposed star formation from optical-UV data is even larger. If we used SFR_{Groves} instead of SFR_{24}, our conclusions about how exposed the star formation is in many of the cool-core BCGs would be revised downward (particularly for targets like A2597), but they would still stand.

Finally, the fact that SFR_{24} exceeds SFR_{Groves} only in the case of A1068 makes sense when considering that A1068 is the only target that is likely to have significant MIR contribution from the light of an AGN (see §4.9).

4.8.5 An estimate of total SFR

The SFR_{I} column in Table 4.11 is the sum of the estimates of obscured star formation from the 24 μm continuum and exposed star formation from optical and ultraviolet continuum (see Table 4.2), and is thus an indicative estimate of total star formation. Calibrations of total star formation rates are usually based on a combination of Hα luminosity and a luminosity taken from either infrared or radio regimes such as L_{24} (Zhu et al. 2008; Kennicutt et al. 2009; Calzetti et al. 2010). For the most IR-luminous targets ($L_{24} \geq 5 \times 10^{43}$ erg s^{-1}), the optical extinction is so extreme that 24 μm alone can be taken as an estimate of total star formation (Calzetti et al. 2010). In our sample, PKS0745 approaches that category, and A1068 and A1835 lie well above that threshold, even if a significant fraction of the 24 μm light for A1068 were ascribed to heating from the AGN instead (see §4.9). As discussed in §4.4.1, we find the Hα evidence of star formation in our targets a promising corroboration of optical continuum evidence, but it is also subject to non-stellar ionization. Future work may focus on employing such a calibration, however, particularly for the closer members of the sample for which the extended Hα emission may be resolved (McDonald et al.

2011a).

In the case of 2A0335, the available $\mathrm{SFR_{opt}}$ from the literature was corrected for internal extinction and thus stands as an approximate measure of $\mathrm{SFR_I}$ on its own. Because the warm-dust continuum is so low in 2A0335, and $\mathrm{SFR_{24}}$ is correspondingly also very low, it does not make much difference whether we add $\mathrm{SFR_{24}}$ to $\mathrm{SFR_{opt}}$ to estimate $\mathrm{SFR_I}$ in this case.

Our estimate of $\mathrm{SFR_I}$ is tentative, resting on many assumptions. The optical component comes from a heterogeneous sample. $\mathrm{SFR_I}$ may be compared to $\mathrm{SFR_{Ne}}$, which is also a measure of total star formation (see Figure 4.16). As noted above, $\mathrm{SFR_{Ne}}$ should be considered an upper limit on total star formation, especially for MS0735, because of a possible second source of heating for the neon. Thus it is not surprising that we find that $\mathrm{SFR_{Ne}}$ generally exceeds $\mathrm{SFR_I}$. However, the two estimates are comfortably within our estimated margin of error (in total, about $3\times$), except for A2597, A0478, PKS0745, and MS0735.

In Figure 4.17, $\mathrm{SFR_{opt}}$ / $\mathrm{SFR_I}$ is plotted against $\mathrm{SFR_I}$, to demonstrate the degree of exposed star formation in the cool-core BCGs. While most of the light of star formation in A1068 and A1835 (marked with a 7 and a 9 respectively) is obscured, resulting in exposed star formation fractions as low as in normal star-forming regions, the rest of the cool-core BCGs have unusually exposed star formation. In these cases, $> 80\%$ of the light of star formation escapes in the optical and ultraviolet without being intercepted by gas or dust.

In an evolved BCG, the major source of fuel for star formation is material from the cooling flow. Therefore, it would be suspicious if the sustained total star formation rate exceeded the cooling rate (see Table 4.1). The discussion of the efficiency with which the cooling ICM of a cool-core galaxy cluster is converted into stars has changed

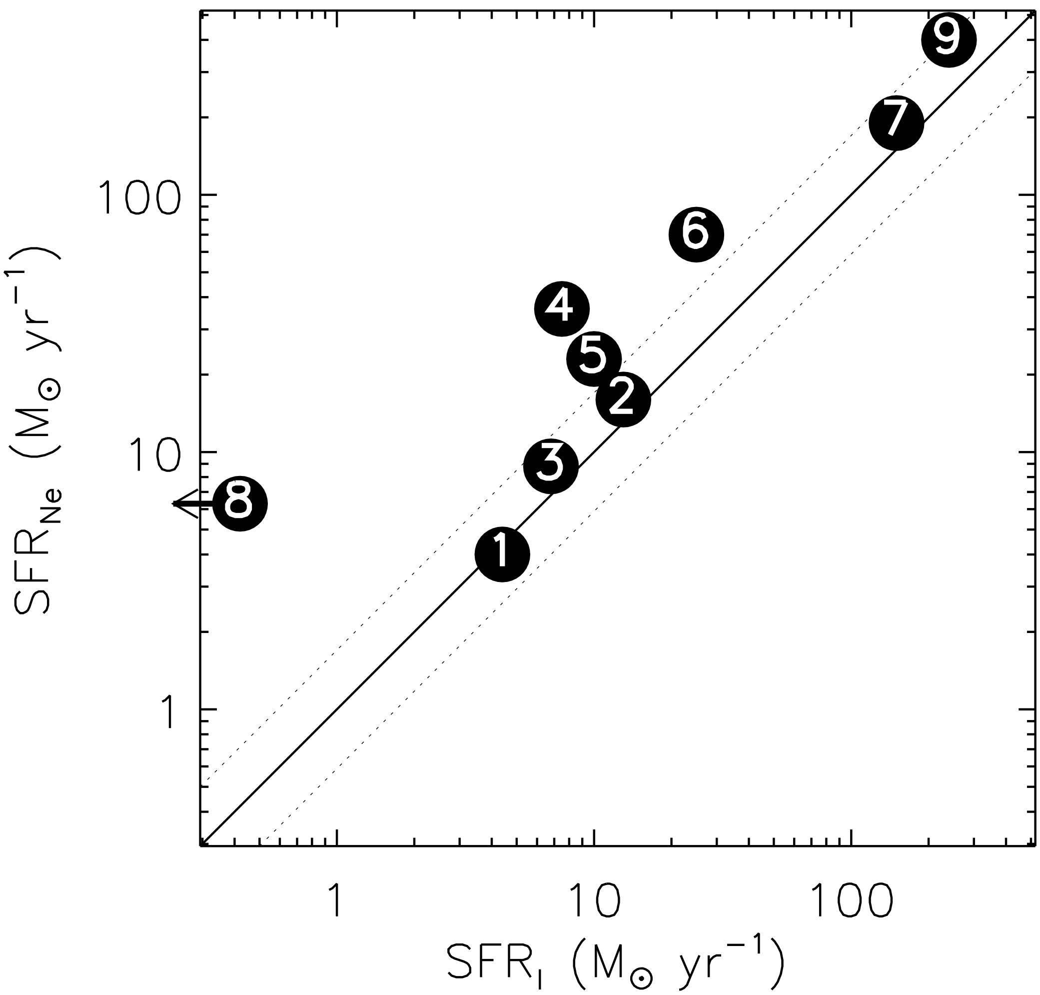

Fig. 4.16.— Estimates of total SFR based on the sum of the [Ne III] and [Ne II] emission lines (SFR_{Ne}) compared to those based on a combination of 24 μm and optical luminosities (SFR_I). The numbers within the black points correspond to those in Table 4.1. The solid line is unity, and the dotted lines show a scatter of a factor of 1.7×.

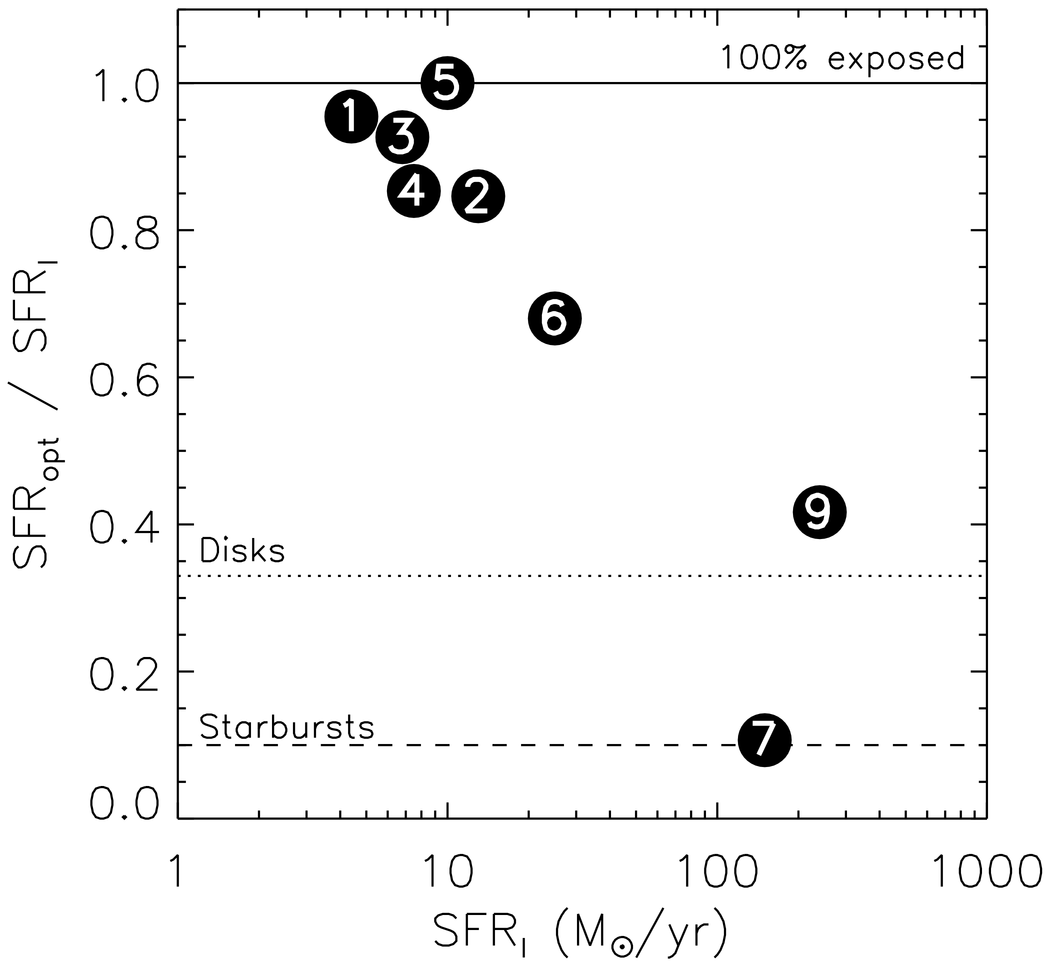

Fig. 4.17.— The ratio of $\mathrm{SFR_{opt}}$ to $\mathrm{SFR_I}$ (the exposed fraction of star formation) is plotted against $\mathrm{SFR_I}$. The numbers within the black points correspond to those in Table 4.1. The solid line represents completely exposed star formation; the dotted line represents the typical level of exposure for high-metallicity spiral disks; and the dashed line represents the typical level of exposure for starbursts.

dramatically as the originally estimated cooling rates have been reduced by about 90% to the current spectroscopically-determined rates of $\sim 10 - 200\ \mathrm{M_\odot\,yr^{-1}}$ (see Table 4.1).

A recent estimate of star formation efficiency in cool-core galaxy clusters, based on FUV and Hα observations without correction for intrinsic extinction, is a rate of 14% with a typical scatter of 10 - 50% (McDonald et al. 2011b). This is consistent with previous results (Rafferty et al. 2006; O'Dea et al. 2008; McDonald et al. 2010). We expect to find higher efficiencies in our sample because we also include obscured star formation in our estimates of total star formation rates, but since the star formation in six of our nine targets is mostly exposed, we do not expect great differences.

A comparison of the cooling rate with the estimated total SFR is displayed in Figure 4.18. For reference, efficiencies of 10% (the empirical minimum for the McDonald et al. (2011b) sample and our own, not including non-star-forming systems such as MS0735) and 100% (the line of unity) are overplotted with dotted and solid lines. Generally among our sample of cool-core BCGs, the cooling rate exceeds the SFR by a factor of several. The observed efficiencies for several systems (2A0335, A2597, A0478 and PKS0745) fall into the same regime as the McDonald et al. (2011b) sample, at $\sim 13 - 25\%$. We find higher efficiencies ($\gtrsim 80\%$) for the other systems. In the case of A1068 (marked with a 7), the SFR exceeds the cooling rate by a factor of 5. These high efficiencies naturally are of great interest and require confirmation. We examine these systems in turn.

In Hydra A and A1795, the 24 μm continuum is so weak (at least relative to the optical evidence for star formation and the PAH and atomic line emission) that the estimate of $\mathrm{SFR_I}$ is dominated by the exposed component, $\mathrm{SFR_{opt}}$ (see Table 4.11). Estimates of the star formation rate utilizing Hα yield rates of only $\sim 1\ \mathrm{M_\odot\,yr^{-1}}$

for these targets (see §4.4.1) compared to rates of $\sim 6 - 11$ $M_\odot\,yr^{-1}$ from optical continuum evidence. However, SFR_{Ne} is more consistent with the continuum rate, even if we assume that a significant fraction ($\sim 50\%$) of the neon is being excited by a source other than star formation. Both sets of measures of exposed star formation rates, continuum and Hα, are heterogenous and are drawn from a variety of apertures or originate in different star formation models. Homogeneous observations and conversions to the star formation rate would help to resolve such questions.

The major star-formers among our sample, A1835 and A1068, have even more extreme star formation rates relative to their cooling rates. There is no doubt that A1835 exhibits powerful star formation; by both obscured and exposed measures, the evidence is unambiguous. What is surprising is that a source which appears to be a starburst galaxy with all the hallmarks of obscured star formation has any optical signs of star formation. When Calzetti et al. (2010) derive a calibration for star formation rate, based upon L_{24} and Hα, targets as 24 μm-bright as A1835 are expected to reprocess all of the ultraviolet light of star formation into the infrared. This is evidently not the case for A1835. One source of uncertainty is the duration selected for calculating SFR_{opt} (see §4.4.2). It may be reasonable to go in either direction for A1835, but even if we selected a longer duration (900 Myr) with a correspondingly smaller star formation rate, SFR_{opt} cannot fall below 50 $M_\odot\,yr^{-1}$, and Hα indicates a SFR of 41 $M_\odot\,yr^{-1}$ (McNamara et al. 2006). When either is combined with SFR_{24}, the estimate of star formation efficiency still approaches 100%. Further exploration of the remarkable nature of star formation in this system is desirable.

In A1068, the estimate of SFR_I is driven by the BCG's great luminosity at 24 μm. Note that the optical and ultraviolet evidence for star formation in A1068 suggests a rate of only 16 $M_\odot\,yr^{-1}$ (consistent with Hα evidence, Rafferty et al. 2006) which is less than the cooling rate of 30 $M_\odot\,yr^{-1}$. It is possible that a longer duration of star formation is more appropriate, but changing this assumption would make little difference, because it would revise SFR_{opt} downward, and the 24 μm luminosity would still dominate.

Star formation in A1068 may be deeply embedded, like in a classical starburst. In that case, the efficiency of star formation relative to the cooling rate may exceed 100%. This is plausible if the BCG has a source of star formation fuel other than the cooling flow (such as significant stellar mass loss or infall of other cluster components) or if star formation is progressing in episodes which temporarily exceed the rate of fuel deposition.

Another explanation is that a non-stellar heating source such as an AGN is contributing to the thermal dust continuum, artificially raising SFR_{24} and thus SFR_I (see §4.9). Assuming that the cooling rate and SFR_{opt} are accurate, this heat source would have to be responsible for $> 90\%$ of the 24 μm continuum emission to lower the true star formation rate below the cooling rate (see Table 4.11). As discussed in §4.9, AGN activity is significant in A1068 but there is no evidence that the effects of AGN radiation (or any other non-stellar source of heating) dominates the MIR spectrum, so we find this explanation less plausible.

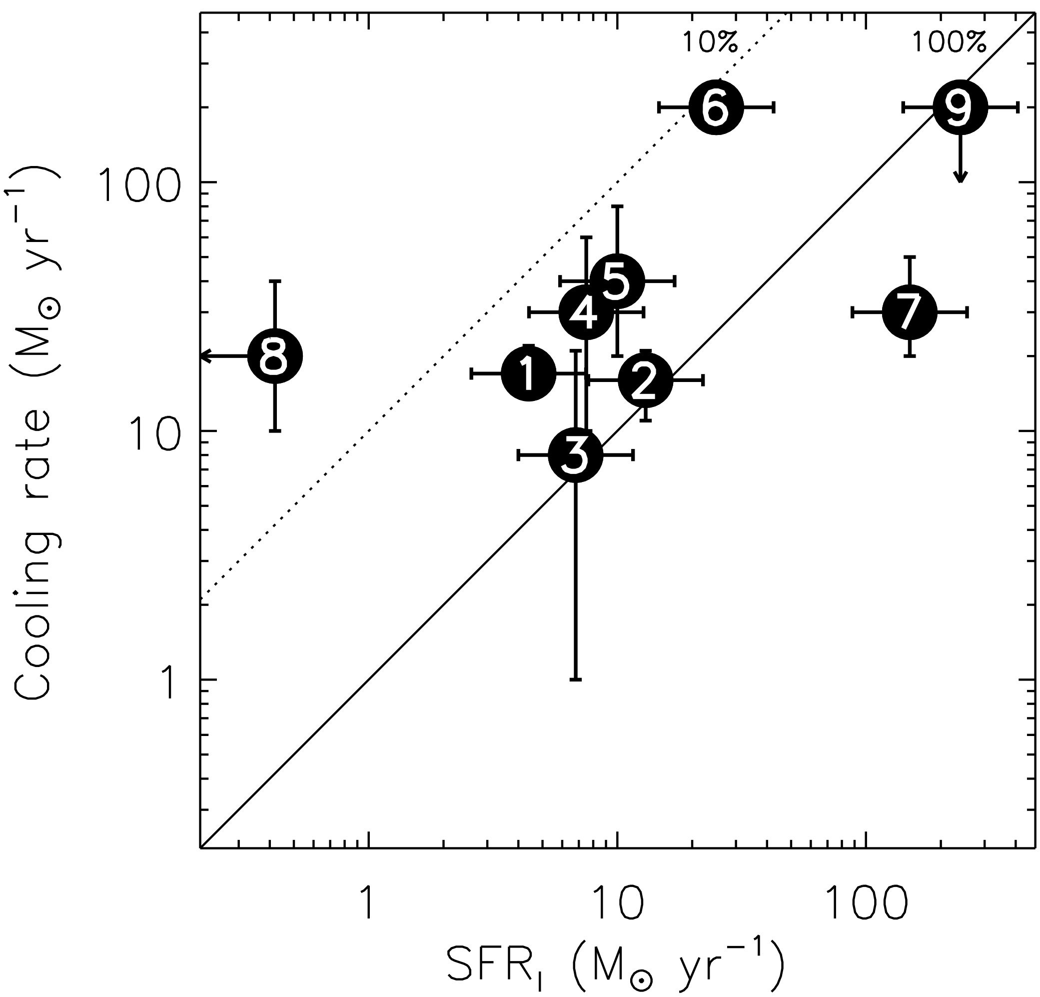

Fig. 4.18.— Total star formation rate estimate SFR_I from Table 4.11 (with uncertainties of 1.7×) compared to cooling rate $\dot{M}_{XS}$ from Table 4.1. The numbers within the black points correspond to those in Table 4.1. The solid line is unity (100% star formation efficiency), and the dotted line represents 10% efficiency.

4.9 AGN activity

When dust grains are located close enough to the nucleus, an AGN may dominate a galaxy's MIR spectrum with a power-law continuum rising to the red, sometimes with a break at about 15 μm (Weedman et al. 2005) (while a classical starburst has a continuum that continues to rise steeply to the red). Small dust grains do not emit as efficiently as larger ones, so at a given radiation field strength, the smaller grains will be hotter than the larger grains. Closer to the AGN, the small grains are hotter and more easily destroyed by sublimation. The strong continuum emitted by AGN-heated dust grains can nearly subsume line emission, particularly at low resolution. However, there is significant diversity in the MIR morphology of AGN systems. They often, but not always, feature a spectrum of emission lines including high-ionization transitions such as [Ne V]14.3 μm. AGN-dominated spectra may exhibit PAH emission features, but these are generally weak compared to starburst-dominated spectra.

Cool core BCGs commonly host AGNs, and are usually radio sources. Feedback from an AGN, wherein the cold gas condensing from a cooling flow provides the fuel to power the jet, is the most likely candidate for the mechanism that evidently maintains most of the overlying ICM in the neighborhood of the BCG at a high temperature.

The cool-core BCGs in this sample have evidence for AGN activity, including radio jets, X-ray cavities (including overlapping cavities and ghost cavities supporting the theory of interrupted cooling flow activity) (see Table 4.1), and some evidence for jet-induced star formation at the interface between the jet and the hot ICM (e.g., O'Dea et al. 2004; Rafferty et al. 2006; Fabian et al. 2006; Ogle et al. 2010).

A1068 hosts a more prominent AGN than most of the other cool-core BCGs in this sample. While optical and far-infrared observations of A1068 indicate the presence of massive stars (Allen 1995; McNamara et al. 2004; O'Dea et al. 2008; Edge et al.

2010b), optical line ratios and IRAC colors also indicate an unresolved red central source consistent with the presence of a dusty AGN (Crawford et al. 1999; Quillen et al. 2008). The discrepancy between the enormous rate of obscured star formation implied by the strong MIR continuum and the much smaller cooling rate for this system could be resolved if most of the MIR continuum is actually powered by an AGN (see §4.8.5). While the AGN appears to contribute significantly to the 24 μm light (Edge et al. 2010b), at this point we see no evidence that the AGN is capable of contributing 80% of the MIR continuum, or that the starburst is weak in A1068 relative to the AGN. Therefore, while considerable uncertainty remains, we still find the total estimate of star formation to be high relative to the cooling rate. We speculate that the rate of star formation may be irregular in A1068, and that it may be undergoing a major burst of star formation to use up a stockpile of fuel that has been slowly accumulating from the cooling flow.

Meanwhile, Hydra A is a well-known strong radio galaxy (included in the analysis of Ogle et al. 2010) with unusually high levels of radio feedback (McDonald et al. 2011a).

In the cool-core Perseus Cluster, the AGN dominates the nuclear spectrum of the BCG, NGC 1275 (Weedman et al. 2005), though that well-studied system is also sufficiently nearby to permit MIR spectral resolution of atomic and H_2 line emission in off-nuclear regions (Johnstone et al. 2007). The off-nuclear MIR spectra of NGC 1275 bear a strong resemblance to several targets in our sample, though in the case of our targets, our apertures include any significant nuclear continuum emission.

None of the MIR spectra of this sample of cool-core BCGs display conclusive evidence for the influence of AGN radiation. Furthermore, the extended star formation observed in most of these targets is at large distances from the nucleus ($\sim 6-50$ kpc) where the radiation field from the AGN is expected to be weak.

The high ionization lines that are strong indicators of AGN activity are largely absent or weak. While we note that these lines are often weak enough to be difficult to detect in low-resolution spectra of classical AGN, they are reliably detected in the most powerful AGN (Weedman et al. 2005). The high-ionization emission line of [Ne V] at 14.3 μm, with an ionization potential of 97.1 eV, is only securely detected in Hydra A and A1835, and [Ne V]24.3 μm is not detected in any cases. [O IV]25.9 μm is a firm signature of AGN activity, but at low resolution it is blended with [Fe II]26.0 μm. The combined feature is detected in Hydra A and PKS0745.

As discussed in Donahue et al. (2011), the ratios of PAH features do not show evidence of trauma from a hard radiation field or sputtering from the hot ICM in most of the BCGs, with the exception of A1068, where the ratio of PAHs at 17 and 11.3 μm indicates the preferential destruction of smaller grains by an agent like the AGN or the hot ICM.

While all of the BCGs in this sample host AGN, radiation from the nucleus does not affect the MIR spectra (except perhaps in A1068). The gas and dust that produce the MIR spectra are not close enough to the AGN to display its signature.

4.10 Dust temperature in CC BCGs

The longwave broadband photometry of the MIPS camera permits the examination of continuum emission from larger and cooler dust grains than those that produce the 24 μm continuum. The 70 μm data point in the SEDs of Figs. 4.4 - 4.6 demonstrates that the SED rises sharply above 30 μm, even in the targets with unusually flat and low MIR continua. The luminosity at 70 μm is correlated with star formation, though with considerably more scatter than the emission at 24 μm (Calzetti et al. 2010).

The ratio of the 70 μm to 24 μm bands (see Table 4.10) yields a diagnostic of the temperature of the dust peak. A cooler dust peak is associated with a larger ratio, as the peak moves out to 70 μm and beyond.

Figure 4.19 is a histogram of the L_{70}/L_{24} ratio for our sample, excluding MS0735 (see Table 4.10), plotted with the SINGS sample (Dale et al. 2007). For a plot of the same ratios against L_{24}, compared with the star-forming galaxies and LIRGS of Calzetti et al. (2010), see Donahue et al. (2011, Fig 7).

While this ratio for most of our targets falls in the normal range for star-forming galaxies, 2A0335, A2597 and A478 have a much cooler dust peak (and higher L_{70}/L_{24} ratio) than normal for star-formers. These three targets are among those with unusually weak indicators of obscured star formation, and low modeled compactness parameters (Donahue et al. 2011) (and see discussion above).

4.11 Conclusions

This sample significantly expands the available library of MIR spectra of BCGs in cool-core galaxy clusters, to a total of thirteen (Egami et al. 2006a; Johnstone et al. 2007; Ogle et al. 2010). All nine are powerful sources of rotational H_2 emission, dis-

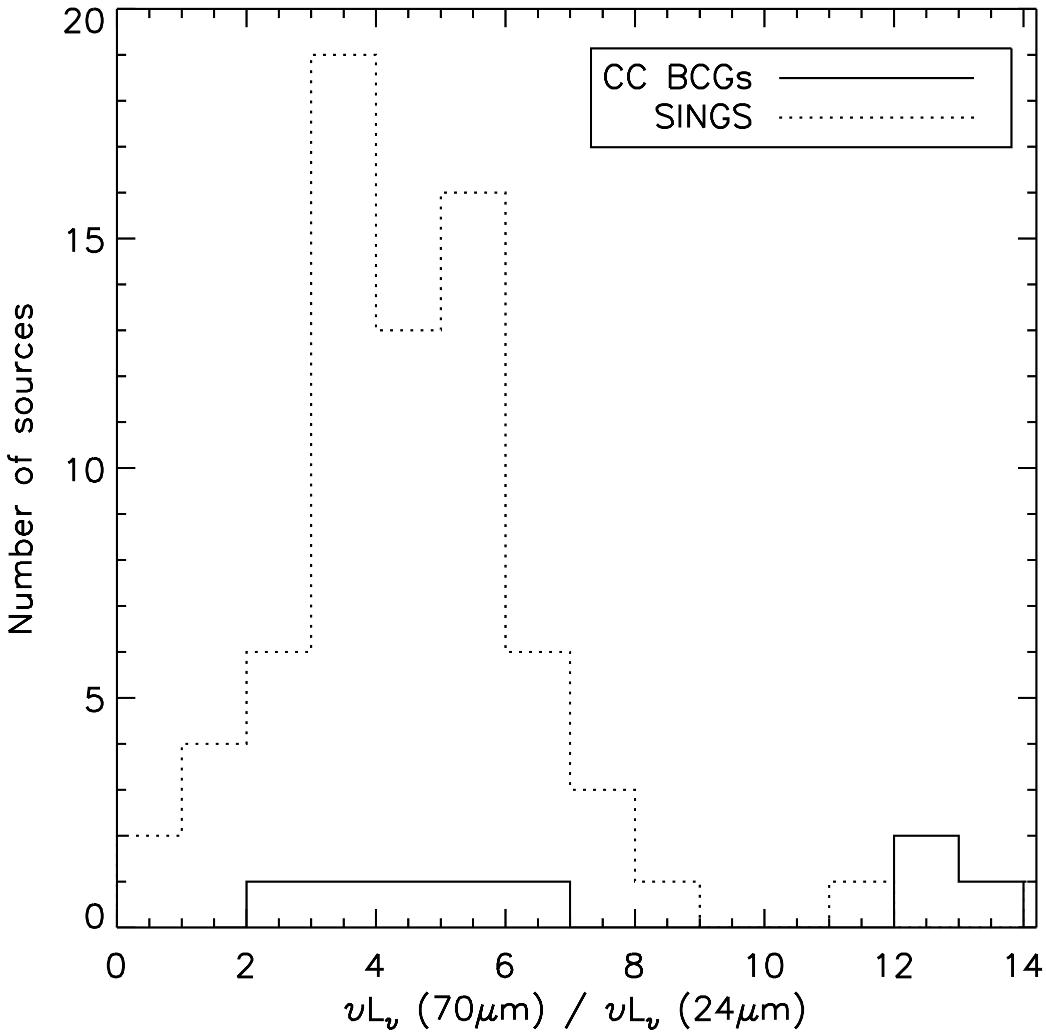

Fig. 4.19.— Histogram of L_{70}/L_{24} for CC BCGs and SINGS sample. For BCG values, see Table 4.10.

cussed in Donahue et al. (2011) and Chapter 5, and feature unresolved low-ionization emission lines such as [Ne II] 12.8 μm.

In all targets, the ratio of the moderately ionized emission line of [Ne III] 15.5 μm to [Ne II] indicates a radiation field weaker than seen in the nuclei of the nearby star-formers of the SINGS sample, but typical or slightly higher than found in starbursts and ULIRGs. (MS0735 is consistent with an even softer radiation field.) The SINGS ratios are high probably because of aperture effects; in the other categories (our targets, starbursts, and ULIRGs), the aperture covers a larger volume including ionized gas more distant from the source of light, softening the measured radiation field.

MS0735 is an outlier among our sample in that it shows no indication of star formation at all. Features in its spectrum like the PAH at 11.3 μm may be stimulated by the soft radiation field of an old stellar population, as in the case of dusty, non-star-forming elliptical galaxies. As in those targets, the ionized gas responsible for the [Ne II] emission line may be heated by the nuclear source (Kaneda et al. 2010), but we propose that the hot ICM is conducting into a set of extended filaments and heating up the H_2 and atomic gas, producing the rotational H_2 and low-ionization atomic emission lines (Fabian et al. 2011a). MS0735 may share these morphological properties with the rest of the sample, but with no active star formation (McNamara et al. 2009).

We divide the rest of the sample up into two main categories of star formation (extended, exposed star formation, and a combination of extended star formation with nuclear starburst activity), all primarily fueled by the cooling flow, with the following summary of features and interpretation.

A1068 and A1835 show the MIR hallmarks of classic and powerful star formers including a strong 24 μm continuum consistent with star formation rates of > 100 M$_{\odot}$ yr^{-1}. PAH emission is strong, especially in A1835, and is generally consistent in profile with normal star formation (for example, the high ratios of PAH 7.7 / 11.3 μm indicate an intense environment of star formation). A1835 in particular has a MIR morphology which resembles normal star-formers except perhaps in its extraordinary luminosity. The data are consistent with the presence of a nuclear or circumnuclear starburst in these two targets. The strong H_2 indicates that these two targets may also have extended structures, where the same type of exposed star formation as the rest of the sample could be occurring. This may explain why A1835 has a strong MIR continuum, typically associated with heavily obscured starburst activity, but also has the optical and ultraviolet indicators of vigorous exposed star formation (~ 100 M$_{\odot}$ yr^{-1}). PAH and neon emission may arise in both sites of star formation, and star formation rates estimated from either type of feature are on the same order as the total amount of star formation estimated from optical and 24 μm light (though neon is stronger, probably because of an additional non-stellar source of heating such as energetic particles from the ICM). Star formation efficiency in A1835 is at 100% of the cooling rate. A1068 may be similar, but has significantly weaker PAHs than A1835 and shows some signs of processing of smaller PAH molecules (Donahue et al. 2011). This source remains something of a mystery in that it has a low cooling rate and thus only a trickle of fuel for star formation (consistent with the observed PAHs), and only moderate AGN activity, yet a very strong MIR continuum whose heating source is thus not understood. The star formation in this target is mostly obscured (if the 24 μm continuum does in fact trace star formation) and is progressing at a rate five times higher than the cooling rate.

The other six BCGs generally fall into a single category as described below, though in some respects Hydra A and PKS0745 form an intermediate category between obscured and exposed star formation. All six generally share the following properties (as well as the ones listed above which are common to the sample):

- Firm optical and ultraviolet evidence for exposed star formation at about $\sim 10\ M_{\odot}\,yr^{-1}$. Spatially resolved optical-UV imaging and spectroscopy of some of the nearer BCGs conclusively indicates that star formation is progressing in extended knots or in chains of H II regions along filaments that, in some cases, are associated with the edges of the radio lobes or the footprint of the radio jet upon the overlying ICM.

- Relatively weak PAH emission. Equivalent widths of the 6.2 μm feature are far lower than in normal star-forming systems. PAH emission is also weaker, compared to neon emission, than observed in normal star formation (this may be due to a second source of heat for the neon emission, which will be discussed in more detail in Chapter 5). The work of (Donahue et al. 2011) indicates that smaller PAHs have not been preferentially destroyed (except perhaps in A2597) and the relatively low ratios of 7.7 to 11.3 μm PAHs is consistent with PAHs in the quiescent ISM. Star formation rates derived from PAH emission ($\sim 1-40\ M_{\odot}\,yr^{-1}$ for this category) are meant to be used as a metric of relative PAH strength rather than as a realistic estimate of star formation rate. The weak PAH emission indicates that the PAHs are further from newly formed stars than in normal star-forming morphologies, and are not experiencing significant heating or destruction from other sources of energy in the cool-core BCG environment.

- Very weak MIR longwave continua. The source of continuum emission is small dust grains, most likely heated by star formation. Star formation estimates based on the 24 μm continuum luminosity measure the degree of obscured star formation ($\sim 0.5 - 8$ $M_\odot\,yr^{-1}$). There is less obscured star formation than exposed star formation in these targets. (If we assume that the calibration of obscured SF based on 24 μm does not apply to the low-compactness environment of star formation in these targets, and apply the SFR based on starburst SEDs instead, the rate of obscured SF increases but still falls short - barely, in the case of A2597 - of the rate of exposed SF, and the overall efficiency of star formation increases.) We compare star formation estimates from neon, PAH, and MIR continuum features as a metric of the relative strengths of those components, and find that the continuum is weak relative to the PAH emission (indicating that the young stars heat the dust even less efficiently than the PAH molecules in these systems) and especially relative to the neon emission (because the neon may trace both obscured and exposed star formation).

- The sum of SFR_{opt} and SFR_{24} is an estimate of the total star formation rate in the cool-core BCGs (SFR_I). It is in generally good agreement with SFR_{Ne}, though the neon is significantly overluminous in several cases, perhaps caused by a non-stellar heating source for the neon (Donahue et al. 2011). SFR_{opt} exceeds SFR_{24}.

- Relative to the cooling rate based on X-ray spectroscopy, SFR_I suggests a moderate to high efficiency of star formation from fuel delivered by the cooling flow ($13 - 80\%$).

- High ratios of $\nu L_\nu(70\ \mu m)$ / $\nu L_\nu(24\ \mu m)$ for several BCGs of this category suggest an unusually cool dust population relative to normal star-formers.

The subluminous warm dust continuum in the majority of BCGs in this sample is the most dramatic indicator among a collection of clues pointing to a picture of an abnormal morphology of star formation in cool-core galaxy cluster BCGs. While some cool-core clusters (A1835, A1068) appear to have a starburst progressing at their heart, and others have entirely quenched star formation (MS0735), the majority have solid optical and ultraviolet evidence for moderate levels of exposed star formation and weak indicators of obscured star formation.

The evidence is not consistent with star formation progressing in a familiar dense, disk-like volume or other normal morphology with young stars embedded within large molecular cores, as found in spirals and starbursts. In those environments, the absorption of optical-FUV light from young stars typically ranges from $\sim 66 - 90\%$ (see §4.2.1). However, in many cool-core BCGs (notably 2A0335, Hydra A, A1795, A2597, and A0478), we find that only $\sim 4 - 15\%$ of the light of star formation is reprocessed into the MIR by small dust grains (the ratio of SFR_{24}/ $\mathrm{SFR}_{\mathrm{I}}$ from Table 4.11).

Two of the models of star formation discussed in §4.2.1 are consistent with this evidence: jet-induced star formation at the interface between the radio-bright structure and the ICM, and extended filaments of star-forming material outside the main body of the BCG. In some cool-core BCGs, there is optical evidence for both types of extended star formation at once, so we do not attempt to separate the mid-infrared evidence for the two models in this work. Both models are associated with the cooling flow (which provides the majority of the fuel of star formation) and the jet from the AGN (which induces star formation via shocks, or may provide the energy to supply the inner region of the ICM with dust from the BCG, dredging the dust up with buoyant radio bubbles). We suggest that the model of NGC 1275 proposed by Fabian et al. (2011a), describing a network of filaments (up to 50 kpc long and ~ 100

pc wide) with a complex, magnetically supported substructure of molecular threads only ~ 0.3 pc in diameter, also applies in these targets, and provides an optically thin environment of star formation. The star formation rates based on optical evidence from extended regions represent most of the star formation in these targets.

We propose that in this environment, dust and PAH molecules are exposed to only a fraction of the light of young stars, allowing most of the UV light to escape in the lateral direction unattenuated. This explains why the PAH emission (especially from smaller, ionized PAH molecules) is weak, and thermal emission from small warm dust grains is even weaker. The extended regions are too far from the nucleus for the dust and PAHs to experience significant radiation from the AGN. This model is also consistent with the unusually cool dust profile in several of these targets, and with the undisturbed (relative to normal star-forming regions) character of the PAHs (Donahue et al. 2011). However, this model requires that the dust and PAHs also escape major trauma from any other source of heat, suggesting that sources of energy in the extended filaments such as conduction or X-ray heating from the ICM, cosmic ray heating, or MHD waves do not have much impact on dust and PAHs.

This model is consistent with the conclusions of Donahue et al. (2011) that the strong emission from low-ionization atomic lines arises in part from the same source of heat as the weak thermal dust emission (namely, star formation) but also receives a boost from non-stellar heating (probably energetic particles from the ICM). The H_2 emission is also well above the level expected in a normal star-forming environment and experiences the same additional source of heat as the atomic gas, as discussed in Chapter 5.

Meanwhile, A1068 and A1835 may have all of the same morphology, in addition to a powerful obscured starburst in the core, and MS0735 may have the same morphology without any active star formation.

After decades of effort to resolve the discrepancy between high cooling rates and low star formation rates in the centers of cool-core galaxy clusters, the cooling rates have been refined downward, and star formation rates have been slightly increased by the addition of mid-infrared evidence, to the point where they have finally come into close agreement. It is normal for cool-core BCGs to have significant exposed star formation in their filamentary networks. However, the observed efficiency of star formation is surprisingly high, even exceeding the cooling rate in the case of the extremely MIR-luminous cluster A1068.

Chapter 5

Warm Molecular Hydrogen in Cool-Core Galaxy Clusters

5.1 Abstract

This third paper in a series on the IRS spectra of a set of nine cool-core BCGs examines the luminous pure rotational H_2 emission, which may be located in a filamentary network associated with Hα emission. We perform excitation analysis to find temperatures and masses of warm H_2, and compare to other luminous sources of warm H_2 emission. We contrast with other MOHEGs, in which H_2 is generally heated by shocks, and consider whether shocks or energetic particles from the ICM are more likely to heat the H_2 in the filaments. We test the efficiency of the H_2 heating relative to the power of star formation, and find that H_2 shares a heating source other than star formation with weakly ionized atomic gas (confirming but revising an earlier result). There are inconsistencies between our data and the type of shocks that power other MOHEGs, and our data are consistent with the energetic particle model, but we do not rule out shock heating.

5.2 Introduction

5.2.1 Molecular hydrogen

The massive reservoirs of cold molecular gas that harbor star-forming regions are difficult to detect directly. Molecular hydrogen, the most abundant molecule in the universe, forms most efficiently in the interstellar medium in the presence of small dust grains (Fabian 1994). It is vulnerable to dissociation by ultraviolet radiation but can survive considerably longer within a dense molecular cloud, where cosmic rays are the main destruction mechanism (Black & Dalgarno 1976). The molecule has no permanent dipole moment and is therefore nearly invisible, though quiescent clouds may be detected in ultraviolet absorption lines (Black & van Dishoeck 1987). In all but the most primordial gas, the metallicity is sufficiently enriched to permit the formation of carbon monoxide (CO) molecules. The detection of CO (Lazareff et al. 1989; Edge 2001; Salomé & Combes 2003) traces the presence of a larger reservoir of quiescent H_2 (Solomon et al. 1987).

H_2 may be detected in emission, however, when disturbed. It may be excited via absorption of ultraviolet photons at wavelengths longer than 912 Å, resulting in dissociation in only 10% of such events. Surviving molecules populate excited rovibrational levels via fluorescence, and eventually decay, on timescales of 10^6 s (Black & van Dishoeck 1987). The cascade is referred to as ultraviolet pumping. H_2 may also be excited or ionized by X-rays and cosmic rays, or be excited during hot formation upon grain surfaces, particularly deep within molecular clouds, followed by a rovibrational cascade (Black & Dalgarno 1976). As discussed below, shocks are also an important heating mechanism for H_2.

The pure rotational and rovibrational quadrupole series of H_2 emission lines, arising in the mid- and near-infrared (MIR and NIR) respectively, serve as important cooling channels for warm molecular gas. Like CO, the warmer phases of H_2 represent only a small fraction of the total mass of the cold gas reservoir, but the transitions associated with the warm H_2 serve as useful tracers. The warm H_2 transitions are also an energetically important coolant for star-forming regions, though not as dominant as [O I] 63 μm, [C II] 158 μm, and [Si II] 34.8 μm (Roussel et al. 2007), and can dominate other coolants in shocked environments and the ISM of radio galaxies (Ogle et al. 2010), perhaps facilitating accretion onto a central active galactic nucleus (AGN). Pure rotational transitions, corresponding to emission lines between 5 and 30 μm, arise from warm gas at temperatures between 100 and 1000 K, while the rovibrational lines originate in hot gas at temperatures between 1000 and 2000 K.

These temperatures may be maintained by intense ultraviolet emission, such as in a photodissociation region (PDR) (Tielens & Hollenbach 1985; Shaw et al. 2009), or by collisional excitation such as in shock-heated gas (Black & van Dishoeck 1987).

The warmer phases of molecular hydrogen have been used to trace star formation itself. While the transitions are highly forbidden and the lines are therefore relatively faint, they are detected in PDRs in normal star-forming regions at a small fraction of the total infrared ($3 - 1100\ \mu$m) power: $L(H_2)/L_{IR} \sim 6 \times 10^{-4}$ (Roussel et al. 2007) where $L(H_2)$ is the sum of the three lowest energy pure rotational transitions. H_2 emission has also been found in ULIRGs, and found to be consistent with an origin in PDRs or perhaps in a massive circumnuclear dusty torus (Higdon et al. 2006). In other ULIRGs, it has been explicitly disconnected from PDRs and probably arises from large-scale shocks (Zakamska 2010).

5.2.2 MOHEGs

Surprisingly powerful emission from warm H_2 has been found in the LIRG NGC 6240 (a late stage major merger and a starburst) (Joseph et al. 1984; Armus et al. 2006), in the shock front in the strongly interacting galaxy group Stephan's Quintet (Appleton et al. 2006), in $\sim 30\%$ of radio galaxies at $z < 0.22$ (Ogle et al. 2007), and in the cool-core central galaxy ZwCl 3146, discussed below (Egami et al. 2006a). MIR spectra dominated by H_2 emission lines led to the establishment of a category of highly luminous molecular hydrogen emission line galaxies (MOHEGs) with $L(H_2)/L_{IR} > 10^{-3}$ (Ogle et al. 2007). The lack of significant star formation in these targets indicates a major source of H_2 emission disengaged from the processes of star formation. Many dusty elliptical galaxies fall into the same category (Kaneda et al. 2008).

The distinction between MOHEGs and sources of H_2 associated with star formation becomes even more clear when the category is redefined as those targets with $L(H_2)/L_{PAH7.7} > 0.04$ (Ogle et al. 2010; Guillard 2010) where $L(H_2)$ is the summed luminosity in the pure rotational series between H_2 0-0 S(0) and H_2 0-0 S(3).[1] $L_{PAH7.7}$ is the luminosity of the broad polycyclic aromatic hydrocarbon feature at 7.7 μm, a useful indicator of star formation activity. This definition of the term MOHEG permits easier classification when FIR data are not available, and is robust across many decades of L_{24}, but also changes the significance of the category (because $L_{PAH7.7}$ may not trace the same energetic processes as L_{IR}).

The category is broad, covering many diverse sources of H_2 emission, and empirical. A unifying factor may be the heating mechanism. Many MOHEGs are linked with interactions or merger activity, including Stephan's Quintet and most of the radio MOHEGs of Ogle et al. (2010). Shocks are certainly responsible for heating the H_2 in these targets. In the case of the radio MOHEGs, the gas has been delivered to the central region of the galaxy by interactions, and then heated by shocks from radio-jet-driven outflows. Star formation, X-ray heating, and the UV emission of AGN have been ruled out as sources of heat in the radio MOHEGs, though cosmic rays are still a distant possibility (Ogle et al. 2010). Note that while star formation is demonstrably not the main heating source for the H_2 in any of these targets, it is possible for shocks to drive both H_2 emission and knots of star formation (Beirão et al. 2009). Shock heating has also been tentatively linked to the warm H_2 emission in other MOHEGs. Ogle et al. (2010) propose that H_2-luminous dusty elliptical galaxies are radio galaxies in a quiescent phase between radio-jet outbursts, and that radio galaxies that are the BCGs of cool-core galaxy clusters have sufficient jet cavity power to produce the H_2 luminosity. In NGC 6240, the H_2 probably arises from slow shocks

[1] This work focuses on the pure rotational emission series; thus, the 0-0 designation is not included but assumed in all following notation. The number S(#) is the lower rotational level J_{lower}, with $\Delta J = -2$ (Hewitt et al. 2009).

between the two galaxy nuclei (Armus et al. 2006). Egami et al. (2006a) found that while a variety of shock mechanisms are required to produce the spectral morphology seen in the cool-core BCG ZwCl 3146, shocks are a plausible heating mechanism.

The significance of the category of MOHEGs may turn out to be that they are all sites of major shock activity. However, the presence and character of shocks in these targets is far from established, and there are many candidates for the H_2 heating mechanism, including non-radiative sources such as cosmic rays, dissipative magnetohydrodynamic (MHD) waves, or conduction from the surrounding hot ICM (Ferland et al. 2008, 2009).

5.2.3 H_2 in cool-core BCGs

The subject of this paper (the third in a series, following Donahue et al. (2011) and Chapter 4) is the luminous pure rotational H_2 emission in a sample of nine elliptical brightest cluster galaxies (BCGs)[2]in the centers of cool-core galaxy clusters. The hot intracluster medium in about half of nearby galaxy clusters has a relatively short cooling time ($\lesssim$ 1 billion years) and low entropy ($K = kTn_e^{-2/3} < 30$ keV cm^{-2}). These clusters, featuring cusps of cool, dense X-ray emitting gas in their centers, are called "cool-core" galaxy clusters and feature a much higher incidence of star formation than non-cool-core galaxy clusters (Fabian 1994; Cavagnolo et al. 2008; Rafferty et al. 2008; Hudson et al. 2010). It is now known that a negative feedback mechanism, probably in the form of AGN feedback, acts to prevent $\sim 90\%$ of the hot gas from cooling down (McNamara & Nulsen 2007). However, the gas that escapes the feedback mechanism is able to cool (referred to as a cooling flow, though this is not the catastrophic cooling event first proposed in cooling flow theory) and fuels star

[2]We refer to most of our targets by the name of the galaxy cluster, though our observations are limited to the region of the BCG.

formation in the BCG.

Star formation rates (SFRs) of up to $\sim 100\ \mathrm{M}_\odot\,\mathrm{yr}^{-1}$ are derived from optical and ultraviolet continuum and emission line observations (Johnstone et al. 1987; McNamara & O'Connell 1989; Fabian 1994; Crawford et al. 1999; Donahue et al. 2010; McDonald et al. 2011b). In some resolved cool-core clusters, the star formation is occurring in knots and filaments (Koekemoer et al. 1999; Conselice et al. 2001; Martel et al. 2002; Donahue et al. 2007a; Fabian et al. 2008; O'Dea et al. 2010; McDonald et al. 2010), and there is evidence that in some cases the star formation traces the edges of radio cavities (van Breugel et al. 1984; McNamara & O'Connell 1993; McNamara et al. 1996; Koekemoer et al. 1999; Conselice et al. 2001; O'Dea et al. 2004; Donahue et al. 2007a; McDonald et al. 2010). Observations of far-infrared excesses also support the correlation between cool-core galaxy clusters and star formation in the BCGs (O'Dea et al. 2008). However, the weak MIR signatures of star formation in many cool-core BCGs suggest that the star formation is not occurring in a normal (centrally concentrated, heavily obscured) environment and that the star-forming regions have a morphology subject to less obscuration than in typical star-forming galaxies (see the second paper in the series, Chapter 4).

Both rotational and rovibrational H_2 emission have been detected in cool-core galaxy clusters and are sometimes associated with the interaction between molecular gas deposited by the cooling flow and jet activity in the BCG (Jaffe & Bremer 1997; Falcke et al. 1998; Edge et al. 2002; Egami et al. 2006a). The H_2 emission is found to be extended in some cases (Jaffe et al. 2005; Johnstone et al. 2007) and to be associated with optical emission line filaments (Donahue et al. 2000; Johnstone et al. 2007). There are indicators of star formation and warm H_2 emission in most cool-core cluster BCGs (Egami et al. 2006a; Donahue et al. 2011) (and see Chapter 4).

However, the strength of H_2 emission in cool-core galaxy clusters is generally not correlated with the strength of the warm dust continuum arising from obscured star formation, though each are correlated with low-ionization line emission in the MIR (Donahue et al. 2011, the first paper in the series). The H_2 is strongly correlated with low-ionization neon emission even when both are scaled by the strength of the 24 μm continuum. The implication is that the H_2 and the ionized atomic gas have a source of heat that boosts their emission above what is expected (relative to the thermal dust continuum) in a normal star-forming environment.

In this paper we will compare our sample of cool-core BCGs to the radio MOHEGs discussed in Ogle et al. (2010). That sample includes four cool-core BCGs (including Hydra A, which appears in this sample). The radio MOHEGs typically have weak indicators of star formation, while our sample of cool-core BCGs, with the exception of MS0735, have star formation rates in the range $5 - 200$ $M_\odot\,yr^{-1}$ (Chapter 4). We will discuss whether shocks, the heating mechanism for the H_2 in the radio MOHEGs, are also likely candidates in our cool-core BCG sample.

The closest and best-studied cool-core galaxy cluster, the Perseus Cluster, hosts a BCG (NGC 1275) with a complex morphology, including a beautiful extended filamentary network of ionized gas (Minkowski 1957; Conselice et al. 2001). Some of the Hα filaments also have optical-UV continua indicating the presence of ongoing star formation, while others clearly do not host star formation (Canning et al. 2010). The filaments have a MIR spectrum dominated by atomic and molecular hydrogen emission (Johnstone et al. 2007) and a powerful AGN that dominates the nuclear MIR spectrum (Weedman et al. 2005). Even in the nuclear region, H_2 emission is detected (Ogle et al. 2010). The mass of warm H_2 ($>$ 100 K) represents a small fraction (about 10^{-6}) of the mass of cold gas (Ferland et al. 2008, 2009). NGC 1275 (or 3C 84) also appears among the radio MOHEGs discussed in Ogle et al. (2010).

5.2.4 Models of H_2 filaments in cool-core BCGs

Based upon NGC 1275, an emerging theory of H_2 in cool-core galaxy clusters describes complex, magnetically-supported filaments of molecular and dusty gas in thermal equilibrium. As observed in many cool-core BCGs, the filaments may extend up to 50 kpc in length but are only 100 pc wide, suggesting that magnetic support is a factor (Martel et al. 2002; McDonald et al. 2010). Magnetic support is possible even for largely neutral bodies of gas, if residual ionization from the neighboring X-ray-emitting ICM provides enough of a binding link (Fabian 1994). In NGC 1275, the filaments start to become resolved at scales less than 70 pc. The mean density within the filaments is ~ 2 cm^{-3} (Fabian et al. 2008; Ferland et al. 2008, 2009).

Models of NGC 1275 describe a delicate substructure, as yet unresolved by observation. The filament volume filling factor is low ($\sim 10^{-5}$) with molecular gas concentrated into distinct threads, each only 0.3 pc in diameter, with an average of 10 pc between each thread (Fabian et al. 2011a). Density in the molecular threads can reach $\sim 10^5$ cm^{-3}, and it is along those threads that chains of H II regions may form stars (though observations indicate that not all molecular filaments host star formation). Each thread is sheathed in a lower-density halo of ionized gas. The magnetic field acts as a shield protecting the filaments, but the most likely source of heat for both the Hα and warm H_2 emission is the penetration of hot ICM particles through the magnetic field and into the filaments (Fabian et al. 2011a).

Shock activity is not required to produce the H_2 emission in this model, though they are certainly present in association with the nuclear radio jet (Fabian et al. 2006; Ogle et al. 2010). Shocks have been considered (along with other non-stellar sources of heat) as the source of ionization for Hα and H_2 emission in other work on NGC 1275, with no consensus (McNamara et al. 1996; Conselice et al. 2001; Johnstone et al. 2007; Fabian et al. 2008; Ferland et al. 2008; Salomé et al. 2008a; McDonald et al. 2011b). There is some evidence that slow continuous shocks are associated with the warm H_2 emission in the cool-core BCG ZwCl 3146 (Egami et al. 2006a). We consider both shocks and energetic particles from the ICM as the most likely sources of H_2 heating in cool-core BCGs, though a thorough shock analysis is beyond the scope of this work.

In Chapter 4, we argue that the Fabian et al. (2011a) model is applicable to the characteristics of star formation in the nine cool-core BCGs in our sample (including one target with no detected star formation and two which appear to also have a classical starburst, which is probably located within the BCG). In this work, we examine the H_2 in these targets in comparison to other strong sources of H_2 and with consideration of this model.

The filaments in cool-core BCGs probably form as part of the cooling flow, as gas at the cooling radius collapses into filamentary structures on its inward fall (Canning et al. 2010; McDonald et al. 2010, 2011a). Interaction with the rising radio bubbles observed in many cool-core BCGs may sculpt the filaments. However, it is possible that the filaments form in the wake of the buoyant bubbles, dredged out of the BCG rather than forming from the cooling flow (Churazov et al. 2000) or that they where the radio lobes interact with the hot ICM or via galaxy mergers (Kenney et al. 2008; Ogle et al. 2010). We consider the metallicity and dust content in the filaments. Though star formation in many our cool-core BCGs is unusually obscured, heating up dust less than in normal star formation, we observe thermal dust emission associated with star formation (Donahue et al. 2011) (and see Chapter 4). We proposed in

Chapter 4 that the weak thermal dust continuum is caused by geometry rather than the absence of dust in the star-forming region. Dust is likely to be a necessary component of warm H_2 emission regions, in order to create enough H_2 to maintain the abundance in the face of predicted destruction rates in proximity to the hot ICM or shocks (Ogle et al. 2010). While the gas in the inner regions of the hot ICM has been processed by earlier generations of stars and has a metallicity of $\sim 0.3 - 0.5$ $Z_\odot$ (Fabian 1994; Hudson et al. 2010), the origin of dust in extended filaments is not so clear. Dust mainly forms in the stellar winds of low-to-medium mass stars in the AGB phase, and is expected to originate in the BCG rather than from the hot ICM. If the filaments are dredged up from the BCG by buoyant radio bubbles, the dust was brought up at the same time. If the filaments form from the cooling flow, they probably contain dust because the entire inner region of the cooling ICM was injected by dust dredged up from the BCG by jet activity; it is also possible that the dust is generated from the stars forming in the filaments (Hansen et al. 1995)

All computations in this paper assume a Hubble constant of 70 km $s^{-1}Mpc^{-1}$ and the cosmological parameters $\Omega_M = 0.3$ and $\Omega_\Lambda = 0.7$.

5.3 Observations and data reduction

The *Spitzer* IRS observations of the cool-core BCGs took place in 2005 and 2006 under *Spitzer* Program IDs 20345 and 3384, encompassing all four low-resolution ($R \sim 50 - 100$) modules of the IRS: SL2 (5.2 - 7.6 μm), SL1 (7.5 - 14.3 μm), LL2 (14.3 - 20.6 μm), and LL1 (20.5 - 37.5 μm). The observations and data reduction are discussed in detail in Donahue et al. (2011) and in Chapter 4. IRS spectra and infrared broadband SED points appear in both works.

In brief, we prepared spectral cubes using the software package CUBISM v1.7

(Smith et al. 2007a), extracted spectra from an aperture of relatively high signal-to-noise, and corrected for MIR light lost beyond the aperture and for mismatches between spectral modules, using the broadband photometry as the master baseline. For the targets without full broadband coverage (see (Donahue et al. 2011, Table 4) for broadband fluxes and apertures), we added up all of the light in each of the SL1 and LL2 modules (which have the highest signal-to-noise) and used the profiles of light along the slit to estimate the distribution of light in our targets and correct for gaps between modules. The effective apertures of the IRS feature strengths are the apertures of the corresponding broadband observations, within 15% uncertainty.

Though the BCGs in this sample are all very luminous sources of H_2 emission, the SED is dominated in some cases by thermal dust continua or by line emission from broad PAH features, with significant contributions from atomic emission lines. The scaling described above is only appropriate for the H_2 emission lines if the H_2 dominates the SL1 and LL2 spectra (as it does in some cases) or if the sources of emission are co-spatial.

For two reasons, we consider the scaling valid for the H_2 emission. First, we added up the H_2 emission in the two modules mentioned above, subtracted continuum, and compared the resulting light profiles (in SL1 and LL2) to the general light profiles used above. For both modules, the FWHM of the H_2 profile is consistent with the FWHM of the general profile, with a scatter in the sample of $\sim 30\%$ in both directions. There is considerable noise in some of the light profiles, and comparing the two pairs of light profiles for each of the targets in the sample uncovered no discernible pattern; therefore, we conclude that there is no evidence that the H_2 has a different spatial distribution than the continuum in any of the targets.

Second, in Chapter 4, we found that star formation in eight of the nine BCGs in the sample is occurring in extended regions like filaments of molecular gas, with low extinction of the optical-UV light of the young stars. (MS0735 has no detected star formation, but has strong H_2 emission and probably shares the same filamentary morphology. A1068 and A1835 probably also have major sites of nuclear star formation.) The environment of these BCGs may resemble NGC 1275 in the core of the well-resolved Perseus cluster, where MIR observations of the network of Hα filaments that surround the BCG have revealed powerful pure rotational H_2 emission similar to the H_2 emission in our targets. The assumption that the H_2 emission is arising from the same extended filaments (sometimes associated with ongoing star formation) which generate the atomic and PAH features is the simplest interpretation of the data, and it is the assumption that we adopt.

The morphology in A1068 and A1835 may be somewhat more complicated. Their MIR spectra are dominated by the signatures of obscured star formation (PAHs and thermal dust emission) which is probably arising from a centrally concentrated star-forming region, while their H_2 emission (and some of the MIR atomic and PAH emission) likely arises in the same type of extended regions as seen in the other BCGs in the sample. Thus, one might expect the H_2 to show a more extended profile than the thermal dust continuum. There is no conclusive evidence. The H_2 may be $\sim 50\%$ more distributed than the continuum emission in A1835, but the same kind of profiles in A1068 suggest that the H_2 has only 50% of the spatial extent of the thermal dust continuum, which is unrealistic because both are point sources in continuum emission.

After spectral extraction, feature strengths were estimated with the empirical spectral fitting package PAHFIT v1.2 (Smith et al. 2007b). Thorough tables of feature strengths including the entire H_2 pure rotational series are included in Chapter 4. Different fit methods can yield significantly discrepant integrated fluxes for the broad

PAH features, but the literature for MOHEGs (Ogle et al. 2010; Guillard 2010) consistently use PAHFIT as well.

Many of these targets have also been observed in the NIR (Falcke et al. 1998; Jaffe et al. 2001; Edge 2001; Edge et al. 2002; Jaffe et al. 2005; Wilman et al. 2011). Future work may integrate the NIR and MIR H_2 observations.

5.4 Analysis

The H_2 S(1) - S(7) pure rotational series is well-detected in all nine sample galaxies, though in a number of cases individual features yielded only 3σ upper limits. The strongest line is the ortho-state S(3). The weak S(0) line at 28.2 μm is not well detected in any target in our sample. In four cases, the line was so weak that PAHFIT could not estimate an upper limit.

The H_2 line luminosities are presented in Table 4.7. The luminosities are extreme. The luminosity of the S(3) line ranges from 0.77×10^{41} erg s^{-1} (for 2A0335) up to 19×10^{41} erg s^{-1} (for A1835).

To compare, sources where the warm H_2 emission originates in PDRs tend to have luminosities summed over S(0) - S(2) of $10^{38} - 10^{40}$ erg s^{-1} (Roussel et al. 2007; Smith et al. 2007b). Much more luminous sources of warm H_2 emission include the first discovered MOHEG, the LIRG NGC 6240 (a late stage major merger and a starburst), which has H_2 emission on the order of 20×10^{41} erg s^{-1} (Joseph et al. 1984; Armus et al. 2006). This emission probably arises from slow shocks between the two galaxy nuclei (Armus et al. 2006). The powerful shock front in Stephan's Quintet, about 40×15 kpc in size, has a total estimated luminosity in all of the rotational lines of $\gtrsim 10^{41}$ erg s^{-1} (Appleton et al. 2006). The observed sum over the S(0) - S(3) lines for the radio MOHEGs of Ogle et al. (2010) range from $\sim 10^{39} - 10^{42}$

erg s^{-1} (their luminosity for Hydra A, or 3C 218, from a slightly smaller aperture is about 30% smaller than ours). Finally, the cool-core BCG ZwCl 3146 has astounding H_2 luminosities of $\gtrsim 10^{43}$ erg s^{-1} (Egami et al. 2006a). The mechanism heating the H_2 in cool-core BCGs, in this sample and elsewhere, is clearly capable of producing H_2 luminosities on the order of the most luminous known sources, all of which are associated with shock heating.

The H_2 normally has an inverse mass-temperature distribution, with a small amount of gas at > 1000 K generating rovibrational lines, a larger amount between 100 and 1000 K generating pure rotational lines, and a vast repository of cold gas. However, radio MOHEGs generally heat $10- \gtrsim 50$ % of their molecular gas to > 100 K (Ogle et al. 2010).

We may describe the H_2 by constructing a model of two components of optically thin warm H_2 (each in local thermodynamic equilibrium (LTE) at a single temperature), making fits to the excitation diagram, and finding the mass corresponding to each temperature. This basic model simplifies the actual, surely far more complex distribution of the H_2. The assumption of LTE is realistic because the critical densities of the upper levels are relatively low and the efficiency of collisional excitation in those levels is high (Higdon et al. 2006; Ferland et al. 2008; Ogle et al. 2010). We also adopt an ortho-to-para (odd to even angular momentum quantum number J) ratio of 3, valid for temperatures around 300 K (Higdon et al. 2006) (at lower temperatures, the ratio decreases).

Our targets are unresolved point sources or poorly resolved extended sources in the MIR (Donahue et al. 2011). The S(3) line, the brightest line in the series, falls in the SL1 module, with an aperture diameter corresponding to the IRAC 8 μm observation (10-20" depending on the target) (Donahue et al. 2011, Table 4). In the case of A1795, which lacks IRAC observations, we assume an effective aperture diameter of 10" based on the original IRS aperture and scaling (Donahue et al. 2011, Table 3). Assuming that the H_2 source uniformly fills the aperture, we calculate the rest-frame surface brightness I_{ji} of each H_2 transition, in units of 10^{-9} W m^{-2} sr^{-1}.

In Figure 5.1, we plot the column density N_j of the upper level of each transition, divided by its statistical weight g_j, in log space against the upper level energy E_u. Following the example of Ogle et al. (2010), we include upper limits in the fit as 2σ detections with 1σ uncertainties, in order to set a better limit on the lower-temperature component; those upper limits are labeled with arrows. (The exception is A0478; we did not include the S(6) upper limit in the fit, because it impaired the higher temperature fit without having much effect on the lower temperature or resulting masses.) We could not obtain an upper limit to the S(0) fit in four cases, nor to the S(6) feature for Hydra A. The color of each point denotes the module in which the emission line was observed. For each emission line, the weighted column density of the upper level is given by

$$N_j/g_j = \frac{4\pi\lambda_{ji}I_{ji}}{hcA_{ji}g_j} \times 10^{0.4A_\lambda} \tag{5.1}$$

where λ_{ji} is the rest wavelength of the emission line, A_{ji} is the transition probability or Einstein coefficient (Turner et al. 1977), g_j is the statistical weight, h is Planck's constant, and c is the speed of light.

A_λ is the extinction at that wavelength in magnitudes. The extinction is likely to be very low unless the H_2 emission arises within the PDRs of normal star-forming regions or starbursts (Higdon et al. 2006; Zakamska 2010). In our targets, we expect the H_2 to be distributed in extended filaments studded with star-forming knots, with unusually low optical-UV extinction by dust and aromatic molecules (see Chapter 4).

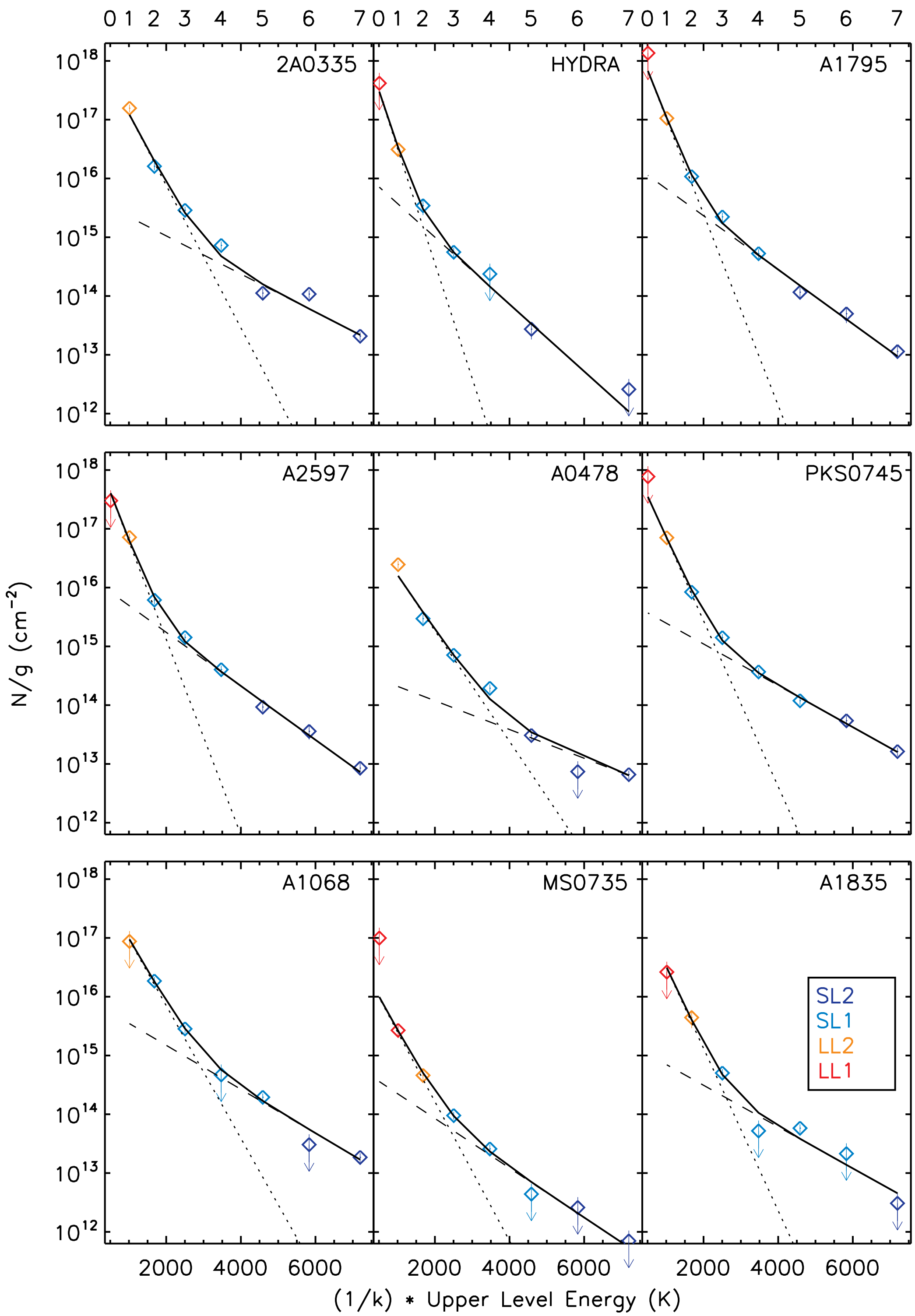

Fig. 5.1.— Excitation diagrams. J_{lower} is labeled at the top of the page. Colors represent the module in which each line is detected (legend in lower right). Warm ($\sim 200-500$ K) temperatures are represented with dotted lines, and hot ($\sim 800-1800$ K) temperatures with dashed lines; the combined fit is a solid line.

Evidence from Donahue et al. (2011) and this work indicates that the primary source of H_2 emission is not star formation. Significant attenuation of H_2 emission by dust seems unlikely, but as discussed above, H_2 is most efficiently created and maintained in the presence of dust. The profile of MIR extinction in such a geometry is not known.

We modeled extinction as part of the PAHFIT spectral decomposition package as described in Chapter 4. PAHFIT models the strength of the extinction based on the continuum shape. In the two targets for which a secure detection of a wavelength-dependent absorption profile was made (A1068 and Hydra A), all feature strengths, including H_2 emission lines, have been extinction-corrected. This may not be appropriate for this work if the H_2 has a different distribution than the dust, which seems especially likely for A1068 (where there may be a separate, nuclear site of obscured star formation; see Chapter 4). The extinction profile has the greatest impact upon the S(3)9.66 μm emission line, which falls near the peak of a major silicate absorption feature. We found an optical depth at 9.7 μm of 0.83 and 0.60 for the two features, respectively.

During our analysis below, we consider whether the S(3) line appears to be over-luminous by a factor of about 2 for those two targets, or whether it appears to be subuminous in any of the other targets (as one would expect if the H_2 is subject to extinction which we have not corrected for).

In the plot of logarithmic N/g in cm^{-2} vs E_u in K, a population of warm H_2 at a single temperature will yield a series of emission lines forming a straight line, of which the absolute value of the reciprocal is the excitation temperature T_{ex} in K (Higdon et al. 2006). Two or more populations will form a curve with lower energy levels falling on a steeper slope (lower temperature) and higher energy levels lying on a shallower slope (higher temperature) (Johnstone et al. 2007).

We fit two temperature populations to each of our targets, using MPFITFUN (Markwardt 2009); the fits are plotted in Fig. 5.1, and the resulting temperatures are tabulated in Table 5.1. We selected two temperatures for consistency, but in some cases a three-temperature fit is helpful (see below). Temperature was permitted to vary up to 2000K. Though we expect the pure rotational series of H_2 to mainly probe gas between 100 and 1000 K, the higher energy transitions may reasonably probe the same temperature range as the NIR rovibrational emission lines.

While the fits are generally excellent, potential sources of error include the following. Major errors in the calibration of the H_2 spectrum would tend to cause unexpected vertical offsets between the data points extracted from different modules, particularly between the LL and SL modules. This would mainly affect the lower fitted temperature. No such offset is prominent or conclusive in Fig. 5.1, though a lower temperature fit may be appropriate for the low-temperature component of the model for A0478.

Regarding extinction, we consider whether the correction applied to the spectra of A1068 and Hydra A appears to have been inappropriate and to have negatively affected the quality of the excitation diagram fits. The most dramatic effect of the correction is upon the S(3) line, which was revised upward by a factor of about 2 in each case by the extinction correction. An examination of Fig. 5.1 suggests that removing the extinction correction would slightly impair both fits, implying that perhaps the extinction correction was appropriate after all for H_2. Meanwhile, if the H_2 emission in any of the other targets (to which no extinction correction has been applied) is subject to significant extinction, the S(3) line is expected to be subluminous, but such a pattern is not evident in any of the targets.

If the ortho- and para- states of H_2 are not in equilibrium, as one might expect in a situation where cold quiescent gas has only recently been shock heated, the effect on the excitation diagram would be the elevation of the para-states (even J) over the ortho-states (odd J) and a zig-zag pattern instead of a smooth curve (Hewitt et al. 2009). Such a situation is marginally plausible for 2A0335, except for the S(2) line. A slight zig-zag pattern is detectable for A1068 and A1835, but it favors the ortho-states instead. Since our adopted ortho-to-para ratio is the expected maximum for LTE (Guillard 2010), we dismiss this variation as noise.

The total mass M_{T} of each population of H_2 may be calculated from the luminosity of each line (therefore, the masses in Table 5.1 are averages incorporating the weights of each data point) as follows.

$$M_{\mathrm{T}} = M_{\mathrm{H}_2} n_{\mathrm{T}} \tag{5.2}$$

where M_{H_2} is the mass of the molecule and n_{T} is the total number of H_2 molecules at that temperature. The latter depends on the luminosity of a given emission line, L_{ji}, which is given in Table 4.7.

$$n_{\mathrm{T}} = \frac{L_{ji} Z_{T_{ex}}}{A_{ji} h\nu g_j e^{-E_u/kT_{ex}}} \tag{5.3}$$

where $Z_{T_{ex}}$ is the partition function, ν is the frequency of the line, and k is Boltzmann's constant.

We calculate the mass based on each of the available emission lines, covering at least three of the four modules, but most of the weight of the resulting mass comes from the better-detected emission lines appearing in the SL1 and SL2.

We have also included in Table 5.1 the estimate of the total mass of cold (< 100 K) H_2, based on the CO observations of Salomé & Combes (2003); Edge (2001).

Table 5.1. H_2 temperature and mass.

Source	T_1 (K)	M_1 (10^6 $M_\odot$)	T_2 (K)	M_2 (10^6 $M_\odot$)	M_{H_2} (cold)[a] (10^9 $M_\odot$)
2A0335	360 ± 30	16 ± 4	1300 ± 100	0.13 ± 0.03	1.5 ± 0.2
Hydra A	220 ± 50	42 ± 38	760 ± 90	0.70 ± 0.24	2.0 ± 0.3
A1795	270 ± 30	54 ± 20	940 ± 80	0.84 ± 0.16	4.8 ± 0.6
A2597	260 ± 20	220 ± 80	950 ± 60	3.9 ± 0.6	< 1.8
A0478	460 ± 40	21 ± 4	1800 ± 400[b]	0.23 ± 0.09	1.7 ± 1.0
PKS0745	310 ± 30	120 ± 30	1200 ± 100	1.5 ± 0.2	4.0 ± 0.9
A1068	380 ± 50	91 ± 47	1200 ± 200	1.9 ± 0.6	42 ± 2
MS0735	370 ± 60	21 ± 9	1000 ± 200	0.90 ± 0.39	-
A1835	310 ± 40	240 ± 160	1200 ± 200	2.3 ± 0.9	68 ± 8

(a) Mass of cold H_2 estimated from CO observations, Salomé & Combes (2003) except for 2A0335, A0478 and A1835 (Edge 2001). (b) The S(6) upper limit was not included in this fit; including it forces this temperature to the upper limit (2000 K) but otherwise has little effect.

5.5 Discussion

5.5.1 H_2 temperature and mass

Two temperatures are adequate to fit the rotational H_2 series in this sample of BCGs. Our lower temperatures fall between 220 and 460 K, while the hotter temperatures range from 760 to 1800 K. The temperatures we fit generally agree within $\sim 1 - 2\sigma$ with the two-temperature fits used in Donahue et al. (2011) to assist in fitting starburst SEDs to the spectra of cool-core BCGs. As expected, our two-temperature fit straddles the single-temperature fit to Hydra A in Donahue et al. (2011). The main purpose of the fits in Donahue et al. (2011) was to remove the H_2 lines to secure a better fit to the rest of the spectrum using the starburst SEDs, so these more careful fits should be considered the replacement.

The masses associated with the $\sim$ 300K temperature populations range from $\sim 10^6$ to 10^8 $M_\odot$, while the hotter ($\sim$ 1200 K) populations correspond to smaller masses of $\sim 10^5 - 10^6$ $M_\odot$. In general, we measure higher masses of warmer and hot H_2 in the targets with enormous reservoirs of cold H_2 (see Table 5.1), but it is interesting to note that A2597 has one of the highest $>$ 300 K H_2 masses and among the lowest masses of cold H_2, implying that the processes in that cool-core BCG are heating up the H_2 more efficiently than in the others.

The radio galaxy H_2 sources of Ogle et al. (2010), which mainly belong to the category of radio MOHEGs, were found to have large amounts of warm gas (100 - 200 K), between $\sim 10^7$ and 10^{10} $M_\odot$, suggesting that shocks from the radio-jet-driven outflow are capable of heating an entire galaxy's mass of molecular gas. In fact, the mass of warm gas exceeds the mass of cold gas in some cases (Ogle et al. 2010, Table 12). The warm gas fraction, defined as the ratio of the mass at $100 - 200$ K and the mass at < 100 K, ranges from about 0.1 to 2 for radio MOHEGs. Egami et al. (2006a) found that the cool-core BCG ZwCl 3146 also has an enormous mass of gas at about this temperature, $\sim 10^{10}$ $M_{\odot}$ at 160 K, with a warm gas fraction of about 0.1.

In many cases, we were able to successfully fit the data with a three-temperature fit, which tends to better probe the $100-200$ K gas. We find correspondingly higher masses of gas in this temperature range: $\sim 10^9$ $M_{\odot}$ at 120 K for MS0735, 5×10^8 $M_{\odot}$ at 170 K for PKS0745, 3×10^8 $M_{\odot}$ at 150 K for 2A0335, and $\sim 10^8$ $M_{\odot}$ at 180 K for Hydra A and A1795. This suggests a warm gas fraction of $\sim 0.02-0.2$ (except for MS0735 for which no cold gas estimate is available). ZwCl 3146, as noted above, falls in the same range.

We are interested in A1068 and A1835, which both have approximately the same amount of cold H_2 gas as ZwCl 3146; all three fall among the highest masses of cold reservoirs among cool-core clusters (Fig. 6, Salomé & Combes 2003). With no successful S(0) measurement, however, we cannot probe the $100-200$K temperature regime. Based on the pattern seen in the targets listed above, we expect that there is $2-60\times$ as much warm gas at 160 K than at 350 K, corresponding to $\sim 2\times10^8-10^{10}$ $M_{\odot}$ at 160 K in A1068 and A1835, and a warm gas fraction between 0.004 and 0.2.

The cool-core BCGs have more gas at intermediate temperatures ($\sim$ 300K) than the radio MOHEGs, which typically have masses in this regime of about 5×10^6 $M_{\odot}$ (ranging from 0.03 to 80×10^6) (Ogle et al. 2010). Meanwhile, at hot temperatures (1000 - 1500 K), the median radio MOHEG has a mass of $\sim 10^5$ $M_{\odot}$ (ranging from 1700 to 7×10^5 $M_{\odot}$), considerably less than most of the cool-core BCGs.

There is one target common to both samples, Hydra A (3C 218). Ogle et al. (2010) publishes similar or slightly smaller line fluxes than ours; their aperture is smaller. At a temperature of 540 K, Ogle et al. (2010) find a mass of 10^6 $M_\odot$. Our fitted temperatures straddle this temperature, and as expected, the masses do as well: we find a higher mass at a lower temperature (220 K) and a lower mass at a higher temperature (760 K). The results are consistent.

At least two categories of cool-core galaxies clusters seem to be emerging. First, there are those like A1068, A1835 and ZwCl 3146, with large deposits of cold H_2 and abundant evidence for both obscured and exposed star formation. See Chapter 4 for a discussion of the environment of star formation. There is also a strong correlation between the supply of cold gas and the degree of Hα emission, associated with star formation (Salomé & Combes 2003).

The rest of the sample has smaller reservoirs of cold gas, consistent with the amount of cold molecular gas toward the higher end of the range of the SINGS sample (Roussel et al. 2007).

However, while some cool-core BCGs appear to be bigger than others in terms of the supply of cold H_2 gas, the processes that heat the H_2 to temperatures > 100 K act relatively equally on all of them. The warm gas fractions are similar in all cool-core BCGs studied here, though with a broad range, and generally fall short of the warm gas fractions found in the radio MOHEGs.

If the H_2 in cool-core galaxy cluster cores does, in fact, tend to reside in magnetically supported extended filaments, in which the H_2 is heated by a non-radiative process such as the penetration of energetic particles from the ICM into the filaments (or another source of heat such as MHD waves or cosmic rays), it is possible that such mechanisms are not as efficient at heating the H_2 as the shocks found in the radio MOHEGs.

5.5.2 Cool-core galaxy cluster BCGs as MOHEGs

Fig. 5.2 recreates Ogle et al. (2010, Fig. 14). The fluxes of four of the pure rotational H_2 lines, S(0) - S(3), are summed and divided by the flux in the PAH feature at 7.7 μm, and plotted against the luminosity at 24 μm. As discussed in Ogle et al. (2010); Donahue et al. (2011) and Chapter 4, the targets to the right have more star formation or AGN power (in our sample, that means star formation, though A1068 may have significant AGN contributions). Ogle et al. (2010) characterize targets higher on the plot as those with more mechanical heating compared to their star formation power.

The lower of the horizontal lines in Fig. 5.2 shows the median level for the normal star-forming galaxies of the SINGS sample, at 0.014 - an average which holds across several decades of L_{24}. Meanwhile, the horizontal line at 0.04 indicates the approximate lower cutoff for MOHEGs.

In our sample, typically more than half of the flux in the sum of H_2 lines comes from the same aperture as the PAH7.7 flux, reducing the impact of aperture effects upon the ratio.

We have overplotted other data of interest, including the radio MOHEGs of Ogle et al. (2010). They appear as red triangles, and are often lower limits because only an upper limit to the PAH feature could be set. The four cool-core BCGs in that dataset (Hydra A or 3C 218, NGC 1275 in the Perseus Cluster or 3C 84, A2052 or 3C 317, and A2199 or 3C 338) have been indicated with black rings. Their datapoint for Hydra A is nearly coincident with our own, validating the comparison between the two samples. We have also plotted the shock front in the interacting galaxy group Stephan's Quintet (SQ) (Appleton et al. 2006), the LIRG NGC 6240 (Lutz et al. 2003), and the cool-core BCG ZwCl 3146 (Egami et al. 2006a).

All cool-core galaxy cluster BCGs for which these parameters have been observed

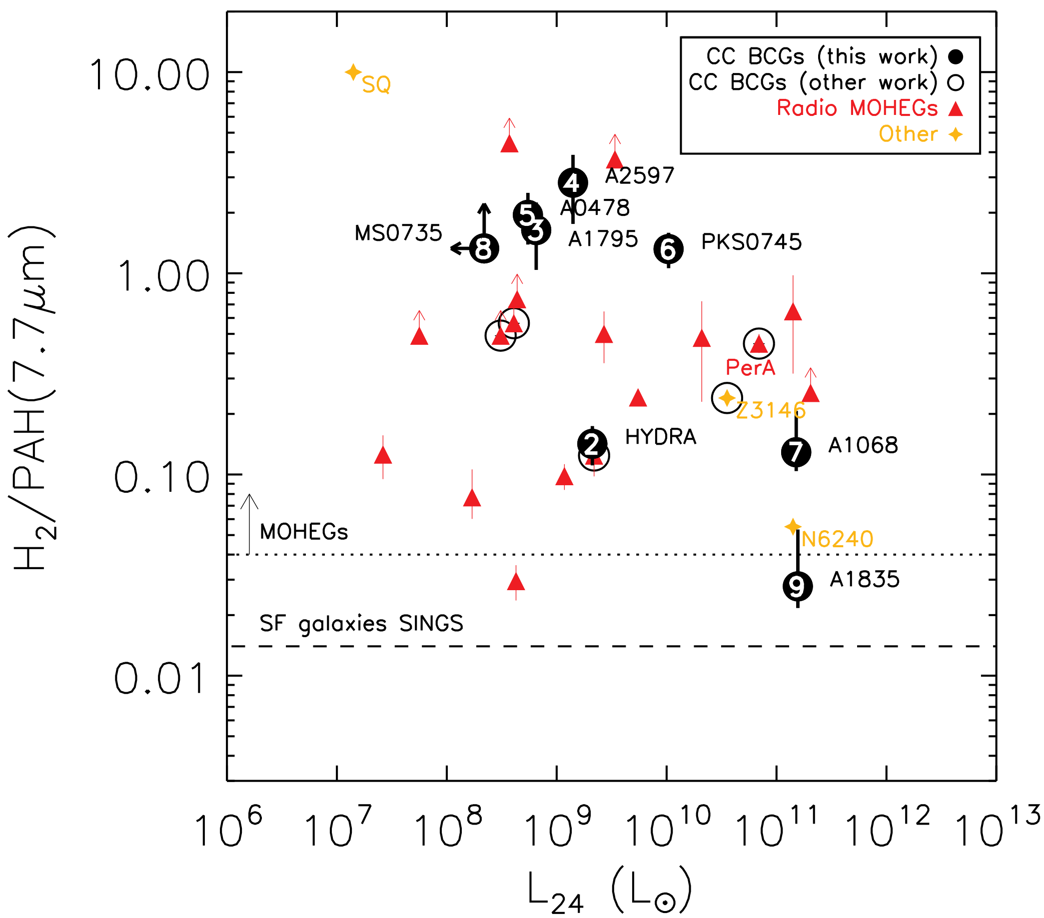

Fig. 5.2.— Ratio of the sum of the fluxes of the rotational series H_2 S(0) - S(3) over the flux of the 7.7 μm PAH feature, plotted against L_{24}. The dotted line shows the lower cut-off for MOHEGs at 0.04, while the dashed line shows the median value for the normal star-forming galaxies from the SINGS sample, 0.014 (Ogle et al. 2010). Our sample is plotted with solid black dots (numbers correspond to those in Table 4.1), while data on CC BCGs from other samples is highlighted with black rings. Red triangles: radio MOHEGs from Ogle et al. (2010). Includes 4 CC BCGs including Perseus A (NGC 1275) and their reduction of Hydra A (overlapped by our data point). Orange stars are other targets of interest: Stephan's Quintet, NGC 6240, and ZwCl 3146.

belong to the category of MOHEGs. To the previous sample of five, we add seven (and confirm Hydra A). A1835 falls below the cutoff because of strong PAH emission arising from star formation, but for the same reasons as the radio galaxy 3C 31, it lies well above the track of normal star-formers like the SINGS spirals and belongs among the other MOHEGs. While we were not able to set a limit on the PAH feature at 7.7 μm in 2A0335, a comparison of the strengths of H_2 and the PAH feature at 6.2 μm among our sample (see Chapter 4) indicates that 2A0335 is likely to fall into the category of MOHEGs as well.

The data point on Fig. 5.2 for NGC 1275 ("PerA") from Ogle et al. (2010) comes from a nuclear aperture on the BCG, as seen in Weedman et al. (2005). This captures the strong dust continuum emission powered by the AGN. The H_2 in the nucleus is strong enough to place NGC 1275 among the other radio MOHEGs, but the contrast becomes more remarkable when the off-nuclear filaments of NGC 1275 are examined (Johnstone et al. 2007). The 24 μm luminosity for positions 2 and 11 have not been published, and the high-resolution spectra do not include coverage of the 7.7 μm PAH, but the weak 11.3 μm PAH and flat long-wave continuum indicate that these filaments should be placed toward the upper left of Fig. 5.2.

MOHEGs are very luminous sources of rotational H_2 compared to the PAH 7.7 μm emission. Ogle et al. (2010) describe the significance of the y-axis in Fig. 5.2 as the relative mechanical (e.g. jet) to star formation power. This does not necessarily apply in cool-core BCGs. Jet interactions are certainly critical to the mechanism of a cooling flow, and may be responsible for dredging gas and dust up from the BCG. The jet power could play a role if it drives shocks or MHD waves that heat the H_2, or if cosmic rays from the radio lobes are responsible, but if particles from the hot ICM is the agent that heats up the H_2, the jet may be unrelated. However, considering that none of those heating mechanisms are known contributors to PAH luminosity, the position of a cool-core BCG on the y axis of Fig. 5.2 may indicate the relative power of the H_2 heating mechanism, regardless of what it is. Assuming that the PAH 7.7 μm feature is an accurate tracer of star formation, the significance of the category is that the H_2 is more luminous than it should be if it is powered by star formation. One efficient source of heat for H_2 is clearly shock activity; the question remains whether another mechanism is capable of the same efficiency.

A group of cool-core BCGs falls near the position occupied by the radio galaxy 3C 326N, the most extreme radio MOHEG, in which the H_2 is shock heated either by a tidal accretion flow from the companion galaxy (Ogle et al. 2007) or by the radio jet (Ogle et al. 2010). Four of these BCGs (A1795, A2597, A0478, and PKS0745) were found in Chapter 4 to have relatively weak signatures of obscured star formation from dust in the MIR ($\sim$ 1 $M_\odot\,yr^{-1}$) compared to optical and ultraviolet evidence of exposed star formation ($\sim$ 10 $M_\odot\,yr^{-1}$). (PKS0745 was found to be something of an intermediate case between exposed and obscured star formation. MS0735, however, has no known indication of star formation at all.) As discussed above, the H_2 in these targets probably resides in filaments outside the main body of the BCG, sometimes filled with chains of relatively exposed H II regions. The penetration of energetic particles from the hot ICM into the filaments has been suggested as a heating mechanism for the Hα and H_2 (Fabian et al. 2011a). There is direct evidence for extended star formation in A1795 and A2597, (McNamara & O'Connell 1993; O'Dea et al. 2004; McDonald et al. 2011b) as well as other cool-core galaxy clusters including NGC 1275 (which is moved to the right in Fig. 5.2 by its AGN-powered dust continuum), A2052, and others (Conselice et al. 2001; Martel et al. 2002; McDonald et al. 2011b). A2052 appears in Fig. 5.2 as one of the two radio MOHEGs with a black ring around it, just below MS0735. If these filament-dominated cool-core BCGs are powered by energetic ICM particles, Fig. 5.2 demonstrates that it can be approximately as efficient at heating H_2 as the most extreme interaction-fueled radio MOHEG.

Hydra A was also found to be an intermediate case. It shares many properties with the above-mentioned group, including the general scale of star formation, though its PAHs are considerably stronger.

Meanwhile, A1835 and A1068 are comparable in Fig. 5.2 to the LIRG NGC 6240 (see above). A1835 and A1068 have the properties of a starburst, with a great deal of obscured star formation, though A1835 also has very strong optical and ultraviolet indicators of exposed star formation. Like NGC 6240, both of these cool-core BCGs have powerful star formation, yet still have warm H_2 emission well above the level of the normal star-forming systems of SINGS. As demonstrated by Fig. 5.1, however, the rotational H_2 series is not detected as cleanly as in most of the other cool-core BCGs.

5.5.3 Source of heat for H_2

In normal star-forming galaxies, warm H_2 emission is stimulated from star formation via ultraviolet pumping (Roussel et al. 2007), and emits via fluorescence. In interacting systems such as Stephan's Quintet and radio MOHEGs, it is heated by shock activity (Appleton et al. 2006; Ogle et al. 2010). Shocks have also been proposed as a heating mechanism in cool-core BCGs (including ZwCl 3146, and those which are also radio MOHEGs). In the filaments of the cool-core BCG NGC 1275, which have MIR spectra remarkably similar to some of the spectra in this sample, Fabian et al. (2011a) proposed that energetic particles from the hot ICM penetrating into the filaments can generate the observed Hα and H_2 emission.

While we have found the latter model promising as an explanation for the unusually exposed star formation in many of our cool-core BCGs, it is also true that shock activity is prominent in cool-core BCGs (see above). Our spectra do not have the spatial resolution to distinguish H_2 arising from filaments from H_2 in interacting regions, and it is beyond the scope of this work to perform a thorough shock analysis. Instead, we focus on characterizing the source of heat for the H_2. We test the claim in Donahue et al. (2011) that the weakly ionized gas and H_2 in the cool-core BCGs both receive more heating than expected from star formation, and quantify the extra heating.

In Donahue et al. (2011), we used the 24 μm continuum as a tracer of star formation power. We found that the low-ionization [Ne II] and [Ne III] emission lines are strongly correlated with L_{24} (with $r > 0.9$), but that the correlation is not linear. As discussed in Donahue et al. (2011) and Chapter 4, this implies either that star formation does not act equally upon the dust that generates the 24 μm continuum and upon the weakly ionized gas that generates the neon emission, or that the neon emission has a source of heat other than star formation.

In Donahue et al. (2011), we found that the H_2 luminosity (traced by the S(2) and S(3) emission lines, which are the most reliably detected in this sample) is uncorrelated with L_{24} ($r = 0.68$). This is an unambiguous indication that the H_2 is receiving an additional source of heat than the 24 μm continuum. We still expect H_2 in the vicinity of star formation to experience normal heating, but the other source of heat dominates.

Most importantly, in Donahue et al. (2011, Fig. 11), we found a strong correlation ($r = 0.98$) between H_2 and neon luminosity when each were divided by L_{24}, which should cancel out the "bigger is bigger" effect. The power-law coefficient is 1.49 ± 0.12. The implication is that the additional heat sources incident upon the neon and H_2 are the same.

It is also interesting to note the broad scatter in this plot. Under the hypothesis that all of the emission is being stimulated by star formation, one would expect the data to be clustered at one point in Donahue et al. (2011, Fig. 11) (governed by the standard ratios of neon or H_2 to continuum emission for normal star-formers), with a total scatter of perhaps $3\times$ on each axis (i.e. a scatter of $1.7\times$ in each direction). Instead, we observe that the [Ne II] / L_{24} ratios have a scatter of about $40\times$, and the (H_2 S(2) + S(3)) / L_{24} ratios have a scatter of $100\times$. (We exclude MS0735 from much of this discussion because star formation is clearly not the source of heat in that target, and it is an outlier on most of these plots.) We do not know where normal star-formers lie on this correlation, but we can reasonably assume that they fall near A1068 and A1835 (which have many normal MIR signatures of star formation) at the bottom end of each range of scatter. We average A1068 and A1835 to get the canonical value of each ratio for normal star-formers. The implication is that the source of heat acting upon the neon in extreme cases like A0478 may be up to $\sim 25\times$ more effective than if only the source of heat acting upon the dust grains (assumed to be star formation) were heating the neon, and the source of heat acting upon the H_2 may be $\sim 100\times$ as effective as if the H_2 were heated by the same source of heat as the dust grains. This is remarkable.

We explored this association further, under the assumption that the thermal dust continuum traces the star formation rate, by comparing standard SFR calibrations based upon neon (Ho & Keto 2007) or H_2 (Treyer et al. 2010) to the SFR derived from the MIR spectrum (using fits to the Groves et al. (2008) models). We found that for

A1068 and A1835, the three SFR calibrations were in rough agreement, though A1835 has relatively weak H_2 (consistent with its position on Fig. 5.2). While we discussed their exposed and probably filamentary star formation in Chapter 4, these two targets appear to be dominated by normal, probably nuclear, starburst activity. For the rest of the sample (excluding MS0735), the SFR estimated from neon is $3-8\times$ larger than the SFR estimated from the 24 μm continuum, which is similar to the results of Table 4.11 in Chapter 4; neon is overluminous compared to the dust continuum associated with star formation. Meanwhile, SFR estimated from H_2 is $5-15\times$ larger than the SFR from the 24 μm continuum (Hydra A, an intermediate case, has a variation of only $\sim 2\times$).

While this analysis demonstrates that the atomic and molecular gas are overluminous compared to the thermal dust continuum, it does not necessarily demonstrate that they are overluminous compared to the power of star formation. The assumption that the 24 μm continuum traces star formation power in most cool-core BCGs was rejected in Chapter 4 (or at least, it traces only a small fraction of the star formation power). Star formation in many cool-core BCGs is highly exposed, supporting our proposal that it occurs in a system of thin (~ 0.3 pc) molecular threads. Under that consideration, we must revise our analysis of Donahue et al. (2011), using a more accurate tracer of star formation analysis than L_{24}. We have chosen the indicative estimate of total SFR from Chapter 4, SFR_I from Table 4.11. It is the sum of an estimate of obscured SFR from the 24 μm continuum and exposed SFR from optical and ultraviolet continuum observations.

In Fig. 5.3(a), we recreate (Donahue et al. 2011, Fig. 11) with this revision. We plot the sum of the well-detected H_2 S(2) and S(3) lines, divided by SFR_I, against the [Ne II] line divided by SFR_I. We find a correlation with a power-law coefficient

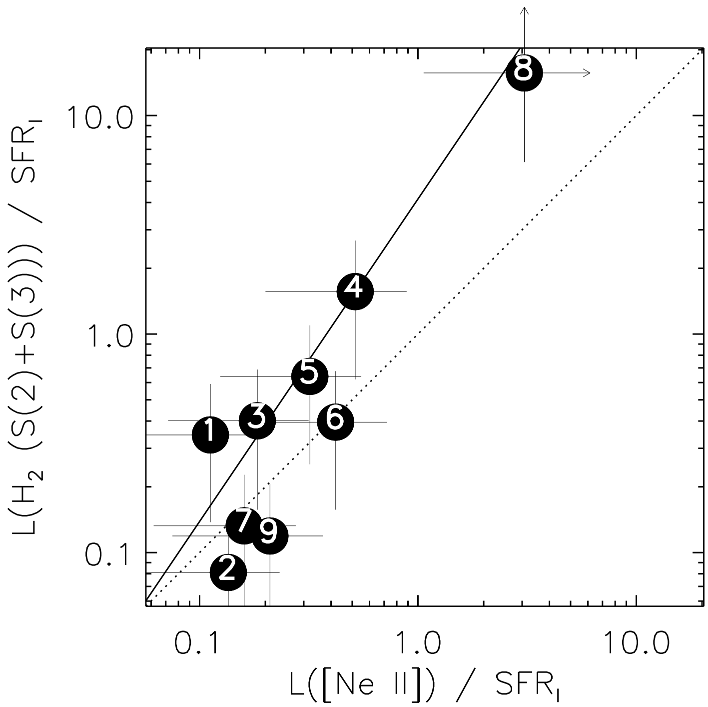

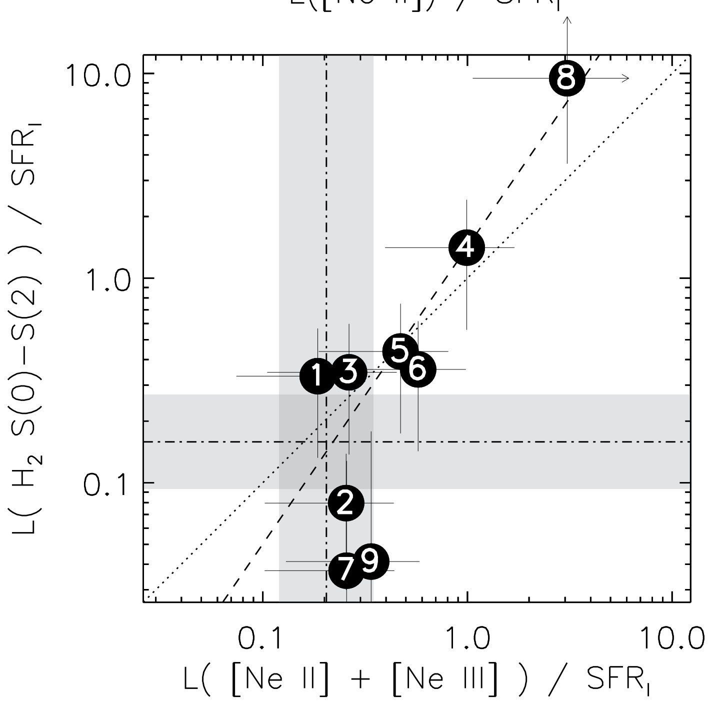

Fig. 5.3.— (a) Luminosities of the H_2 S(2) + S(3) lines and [Ne II] (all in rest-frame 10^{41} erg s^{-1}, see Table 4.7) scaled by the estimate of the total SFR in $M_\odot\,yr^{-1}$ (see Table 4.11). CC BCGs are plotted with black dots (numbers correspond to those in Table 4.1). The dotted line is unity, and the solid line is the best fit, with a power-law coefficient of 1.5 ± 0.6. (b) Similar plot, with the sum of the H_2 S(0), S(1) and S(2) lines versus the sum of the [Ne II] and [Ne III] lines. Dashed line is the best fit, with a power-law coefficient of 1.5 ± 0.5 (R=0.90). The dash-dot lines are the SFR calibrations based on neon (Farrah et al. 2007, or see Eq. 4.3) and H_2 (Treyer et al. 2010), with a scatter of 1.7× in each direction.

of 1.5 ± 0.6, in agreement with the correlation found by (Donahue et al. 2011). The existence of a correlation confirms that the H_2 and weakly ionized gas share a source of heat beyond star formation.

However, the scatter has tightened up considerably. The range in the ratio of neon to SFR_I is only $6\times$, and the range in the ratio of H_2 to SFR_I is $\sim 30\times$. (It makes no significant difference whether we include MS0735 in the correlation, because of its large errorbars, but we exclude it from the discussion of scatter.) We still do not have a reference point for normal star formation, but if we assume that A1068 and A1835 are representative, most of the targets fall within the expected scatter for normal star formation ($\sim 1.7\times$) around the ratio of [Ne II] / SFR_I (about 0.2 for those two targets). A2597, A0478, and PKS0745 (marked with a 4, 5 and 6 on the plot respectively) exceed this range, but not by much. The source responsible for heating the neon is up to $\sim 3\times$ as efficient as star formation alone, in the extreme case of A2597. This suggests that while neon shares an additional source of heat with H_2, it is not much more effective at heating the neon than star formation; in other words, star formation could be responsible for generating all of the neon emission seen in most of the BCGs. In targets like A2597, star formation probably contributes 1/3 of the observed warm H_2 emission, and another process contributes the other 2/3.

Though the scatter is reduced compared to the analysis that used L_{24} as a metric of star formation power, it is still high for the ratio of H_2 to SFR_I relative to A1068 and A1835, our best examples of normal star formation. Their ratio is about 0.13. All of the other BCGs (except Hydra A, marked with a 2 on the plot) are above the expected range for normal star formation. This analysis implies that it is impossible for star formation to generate the observed H_2 emission in these targets. The efficiency of H_2 heating in A2597 may be $15\times$ as efficient as in a normal star-forming region.

The assumption that A1068 and A1835 characterize normal star formation leaves much to be desired. In Chapter 4, we proposed that they are hosts to sites of both normal, starburst-like star formation in their cores and extended, exposed star formation in their filamentary networks. They are not perfectly understood.

Therefore, in Fig. 5.3(b), we select indicators of neon and H_2 emission that have been linked to standard calibrations of star formation, still scaled by our estimate of total SFR_I. [Ne II] + [Ne III] have been correlated to SFR by Ho & Keto (2007); Farrah et al. (2007). We use the latter, as in Eq. 4.3. That calibration is plotted with a vertical dash-dot line, with the expected scatter of $1.7\times$ in each direction shaded in gray. The sum of the three reddest rotational H_2 lines, S(0), S(2), and S(3), is plotted on the other axis. Their sum has been correlated to SFR by Treyer et al. (2010), and the calibration appears as a horizontal dash-dot line with the expected scatter shaded in gray.

The two ratios are still correlated with a power-law coefficient of 1.5 ± 0.5 ($r = 0.90$). As above, including MS0735 makes little difference to the correlation. The neon analysis is much the same as above; most BCGs have the expected neon luminosity for their degree of star formation. A2597, A0478 and PKS0745 have higher neon luminosity (though the discrepancy is only decisive for A2597), implying an additional source of heat beyond star formation which is up to $5\times$ as efficient for A2597 than star formation alone.

We do not securely detect the H_2 S(0) line in any of our targets. We plot the sum of the S(1) and S(2) lines when detected, and add upper limits to the upper errorbar. Therefore, the upper uncertainties should receive additional attention when determining whether a target has normal H_2 luminosity. Indeed, while Hydra A, A1068 and A1835 fall short of the expected range of normal star formation, the errorbars in all three extend upward into that range. They may have relatively weak H_2 for their level of star formation, but Fig. 5.2 suggests otherwise.

The other BCGs are systematically high ($\sim 2.3\times$ the standard calibration) but are also consistent within uncertainty with the normal range of H_2 luminosity for star-forming regions, except for A2597, which is $\sim 10\times$ more luminous in H_2 than can be accounted for with star formation alone.

In summary, the warm H_2 gas is being heated by a process other than star formation in A2597 and MS0735, and perhaps in some of the other BCGs as well. In general, star formation can account for the weakly ionized atomic emission. However, the correlation between the H_2 and atomic emission, when the power of star formation has been scaled out, suggests that the two may share a source of heat.

We suggest that the method proposed by Fabian et al. (2011a), where hot ICM particles turbulently penetrate through the magnetic shielding and into the filament, may act upon the molecular gas as it does upon the Hα-emitting gas. This may be the only source of heat for the H_2 and low-ionization atomic emission in MS0735, where no star formation is detected.

By scaling by our most realistic estimate of total star formation and comparing to standard star formation calibrations, we find that neither neon nor H_2 experience the extreme heating which is implied when they are scaled by the 24 μm continuum. This is another way of saying that the thermal dust continuum is weak in many of these targets, relative to many reference points including neon and H_2 emission.

The neon and H_2 luminosities are systematically high ($\gtrsim 2.3\times$) relative to the standard star formation calibrations for several cool-core BCGs, but the only star-forming BCG with remarkable neon and H_2 excesses is A2597, where the heating of neon and H_2 is 5 and $10\times$ more efficient (respectively) than by star formation alone.

This BCG is also extreme among cool-core BCGs in terms of H_2 luminosity relative to PAH luminosity (see Fig. 5.2) and has a spectacular filamentary emission line system and blue continuum lobes (Koekemoer et al. 2002).

To test whether shocks or energetic particles are the more likely heating mechanism, we are interested in the normal relationship between H_2 and neon emission in shocked systems such as most of the non-cool-core-BCG MOHEGs in Fig 5.2. Egami et al. (2006a) found that shocks were capable of producing neon emission in the cool-core BCG ZwCl 3146, but not the same type of shock as that generating the H_2 emission. They also note that such co-existence of different shock types has been discovered in other targets, but it is not clear whether such a morphology would produce the correlation between H_2 and neon luminosities shown in Fig. 5.3.

Low-ionization neon emission is found in the main shocked region in Stephan's Quintet, but it is weak compared to in our sample, with a fractional flux in the [Ne II] line of 0.58 of the flux in the H_2 S(2) line (Cluver et al. 2010). The radio MOHEG 3C 326 N has a ratio of In our sample, that fraction ranges from 1.3 (2A0335) to 6.2 (Hydra A). MS0735 is an outlier (having no boost to the neon emission from star formation), with a ratio of 0.87, almost as low as Stephan's Quintet. However, among the radio MOHEGs, there is a wide range of neon strengths relative to H_2: 5.0 ± 4.9 (Ogle et al. 2010). Targets like NGC 1275 tend to have high fractional neon emission (6.5) while the interacting galaxy 3C 326 N has a lower ratio of about 1.1. Thus, in general it appears that the shocks found in interacting systems may not be capable of producing the same relationship between H_2 and low-ionization atomic emission as observed in our sample, but this is a preliminary conclusion, and many of the radio MOHEGs have ratios of [Ne II] / H_2 S(2) similar to ours.

There is no prediction for the normal relationship between H_2 and neon luminosity in the energetic particle model of Fabian et al. (2011a). However, the model is based upon the filaments of the cool-core BCG NGC 1275. In those filaments, the fraction of [Ne II] to H_2 S(2) is ~ 1 (in position 2) and ~ 1.5 (in position 11), comparable to our sample (Johnstone et al. 2007). This does not support the energetic particle model in particular (because some other mechanism, perhaps a different type of shock, could be acting in that system instead of energetic particles from the ICM). However, our data are consistent with the environment that the model is based on, and inconsistent with at least some systems where H_2 and neon are being generated by shocks from interacting systems.

A comparison between the ordinates of Fig. 5.2 and Fig. 5.3(b) suggests that the definition of MOHEGs may be refined by replacing the ratio of H_2/ PAH(7.7 μm) with the ratio of H_2/SFR. The PAH luminosity is easier to measure in a consistent manner (at least when fit with the same method such as PAHFIT; see §4.5.6) and there have been many correlations between PAH luminosity and SFR (Roussel et al. 2001; Elbaz et al. 2002; Houck et al. 2007; Farrah et al. 2007; Zhu et al. 2008; Menéndez-Delmestre et al. 2009; Hiner et al. 2009). However, these attempts are hindered by the complex and variable nature of the PAH emission and by multiple sources of contamination (see Chapter 4 for more discussion). Even when a SFR based on PAH emission can be relied upon, it traces obscured star formation, which is adequate to estimate total SFR in the case of normal star formation (where $\sim 66 - 90\%$ of the optical-UV light of young stars may be obscured) but insufficient for extremely exposed star formation such as we see in many cool-core BCGs (see Chapter 4).

We consider what known MOHEGs may look like on such a plot. The radio MOHEGs generally have weak star formation, suppressed by the radio jet; SFR estimated with PAH7.7 is low (Ogle et al. 2010). No significant exposed star formation is expected. For the most part, they will not shift relative to normal star-formers, and serve as a baseline. Among the cool-core BCGs included in the radio MOHEGs sample, 3C 317 (A2052) and 3C 338 (A2199), which lie close to each other in Fig. 5.2, do not have indications of star formation at more than $\sim 2\mathrm{M}_\odot\,\mathrm{yr}^{-1}$ (Cardiel et al. 1998; Martel et al. 2002; Hicks et al. 2010) and thus are unlikely to shift. However, the filaments of NGC 1275 have been shown to have at least $20\mathrm{M}_\odot\,\mathrm{yr}^{-1}$ of exposed star formation (Canning et al. 2010). Relative to the other radio MOHEGs, it will shift downward. A1835 would stay in about the same place (its SFR based on PAHs is about the same as our total estimate of $\mathrm{SFR_I}$, see Table 4.11) as would MS0735 (its PAH7.7 μm is only an upper limit, as is its $\mathrm{SFR_I}$). The rest of the cool-core BCGs would move downward in the plot because their estimates of $\mathrm{SFR_I}$ are higher than those based upon PAHs, by factors of $\sim 3-8$ (see Table 4.11). The estimated result is that cool-core BCGs would be more tightly clumped on such a plot, falling among typical or weak radio MOHEGs rather than among the strongest. Such a plot would measure the strength of H_2 (and its energy source) relative to total star-forming power, rather than only obscured star formation. The BCGs with the highest H_2 to $\mathrm{SFR_I}$ ratios, like A2597, would appear at a level $\sim 10\times$ that of the normal star-forming galaxies of SINGS. The ratio of H_2 to $\mathrm{SFR_I}$, indicating the power of the heat source for the H_2, probably correlates with the cool H_2 fraction.

5.6 Conclusions

Massive reservoirs of molecular hydrogen, generally formed on dust grain surfaces, act as important absorbing agents and coolants in many types of galaxy systems. Emission lines of warm H_2 are detected in PDRs, where the H_2 serves as a shield and coolant for star formation in cold dark molecular cores. They are detected in dusty elliptical galaxies, ULIRGs, and most of all in shocked systems such as interacting galaxies, motivating the establishment of a category of galaxies (MOHEGs) defined by strong H_2 proportional to indicators of star formation ($> 4\%$ of PAH emission at 7.7 μm) (Ogle et al. 2010).

The BCGs of cool-core galaxy clusters are also major sources of pure rotational and rovibrational H_2 emission. Powerful emission from warm H_2 is present in all nine BCGs of this sample (and in four other cool-core BCGs not included in this sample). As discussed in Chapter 4, eight of the nine targets have indicators of both obscured star formation (based on MIR characteristics such as L_{24}) and exposed star formation (based on optical-UV continuum observations). Two (A1068 and A1835) have large total star formation rates ($150 - 240 M_\odot\, yr^{-1}$) that are mostly obscured, while the rest have moderate star formation ($5 - 25 M_\odot\, yr^{-1}$) which is mostly exposed.

Observations and models of another cool-core cluster, NGC 1275, indicate that warm H_2 originates in intricate magnetically-supported filaments which are associated with ionized line emission and sometimes with chains of H II regions. Energetic particles from the ICM may be the primary heating source for the Hα and H_2 emission in the filaments, but shocks are present in cool-core BCGs and may also be a plausible source. In Chapter 4, we find that such filaments or other extended environments of star formation are the most plausible explanation for the exposed star formation found in most of the sample (though not all filaments host star formation, and two of our targets probably also have a major site of nuclear, normal starburst activity as well). Filaments such as those in NGC 1275 are also a promising environment for the strong H_2 emission found in all nine cool-core BCGs in the sample.

We fit two-temperature models to the warm H_2 and found that some cool-core BCGs may be consistent with ZwCl 3146 in heating up as much as 10% of their large reservoirs of cold gas to a warm (> 100 K) state. Cool-core BCGs generally do not heat their H_2 gas as efficienctly as radio MOHEGs, which serve as an example of a shocked system.

All cool-core BCGs which have been examined are MOHEGs by the definition of Ogle et al. (2010), and some are among the most extreme MOHEGs known. (A1835 is a marginal case.) H_2 scaled by PAH emission is a measure of the power of the energy source for the H_2 (definitely shocks in most cases) relative to the star formation power. However, when H_2 is scaled by total star formation instead of by PAH 7.7 μm emission (a measure of obscured star formation, which is adequate for most normal star formation but not for the exposed star formation environments found in many cool-core BCGs), we estimate that cool-core BCGs become more moderate. They still have high H_2 emission relative to normal star-formers, but their H_2 heating mechanism may not be as efficient as the most extreme radio MOHEGs and the shock front in Stephan's Quintet.

We gauge the efficiency of the heating mechanism for the H_2 by comparing its luminosity to normal star formation calibrations, and correlating to weakly ionized neon emission scaled the same way. Star formation may account for the atomic emission, but it cannot account for the H_2 emission in at least two targets and perhaps in others as well. Furthermore, the atomic gas and H_2 are correlated when the power of star formation is scaled out, suggesting that they share a heat source which may not be star formation. The second heat source only stands out in the case of A2597, where it heats the neon 5$\times$ as efficiently as star formation alone, and heats the H_2 10$\times$ more efficiently than star formation alone, and in the case of MS0735, where there is no star formation detected at all.

We seek to distinguish between energetic particles from the ICM and shocks as the source of H_2 emission in cool-core BCGs. The efficiency with which the heating source heats up the cold gas reservoir offers some clues. Cool-core BCGs convert at most 10% of their cold H_2 gas to a cool state; most convert substantially less. However, 10% is the *minimum* cool gas fraction for radio MOHEGs (Ogle et al. 2010), indicating that the mechanism in cool-core BCGs is inherently less efficient at heating cold H_2 than the types of shock systems (associated with galaxy interactions and radio-jet outflows) found in the radio MOHEGs. This is not conclusive because there are many types of shocks, and the model of energetic particles discussed in Fabian et al. (2011a) does not predict the efficiency with which the hot ICM will convert large reservoirs of cold H_2 to a cool state.

Another clue is that the heating source acts upon both the H_2 and neon, but approximately twice as efficiently upon the H_2 relative to the effect of star formation alone. We found that the relationship between neon and H_2 luminosities in our sample is consistent with the ratio in the filaments of NGC 1275 (upon which the Fabian et al. (2011a) model was based) but not with some systems where the H_2 is generated in shocks caused by interacting systems. More analysis may determine whether shocks are capable of producing neon and H_2 which are correlated in the same way as in cool-core BCGs.

This is far from a proof of the energetic particle model, or a refutement of all shock types as the source of the H_2 heating. In fact, considering that all MOHEGs until this sample have been associated with shock heating of H_2, it would take extraordinary evidence to demonstrate that another mechanism can generate such luminous H_2 relative to indicators of star formation. However, we have demonstrated that the model of shocks in interacting systems or other large-scale motions of gas within a system does not consistently describe the H_2 in cool-core BCGs. Specifically, the cool-core BCGs may not heat their cold reservoirs of H_2 as efficiently as shocks typically do, and the relationship between H_2 and neon emission may be different in shocked systems than it is in our targets. These results, along with those in Chapter 4, are consistent thus far with the Fabian et al. (2011a) model, though the predictions of that model have not been rigorously tested on this sample. Rather than being an abnormal case, NGC 1275 may provide a template for the extended filamentary systems of cool-core BCGs. Other heating mechanisms may also be relevant, such as magnetohydrodynamic waves driven by the jet, or cosmic rays from the hot radio lobes.

Cool-core BCGs resist reduction in their analysis because some have no star formation and others have multiple and simultaneous environments of star formation (chains of H II regions in extended filaments, extended jet-induced SF, or nuclear starbursts). Moreover, the AGN in some cool-core BCGs produces a powerful warm dust continuum and all of the MIR hallmarks of a radio galaxy, while the AGN in others has little impact on the MIR spectrum. Thus far, however, all cool-core BCGs are consistent with a network of molecular filaments raining in from the cooling radius (though enriched by gas and dust from the central mixing region of the ICM) where hot ICM particles penetrate the filament and stimulate $H\alpha$ and warm H_2 emission.

Chapter 6

Summary

In Chapter 2, we present and study a rich MIR data cube of the nearest super star cluster, 30 Doradus. Aromatic dust emission features are of modest strength, concentrated in the arc-like two-lobed ridge coincident with CO emission and partially encircling the central R136 cluster. The dust temperature is high. Rotational H_2 lines are weak, though the H_2 0-0 S(3) line is detected. Three distinct regions of high extinction are found. The dominant spectral features are low to moderate ionization emission lines, which are sensitive to the physical conditions in the ionized gas. We map excitation in 30 Doradus and find that it generally follows the "ridge and bubble" morphology. We find local photoionization by hot stars to be dominant in the region, more than distance from R136, and identify several "hot spots."

In Chapter 3, we presented the IRS spectra and IRAC / MIPS broadband photometry of a sample of nine cool core BCGs. We detected very bright molecular hydrogen rotational transitions, PAH features, and forbidden lines from ionized gas (Ne II, Ne III), in addition to dust continuum at $15-25$ μm. These galaxies were known previously to have prominent optical and ultraviolet indications of star formation. The PAHs in this sample have ratios indicating that the PAHs in such BCGs are heated by star formation and are similar in size and ionization distributions to PAHs in spiral galaxies, though also suggesting a weaker radiation field. The PAHs appear not to have been traumatized by the destructive X-ray radiation and fast-moving thermal particles in the hot ICM.

Fits of simulated starburst models show that the star formation rates inferred from the $5-25$ μm spectra are consistent with star formation rates inferred from our 70 μm MIPS photometry. The luminosity of the warm ionized gas, traced by the [Ne II]12.6 μm emission line, is also correlated with the dust luminosity, so it is likely that the star formation powering the dust luminosity is also contributing to the heating of the warm ISM. However, the relation is distinctly non-linear, in the sense that the systems with lower IR luminosities have larger [Ne II]/IR ratios. All of the systems are over-luminous in [Ne II] compared with PAH or dust emission. Even more strikingly, the molecular hydrogen luminosities of BCGs are very high compared to that expected from star-forming galaxies of similar infrared luminosities. The H_2 luminosities are only weakly correlated with the mid IR or PAH luminosities, suggesting that the H_2 emission line power source is nearly independent of that powering the dust. The strong correlation of the molecular hydrogen line luminosity scaled by L_{24} with [Ne II] scaled in the same way suggests that the warm gas has a second heat source that may be related to the primary power source for the molecular hydrogen emission lines, a scenario consistent with excess heating by energetic particles and/or conduction from the hot intracluster gas.

In Chapter 4, we compare the optical and ultraviolet (exposed) vs infrared (obscured) indicators of star formation. Considering the thermal dust continuum (which is surprisingly weak in most cases), the PAH emission, and low-ionization emission, we find that one target (MS0735) has no indicators of star formation, six have unusually exposed star formation, and the remaining two (A1068 and A1835) seem to have both obscured and exposed star formation, which may arise in different spatial regions. Most cool-core BCGs which are close enough to resolve demonstrate signs of extended emission such as filaments that emit Hα and warm H_2 light, in which knots of star formation are sometimes found.

Normal star formation in a central disk-like environment or starburst, with a relatively high ($\gtrsim 60\%$) degree of extinction of optical-UV light from young stars, is not able to reproduce our results. We consider in particular whether a model of the filaments in NGC 1275 applies to our targets. In this model, the observed filaments

(~ 50 kpc long, ~ 100 pc wide) have an intricate substructure of fine threads (~ 0.3 pc wide) with 10 pc of separation on average between each. We find that this model may explain the exposed environment of star formation that we find in cool-core BCGs, and the unusually cool dust profile and undisturbed PAHs in some of the cool-core BCGs. In MS0735, we conclude that the same filamentary network is present, but not forming stars. In A1068 and A1835, the filamentary network is forming stars, but there is also a large body of normal, obscured star formation which might arise in an environment like a nuclear starburst.

We estimate the total (obscured + exposed) star formation in the cool-core BCGs and find that the efficiency of star formation relative to the cooling rate (which presumably supplies most of the fuel of star formation) ranges from $\sim 13\%$ to (in A1068) well above 100%.

In Chapter 5, we analyze the properties of the extraordinarily luminous pure rotational emission from warm H_2. We consider whether the proposed heating mechanism in the filamentary model mentioned above, saturated conduction into the filaments from the surrounding hot ICM, is realistic, and we consider shocks (which are associated with all other sources where H_2 is particularly luminous relative to indicators of star formation).

We perform excitation analysis to find temperatures and masses of warm H_2, and compare to other luminous sources of warm H_2 emission. While A1068 and A1835 may be consistent with ZwCl 3146 in heating up as much as 10% of their large reservoirs of cold gas to a cool (> 100 K) state, the others have smaller reservoirs of cold gas and do not heat it efficiently (cool gas fractions are $\lesssim 1$ %) though there are some indications that they tend to have a larger hot gas fraction ($\gtrsim 1000$ K) than comparable radio galaxies.

All cool-core BCGs which have been examined belong in the category of molecular hydrogen emission galaxies (MOHEGs). The significance of the category may be that the source of heat for H_2 is much more efficient than star formation alone. While many of our cool-core BCGs fall among the most extreme MOHEGs by the criteria used, we suggest that the criteria depend upon measurements of obscured star formation, and that if the exposed star formation were taken into account, cool-core BCGs would be found to be consistently moderate among MOHEGs, not heating their H_2 as efficiently as some of the most extreme interacting systems.

We test the efficiency of the H_2 heating relative to the power of star formation. We include measures of exposed and obscured star formation. We confirm that H_2 and atomic line emission are still correlated when scaled by the power of star formation, but the additional source of heating is not as extreme as previously thought. Star formation may account for the atomic gas emission, but not for the H_2 emission in at least two (and possible more) targets.

We consider whether shocks or saturated conduction from the ICM are more likely to heat the H_2 in the filaments. Our results are consistent with the model of saturated conduction, though more rigorous tests are called for. The model of shocks in interacting systems or other large-scale motions of gas within a system does not consistently describe the H_2 in cool-core BCGs. Specifically, the cool-core BCGs may not heat their cold reservoirs of H_2 as efficiently as shocks typically do, and the relationship between H_2 and neon emission may be different in shocked systems than it is in our targets. However, we do not rule out shock heating in cool-core BCGs.

Cool-core BCGs resist reduction in their analysis because some have no star formation and others have multiple and simultaneous environments of star formation (chains of H II regions in extended filaments, extended jet-induced SF, or nuclear starbursts). Moreover, the AGN in some cool-core BCGs produces a powerful warm dust continuum and all of the MIR hallmarks of a radio galaxy, while the AGN in others has little impact on the MIR spectrum. Thus far, however, all cool-core BCGs are consistent with a network of molecular filaments raining in from the cooling radius (though enriched by gas and dust from the central mixing region of the ICM) where hot ICM particles penetrate the filament and stimulate Hα and warm H_2 emission.

References

Abel, N. P., & Satyapal, S. 2008, ApJ, 678, 686

Allamandola, L. J., Tielens, A. G. G. M., & Barker, J. R. 1985, ApJ, 290, L25

—. 1989, ApJS, 71, 733

Allen, S. W. 1995, MNRAS, 276, 947

Allen, S. W., et al. 1992, MNRAS, 259, 67

Alonso-Herrero, A., Rieke, G. H., Rieke, M. J., Colina, L., Pérez-González, P. G., & Ryder, S. D. 2006, ApJ, 650, 835

Appleton, P. N., et al. 2006, ApJ, 639, L51

Armus, L., et al. 2006, ApJ, 640, 204

—. 2009, PASP, 121, 559

Asplund, M., Grevesse, N., & Sauval, A. J. 2005, in Astronomical Society of the Pacific Conference Series, Vol. 336, Cosmic Abundances as Records of Stellar Evolution and Nucleosynthesis, ed. T. G. Barnes III & F. N. Bash, 25–+

Balogh, M. L., Pearce, F. R., Bower, R. G., & Kay, S. T. 2001, MNRAS, 326, 1228

Beirão, P., Appleton, P. N., Brandl, B. R., Seibert, M., Jarrett, T., & Houck, J. R. 2009, ApJ, 693, 1650

Bendo, G. J., et al. 2008, MNRAS, 389, 629

Bernard, J., et al. 2008, AJ, 136, 919

Bigiel, F., Bolatto, A. D., Leroy, A. K., Blitz, L., Walter, F., Rosolowsky, E. W., Lopez, L. A., & Plambeck, R. L. 2010a, ApJ, 725, 1159

Bigiel, F., Leroy, A., Walter, F., Blitz, L., Brinks, E., de Blok, W. J. G., & Madore, B. 2010b, AJ, 140, 1194

Bildfell, C., Hoekstra, H., Babul, A., & Mahdavi, A. 2008, MNRAS, 389, 1637

Bîrzan, L., Rafferty, D. A., McNamara, B. R., Wise, M. W., & Nulsen, P. E. J. 2004, ApJ, 607, 800

Black, J. H., & Dalgarno, A. 1976, ApJ, 203, 132

Black, J. H., & van Dishoeck, E. F. 1987, ApJ, 322, 412

Boulanger, F., Boisssel, P., Cesarsky, D., & Ryter, C. 1998, A&A, 339, 194

Bower, R. G., Benson, A. J., Malbon, R., Helly, J. C., Frenk, C. S., Baugh, C. M., Cole, S., & Lacey, C. G. 2006, MNRAS, 370, 645

Brandl, B. R., et al. 2006, ApJ, 653, 1129

Brandner, W., Grebel, E. K., Barbá, R. H., Walborn, N. R., & Moneti, A. 2001, AJ, 122, 858

Bregman, J. D., Bregman, J. N., & Temi, P. 2008, in Astronomical Society of the Pacific Conference Series, Vol. 381, Infrared Diagnostics of Galaxy Evolution, ed. R.-R. Chary, H. I. Teplitz, & K. Sheth, 34–+

Bressan, A., et al. 2006, ApJ, 639, L55

Breysacher, J., Azzopardi, M., & Testor, G. 1999, A&AS, 137, 117

Burns, J. O. 1990, AJ, 99, 14

Buson, L., et al. 2009, ApJ, 705, 356

Calzetti, D., et al. 2010, ApJ, 714, 1256

Canning, R. E. A., Fabian, A. C., Johnstone, R. M., Sanders, J. S., Conselice, C. J., Crawford, C. S., Gallagher, III, J. S., & Zweibel, E. 2010, ArXiv e-prints

Cardiel, N., Gorgas, J., & Aragon-Salamanca, A. 1998, MNRAS, 298, 977

Castelli, F., & Kurucz, R. L. 2004, ArXiv Astrophysics e-prints

Cavagnolo, K. W., Donahue, M., Voit, G. M., & Sun, M. 2008, ApJ, 683, L107

Chapman, S. C., Blain, A. W., Smail, I., & Ivison, R. J. 2005, ApJ, 622, 772

Chiar, J. E., & Tielens, A. G. G. M. 2006, ApJ, 637, 774

Chu, Y., Gruendl, R. A., Chen, C., Lazendic, J. S., & Dickel, J. R. 2004, ApJ, 615, 727

Churazov, E., Brüggen, M., Kaiser, C. R., Böhringer, H., & Forman, W. 2001, ApJ, 554, 261

Churazov, E., Forman, W., Jones, C., & Böhringer, H. 2000, A&A, 356, 788

Cleary, K., Lawrence, C. R., Marshall, J. A., Hao, L., & Meier, D. 2007, ApJ, 660, 117

Clemens, M. S., Bressan, A., Panuzzo, P., Rampazzo, R., Silva, L., Buson, L., & Granato, G. L. 2009, MNRAS, 392, 982

Cluver, M. E., et al. 2010, ApJ, 710, 248

Colless, M., et al. 2003

Conroy, C., & Ostriker, J. P. 2008, ApJ, 681, 151

Conselice, C. J., Gallagher, III, J. S., & Wyse, R. F. G. 2001, AJ, 122, 2281

Cox, D. P., & Raymond, J. C. 1985, ApJ, 298, 651

Crawford, C. S., Allen, S. W., Ebeling, H., Edge, A. C., & Fabian, A. C. 1999, MNRAS, 306, 857

Croton, D. J., et al. 2006, MNRAS, 365, 11

Dale, D. A., & Helou, G. 2002, ApJ, 576, 159

Dale, D. A., et al. 2006, ApJ, 646, 161

—. 2007, ApJ, 655, 863

—. 2009, ApJ, 693, 1821

Dickel, J. R., Milne, D. K., Kennicutt, R. C., Chu, Y., & Schommer, R. A. 1994, AJ, 107, 1067

Donahue, M., de Messières, G. E., O'Connell, R. W., Voit, G. M., Hoffer, A., McNamara, B. R., & Nulsen, P. E. J. 2011, ArXiv e-prints

Donahue, M., Mack, J., Voit, G. M., Sparks, W., Elston, R., & Maloney, P. R. 2000, ApJ, 545, 670

Donahue, M., Sun, M., O'Dea, C. P., Voit, G. M., & Cavagnolo, K. W. 2007a, AJ, 134, 14

Donahue, M., et al. 2007b, ApJ, 670, 231

—. 2010, ApJ, 715, 881

Dopita, M. A., et al. 2006, ApJ, 639, 788

Draine, B. T., & Li, A. 2007, ApJ, 657, 810

Dudik, R. P., Weingartner, J. C., Satyapal, S., Fischer, J., Dudley, C. C., & O'Halloran, B. 2007, ApJ, 664, 71

Dunn, R. J. H., & Fabian, A. C. 2006, MNRAS, 373, 959

Edge, A. C. 2001, MNRAS, 328, 762

Edge, A. C., Wilman, R. J., Johnstone, R. M., Crawford, C. S., Fabian, A. C., & Allen, S. W. 2002, MNRAS, 337, 49

Edge, A. C., et al. 2010a, A&A, 518, L46+

—. 2010b, A&A, 518, L47+

Edwards, L. O. V., Hudson, M. J., Balogh, M. L., & Smith, R. J. 2007, MNRAS, 379, 100

Egami, E., Rieke, G. H., Fadda, D., & Hines, D. C. 2006a, ApJ, 652, L21

Egami, E., et al. 2006b, ApJ, 647, 922

Elbaz, D., Cesarsky, C. J., Chanial, P., Aussel, H., Franceschini, A., Fadda, D., & Chary, R. R. 2002, A&A, 384, 848

Elston, R., & Maloney, P. 1994, in Astrophysics and Space Science Library, Vol. 190, Astronomy with Arrays, The Next Generation, ed. I. S. McLean, 169–+

Fabian, A. C. 1994, ARA&A, 32, 277

Fabian, A. C., Johnstone, R. M., Sanders, J. S., Conselice, C. J., Crawford, C. S., Gallagher, III, J. S., & Zweibel, E. 2008, Nature, 454, 968

Fabian, A. C., Sanders, J. S., Taylor, G. B., Allen, S. W., Crawford, C. S., Johnstone, R. M., & Iwasawa, K. 2006, MNRAS, 366, 417

Fabian, A. C., Sanders, J. S., Williams, R. J. R., Lazarian, A., Ferland, G. J., & Johnstone, R. M. 2011a, ArXiv e-prints

Fabian, A. C., Voigt, L. M., & Morris, R. G. 2002, MNRAS, 335, L71

Fabian, A. C., et al. 2011b, ArXiv e-prints

Falcke, H., Rieke, M. J., Rieke, G. H., Simpson, C., & Wilson, A. S. 1998, ApJ, 494, L155+

Farrah, D., et al. 2007, ApJ, 667, 149

Fazio, G. G., et al. 2004, ApJS, 154, 10

Ferland, G. J., Fabian, A. C., Hatch, N. A., Johnstone, R. M., Porter, R. L., van Hoof, P. A. M., & Williams, R. J. R. 2008, MNRAS, 386, L72

—. 2009, MNRAS, 392, 1475

Ferland, G. J., Korista, K. T., Verner, D. A., Ferguson, J. W., Kingdon, J. B., & Verner, E. M. 1998, PASP, 110, 761

Förster Schreiber, N. M., Roussel, H., Sauvage, M., & Charmandaris, V. 2004, A&A, 419, 501

France, K., McCandliss, S. R., & Lupu, R. E. 2007, ApJ, 655, 920

Galliano, F., Dwek, E., & Chanial, P. 2008a, ApJ, 672, 214

Galliano, F., Madden, S. C., Tielens, A. G. G. M., Peeters, E., & Jones, A. P. 2008b, ApJ, 679, 310

Genzel, R., & Cesarsky, C. J. 2000, ARA&A, 38, 761

Genzel, R., et al. 1998, ApJ, 498, 579

Gómez, P. L., Loken, C., Roettiger, K., & Burns, J. O. 2002, ApJ, 569, 122

Gordon, K. D., et al. 2007, PASP, 119, 1019

Groves, B., Dopita, M. A., Sutherland, R. S., Kewley, L. J., Fischera, J., Leitherer, C., Brandl, B., & van Breugel, W. 2008, ApJS, 176, 438

Guillard, P. 2010, PhD thesis, Institut Astrophysique Spatiale

Guo, F., & Oh, S. P. 2009, MNRAS, 400, 1992

Guo, F., Oh, S. P., & Ruszkowski, M. 2008, ApJ, 688, 859

Hansen, L., Jorgensen, H. E., & Norgaard-Nielsen, H. U. 1995, A&A, 297, 13

Hansen, L., Jørgensen, H. E., & Nørgaard-Nielsen, H. U. 1997, Ap&SS, 257, 311

Hartigan, P., Raymond, J., & Hartmann, L. 1987, ApJ, 316, 323

Hatch, N. A., Crawford, C. S., Fabian, A. C., & Johnstone, R. M. 2005, MNRAS, 358, 765

Heckman, T. M., Baum, S. A., van Breugel, W. J. M., & McCarthy, P. 1989, ApJ, 338, 48

Helou, G. 1999, in ESA Special Publication, Vol. 427, The Universe as Seen by ISO, ed. P. Cox & M. Kessler, 797–+

Hewitt, J. W., Rho, J., Andersen, M., & Reach, W. T. 2009, ApJ, 694, 1266

Hicks, A. K., & Mushotzky, R. 2005, ApJ, 635, L9

Hicks, A. K., Mushotzky, R., & Donahue, M. 2010, ApJ, 719, 1844

Higdon, S. J. U., Armus, L., Higdon, J. L., Soifer, B. T., & Spoon, H. W. W. 2006, ApJ, 648, 323

Higdon, S. J. U., et al. 2004, PASP, 116, 975

Hill, J. M., & Oegerle, W. R. 1993, AJ, 106, 831

Hiner, K. D., Canalizo, G., Lacy, M., Sajina, A., Armus, L., Ridgway, S., & Storrie-Lombardi, L. 2009, ApJ, 706, 508

Ho, L. C., & Keto, E. 2007, ApJ, 658, 314

Hollenbach, D., & McKee, C. F. 1989, ApJ, 342, 306

Houck, J. R., Weedman, D. W., Le Floc'h, E., & Hao, L. 2007, ApJ, 671, 323

Houck, J. R., et al. 2004, ApJS, 154, 18

Hu, E. M., Cowie, L. L., & Wang, Z. 1985, ApJS, 59, 447

Hubeny, I., & Lanz, T. 1995, ApJ, 439, 875

Huber, K., & Herzberg, G. 1979, Molecular Spectra and Molecular Structure IV. Constants of Diatomic Molecules (Van Nostrand)

Hudson, D. S., Mittal, R., Reiprich, T. H., Nulsen, P. E. J., Andernach, H., & Sarazin, C. L. 2010, A&A, 513, A37+

Hunstead, R. W., Murdoch, H. S., & Shobbrook, R. R. 1978, MNRAS, 185, 149

Hunter, D. A. 1999, in IAU Symposium, Vol. 190, New Views of the Magellanic Clouds, ed. Y.-H. Chu, N. Suntzeff, J. Hesser, & D. Bohlender, 217–+

Hunter, D. A., & Kaufman, M. 2007, AJ, 134, 721

Hyland, A. R., Straw, S., Jones, T. J., & Gatley, I. 1992, MNRAS, 257, 391

Indebetouw, R., et al. 2005, ApJ, 619, 931

—. 2009, ApJ, 694, 84

Jaffe, W., & Bremer, M. N. 1997, MNRAS, 284, L1

Jaffe, W., Bremer, M. N., & Baker, K. 2005, MNRAS, 360, 748

Jaffe, W., Bremer, M. N., & van der Werf, P. P. 2001, MNRAS, 324, 443

Johansson, L. E. B., et al. 1998, A&A, 331, 857

Johnson, K. E. 2004, New Astronomy Review, 48, 1337

Johnstone, R. M., Fabian, A. C., & Nulsen, P. E. J. 1987, MNRAS, 224, 75

Johnstone, R. M., Hatch, N. A., Ferland, G. J., Fabian, A. C., Crawford, C. S., & Wilman, R. J. 2007, MNRAS, 382, 1246

Joseph, R. D., Wade, R., & Wright, G. S. 1984, Nature, 311, 132

Kaneda, H., Onaka, T., & Sakon, I. 2005, ApJ, 632, L83

Kaneda, H., Onaka, T., Sakon, I., Kitayama, T., Okada, Y., & Suzuki, T. 2008, ApJ, 684, 270

Kaneda, H., Onaka, T., Sakon, I., Kitayama, T., Okada, Y., Suzuki, T., Ishihara, D., & Yamagishi, M. 2010, ApJ, 716, L161

Kemper, F., Vriend, W. J., & Tielens, A. G. G. M. 2004, ApJ, 609, 826

Kenney, J. D. P., Tal, T., Crowl, H. H., Feldmeier, J., & Jacoby, G. H. 2008, ApJ, 687, L69

Kennicutt, R. C., et al. 2009, ApJ, 703, 1672

Kennicutt, Jr., R. C. 1990, in Astrophysics and Space Science Library, Vol. 161, The Interstellar Medium in Galaxies, ed. H. A. Thronson Jr. & J. M. Shull, 405–435

Kennicutt, Jr., R. C. 1998a, ARA&A, 36, 189

—. 1998b, ApJ, 498, 541

Kennicutt, Jr., R. C., et al. 2003, PASP, 115, 928

Kereš, D., Katz, N., Weinberg, D. H., & Davé, R. 2005, MNRAS, 363, 2

Kim, S. 2007, in Astronomical Society of the Pacific Conference Series, Vol. 362, The Seventh Pacific Rim Conference on Stellar Astrophysics, ed. Y. W. Kang, H.-W. Lee, K.-C. Leung, & K.-S. Cheng, 297–+

Kirkpatrick, C. C., Gitti, M., Cavagnolo, K. W., McNamara, B. R., David, L. P., Nulsen, P. E. J., & Wise, M. W. 2009, ApJ, 707, L69

Koekemoer, A. M., O'Dea, C. P., Sarazin, C. L., McNamara, B. R., Donahue, M., Voit, G. M., Baum, S. A., & Gallimore, J. F. 1999, ApJ, 525, 621

Koekemoer, A. M., O'Dea, C. P., Sarazin, C. L., McNamara, B. R., Donahue, M., Voit, M., Baum, S. A., & Gallimore, J. F. 2002, New Astronomy Review, 46, 149

Lacy, J. H., et al. 2007, ApJ, 658, L45

Laine, S., Appleton, P. N., Gottesman, S. T., Ashby, M. L. N., & Garland, C. A. 2010, AJ, 140, 753

Laurent, O., Mirabel, I. F., Charmandaris, V., Gallais, P., Madden, S. C., Sauvage, M., Vigroux, L., & Cesarsky, C. 2000, A&A, 359, 887

Lazareff, B., Castets, A., Kim, D.-W., & Jura, M. 1989, ApJ, 336, L13

Lazendic, J. S., Dickel, J. R., & Jones, P. A. 2003, ApJ, 596, 287

Lebouteiller, V., Bernard-Salas, J., Brandl, B., Whelan, D. G., Wu, Y., Charmandaris, V., Devost, D., & Houck, J. R. 2008, ApJ, 680, 398

Lebouteiller, V., Bernard-Salas, J., Sloan, G. C., & Barry, D. J. 2010, PASP, 122, 231

Lefloch, B., Cernicharo, J., Cabrit, S., Noriega-Crespo, A., Moro-Martín, A., & Cesarsky, D. 2003, ApJ, 590, L41

Leger, A., & Puget, J. L. 1984, A&A, 137, L5

Leitherer, C., et al. 1999, ApJS, 123, 3

Li, A., & Draine, B. T. 2001, ApJ, 554, 778

Lodders, K. 2003, ApJ, 591, 1220

—. 2008, ApJ, 674, 607

Lu, N., et al. 2008, PASP, 120, 328

Lutz, D., Sturm, E., Genzel, R., Spoon, H. W. W., Moorwood, A. F. M., Netzer, H., & Sternberg, A. 2003, A&A, 409, 867

Madden, S. C., Galliano, F., Jones, A. P., & Sauvage, M. 2006, A&A, 446, 877

Maercker, M., & Burton, M. G. 2005, A&A, 438, 663

Markwardt, C. B. 2009, in Astronomical Society of the Pacific Conference Series, Vol. 411, Astronomical Data Analysis Software and Systems XVIII, ed. D. A. Bohlender, D. Durand, & P. Dowler, 251–+

Martel, A. R., Sparks, W. B., Allen, M. G., Koekemoer, A. M., & Baum, S. A. 2002, AJ, 123, 1357

Martín-Hernández, N. L., et al. 2002, A&A, 381, 606

Martínez-Galarza, J. R., Groves, B., Brandl, B., de Messières, G. E., Indebetouw, R., , & Dopita, M. 2011, submitted

Mazzotta, P., Edge, A. C., & Markevitch, M. 2003, ApJ, 596, 190

McDonald, M., Veilleux, S., & Mushotzky, R. 2011a, ApJ, 731, 33

McDonald, M., Veilleux, S., Rupke, D. S. N., & Mushotzky, R. 2010, ApJ, 721, 1262

McDonald, M., Veilleux, S., Rupke, D. S. N., Mushotzky, R., & Reynolds, C. 2011b, ArXiv e-prints

McNamara, B. R. 1995, ApJ, 443, 77

—. 2002, New Astronomy Reviews, 46, 141

McNamara, B. R., Jannuzi, B. T., Sarazin, C. L., Elston, R., & Wise, M. 1999, ApJ, 518, 167

McNamara, B. R., Kazemzadeh, F., Rafferty, D. A., Bîrzan, L., Nulsen, P. E. J., Kirkpatrick, C. C., & Wise, M. W. 2009, ApJ, 698, 594

McNamara, B. R., & Nulsen, P. E. J. 2007, ARA&A, 45, 117

McNamara, B. R., & O'Connell, R. W. 1989, AJ, 98, 2018

—. 1993, AJ, 105, 417

McNamara, B. R., O'Connell, R. W., & Sarazin, C. L. 1996, AJ, 112, 91

McNamara, B. R., Wise, M. W., & Murray, S. S. 2004, ApJ, 601, 173

McNamara, B. R., et al. 2001, ApJ, 562, L149

—. 2006, ApJ, 648, 164

Meixner, M., et al. 2006, AJ, 132, 2268

Mendoza, C., & Zeippen, C. J. 1982, MNRAS, 199, 1025

Menéndez-Delmestre, K., et al. 2009, ApJ, 699, 667

Micelotta, E. R., Jones, A. P., & Tielens, A. G. G. M. 2010, A&A, 510, A37+

Minkowski, R. 1957, in IAU Symposium, Vol. 4, Radio astronomy, ed. H. C. van de Hulst, 107–+

Molinari, S., & Noriega-Crespo, A. 2002, AJ, 123, 2010

Morisset, C., Schaerer, D., Bouret, J., & Martins, F. 2004, A&A, 415, 577

Neufeld, D. A., Hollenbach, D. J., Kaufman, M. J., Snell, R. L., Melnick, G. J., Bergin, E. A., & Sonnentrucker, P. 2007, ApJ, 664, 890

Neufeld, D. A., et al. 2006, ApJ, 649, 816

Noriega-Crespo, A., Moro-Martin, A., Carey, S., Morris, P. W., Padgett, D. L., Latter, W. B., & Muzerolle, J. 2004a, ApJS, 154, 402

Noriega-Crespo, A., et al. 2004b, ApJS, 154, 352

O'Dea, C. P., Baum, S. A., Mack, J., Koekemoer, A. M., & Laor, A. 2004, ApJ, 612, 131

O'Dea, C. P., et al. 2008, ApJ, 681, 1035

O'Dea, K. P., et al. 2010, ApJ, 719, 1619

Ogle, P., Antonucci, R., Appleton, P. N., & Whysong, D. 2007, ApJ, 668, 699

Ogle, P., Boulanger, F., Guillard, P., Evans, D. A., Antonucci, R., Appleton, P. N., Nesvadba, N., & Leipski, C. 2010, ApJ, 724, 1193

Okamoto, Y. K., Kataza, H., Yamashita, T., Miyata, T., & Onaka, T. 2001, ApJ, 553, 254

Panuzzo, P., et al. 2007, ApJ, 656, 206

Parker, J. W. 1993, AJ, 106, 560

Peck, A. B., Goss, W. M., Dickel, H. R., Roelfsema, P. R., Kesteven, M. J., Dickel, J. R., Milne, D. K., & Points, S. D. 1997, ApJ, 486, 329

Peeters, E., Spoon, H. W. W., & Tielens, A. G. G. M. 2004, ApJ, 613, 986

Peeters, E., et al. 2002, A&A, 381, 571

Peterson, J. R., Kahn, S. M., Paerels, F. B. S., Kaastra, J. S., Tamura, T., Bleeker, J. A. M., Ferrigno, C., & Jernigan, J. G. 2003, ApJ, 590, 207

Poglitsch, A., Krabbe, A., Madden, S. C., Nikola, T., Geis, N., Johansson, L. E. B., Stacey, G. J., & Sternberg, A. 1995, ApJ, 454, 293

Quillen, A. C., et al. 2008, ApJS, 176, 39

Rafferty, D. A., McNamara, B. R., & Nulsen, P. E. J. 2008, ApJ, 687, 899

Rafferty, D. A., McNamara, B. R., Nulsen, P. E. J., & Wise, M. W. 2006, ApJ, 652, 216

Rakowski, C. E., Raymond, J. C., & Szentgyorgyi, A. H. 2007, ApJ, 655, 885

Raymond, J. C. 1979, ApJS, 39, 1

Rieke, G. H., Alonso-Herrero, A., Weiner, B. J., Pérez-González, P. G., Blaylock, M., Donley, J. L., & Marcillac, D. 2009, ApJ, 692, 556

Rieke, G. H., et al. 2004, ApJS, 154, 25

Rigby, J. R., & Rieke, G. H. 2004, ApJ, 606, 237

Romanishin, W. 1987, ApJ, 323, L113

Romanishin, W., & Hintzen, P. 1988, ApJ, 324, L17

Rosa, M., & Mathis, J. S. 1987, ApJ, 317, 163

Rosenberg, J. L., Wu, Y., Le Floc'h, E., Charmandaris, V., Ashby, M. L. N., Houck, J. R., Salzer, J. J., & Willner, S. P. 2008, ApJ, 674, 814

Roussel, H., Sauvage, M., Vigroux, L., & Bosma, A. 2001, A&A, 372, 427

Roussel, H., et al. 2007, ApJ, 669, 959

Rubio, M., Barbá, R. H., Walborn, N. R., Probst, R. G., García, J., & Roth, M. R. 1998, AJ, 116, 1708

Sakon, I., Onaka, T., Ishihara, D., Ootsubo, T., Yamamura, I., Tanabé, T., & Roellig, T. L. 2004, ApJ, 609, 203

Salim, S., et al. 2009, ApJ, 700, 161

Salomé, P., & Combes, F. 2003, A&A, 412, 657

Salomé, P., Combes, F., Revaz, Y., Edge, A. C., Hatch, N. A., Fabian, A. C., & Johnstone, R. M. 2008a, A&A, 484, 317

—. 2008b, A&A, 484, 317

Sargsyan, L. A., & Weedman, D. W. 2009, ApJ, 701, 1398

Sauvage, M., Tuffs, R., & Popescu, C. 2005, Space Science Reviews, 119, 313, 10.1007/s11214-005-8071-0

Schaefer, B. E. 2008, AJ, 135, 112

Schaerer, D., & de Koter, A. 1997, A&A, 322, 598

Schmitt, H. R., Storchi-Bergmann, T., & Cid Fernandes, R. 1999, MNRAS, 303, 173

Schutte, W. A., Tielens, A. G. G. M., & Allamandola, L. J. 1993, ApJ, 415, 397

Shaver, P. A., McGee, R. X., Newton, L. M., Danks, A. C., & Pottasch, S. R. 1983, MNRAS, 204, 53

Shaw, G., Ferland, G. J., Henney, W. J., Stancil, P. C., Abel, N. P., Pellegrini, E. W., Baldwin, J. A., & van Hoof, P. A. M. 2009, ApJ, 701, 677

Sheth, K. 2006, in Spitzer Data Analysis Workshop #4

Simpson, J. P., Colgan, S. W. J., Cotera, A. S., Erickson, E. F., Hollenbach, D. J., Kaufman, M. J., & Rubin, R. H. 2007, ApJ, 670, 1115

Sloan, G. C., Hayward, T. L., Allamandola, L. J., Bregman, J. D., Devito, B., & Hudgins, D. M. 1999, ApJ, 513, L65

Smith, J. D. T., et al. 2007a, PASP, 119, 1133

—. 2007b, ApJ, 656, 770

Smith, L. J., Norris, R. P. F., & Crowther, P. A. 2002, MNRAS, 337, 1309

Smith, R. J., et al. 2004, AJ, 128, 1558

Snijders, L., Kewley, L. J., & van der Werf, P. P. 2007, ApJ, 669, 269

Sofia, U. J., & Jenkins, E. B. 1998, ApJ, 499, 951

Soker, N. 2008, ApJ, 684, L5

Solomon, P. M., Rivolo, A. R., Barrett, J., & Yahil, A. 1987, ApJ, 319, 730

Sparks, W. B., Macchetto, F., & Golombek, D. 1989, ApJ, 345, 153

Spitzer Science Center. 2006, Spitzer Space Telescope Observer's Manual, Spitzer Science Center, Version 7.1

Spoon, H. W. W., Marshall, J. A., Houck, J. R., Elitzur, M., Hao, L., Armus, L., Brandl, B. R., & Charmandaris, V. 2007, ApJ, 654, L49

Springel, V., Di Matteo, T., & Hernquist, L. 2005, ApJ, 620, L79

Stasińska, G., & Schaerer, D. 1997, A&A, 322, 615

Stocke, J. T., Morris, S. L., Gioia, I. M., Maccacaro, T., Schild, R., Wolter, A., Fleming, T. A., & Henry, J. P. 1991, ApJS, 76, 813

Sturm, E., Lutz, D., Tran, D., Feuchtgruber, H., Genzel, R., Kunze, D., Moorwood, A. F. M., & Thornley, M. D. 2000, A&A, 358, 481

Sturm, E., Lutz, D., Verma, A., Netzer, H., Sternberg, A., Moorwood, A. F. M., Oliva, E., & Genzel, R. 2002, A&A, 393, 821

Tayal, S. S., & Gupta, G. P. 1999, ApJ, 526, 544

Thornley, M. D., Schreiber, N. M. F., Lutz, D., Genzel, R., Spoon, H. W. W., Kunze, D., & Sternberg, A. 2000, ApJ, 539, 641

Tielens, A. G. G. M. 2008, ARA&A, 46, 289

Tielens, A. G. G. M., & Hollenbach, D. 1985, ApJ, 291, 722

Townsley, L. K., Broos, P. S., Feigelson, E. D., Brandl, B. R., Chu, Y., Garmire, G. P., & Pavlov, G. G. 2006, AJ, 131, 2140

Treyer, M., et al. 2010, ApJ, 719, 1191

Tsamis, Y. G., & Péquignot, D. 2005, MNRAS, 364, 687

Turner, J., Kirby-Docken, K., & Dalgarno, A. 1977, ApJS, 35, 281

van Breugel, W., Fragile, C., Anninos, P., & Murray, S. 2004, in IAU Symposium, Vol. 217, Recycling Intergalactic and Interstellar Matter, ed. P.-A. Duc, J. Braine, & E. Brinks, 472–+

van Breugel, W., Heckman, T., & Miley, G. 1984, ApJ, 276, 79

Van Kerckhoven, C., et al. 2000, A&A, 357, 1013

Veilleux, S., et al. 2009, ApJS, 182, 628

Verma, A., Lutz, D., Sturm, E., Sternberg, A., Genzel, R., & Vacca, W. 2003, A&A, 403, 829

Vermeij, R., Peeters, E., Tielens, A. G. G. M., & van der Hulst, J. M. 2002, A&A, 382, 1042

Voit, G. M. 1992a, MNRAS, 258, 841

—. 1992b, ApJ, 399, 495

Voit, G. M., & Donahue, M. 1997, ApJ, 486, 242

Walborn, N. R. 1991, in IAU Symposium, Vol. 148, The Magellanic Clouds, ed. R. Haynes & D. Milne, 145–+

Weedman, D., et al. 2006, ApJ, 653, 101

Weedman, D. W., et al. 2005, ApJ, 633, 706

Weingartner, J. C., & Draine, B. T. 2001, ApJ, 548, 296

Werner, M. W., et al. 2004, ApJS, 154, 1

Wilman, R. J., Edge, A. C., McGregor, P. J., & McNamara, B. R. 2011, ArXiv e-prints

Wu, Y., et al. 2010, ApJ, 723, 895

Zabludoff, A. I., Huchra, J. P., & Geller, M. J. 1990, ApJS, 74, 1

Zakamska, N. L. 2010, Nature, 465, 60

Zhu, Y.-N., Wu, H., Cao, C., & Li, H.-N. 2008, ApJ, 686, 155

ZuHone, J. A. 2011, ApJ, 728, 54